Utilising an In Silico Approach to Determine Vulnerability to Reentrant Arrhythmias

Hill, Yolanda Roselle

Awarding institution:
King's College London

Utilising an *In Silico* Approach to Determine Vulnerability to Reentrant Arrhythmias

Yolanda R. Hill

Department of Imaging Sciences and Biomedical Engineering

School of Medicine

King's College London

October 2015

This thesis is submitted for the degree of Doctor of Philosophy

For my family...

Acknowledgements

I would like to thank my supervisors Dr Martin Bishop and Professor Nic Smith for their guidance throughout my PhD. I would also like to thank them for accepting me, having just completed my undergraduate degree in Biology with Psychology, as their PhD student, providing me with a pathway into the Biomedical Engineering sphere. My thanks go to Martin for his hands-on help with the technical aspects of the research as well as for guiding the project to fit my research interests. I extend my thanks to Nic for lending his invaluable expertise to the overall guidance of the research.

All of the simulations performed during this research were conducted using the CARP software and I would therefore, sincerely like to thank Dr Gernot Plank for allowing me to use the software which has been so vital to this work. The study of the RVI was a collaborative process and so thanks are also given to Professor Peter Taggart, Dr Ben Hanson and Dr Nick Child for the always interesting and constructive meetings that we had and for their valued counsel.

I would like to acknowledge that the work presented in this thesis was funded by the King's College London Medical Engineering Centre (MEC) which is supported by the Wellcome Trust and the Engineering and Physical Sciences Reseach Council (EPSRC).

Thank you to my wonderful friends, not only for their extensive technical help but also for their much appreciated advice, support and willingness to talk things through over a hot drink! Particularly, I would like to say a huge thank you to Abdul Haji Dheere, Sara Gattoni, Kirsten Christensen-Jeffries, Markus Schirmer, Giulio Ferrazzi, Arian Beqiri, Elaine Damato, Anastasia Nasopoulou, Myria Hadjicharalambous, Bojan Blazevic, Rui Texeira, Silvia Lorrio-Gonzalez, Adam Connolly and many others who have brightened my day with a smile and a kind word.

Finally, I would like to thank my family for their continual love, support and encouragement. Thank you Youssef for not only your help with computational issues but for your positivity, strength, and for sharing the journey with me. Dad, thank you for teaching me the fundamentals of coding and your willingness to help me with the maths, for your level-headed words of wisdom and for being a massive source of inspiration to me. Mum, thank you for looking after me as I finish writing, for proofreading my thesis, for our endless natterings which light up my day and for always listening. Thank you Oli, for the insightful biological discussions and for teaching me the importance of enjoying life!

Abstract

Post-myocardial infarction arrhythmias are a leading cause of death in developed countries, motivating research to improve treatment strategies. Ischemic damage occurring due to a myocardial infarction results in the formation of inexcitable infarct scars. Electrical activation waves circumvent these structural barriers and can propagate in perpetual reentrant circuits giving rise to ventricular tachycardia. The success of reentrant propagation depends on the wavelength of the activation wave with respect to the physical path length, determining the extent of wavefront-waveback interactions.

A wide variety of animal and computational models are used to perform research however, the optimal species for studying clinical arrhythmias is unknown. One aim of the research in this Thesis was to suggest a species model which most closely replicates clinical arrhythmia dynamics. Computational models were utilised to compare the susceptibility to reentry, by calculating the effective electrical size of the heart, which takes into consideration both the size of the wavelength and the physical size of the heart. Results suggested that species differences in effective size exist between human and animal models. However, the effective size of the rabbit model was most similar to the human. This conclusion was utilised to formulate methodologies for the following studies.

Current techniques employed to locate ablation lesion sites during radiofrequency catheter ablation are inaccurate, leading to insufficient procedure success rates. Here, a method to accurately locate optimal ablation lesion targets was investigated utilising computational models. Quantification of wavelength permitted the observation of wavefront-waveback interactions to predict susceptibility to reentry. The clinical application of the methodology was modelled to ensure that ablation of the susceptible tissue could terminate reentry and that the limitations of clinical data acquisition did not invalidate the technique. The method accurately located a region of tissue where reentry could potentially occur and ablation of the region terminated reentry even when clinical protocol was simulated.

This research suggests the most suitable species models to research ventricular tachycardia, guiding further *in vivo* and *in silico* methodologies. Additionally, a protocol to improve the success of the ablation procedure has been further investigated. Clinical implementation of this technique could vastly improve the treatment of post-myocardial infarction arrhythmias.

Publications

The following publications are directly related to the work presented in this Thesis.

- Child, N., Bishop, M. J., Hanson, B., Coronel, R., Opthof, T., Boukens, B. J., Walton, R. D., Efimov, I. R., Bostock, J., Hill, Y., Rinaldi, C. A., Razavi, R., Gill, J., Taggart, P. (2015). An activation-repolarisation time metric to predict localized regions of high susceptibility to reentry. *Heart Rhythm.* **12**(7), p.1644-1653.

- Hill, Y., Plank, G., Smith, N., Bishop, M. (2013). Comparison of changes in effective electrical size with activation rate between small mammalian and human ventricular models. In: Ourselin, S., Rueckert, D., Smith, N. (eds). *Functional Imagining and Modelling of the Heart. 7th international conference proceedings.* LNCS 7945. London: Springer.

Contents

List of Figures

List of Tables

Acronyms

AP Action Potential

APD Action Potential Duration

ARI Activation Recovery Interval

AT Activation Time

ATP Adenosine Triphosphate

BCL Basic Cycle Length

BDB Bi-Directional Block

BZ Border-Zone

CARP Cardiac Arrhythmias Research Package

CO Cardiac Output

CV Conduction Velocity

DI Diastolic Interval

ECG Electrocardiogram

ERP Effective Refractory Period

FE Finite Element

FEM Finite Element Method

FF Fibrillation Factor

ICD Implantable Cardioverter Defibrillator

IDP Isolated Diastolic Potential

LAD Left Anterior Descending

LV Left Ventricle

MI Myocardial Infarction

MRI Magnetic Resonance Imaging

NCX Sodium Calcium Exhange Pump

ODE Ordinary Differential Equation

RT Repolarisation Time

RV Right Ventricle

RVI Reentry Vulnerability Index

SCD Sudden Cardiac Death

SERCA Sarcoplasmic Reticulum Ca^{2+} ATPase

SR Sarcoplasmic Reticulum

UDB Uni-Directional Block

VF Ventricular Fibrillation

VT Ventricular Tachycardia

XMR X-ray Magnetic Resonance

Nomenclature

λ	Wavelength
ϕ_e	Extracellular potential
ϕ_i	Intracellular potential
σ	Conductivity
F	Faraday constant
R	Gas constant
T	Temperature
Z	Valency of an ion
$_i$	Intracellular
$_o$	Extracellular
BZ_{APD}	BZ region of the model displaying lengthened APD
BZ_{cond}	BZ region of the model displaying slow CV
C_m	Membrane capacitance
E	Equilibrium potential/Nernst potential
g	Conductance of the membrane
G_{Ks}	Conductance of I_{Ks}
I	Effective electrical size of the heart
I_c	Capacitative current

I_K Potassium current

I_m Transmembrane current (in cable theory $I_m = I_{ion} + I_c$)

I_{CaL} L-type calcium current

I_{ion} Total transmembrane current

I_{K1} Inward rectifying potassium current

I_{Kr} Rapid delayed rectifying potassium current

I_{Ks} Slow delayed rectifying potassium current

I_{leak} Background leak current

I_{NaCa} Sodium-calcium exchange pump current

I_{NaK} Sodium-potassium pump current

I_{Na} Sodium current

I_{stim} Stimulus current

I_{to} Transient outward potassium current

J Electrical current density

P Permeability

R Resistance

r Radius

r_s Search radius

$RVI_{area<50}$ Area of model displaying RVI less than 50ms

RVI_{min} Minimum RVI in the model

V_m Membrane potential

V_{rest} Resting membrane potential

$\sqrt[3]{M}$ Cube root of the mass of the heart

[ ]	Concentration of species within bracket
APD_{50}	APD calculated at 50% repolarisation
APD_{90}	APD calculated at 90% repolarisation
Cl^-	Chloride ions
Cx43	Connexin-43
K^+	Potassium ions
Na^+	Sodium ions
Q	Charge

Chapter 1

Introduction

1.1 Motivation

Non-communicable diseases are an increasing health concern as the average life expectancy increases alongside escalating risk factors such as high cholesterol, diabetes and obesity. Heart disease is a non-communicable disease which currently accounts for approximately a quarter of all deaths in the UK and costs the National Health Service in the region of £6 billion each year[1]. These statistics illustrate the necessity for research into the causes, pathologies and possible treatment strategies of heart disease to lessen the health and economic burdens imposed on society by the related disorders.

In particular, sudden cardiac death (SCD) is the cause of approximately 100,000 deaths in the UK each year[2] and is characterised by a sudden loss of cardiac function. The most common cause of SCD is the occurrence of an abnormal heart rhythm. The function of the heart is to pump blood around the body to supply vital oxygen to the tissues as a result of its consistent, rhythmic, mechanical contraction. A disruption of the rhythm may cause insufficient oxygen to be supplied to the heart and the brain, resulting in death within minutes.

Ventricular tachycardia (VT) is a disturbance of the heart rhythm, otherwise termed an arrhythmia, in which the heart rate is increased. Electrical activation waves propagate across the walls of the heart and generate mechanical contractions. The regular, synchronous propagation of the activation waves ensures that the contractions are rhythmic, thus maintaining efficient cardiac function. VT occurs due to alterations to the physi-

[1]Source: British Heart Foundation https://www.bhf.org.uk/publications/statistics/cardiovascular-disease-statistics-2014

[2]Source: National Health Service http://www.nhs.uk/Livewell/Healthyhearts/Pages/Arrhythmias.aspx

cal path along which the waves propagate, in turn altering the rhythm of contraction. The disruption and increased rate of wave propagation which occurs during VT can be a precursor to more serious arrhythmias such as ventricular fibrillation (VF). In VF, wave propagation further destabilises as a result of the increase in activation rate during VT, causing the wavefronts to break up. Instead of one homogeneous wavefront propagating over the walls of the heart to produce synchronous contractions, many small dynamically changing wavefronts exist, causing rapid, irregular contractions. This leads to severly impaired cardiac function and unless treated, SCD (Weiss et al., 2000).

A common cause of VT stems from the prior occurrence of a heart attack, otherwise known as a myocardial infarction (MI), in which a lack of blood supply to parts of the heart causes scar tissue to form there as a result of ischemic injury. In fact, approximately 125,000 heart attacks occur each year in the UK[3] and contribute to ischemic heart disease being a leading cause of death in the country[4]. As a result of an MI, regions of infarct scar tissue lose the essential electrical properties of the myocardium and become unable to conduct the electrical activation waves. Therefore, wavefronts are diverted around scar tissue, altering the path of wave propagation. Waves are only able to propagate through surviving tissue around the scar which often results in circuitous paths of activation. Crucially, wave propagation around a region of scar can be sustained in what is termed a reentrant circuit which, due to the short path length of the circuit, increases the heart rate as contraction follows the pattern of disturbed activation.

1.2 Cardiac Excitation Wavelength

The electrical property of cardiac function is conferred on the myocardium due to a potential difference being invoked by the movement of ions into and out of the cells. Broadly speaking, when the movement of ions in a region of tissue produces a deflection in the potential difference, the tissue is said to be activated. Activation of the tissue occurs as the ions move across the myocardium, producing waves of electrical activation which spread throughout the tissue. A fundamental parameter of an activation wave is the wavelength which is defined as the length of tissue which is activated at a particular moment in time. An important control mechanism of cardiac function ensures that only tissue which is inactive can be activated, so that waves can only propagate into a region which is inactive.

[3]Source: Heart Rhythm Institute http://www.hriuk.org/about-heart-disease/heart-facts/
[4]Source: Office for National Statistics http://www.ons.gov.uk/ons/dcp171778 381807.pdf

Considering that the wavelength of a wave describes an activated region of tissue, it is conceivable that the wavelength can determine the success of wave propagation throughout the tissue. A wave travelling across the myocardium will be terminated or diverted if it collides with tissue which is already activated, or a structural obstacle, ultimately altering the dynamics of wave propagation (Hayden et al., 1967; Azene et al., 2001). Moreover, wavelength is rate-dependent due to time-dependent mechanisms which control the cellular flux of ions, and varies with varying heart rate, dynamically altering the conduction of waves across the myocardium (Smeets et al., 1986; Girouard and Rosenbaum, 2001; Matthews et al., 2013). Theoretically, in the most simplified examples, a larger wavelength will produce more wavefront-waveback interactions resulting in a disruption of the normal wave patterns. However, the many variables affecting wave propagation dynamics may interact in complex ways producing a variety of outcomes.

At the turn of the 20th century, a pioneering electrophysiologist, George Mines, was conducting some of the first experiments which would uncover how the activation wavelength could determine the progression of complex wave patterns in the heart (Mines, 1913, 1914). Initally, his experiments showed that the nature of the heart beat changed in response to a change in the frequency of the stimulation of the heart. This observation prompted Mines to further investigate the impact of the rate dependency of the heart beat on wave propagation. Using simple heart tissue ring preparations from rays, dog-fish, frogs, tortoises, cats and dogs, Mines stimulated the preparations at varying frequencies and observed that, at a particular, relatively fast frequency of stimulation, the excitation wave propagated around the ring of tissue in a self-sustaining circuit, re-activating the ring without further external stimuli. These experiments highlighted the importance of a short and slow activation wave, occurring due a change in stimulation frequency, in order for the wave to continue to re-excite the tissue within the circuit without terminating due to wavefront-waveback interactions. Mines proposed that this reentrant activation could cause the observed pathologies of tachycardia and fibrillation.

It is vital to understand the mechanisms which underlie reentrant propagation in order to be able to further investigate these arrhythmias and potential treatment strategies. In particular, using metrics of wavelength can elucidate the nature of wave propagation and can be used to infer the propensity of the tissue to reentry.

1.3 Computational Modelling of Cardiac Arrhythmias

Implementing research to study cardiac electrical activity in patients is fraught with difficulties. Research conducted on patients is subject to strict ethical constraints. Specifically, the research must not cause any undue negative impact on the patient (Taggart et al., 2014). In fulfilling this requirement, research is often carried out during prerequired procedures. As a result, investigations must be performed within the limited time frame of the procedure and must utilise techniques which do not increase the invasiveness or danger of the procedure. Due to these restrictions, sample sizes of clinical research remain small, limiting the validity of the results. In all, whilst ethical review is essential for maintaining high standards of patient care during research activities, it limits the scope of clinical research. Despite these constraints, ventricular arrhythmias are studied in patients, usually by acquiring electrical activation data from the surface of the heart during cardiac surgery, utilising techniques that are no more invasive than the surgery being carried out (Nanthakumar et al., 2004; Nash et al., 2006). The dynamic nature of wave propagation and the progression of arrhythmias across the myocardium require the acquisition of data at multiple sites to sample the transit of the waves in order to be able to effectively study arrhythmias (Taggart et al., 2014). However, acquiring adequate data for this purpose is not without difficulty. In order for the data to adequately represent wave propagation, it is necessary to record a vast amount of data. Consequently, storing and processing such quantities of data becomes a limiting factor in clinical research. Significant expertise and skill is necessary to manipulate the recording device to sample data from the correct locations and avoid acquiring very noisy data. In addition, recording the data from a patient is a time consuming process and must be performed within the procedure time frame, reducing the amount of data which is able to be recorded. It is inevitable that with the limitation imposed by the manual manipulation of the recording device and the relatively short time frame, the spatial resolution of recorded data is limited and may not faithfully represent all wave propagation dynamics. Crucially, electrical activation waves propagate throughout the myocardial wall which also requires sampling if wave propagation is to be thoroughly and reliably investigated. However, temporal data of electrical activation waves are only routinely recorded from the surface of the heart in the clinic, hindering the ability to observe transmural propagation which could be vital to understand the initiation and mechanism of clinical arrhythmias.

Investigating arrhythmias in animal models reduces some of the limitations imposed by the ethical review of clinical research, although animal research is also regulated by ethical legislation. As such, animal models are often used to investigate arrhythmias with techniques which are not available in the clinic. For example, voltage-sensitive dyes are used to image wave propagation across the myocardium in real-time, with very much higher spatial resolution than is permitted by clinical data recording (Gray et al., 1998; Chen et al., 2000; Wu et al., 2004). Such data can provide exceptionally detailed information about the initiation, maintenance and termination of arrhythmias without requiring the degree of computational data storage and analysis demands which clinical investigation requires. However, the methodology used is still only confined to acquiring data on the surface of the heart, again potentially omitting vital information about the propagation of the disturbed activation waves throughout the myocardium. Moreover, significant differences in both the anatomy and electrophysiology occur between animals and humans rendering it difficult to extrapolate reliable conclusions from animal models to inform clinical scenarios (Coronel et al., 1997; Fink et al., 2011; O'Hara and Rudy, 2012) as both factors may play important roles in the mechanism of an arrhythmia. Additionally, ethical and financial burdens of animal research are not neglible and need to be taken into consideration when proposing methodological protocols (Mirams et al., 2012; Taggart et al., 2014). Although animal models are able to provide important data which can be used in investigating arrhythmias, significant drawbacks remain, motivating the use of alternative investigative approaches.

In light of the problems encountered by using patient and animal model data, computational models have been developed, utilised and thoroughly validated over the past few decades. Further, *in silico* models can provide novel insight into arrhythmia mechanisms which are otherwise unattainable from *in vivo* investigation. Of great importance is the ability to simulate cardiac function over multiple scales, from the cellular biophysics underlying the electrical properties, to the whole heart activation and contraction patterns (Clayton and Panfilov, 2008; Trayanova and Rice, 2011; Trayanova, 2011). The ability to model the system in a multiscale framework, provides the opportunity to investigate the mechanisms of a phenotype involved in arrhythmia dynamics as part of the integrated physiology of the heart (Evans, 2000; Lee et al., 2009; Niederer et al., 2009). In certain circumstances, experimental data alone cannot elucidate the detailed mechanism behind an observed feature, but when integrated into a multiscale modelling framework, the mech-

anism is contextualised and may be understood (Collins et al., 2003; Deisboeck et al., 2009; Niederer and Smith, 2012). However, in such complex models, it may be difficult to tease out individual components and draw conclusions about the mechanisms involved at a particular scale. Computational models can also be utilised to study single components of cardiac function, in order to reduce complexity of the models and identify detailed mechanisms giving rise to the arrhythmia. These models can also be predictive and so can prove invaluable in supplementing clinical research, for example to reduce performing unnecessary experiments in the clinic (Yang and Saucerman, 2011). Moreover, due to the limitations of clinical research, *in silico* models enable investigations which cannot be performed in the clinic (Yang and Saucerman, 2011). One important example of this is that clinical protocol only allows recording of electrical activation data from the surface of the heart, whereas computational models can be utilised to observe transmural propagation dynamics, providing insight into the complex 3D nature of arrhythmias. Likewise, the spatial and temporal resolution of data available from *in silico* modelling can be used to research the fine-scale details of wave propagation which may be missed by clinical recording techniques. Computational models therefore, provide a mechanism for studying arrhythmia dynamics in much more detail than can be done in patients, without such ethical and financial demands as encountered during clinical research.

Mathematical models of electrophysiology are used in *in silico* modelling studies to simulate the ion flux within a single cell which drives the electrical activation. Species specific models of electrophysiology are available including human and a variety of mammalian species models (Rudy and Silva, 2006; Clayton and Panfilov, 2008; Fenton and Cherry, 2008; Holzem et al., 2014). Studies which simulate cardiac function at the organ level require an electrophysiological component which simulates ion flux over the whole tissue, a mechanical contraction component, and a detailed anatomical model. Such models are also available for different species (Clayton and Panfilov, 2008; Trayanova and Rice, 2011; Trayanova, 2011) and have been utilised to investigate arrhythmias (Panfilov and Keener, 1995; Plank et al., 2008; Trayanova, 2011; Holzem et al., 2014; Trayanova and Rantner, 2014). The variety of models available make it possible to research arrhythmias in different species on many scales of complexity. As previously discussed, if possible, modelling human physiology is preferable to draw conclusions which may be of use in the clinic due to physiological differences between species. However, modelling the human heart, particularly in a multiscale framework, is exceptionally demanding in terms of computational

data storage and analysis, and requires the use of high-performance computing which is both costly and not universally available. As a consequence, computational models of animal species are used to study arrhythmias with reduced computational demands. In addition, *in silico* animal models are useful in order to determine how conclusions from *in vivo* animal studies may relate to the clinical scenario and to validate such conclusions.

1.4 Thesis Goal

The research in this Thesis uses a computational modelling approach to study how wavelength can be used to determine the susceptibility of the tissue to reentrant propagation. Metrics of wavelength are used to investigate species differences in arrhythmia dynamics as well as, in the context of scar-related arrhythmias, to investigate a novel method to locate a reentrant circuit in order to guide the ablation procedure. The concepts investigated are of significant interest as they may contribute directly to guiding arrhythmia research and clinical treatment strategies.

Animal models are extensively used to research arrhythmias and the conclusions are often extrapolated to the clinic. However, due to the physiological differences between species, some animal model studies may not be able to replicate clinical arrhythmias and hence, the resulting conclusions which may be drawn upon in the clinic, should be regarded with caution. The first aim of this Thesis is to investigate which species model most closely replicates the arrhythmia dynamics observed in the clinic, for the purposes of suggesting the most useful animal model to use in future research pertaining to VT arrhythmias. Both wavelength and heart size are critical determinants of wave propagation patterns and vary between species, suggesting that as a result, arrhythmia dynamics also vary significantly between species. A metric called the effective electrical size of the heart (which takes into consideration both the wavelength and the heart size) has been suggested to determine the similarity between species in terms of VF dynamics (Panfilov, 2006). Here we extend the previous study by observing how species differences in electrophysiological properties during conditions indicative of VT, combine to affect the wavelength of each species. Moreover, we investigate the species differences in the rate-dependency of wavelength, in order to determine whether each species displays similar rate-dependent effects on wavelength, or whether the differences in arrhythmia dynamics between species may increase with varying physiological parameters. The effective size calculation is performed

to study the combined effects of rate-dependent wavelength and the size of the hearts of different species to quantify the potential similarities in VT arrhythmia dynamics. Crucially, VT often occurs as a result of reentrant propagation around infarct scars caused by ischemic damage to the tissue. Ischemia also alters the electrophysiological properties of the myocardium, and hence wavelength, in the surviving tissue surrounding the infarction. The effective size calculation is used to determine whether species differences occur in effective size as a result of ischemic damage, in order to suggest whether a particular species model can replicate wave propagation dynamics of the human in both health and disease.

The second aim of this Thesis is to investigate the possibility of improving the treatment of post-MI VT utilising metrics of wavelength to determine the success of reentrant propagation. Currently, ablation therapy seeks to disrupt the physical path along which reentrant waves propagate to form reentrant circuits resulting in VT. As it stands, the lack of a sufficient methodology for locating the optimal region to disrupt the circuit results in poor treatment success rates and requires the induction of VT, which increases the risk of the procedure. A previous methodology utilised metrics of wavelength to determine whether reentry could occur around a simple circuit based on wavefront-waveback interactions in a porcine *in vivo* model. We utilise the fundamental concept to investigate whether the technique can be built upon and used to accurately locate reentrant circuits in the clinic without the danger to the patient of inducing VT. In addition to studying this technique in a human *in silico* model over a range of physiological conditions, including the addition of infarct scar obstacles into tissue level models, we aim to thoroughly examine the potential use of the technique in the clinic and optimise the algorithm by performing sensitivity analyses of the parameters implemented in the calculation. In particular, we determine whether the technique remains accurate when only data from the surface of the heart are available. In addition, we observe the impact that low resolution clinical recording has on the ability to locate the critical circuit in order to be able to conclude whether the technique could be of significant use in the clinic.

1.5 Thesis Outline

The Thesis begins with the presentation of the fundamental background information on cardiac physiology in Chapter 2, describing cardiac anatomy and in particular, outlining

how the movement of ionic particles causes the fundamental electrical activity of the myocardium at the single cell level. The chapter progresses with an account of the mechanism behind tissue level excitation leading to wave propagation. Both the characterisation and implication of the rate-dependency of electrophysiological properties are discussed. Background information is then presented on how data are recorded in *in vivo* studies and in the clinic. Following that account, the methodology behind representing single cell electrophysiology and activation of cardiac tissue with mathematical equations is explained. Importantly, an account of the pathology of MI is discussed, including the causes and progression of the disease in relation to VT and the chapter concludes with an overview of the ablation therapy used to treat VT.

A review of the relevant literature is presented in Chapter 3, beginning with an account of the work which reports and describes the mechanisms behind the occurrence of Post-MI VT. An outline of previous studies which have utilised animal models to study arrhythmias is then given, followed by a review of *in silico* models which have been utilised to investige arrhythmias. A presentation of the foundational study which implied that the effective size could determine the most suitable model to replicate clinical arrhythmias follows. We present an account of past and present ablation treatment strategies and their downfalls with a mention of how the procedure could be improved. An overview of the work which preceeds the research in Chapters 5 and 6, illustrating how measures of activation wavelength in a potential reentrant circuit can predict the success of reentry is then presented. The literature review ends with a discussion about where further research could enhance the literature which has been acknowledged in this chapter, further motivating the research presented as part of this Thesis.

Chapter 4 constitutes the first research chapter of the Thesis. The work in this chapter builds upon previous research suggesting that calculating the effective size of the heart can quantify species differences in wave propagation dynamics based upon wavelength and heart size. We use a simplified 2D geometrical model to simulate the electrophysiology of four small animal species using existing mathematical models. Observations of rate-dependent electrophysiological properties and their effects on wavelength are studied in order to investigate the rate-dependent species differences in effective size. Additionally, electrophysiological alterations as a result of MI are incorporated into the models, in order to observe their effect on the effective size of the hearts of different species.

In Chapter 5 we begin our research investigating the possibility of improving the ac-

curacy and success rates of the ablation procedure, by utilising metrics of wavelength to locate regions of tissue susceptible to reentry. We validate the technique in a simple 2D geometrical model using a human model to simulate cardiac electrophysiology. In this chapter we investigate whether the proposed technique is robust in the human model, across varying physiological conditions and considering the limitations imposed by clinical data recording, such as decreased resolution of the data. Crucially, we introduce a simplified obstacle to represent an MI scar and model the wave propagation around the scar to observe whether the technique can locate regions susceptible to reentry in more complex clinical scenarios.

The final results chapter (Chapter 6) presents the research conducted to thoroughly investigate the potential use of the technique to improve the ablation procedure in the clinical scenario. As such, a highly detailed geometrical model of the rabbit ventricles was utilised to minimise computational demand in return for the ability to conduct many simulations testing a variety of variables. We study the ability of the technique to locate regions of the heart susceptible to reentry utilising varying simplified scar geometries to simulate patient variation. Again, we investigate the impact of low resolution data recording on the surface of the heart in the clinic. The research presented in this chapter determines whether the technique to locate regions susceptible to reentry can guide the ablation procedure with increased accuracy and success rates.

Chapter 7 concludes the Thesis by presenting a summary of the results of the research conducted here, highlighting the impact of the results on the clinical treatment of post-MI VT. Following the summary, possible future directions to further validate and investigate the technique to guide the ablation procedure are discussed.

Chapter 2

Background Information

Presented in this chapter are the fundamental concepts of the structure and function of the heart in health and after an MI. Particularly, the excitability of the heart is described in sections which discuss the cellular mechanisms of the cardiac action potential and the action of excitation wave conduction across the myocardium. In addition, a discussion of the methodology behind both single cell and tissue level computational modelling is given. Following that, pathological alterations in cellular function and the subsequent disruption of the heart rhythm as a result of an MI are discussed. The chapter concludes with a description of radiofrequency catheter ablation therapy employed in the treatment of MI.

2.1 Cardiac Function

The function of the heart is to pump blood around the body, transporting oxygen and nutrients to cells which are required ubiquitously for maintaining cellular function and removing the by-products of cellular metabolism. Within one heartbeat, oxygenated blood is transported systemically to deliver oxygen and nutrients to the tissues and deoxygenated blood is returned to the heart to be pumped into the lungs for reoxygenation. The constant transportation of oxygenated blood throughout the circulatory system is essential to maintaining life, for in its absence, loss of consciousness and cardiac arrest, or SCD, occurs within minutes.

The heart must beat synchronously in order to maximise its efficiency. The myocardial wall contracts during systole to force blood out of the heart, to the lungs via the pulmonary system and around the body via the systemic system. Relaxation of the chambers occurs during diastole to allow blood to flow back into the heart. In the event that

contraction of the heart muscle becomes desynchronised, and the chambers contract out of phase with each other, the cardiac output (CO) of the heart is compromised due to insufficient presystolic filling. Thus, maintenance of the heart's function must be sustained and consistent throughout a lifetime, representing a vast amount of physical work and requiring sophisticated protective mechanisms. In health, the CO is maintained throughout varying physiological conditions to fulfil systemic oxygen demand.

2.2 Cardiac Anatomy

2.2.1 Gross Anatomy

The heart measures approximately 12cm from the apex (inferior) to the base (superior), 8cm in the lateral direction and 6cm in the anteroposterior direction. Figure 2.1 depicts

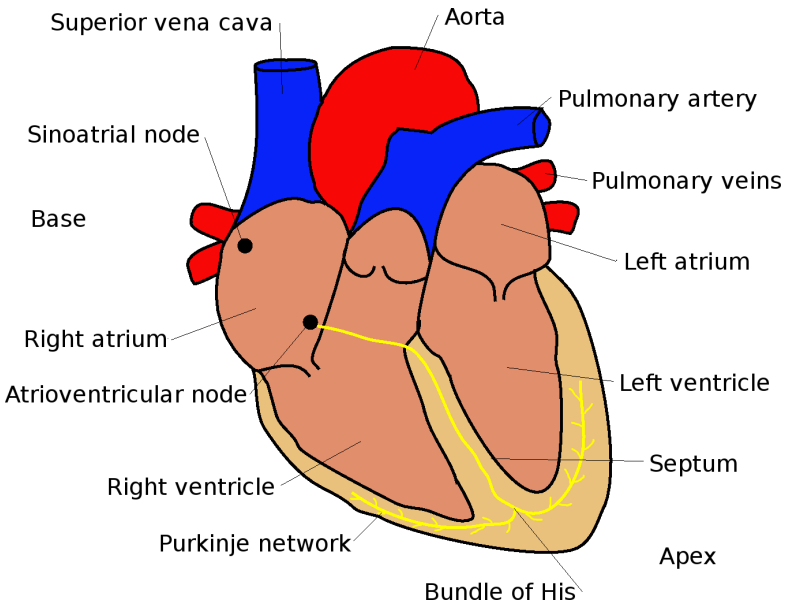

Figure 2.1: Diagram of the heart.

the gross geometry of the heart and its vessels. The compartmentalisation of the heart into four chambers facilitates the separation of oxygenated and deoxygenated blood and maintains the differentiated pressure gradients, required for the simultaneous transport of blood through the systemic and pulmonary circulatory systems. Valves separate the basal atria from the apical ventricles to maintain pressure gradients and ensure one-directional flow. Blood leaves the heart via the aorta and pulmonary artery and returns to the heart through the vena cava and pulmonary veins. The right and left ventricles (RV & LV respectively) are separated by myocardium named the interventricular septum which

forms part of the LV chamber. LV wall thickness increases from the apex to the base with an average depth of approximately 1cm. A thickened LV wall is required to withstand high pressures generated for the systemic transportation of blood. The inner surface of the heart chambers is termed the endocardium and the outer surfaces are termed the epicardium.

2.2.2 Cellular Anatomy

The myocardium is primarily comprised of electrically excitable, contractile myocytes. A fluid mosaic lipid bi-layer membrane called the sarcolemma, separates the myocytes from both each other and the extracelluar space. The sarcolemma forms due to the polar nature of phospholipid molecules which constitute the membrane. Ion channels and active transport pumps are incorporated into the sarcolemma and span the membrane, connecting the intracellular and extracellular spaces. Either subunits or single polypeptide chains make up the ion channels, which arrange to form pores through the membrane. It is the flux of ions through these membrane proteins which confers on the myocardium its electrical property. Selectivity to ion species is crucial for the electrical activity of the cell and is inferred either by the physical size of the pore, or by the charge or size of amino acids surrounding the pore. The protein molecules forming the ion channels are allosteric proteins which can attain open, closed or inactivated states. Conformational changes of the amino acid residues serve to either open or occlude a given channel in response to changes in voltage or time. Similarly, conformational changes in active transport pumps facilitate the uptake and release of ions at either side of the membrane. In Section 2.3, the importance of the mechanisms controlling the flux of ions across the membrane will be discussed as they are essential characteristics of cellular electrical activity.

Within the sarcoplasm of each cell, the units responsible for generating contractile force, the sarcomeres, are arranged to form long strands called myofibrils (Figure 2.2 (*left, top and middle*)). Sarcomeres contract longitudinally and so due to their intracellular arrangement, contractile force is generated in the direction parallel to the myofibrils. The importance of this property is contextualised in the following paragraph which describes how myocytes arrange to form cardiac tissue.

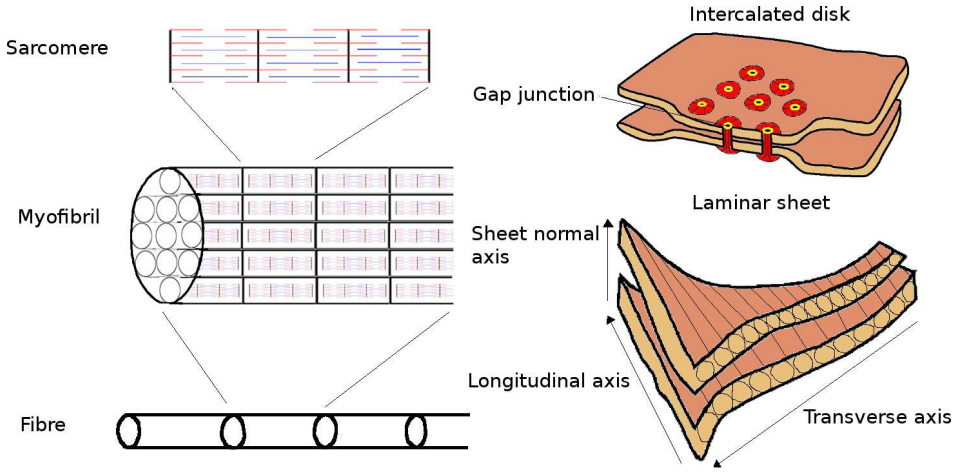

Figure 2.2: Structure of the myocardium. *Left, top to bottom* - Sarcomeres join to form myofibrils within the myocytes, and myocytes join to form longitudinal fibres. *Right, top* - Gap junctions within intercalated disks adjoin neighboring myocytes . *Right, bottom* - Myocyte fibres form laminar sheets with orthogonal fibre axes.

2.2.3 Myocardial Structure

Myocytes arrange end-to-end into longitudinal fibres (Figure 2.2 (*left, bottom*)), the direction of which determines the contractile strength of the myocardium. These fibres coalesce to form laminar sheets of myocardial tissue, a few cells thick (Figure 2.2 (*right, bottom*)). Importantly, the arrangement of the myocyte fibres within the myocardial wall, play a role in not only the anisotropic strength of contraction but also the anisotropic conduction of electrical activation waves through the myocardium, which will be discussed further in Section 2.3. The myocardium can be described as an orthotropic material with an axis parallel to the longitudinal fibre direction, an orthogonal axis in the transverse fibre direction in the plane of the sheet and a third orthogonal axis in the sheet normal direction. The angle of the fibres with respect to the apex-base axis of the heart is called the helix angle. The helix angle of the fibres varies from the epicardium to the endocardium, with the angle at the epicardium approximately tangential to the wall at $-60°$, transitioning through $0°$ in the midmyocardium to $+70°$ and tangential to the endocardial wall at the endocardium.

2.2.4 Intercellular Coupling

Neighbouring myocytes are coupled together via gap junctions in the sarcolemma (Figure 2.2 (*right, top*)), forming a syncytium in which the sarcoplasms of the myocytes are continuous. The continuity of the sarcoplasms plays a role in the conduction of electrical

activation waves throughout the tissue (see Section 2.3). Regions of the sarcolemma of two adjacent cells come into close proximity to each other (approximtely 2nm) at sites called intercalated disks. Gap junctions occur at the intercalated disks forming small pores called connexons which span from the sarcoplasm of one cell, through the extracellular space, into the sarcoplasm of an adjacent cell. The structure of the pore is formed by six integral membrane proteins called connexins (Connexin-43 (Cx43) predominates in the ventricles) and has a surface area of approximately 0.005μm. The pore of the gap junction allows molecules such as ions to flow from the sarcoplasms of adjacent cells whilst remaining discontinuous with the extracellular medium, forming a path of low resistance between myocytes.

On average, 11 myocytes are connected to each other via intercalated disks. Approximately 50% of gap junctions in a cell membrane are located at the ends of the myocyte and 50% are located along the edges (Saffitz, 1994). However due to the elongated cylindrical shape of the myocytes, a greater density of gap junctions occurs within the smaller surface areas of the ends than at the side edges. Gap junctions are dynamic structures within the sarcolemma whose connexin subunits are deposited and degraded every few hours. This high turnover of gap junction proteins facilitates the relocation and altered regulation of the gap junctions within the myocyte, in states of disease.

2.3 Cardiac Electrophysiology

The electrical property of cardiac tissue underlies the contractile mechanism of the heart and is therefore vital to cardiac function as a whole. The research presented in Chapters 4, 5 and 6 involves modelling electrical activity at the single cell and tissue level and so an understanding of the generation and propagation of electrical signals in the heart is essential and is discussed in this section. In addition, we consider how electrical signals generate cardiac contraction and lastly, look at a protective mechanism, cardiac restitution, which ensures that, despite an increase in heart rate, the heart maintains its functional capability.

2.3.1 The Membrane Potential

The phospholipid bilayer structure of the sarcolemma (discussed in Section 2.2) renders the membrane impermeable to ions, with ion channels facilitating transport of ionic species

into and out of the cell, conferring a selective permeability on the membrane. The conformational changes in the ion channels, commonly referred to as the gating mechanism, alters the permeability of the sarcolemma to specific ions. The regulated transportation of cations across the sarcolemma produces a difference in ionic concentration between the intra- and extracellular spaces, causing a potential difference which evokes the electrical property of the myocardium.

The diffusion of ions through species-selective gated ion channels is controlled by electrochemical gradients of the ions across the membrane. A specific species of ion diffuses across the sarcolemma through ion channels from a region of high concentration of that ion, to a region of low concentration of that ion, to balance its electrochemical concentration across the membrane. Differences in concentration of charge across a membrane occur, due to the permeability of the membrane to that ion and the ion's flux, causing a potential difference. When the electrical gradient is large enough to cause the net movement of the ion across the sarcolemma to cease, electrochemical equilibrium is reached. The potential difference across the membrane required to maintain this equilibrium is called the equilibrium potential (E). The Nernst equation (Equation 2.1) describes the equilibrium potential for a single ionic species (E_{ion}) where $[ion]_o$ denotes the extracellular concentration of the ion, $[ion]_i$ is the intracellular concentration of the ion, R is the gas constant, T is the temperature, Z is the valency of the ion and F is the Faraday constant.

$$E_{ion} = (\frac{\mathrm{RT}}{\mathrm{ZF}})ln(\frac{[ion]_o}{[ion]_i}) \tag{2.1}$$

An extension of the Nernst equation gives the Goldman equation (Equation 2.2) which produces the potential difference across the membrane, the membrane potential (V_m), considering that the membrane is permeable to more than one ion. In the case of cardiac myocytes, the membrane is primarily permeable to potassium (K^+), sodium (Na^+) and chloride (Cl^-) ions.

$$V_m = (\frac{\mathrm{RT}}{\mathrm{F}})ln(\frac{P_K[K^+]_o + P_{Na}[Na^+]_o + P_{Cl}[Cl^-]_i}{P_K[K^+]_i + P_{Na}[Na^+]_i + P_{Cl}[Cl^-]_o}) \tag{2.2}$$

where P is the permeability of the membrane to the ionic species. In contrast to ion channels which allow the passive diffusion of ions down the electrochemical gradient, active transport pumps transport particles across the membrane against the electrochemical gradient and require adenosine triphosphate (ATP) to do so.

2.3.2 The Cardiac Action Potential

The membrane potential of the cell at rest (V_{rest}) is approximately -80mV. At rest, the membrane is most permeable to K^+ and relatively impermeable to other cations. As such, V_m approaches the equilibrium potential of K^+ (E_K) at -85mV. However, V_m is slightly more positive than E_K due to a small inward potassium current through potassium leak channels, referred to as the inward rectifier current (I_{K1}).

Depolarisation of the cell membrane from V_{rest} constitutes an action potential (AP), the electrical signal that is transmitted across the heart to stimulate contraction. Figure 2.3 displays an AP and highlights the occurrence of four distinct phases caused by different ionic currents. As a positive current from a neighbouring cell depolarises the membrane

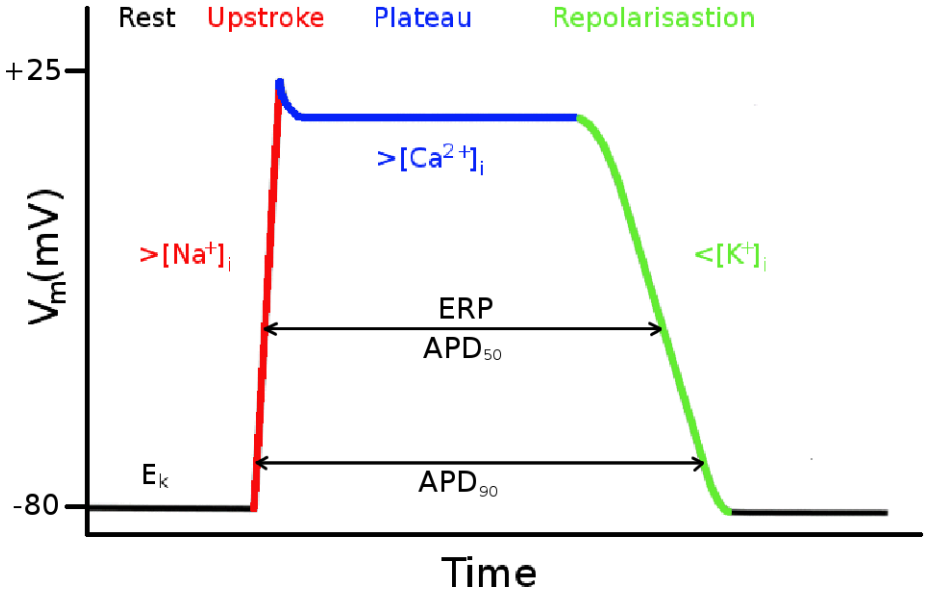

Figure 2.3: Diagram of a cardiac AP. E_K and the flux of ion concentrations driving the membrane potential are indicated. Approximate representations of ERP, APD_{50} and APD_{90} are labelled on the diagram.

from V_{rest} to approximately -65mV, the voltage gated sodium channels open, allowing an influx of Na^+ into the cell (*red*). This sodium current (I_{Na}) rapidly depolarises the cell membrane during the upstroke phase of the action potential. A second inward current of Ca^{2+} (I_{CaL}), initiated by the voltage-dependent gating of the ion channels at approximately -45mV, also contributes to the upstroke of the AP which terminates when V_m reaches its peak at approximately $+25$mV. Both I_{Na} and I_{CaL} inactivate after specific time periods. The plateau phase (*blue*) is a major contributor to the refractoriness of the tissue, a property which is vital in maintaining the regular contraction of the heart.

The initial part of this phase of the AP is due to I_{CaL} but this current plays another important role in the plateau phase. The influx of Ca^{2+} due to I_{CaL} causes the release of Ca^{2+} from intracellular stores within the sarcoplasmic reticulum (SR), maintaining the positive V_m at approximately 0mV. Also contributing to the plateau phase is the reduced permeability of the membrane to K^+ at higher V_m and the net influx of Na^+ through the sodium-calcium exchange pump (NCX), which extrudes one Ca^{2+} in exchange for the influx of three Na^+. Repolarisation of the membrane (*green*) occurs as sarcoplasmic calcium is taken up into the SR. Time-dependent potassium channels open causing an outward potassium current. In addition, the permeability of the membrane to K^+ increases as V_m falls, further repolarising the membrane until it reaches V_{rest}.

Refractoriness is the property of the tissue which ensures that ectopic stimulation (an abnormal stimulus occurring out of normal rhythm) of the membrane cannot elicit an AP. This feature safeguards the heart from possible ectopic beats and hence irregular or tetanic contractions which would cause inefficient cardiac function and impaired CO. During sinus rhythm, the action potential duration (APD) from the upstroke to repolarisation, is approximately $200 - 400$ms and is contributed to by the large plateau phase of the human cardiac AP. The effective refractory period (ERP) is described as the period in which no amount of further stimulation of the membrane can elicit another AP and ends slightly before total repolarisation of the membrane. The relative refractory period denotes a period of time after the ERP when the membrane is not at rest, but an AP can be initiated under the right circumstances. The time-dependent inactivation of sodium channels ensures that further APs cannot be initiated whilst these channels are inactive. The period of sodium channel inactivation produces the ERP and lasts until the membrane is nearly fully repolarised, when inactivation of the voltage-gated sodium channels ceases. The relative refractory period is produced by the voltage-dependence of the sodium channels, which must see a rise of approximately 15mV from V_{rest} before an AP is initiated. Hence, a large influx of positive current must occur during the relative refractory period in order to elicit an AP.

2.3.3 Conduction of Electrical Signals

Having described the mechanism of initiating an electrical potential at the single cell level, it is important to consider how these APs are conducted to produce waves of excitation which travel across the heart and cause mechanical contractions. Initially, we focus on

how the electrical potential is initiated in the pacemaker cells of the heart and go on to consider how that potential is conducted across the tissue.

Impulse Initiation

Initial electrical potential is conferred on the heart by the spontaneous activity of the autorhythmic cardiac pacemaker cells in the sinoatrial node. An electrical potential is initated across the membrane of these myocytes due to changes in the membrane conductance of ions. The autorhythmycity of these cells ensures the essential continuous rhythmic contraction of the heart, but the rate of autorhythmicity of the cells is controlled by the autonomic nervous system which alters membrane conductance, due to the stimulation of either β-adrenergic (excitatory) or nicotinic (inhibitory) receptors. The electrical potential then propagates across the atria, causing contraction of the atria, forcing blood into the ventricles. The electrical signal then reaches the atrioventricular node at which point, the activation spreads along fast-conducting impulse pathways down the bundle of His ($4 - 5\text{m/s}^{-1}$) to the apex of the heart and into the Purkinje system, from which homogeneous propagation of the ventricles begins simultaneously across the heart (0.5m/s^{-1}), forcing blood out of the ventricles. However, the Purkinje network is connected to the endocardium so that propagation of the electrical wave occurs primarily at the endocardium, spreading towards the epicardium in an apical-basal direction.

Electrotonic Current

The structure and location of gap junctions connecting the sarcoplasms of adjoining cells into a syncytium has already been discussed in Section 2.2. Their function is to electrically couple myocytes together, providing a low resistance pathway for ionic species to travel between cells. This continuity between cells allows the rapid transmission of electrical signals which enables synchronous depolarisation and contraction across the tissue. Gap junctions are gated via a complex voltage and time dependent mechanism, opening when the voltage across the gap junction is near to 0mV and closing at very positive or very negative voltages. When gap junctions are open, cations flow from the depolarised cell to neighbouring hyperpolarised cells, initiating an AP in adjacent cells. This flow of cations through gap junctions is called the electrotonic current, the magnitude of which is dependent on the number of gap junctions and gap junctional conductivity. An increase in electrotonic current increases the conduction velocity (CV) of the electrical signal. The

voltage sensitivity of the gating mechanism facilitates the flow of ions in one direction, ensuring that the propagation of the electrical signal flows in one direction. Thus, the flux of cations through the syncytium causes an electrical activation wave to propagate across the tissue with a largely homogeneous wavefront.

Electrical current is only transferred between cells through gap junctions and so the position of the gap junctions throughout the myocardium affects the shape of the wave as it propagates throughout the heart. Due to the higher concentration of gap junctions at the ends of the cylindrical myocytes and the more diffuse gap junctions positioned along the edges of the myocyte, electrotonic current flows faster longitudinally along the direction of the fibre than transversely between the edges of the myocytes. The anisotropic conductivity across the myocardium causes the CV in the longitudinal direction to be approximately three times faster than in the transverse direction. As a result of this anisotropy, the direction of the fibre affects the morphology of the wavefront. Due to the increased helix angles at the epi- and endocardium where fibre direction is approximately tangential to the wall, CV in the apical-basal direction is faster here than at the midmyocardium because of the preferential conduction along the fibre.

The success of the wave propagation is determined by the so-called source/sink relationship. The source is the current of the electrical signal and is provided by the influx of cations into a myocyte. The sink is the tissue which the source could potentially excite. A large source (whether it is a large current or current stemming from a large volume of tissue) and small sink will ensure safe and fast propagation of the electrical wave through the myocardium. Whereas large sinks and a small source (either a small current or current emanating from a small volume of tissue) will slow CV and possibly terminate the wave. In addition, resistance to the source current through the sarcoplasm and the gap junctions affects the sink and alters wave propagation success. These source/sink effects ultimately determine the shape of the propagation wave, the speed of conduction and the success of propagation.

2.3.4 Electromechanical Contraction

Blood is able to be actively pumped out of the heart because it is a muscle, contracting to force blood out of the ventricles in systole and relaxing to allow blood to flow back into the heart in diastole. As electrical signals propagate across the heart, each myocyte contracts due to a rise in intracellular calcium. The subcellular units responsible for generating

contractile force, the sarcomeres, are composed of actin filaments interspersed with myosin filaments which are held together by cross bridges. Contraction occurs when the myosin filament slides along the actin filament, shortening the length of the sarcomere. In a relaxed state, steric hindrance occurs between the actin and myosin filaments, preventing cross bridges forming. Calcium ions are able to relieve the steric inhibition allowing cross bridges to form between the filaments and the sliding mechanism which generates the contraction can occur. Sarcoplasmic concentration of calcium is very low when the cell is at rest so a rise in calcium is required for the initiation of contraction. This rise in calcium occurs during an AP, when the sarcoplasmic concentration of calcium is increased by in the influx of Ca^{2+} via I_{CaL} and via the release of Ca^{2+} from the SR, enabling the initiation of contraction.

2.3.5 Cardiac Restitution

Cardiac restitution is a cardio-protective mechanism which ensures regular contraction of the heart as the heart rate (synomymous with stimulation frequency) varies, maintaining efficient CO. The research presented in Chapters 4, 5 and 6 of this Thesis focuses on arrhythmias, a physiological condition which arises due to a disruption of the heart rhythm. Although this can be brought about by varying causes, increases in heart rate often facilitate the occurrence of arrhythmias. As will become evident in this section, APD, CV and wavelength all decrease as heart rate increases in order to preserve cardiac function. However, a concept which is fundamental to this Thesis and is discussed in Sections 2.6 and 3.2 and in Chapters 4, 5 and 6, is that a decrease in wavelength due to restitution effects increases the likelihood that an arrhythmia will occur. Therefore, an understanding of the mechanism and the implications of cardiac restitution is necessary to contextualise the research presented here.

Restitution is defined as the relationship between the APD and the interval between APs, the diastolic interval (DI). The APD is defined as the time between the upstroke and repolarisation of the AP. The upstroke occurs over a very short time period, typically a few milliseconds, whereas the repolarisation phase is longer. As such, it is possible to define repolarisation at different times, such as at 50% or 90% of repolarisation. Thus, the APD can be defined as the time between the upstroke and the time it takes to reach 50% of repolarisation (APD_{50}) and can also be defined as the time between the upstroke and the time it takes to reach 90% of repolarisation (APD_{90}). The DI is the interval

between APs during which the membrane is at rest and the heart is relaxed. The DI can be governed by the duration of time between stimuli, otherwise referred to as the basic cycle length (BCL) and so in terms of restitution, the relationship between APD and DI is analagous to the relationship between APD and BCL.

Restitution Pacing Protocols

Restitution protocols are performed to analyse the restitution relationship, the relationship between APD and DI, with varying pacing frequency. Two primary protocols are utilised to investigate the relationship; the dynamic and the S1S2 protocol.

The dynamic pacing protocol implements a gradual change in frequency and is illustrated on the *right* of Figure 2.4. Typically, x number of beats are paced at a certain

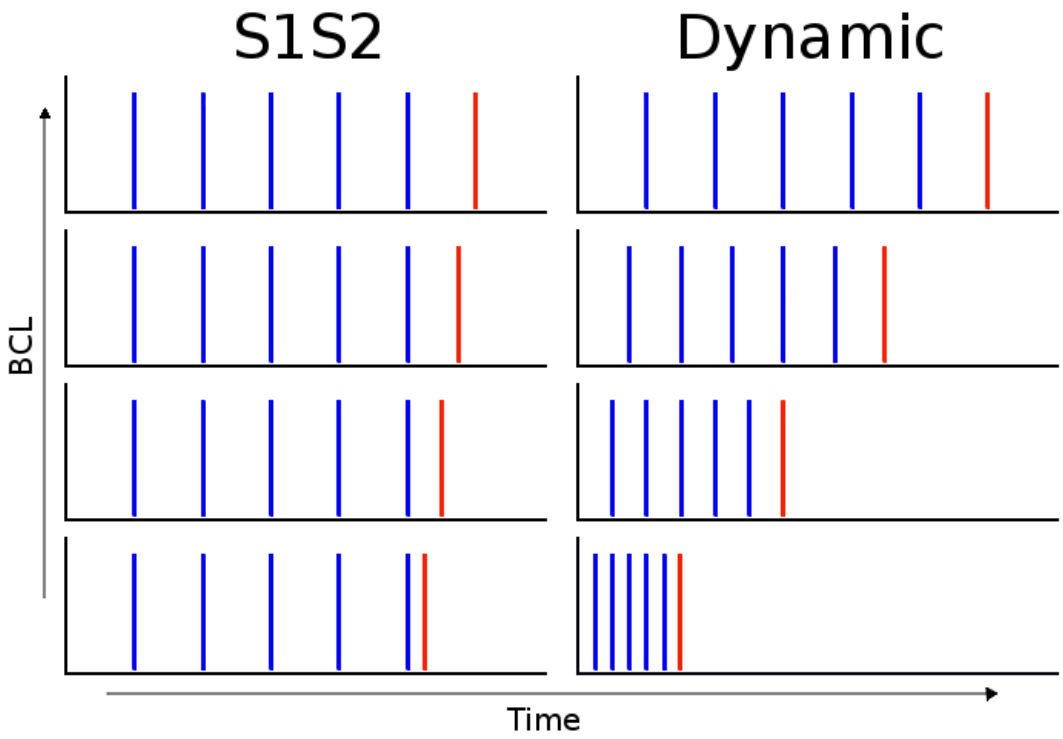

Figure 2.4: Restitution pacing protocols. $Left$ - S1S2 pacing protocol. *Right* - dynamic pacing protocol. Each vertical line represents a stimulus. BCL decreases from *top* to *bottom*. Stimulus from which AP data are recorded is shown in *red*.

BCL before the BCL is reduced. Another x number of beats are paced at the new BCL, and the pattern is repeated, decreasing the BCL each time. The APDs used in restitution

analysis are sampled at the end of each train of beats at a particular BCL, just before the stimulus train at a new BCL begins.

The S1S2 pacing protocol provides a more sudden change in pacing frequency and is illustrated on the *left* of Figure 2.4. The S1 stimulus constitutes pacing at a long BCL for x number of beats, shown in *blue* in the figure. A single, premature beat that is paced at a shorter BCL (*red*) is the S2 stimulus. The S1 phase is repeated with the intervening S2 beats paced at decreasing BCLs. The APD data are recorded from the premature S2 beats.

APD Restitution

APD displays rate dependency. As BCL decreases, the APD decreases ensuring that complete APs occur, to maintain efficient contraction of the myocardium and hence, cardiac function. Ion channels involved in an AP are controlled by complex gating mechanisms. Many channels such as the sodium channels, proceed to an inactive state after the open and closed states have taken place. The inactivation phase is time-dependent and hence, a particular period of time is required for the channels to recover from inactivaion before another AP can occur. Thus, the APD is dependent on the length of the previous DI. If a preceding DI is short, the subsequent APD will also be short due to insufficient recovery of the ion channels from inactivation. At very short BCLs, after a shortened AP, the DI may be slightly longer due to the premature repolarisation of the previous beat and so the subsequent AP occurring after the lengthened DI may be longer. The cycling of long-short-long-short APs is termed alternans. Calcium plays an important role in initiating and maintaining alternans. Due to the calcium-induced-calcium-release from the SR, a decrease in I_{CaL} decreases the release of SR calcium, decreasing the calcium transient which maintains the plateau phase of the AP and so decreases the APD. The instability of the calcium transient underlies the occurrence of APD alternans. The monotonic relationship between APD and BCL (*left*, *top*) and the occurrence of alternans (*right*, *top*) is displayed in Figure 2.5 during trains of APs stimulated at decreasing BCLs. As displayed on the *left* of the *lower* panel in Figure 2.5, a graph of APD against BCL or DI produces a restitution curve which displays the monotonic decrease in APD with decreasing BCL. Graph bifurcations at small BCLs indicate that the APD varies between two beats and signifies the presence of alternans.

Alternans can be spatially discordant throughout the tissue. In some regions APD may

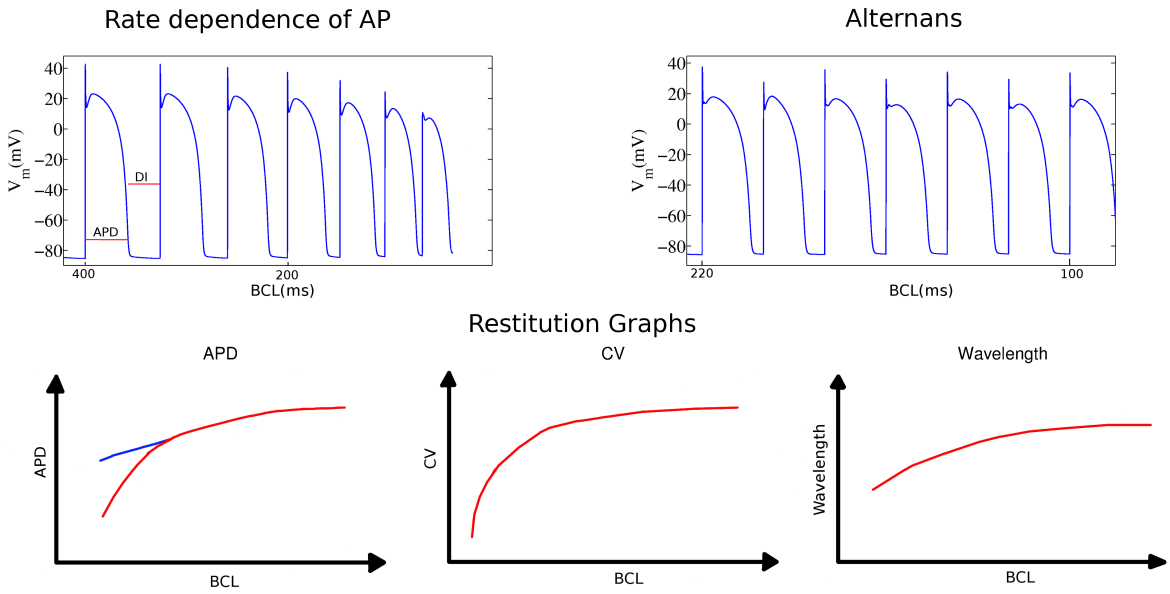

Figure 2.5: Cardiac restitution. AP traces display decreasing APD as BCL decreases (*left*, *top*) and APD alternans at short BCLs (*right*, *top*). The *lower* panel displays an APD restitution curve for two subsequent APs shown in *blue* and *red*, and CV and wavelength restitution curves.

be long, whilst in other regions APD may be short. This heterogeneity results in wave break and fibrillation. Nolasco and Dahlen (1968) proposed a graphical representation to predict the occurrence of alternans at fast pacing freqencies. They concluded that if the restitution graph has a slope greater than 1, the system becomes unstable leading to alternation in APD which can lead to wave break. A restitution graph with a slope less than one predicts stable APD values and stable propagation.

CV Restitution

CV of the excitation wave also varies as the frequency of stimulation varies. The CV decreases as the rate of stimulation increases (Figure 2.5 (*middle*, *bottom*)) due to the time it takes the sodium channels to recover from inactivation. As electrotonic current passes into the cell, if sodium channels remain inactivated, an AP will not occur and conduction through the myocyte will be delayed until the sodium channels have recovered from inactivation. Therefore, at short BCLs, sodium channels are more likely to be inactive due to the short preceding DI and so CV decreases. Decreasing CV enables previously activated tissue to recover before the current activation wave arrives. In situations of irregular propagation such as wave break, decreased CV often facilitates continued propagation of an irregular wave.

Wavelength Restitution

The activation wavelength is the length of tissue in which all myocytes are depolarised. However, not all myocytes are depolarised to the same degree. In Figure 2.6, the AP from

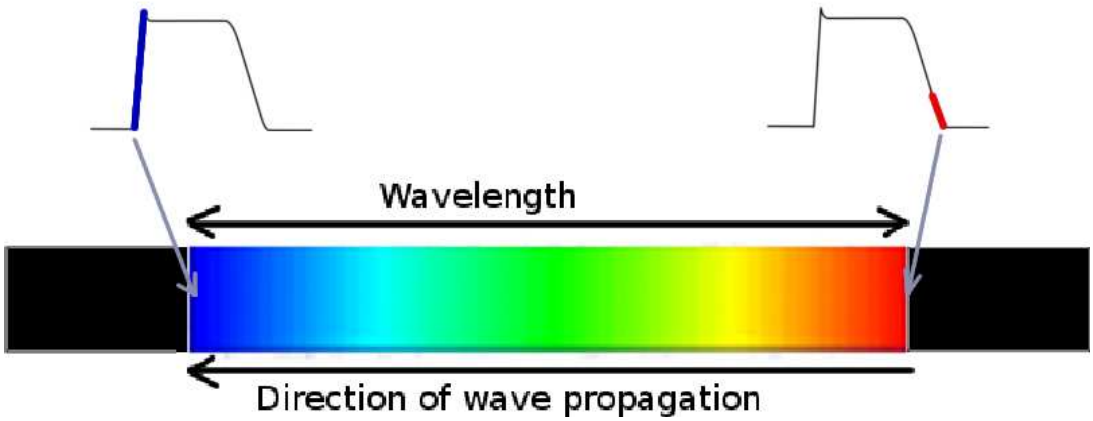

Figure 2.6: Wave propagation across a tissue model.

the front of the wave illustrates that myocytes in this region are only just being depolarised by the electrotonic current of the neighbouring activated cell and are at the beginning of the upstroke phase of the AP. In the same instant, cells at the back of the wave are very nearly repolarised and ready to be reactivated by the next wavefront. Wavelength (λ) is described by the equation,

$$\lambda = ERP \times CV \tag{2.3}$$

the ERP determining when the tissue is able to be reactivated. In most circumstances, the ERP, occurring during the repolarisation phase of the AP, is very similar to the APD. However, in certain circumstances, the ERP is sustained after the cell has repolarised back to V_{rest}. This post-repolarisation-refractoriness may occur in cells which have been altered by ischemia. Due to the similarity between the APD and ERP prevailing in most cases, the equation for λ is often defined as

$$\lambda = APD \times CV \tag{2.4}$$

(Lou et al., 2012; Weiss et al., 2000; Matthews et al., 2013; Garfinkel et al., 2000; Girouard and Rosenbaum, 2001), so that λ can be calculated without requiring data on the recovery of sodium channels from inactivation which determines the ERP. Due to the frequency dependence of both APD and CV, wavelength also varies as a function of stimulation

frequency. As stimulation frequency increases, both APD and CV decrease so wavelength decreases also (Figure 2.5 (*right*, *bottom*)). This decrease in wavelength due to increased pacing frequency facilitates propagation of unsynchronised, disruptive waves leading to cardiac dysfunction.

2.4 Acquisition of Electrophysiological Data

In Chapter 1, the use of *in vivo* research in both the clinic and animal models, as well as the use of *in silico* models to research arrhythmias was discussed. Irrespective of the medium, in many cases, acquisition of electrophysiological data is required to carry out research pertaining to single cell ionic mechanisms and tissue level electrical wave propagation during arrhythmias. The research presented in Chapters 4, 5 and 6 rely upon mathematical models which have been formulated based upon animal data. The research in Chapter 6 has a significant clinical application and indeed, comparisons are drawn between this modelling study and relevant clinical studies. Understanding the acquisition of electrophysiological data from both patients and animal models, the characteristics of the data and their limitations is important in order to be able to fully understand the results of the modelling studies presented in this Thesis and crucially, to be able to compare these results to clinical studies, which is particularly relevant to the work discussed in Chapter 6.

2.4.1 Animal data

Single Cell Electrophysiological Data

Measurements of cellular ionic mechanisms are often obtained from isolated animal hearts. The membrane potential can be measured using microelectrodes in intracellular recordings. Microelectrodes are approximately a micron in diameter and are filled with a conducting buffer solution. One of the microelectrodes is inserted into the sarcolemma and a tight seal is reformed around the electrode. The other microelectrode is placed in the extracellular space and the potential difference is measured across the membrane to provide a measure of V_m. Current flow through a specific ion channel can be measured using patch clamp recordings in which a strong suction seal is created, rupturing the membrane around a single ion channel so that flux of ions through the channel can be measured. Both membrane potential and ionic current data are invaluable to electrophysiological research,

as such *in vivo* measurements can provide information about cellular APs, restitution effects and even the biophysical mechanisms underlying such phenomena.

Isolating the heart to obtain the required measurements involves administering analgesics and tranquilisers such as ketamine and azaperone which are antagonists of neuroreceptors. In addition, animals are anaesthetised with drugs such as pentobarbital and isoflurane which are agonists of inhibitory neurotransmitters and lower the heart rate. These drugs affect the heart via multiple mechanisms, all of which are not fully understood. As such, it is important to consider that the cocktail of drugs administered to the animal before acquistion of the data may affect the resulting data.

The process of rupturing the cell membrane during intracellular recording causes the release of intracellular calcium stores. A buffer solution is required to diminish fluctuations in intracellular calcium. The buffer solution is also used to create a good seal with the membrane which is essential for accurate measurement, to maintain continuity of medium and to retain turgidity of the cell as the membrane is ruptured. EGTA, a calcium chelator, is commonly used in the buffer solution which may cause inaccurate recordings of many currents due to the interdependence of currents on intracellular calcium levels. In fact, the abnormal restitution curve of the rat model used in Chapter 4 may be attributed to the model being formulated from data which are adversely affected by the use of EGTA in the buffer solution. This is further discussed in Chapters 4 and 7.

In vivo ion channel and ionic current data are used to develop mathematical models of cardiac AP. As described in the previous paragraphs, the techniques used to acquire the data may result in recorded data not accurately reflecting *in vivo* electrophysiology. As a result, mathematical models formulated from such data also have the potential to display characteristics which deviate from true *in vivo* function. However, it is important to note that widely used mathematical models of cellular electrophysiology have been validated against numerous data to ensure that parameters which describe the morphology of the AP and its function fit with other experimental data sets. If the models are validated against such data and are able to replicate gross *in vivo* cardiac electrophysiology, the model may be relied upon to produce physiological results. As such, mathematical models replicating cellular electrophysiology are used throughout the research conducted for this Thesis.

Tissue Level Electrophysiological Data

Optical mapping provides a technique to observe and measure wave propagation across a tissue. To do this, tissue is perfused with a voltage sensitive dye, the tissue can then be stimulated and the dye excited by a light source. Emitted fluorescence is then a marker by which to observe and record membrane potentials travelling across the tissue.

Common voltage sensitive dyes used in this context are from the ANEP family of dyes and it has been suggested that the dye used in the protocol may have an effect on the membrane potential and the channels affecting repolarization and restitution, thus affecting CV and wavelength. In addition, mechanical uncoupling agents are used in order to stem contraction of the cardiac tissue for the purposes of reducing noise in data acquisition. It has been reported that mechanical uncoupling agents may also alter ionic currents which in turn alter AP properties (Liu et al., 1993; Banville and Gray, 2002; Baker et al., 2004; Fedorov et al., 2007).

Again, such tissue level data are important for investigating wave propagation and validating single cell research. However, it must be noted that the methodology of data acquisition does not produce infallible data. Therefore, when drawing conclusions from models or research using such data, the limitations of the data should be taken into consideration.

2.4.2 Clinical Data

Electrocardiogram

Clinical recording of electrophysiological data is necessary primarily for diagnostic purposes to observe the functioning of the heart but is also widely utilised in research. 12-lead surface electrocardiograms, commonly referred to as ECGs, are obtained by placing electrodes on the surface of the body. Due to the large changes in potential over the cardiac cycle, average potentials can be measured from surface ECG leads. Characteristic ECG traces indicate the depolarisation of the ventricles by the presence of the QRS complex, the major upward deflection of the trace. The smaller deflection occurring after the QRS complex, known as the T wave indicates the repolarisation of the ventricles. The ventricular APD can be estimated as the difference in time between the T wave and the peak of the QRS complex.

Abnormalities in cardiac function can be diagnosed by comparing patient traces with

that of characteristic traces and observing any deviations in rate, magnitude and intervals between complexes. They provide an invaluable diagnostic tool but lack the ability to be able to provide investigative techniques to uncover the details of a pathology. For example, if VT is observed on an ECG trace, the cause of the VT remains unknown from the ECG data available.

Intracardiac Recording

Intracardiac studies may also be conducted if an ECG indicates an abnormality or if ischemia and structural heart disease is suspected. Such studies are conducted to provide additional details about the pathology. For example, if VT is suggested by an ECG trace, intracardiac recordings could be used to observe abnormalities in electrical activity across the tissue such as those which may occur as a result of ischemic damage. Importantly, intracardiac recordings are used during ablation procedures as discussed in Sections 2.6 and 3.7 and the data are used to indicate where the clinician should ablate the tissue based on observing signs of reentrant circuits in the patterns of electrical activity. In addition, the research presented in Chapter 6 aims to investigate the clinical application of a technique to guide the ablation procedure and highlights some of the major limitations of intracardiac electrogram data. An overview is given here.

Most commonly, catheter electrodes are inserted into the heart through a blood vessel to gain access to the endocardium although in some cases, access to the epicardium via a percutaneous approach is performed. Considering an endocardial intracardiac study, unipolar electrograms are obtained by taking the difference between the membrane potential at a reference electrode and the membrane potential at a recording electrode (Taggart et al., 2014). An electrogram records average voltage changes in the extracellular space, produced by the flux of ions into and out of the myocytes during an AP. The recording electrode catheter can be moved around the endocardium to record signals from different areas of the heart. Thus, it is possible to both localise regions of tissue with altered electrical properties and record abnormal excitation wave propagation across the tissue. It is also possible to approximate the time at which the tissue is activated (activation time (AT)), the time at which the tissue repolarises (repolarisation time (RT)) and the APD using the activation-recovery interval (ARI) (difference between the repolarisation time and the activation time) obtained from the electrogram (Coronel et al., 2006). These measures would be used in the clinical application of the technique studied in Chapter 6.

Intracardiac electrophysiology studies provide detailed insight in to the excitability of the tissue which can be of great use in treating an arrhythmia. Although this recording technique bypasses the methodological problems which have been discussed in relation to animal research, there are limitations to this method of data acquisition. Firstly, unlike patch clamp recordings performed in animal models, information about the single cell biophysics and ionic currents which underlie electrical activation of cardiac tissue is not routinely available. There are methods which describe recording cellular action potentials by taking myocardial biopsies (Taggart et al., 2014), however this is not routinely practised in the clinic. Most commonly, data are recorded from the endocardial surface, neglecting the fact that wave propagation occurs transmurally. Again, there are techniques available to study transmural propagation using so-called plunge electrodes (Taggart et al., 2001) but they are not commonplace. The resolution of acquired data is also a limiting factor and has been discussed in Chapter 1. Data recorded from clinical intracardiac studies are generally of low resolution due to the manual manipulation of the catheters and the limited time period in which data can be obtained. *In silico* models allow investigation of 3D, transmural propagation and sampling of *in silico* data at exceptionally high resolutions.

The work presented in Chapter 6 which concludes the research in this Thesis utilises high resolution, transmural data from mathematical models of single cell electrophysiology which have been formulated from animal data, to investigate the application of a methodology to the clinic, considering the limitations of clinical data. In fact, taking into consideration the benefits and limitations of both *in silico* and clinical data, significantly contributes to the value of this investigation into the clinical application of the methodology.

2.5 Computational Modelling of Cardiac Electrical Activity

The benefits of utilising computational models have been discussed in Chapter 1 and in Section 2.4. The research presented in this Thesis utilises computational models throughout and so a discussion of modelling methodologies is required here in order to understand the techniques implemented throughout the following research. In this section we discuss the methods which are commonly utilised to model both single cell APs and tissue level wave propagation.

2.5.1 Modelling the Action Potential in a Single Cell

Deriving the Membrane Potential

Mathematical models of AP model the cell as an electrical circuit, with the sarcolemma represented as a capacitor, separating the charge between the extracellular and intracellular spaces. Resistors in parallel to the capacitor are analagous to ion channels in the sarcolemma. The currents through these ion channels (I_{ion}) drive the membrane potential. Thus, V_m can be solved with an ordinary differential equation (ODE) given by

$$\frac{dV_m}{dt} = -\frac{I_{ion}}{C_m} \tag{2.5}$$

where the capacitance of the membrane is C_m.

Mathematical Representations of Ionic Currents

The ionic current, I_{ion}, utilised in the calculation of the membrane potential (Equation 2.5) can be calculated in various ways depending on the nature of the ion channel or pump and its gating mechanisms. Different methods for calculating I_{ion} are presented here.

It has previously been discussed in Section 2.3 that the Nernst equation provides the equilibrium potential of the cell membrane when it is permeable to only one ion and the Goldman equation calculates the equilibrium potential of the cell membrane when it is permeable to more than one ion. Both the Nernst and Goldman equations can be rewritten to calculate ionic current via a current-voltage relationship. The ionic current for one particular ionic species derived from the Nernst equation is given as

$$I_{ion} = g_{ion}(V_m - E_{ion}) \tag{2.6}$$

where g_{ion} is the conductance of the membrane to the ionic species and E_{ion} is the Nernst potential for the ionic species. The current-voltage relationship derived from the Goldman equation, gives the Goldman current equation, which models the ionic current of a particular ionic species considering varying intracellular ($[Ion]_i$) and extracellular ($[Ion]_o$) ionic concentrations. The Goldman current equation is denoted by

$$I_{ion} = P_{ion}\frac{\mathrm{F}^2}{\mathrm{RT}}V_m\frac{[Ion_i] - [Ion_e]exp(\frac{-V_m\mathrm{F}}{\mathrm{RT}})}{1 - exp(\frac{-V_m\mathrm{F}}{\mathrm{RT}})} \tag{2.7}$$

where P_{ion} is the permeability of the membrane to that ion, F is the Faraday constant, R is the ideal gas constant and T is temperature.

Ion channels are rarely permeable to an ionic species consistently, but instead are controlled by sometimes complex gating mechanisms which may be voltage- or time-dependent. Therefore, the calculation of I_{ion} must represent this stochastic mechanism. Other formulations of I_{ion} vary in their complexity and ability to model the complexity of the ionic gating mechanisms. Perhaps the best known is the Hodgkin-Huxley formulation which presents a method for calculating I_{ion} through gated ion channels (Hodgkin and Huxley, 1952). In fact, the models of membrane electrophysiology utilised throughout this Thesis, as well as many others, are based upon the Hodgkin-Huxley formulation. In the following paragraphs, the Hodgkin-Huxley formulation to determine I_{ion} is presented.

From empirical evidence, Hodgkin and Huxley proposed that the membrane potential was primarily determined by the currents I_{Na}, I_K and I_{leak}. Each ionic current can be calculated by the equation

$$I_{ion} = g_{ion}(V_m - E_{ion}) \tag{2.8}$$

The ionic currents involved in driving V_m are determined by the conductance (g) of the membrane to each ionic species. g_{leak} is a linear term. However, g_{Na} is dependent on the activation, m and inactivation, h gating variables of the sodium channel. Likewise, g_K is dependent on the potassium activation gating variable n. Each of the gating variables is time dependent and effects g_{ion} by the relationships

$$g_{Na} = \overline{g}_{Na} m^3 h \tag{2.9}$$

$$g_K = \overline{g}_K n^4 \tag{2.10}$$

Ion channels can either occupy an open or a closed state and the gating variable determines which state the ion channel is in. Each gating variable (x) is time and voltage dependent which is represented by the equation

$$\frac{dx}{dt} = \alpha(V_m)(1 - x) - \beta(V_m)x \tag{2.11}$$

where x is a gating variable, α is the voltage-dependent rate constant of the channel closing and β is the voltage-dependent rate constant of the channel opening. For each x, an α and β value is obtained experimentally.

Incorporating the complexity of the gating mechanisms of each channel within the g term, the total ionic current across the membrane (I_{ion}) is given as

$$I_{ion} = C_m \frac{dV_m}{dt} + g_K(V_m - E_K) + g_{Na}(V_m - E_{Na}) + g_{leak}(V_m - E_{leak}) \tag{2.12}$$

Thus, each ionic current can be calculated by four ODEs: three ODEs for the time and voltage-dependent gating mechanisms for each of the gating variables m, h and n (Equation 2.11), and the ODE calculating the total current across the membrane (Equation 2.12). The membrane potential for a single cell can be solved by the equation

$$\frac{dV_m}{dt} = \frac{I_{stim} - (I_{Na} + I_K + I_{leak})}{C_m} \tag{2.13}$$

2.5.2 Modelling Propagation of an Electrical Activation Wave

Cable Theory

Conduction of electrical propagation is modelled as continuous propagation along a cable via the cable equation. At a particular point (x) and time (t) in the cable, the V_m is defined as $V_m(x,t)$. The resistance of the cable is R_a over a specific area and the current which propagates along the cable is I_a. Another current, analagous to the transmembrane current of the myocyte is denoted I_m.

The transmembrane current I_m is the sum of I_{ion} and the current across the capacitor, the capacitative current (I_c). The capacitance of the membrane (C_m) is

$$C_m = \frac{Q}{V_m} \tag{2.14}$$

where Q is the charge stored by the sarcolemma. Since, current (I) is

$$I = \frac{dQ}{dt} \tag{2.15}$$

it follows that I_c is denoted by

$$I_c = Cm \frac{dV_m}{dt} \tag{2.16}$$

Hence, I_m can be written as

$$I_m = C_m \frac{dV_m}{dt} + I_{ion} \tag{2.17}$$

where V_m is

$$V_m = \phi_i - \phi_e \tag{2.18}$$

(ϕ_i = intracellular potential and ϕ_e = extracellular potential).

Implementing Ohm's Law, the changing voltage along the cable can be determined by the differential equation

$$\frac{dV_m}{dx} = -R_a I_a \tag{2.19}$$

Considering Kirchhoff's Law of the conservation of charge, charge can only leave the cable by I_m between x and $x + dx$, giving

$$I_m = -\frac{dI_a}{dx} \tag{2.20}$$

Substituting the I_m term from Equation 2.17 and differentiating 2.19 with respect to x, the 1D monodomain cable equation is

$$\frac{d^2V_m}{dx^2} = R_a(I_{ion} + C_m\frac{dV_m}{dt}) \tag{2.21}$$

Monodomain Representation of the Bidomain Model

It is first necessary to mention the bidomain model which models the propagation of electrical activation thoughout the myocardium. The bidomain model considers both the intracellular space and the extracellular space which are coupled together by transmembrane currents, so that any current leaving the intracellular domain is a transmembrane current which must pass into the extracellular domain. This gives rise to two bidomain equations involving intracellular and extracellular conductivities.

Note that the V_m is represented by Equation 2.18, which takes into consideration the intra- and extracellular potentials. Electrical current density (J) is the product of the conductivity (σ) and the electric field which can be defined as the negative spatial gradient of potential (ϕ). Hence, intracellular and extracellular current densities can be defined as

$$J_i = -\sigma_i \bigtriangledown \phi_i \tag{2.22}$$

and

$$J_e = -\sigma_e \bigtriangledown \phi_e \tag{2.23}$$

Considering that current densities in a region of tissue β must equal I_m, using Equations 2.22, 2.23 and the conservation of current in Equation 2.20, the two bidomain equations can be written as

$$\bigtriangledown \cdot \sigma_i \bigtriangledown \phi_i = \beta I_m \tag{2.24}$$

and

$$\bigtriangledown \cdot \sigma_e \bigtriangledown \phi_e = -\beta I_m \tag{2.25}$$

A monodomain representation of the bidomain model serves to model the conductivity through the myocardium with a reduced form of the bidomain model, reducing computational demand in simulations which don't require separation of the intracellular and extracellular conductivities, such as in simulations where no extracellular stimulus is applied. The monodomain formulation is derived from the bidomain equations above (Equations 2.24 and 2.25).

However, in the monodomain model, conductivity is assumed to be anisotropic between the extracellular and intracellular domains. As such, the conductivity of the system is represented by the intracellular conductivity σ, resulting in the monodomain equation

$$\bigtriangledown \cdot (\sigma \bigtriangledown V_m) = \beta_m (I_{ion} + C_m \frac{dV_m}{dt}) + I_{stim} \tag{2.26}$$

where I_{stim} is the applied stimulus current.

The Finite Element Method

In the context of cardiac computational modelling, the finite element method (FEM) simplifies the complex geometry of the heart into discrete elements. As such, differential equations which require solving to calculate membrane potential across the domain can be reduced to linear matrix problems where linear algebra can solve the V_m equations at each element. In other words, between the boundaries of each element, linear equations are used to approximate the more complex differential functions over the same domain.

Linear basis functions describe the straight line connecting two nodes at the boundaries of an element whose elemental coordinates vary between 0 and 1. Global nodes can be mapped to local element nodes by a connectivity matrix so that interpolation between nodes is possible, given the linear basis functions between nodes. The value of the function at connected nodes is implicitly continuous.

The basis functions can also be thought of as weighting functions on the nodes so that, at a point between nodes, there is a linearly varying dependence on the nodal parameters. For example, between two nodes 1 and 2, the value of the function at node 1 has no dependence on node 2 whereas the value of the function half way between nodes is equally dependent on both nodes 1 and 2. This concept of linear independence on the basis functions also holds for elements with more than two nodes. Crucially, the weighting functions can be thought of as global functions, so that the weighting functions of a global nodal parameter decays linearly within each connected element. Although the equations are solved at the nodal points in the domain, the value of V_m can be determined at any point in the domain by interpolation of the solution across a distance between nodes, thus V_m can be linked to a particular physical coordinate.

Tissue simulations are performed on finite element (FE) geometrical meshes and so implementing the FEM, equations calculating V_m and the conduction of the activation wave across the myocardium are solved at each discrete element in the mesh. Fibre direction, a parameter crucial to the propagation of the wavefront, is defined at the centroid of each element enabling complex, anatomically accurate fibre directions to be incorporated into the geometrical model. The spatial discretization of the mesh into elements also allows heterogeneous parameterisation of the model. For example, ionic parameters may be altered in specific areas of the model by altering those parameters during equation solves at prespecified element centroids.

2.5.3 The Cardiac Arrhythmias Research Package Software

The Cardiac Arrhythmias Research Package (CARP) (carp.meduni-graz.at) utilises the FEM to simulate the electrophysiology of the myocardium and is used in Chapters 4, 5 and 6. As more complex models of AP are created and more equations need to be solved for each ionic current governing the AP, computational demand increases. CARP permits the use of complex ionic models in whole heart simulations by reducing computational load.

A parabolic and an elliptical solver component of the software, solve the bidomain equations and an ionic current component from a library of electrophysiological models determines the cellular membrane potential. The monodomain equation can also be solved by CARP, by solving only the parabolic equation. However, if the monodomain equation is being solved, the bulk conductivity tensor replaces σ_i and is calculated as the geometric

mean of the conductivities:

$$\sigma = \sigma_i \sigma_e (\sigma_i + \sigma_e)^{-1} \tag{2.27}$$

A FE geometrical mesh is required as an input to simulate membrane potential across the domain with files containing node and element information. Within CARP, element files can be tagged in order to alter ionic or conductivity parameters at tagged elements. An ionic membrane model is specified for the simulation and stimulus parameters such as frequency, location, strength and duration are required. Intracellular and extracellular, transverse and longitudinal conductivities are inputted for simulation.

Equations are solved at each node in the model outputting V_m for each time step to simulate an electrical wave propagating in space and time. Simulations of cardiac electrophysiology can be run on desktop computers within acceptable time frames, and parameters of the ionic models as well as stimulation, solver and output parameters, are easily altered for thorough investigation of both cellular and tissue electrophysiology. Single cell simulations are performed by the CARP subpackage BENCH.

2.6 Myocardial Infarction

Myocardial infarction is a common pathology causing a large proportion of deaths worldwide due to the altered electrophysiological properties of the heart stemming from the myopathy, causing arrhythmias. Arrhythmias resulting from an MI are characterised by the reentrant circuits which propagate around non-excitable tissue caused by ischemic damage during the MI, resulting in VT. The work presented in Chapters 4, 5 and 6 investigates the susceptibility of the tissue to post-MI reentrant arrhythmias. In this section, we discuss how ischemia-induced alterations of the tissue may contribute to the initiation and maintenance of VT, properties which are essential to the understanding of the work of this Thesis. Termination of VT by the ablation procedure is also discussed here as the work in Chapter 6 is focussed on improving this treatment strategy.

2.6.1 Aetiology

The heart itself requires an oxygen supply and so is suffused with blood from coronary vessels surrounding the heart. Coronary arteries stem from the base of the aorta and encompass the heart. MI is characterised by the cessation of flow due to occlusion of these coronary vessels by plaque deposition and stenosis of the vessel resulting in hypoxia

in regions of the myocardium. The resulting ischemia causes cell death by necrosis and formation of a myocardial infarct scar.

2.6.2 Myocardial Infarct Scar

In response to necrosis of a portion of the myocardium, the process of fibrosis produces excess connective tissue in the region of the necrotic tissue. The process of fibrosis exists to form a rigid structure, protecting the damaged myocardium from further injury which may be sustained due to the high pressures developed in the cardiac cycle. Fibrotic tissue is not excitable and so does not display the characteristics of healthy myocardium and cannot conduct electrical activation waves. However, the resulting scar tissue is not completely fibrotic, rather regions of non-conducting fibrotic tissue are interspersed with tracts of surviving myocardium. Figure 2.7, (*middle*) represents tracts of surviving myocardium (*white*) dispersed throughout regions of fibrosis (*black*). Cardiac activation waves can

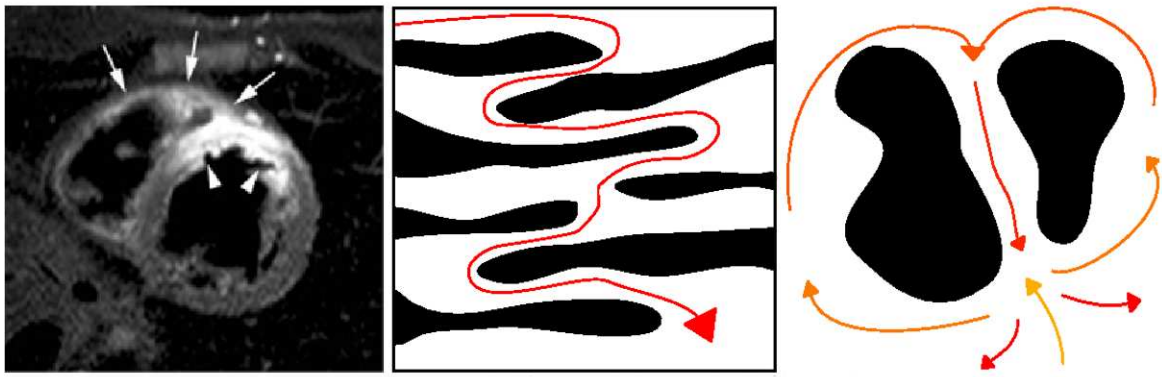

Figure 2.7: Myocardial infarction and diverted wave propagation. $Left$ - MRI displays infarct in white. $Middle$ - Path of activation wave (*red*) through surviving tracts of myocardium around fibrotic tissue (*black*). *Right* - Proposed circuit of propagation (*yellow to red*) around infarct scar (*black*).

propagate along the myocardial tracts but not through fibrotic tissue and so the activation wave propagates across the scar region along tortuous routes of viable myocardium (*red*). A magnetic resonance imaging (MRI) image of cardiac tissue is displayed in Figure 2.7 ($left$) with a diffuse region of infarct scar tissue shown in *white* which may be comprised of dense fibrotic scar or fibrosis interspersed with surviving myocardium. The image on the *right* of Figure 2.7 displays a proposed route of conduction (*yellow to red*) around two regions of non-excitable fibrotic scar tissue (*black*). The excitation wave may initially be diverted due to alterations in electrophysiological properties of the tissue surrounding the

scar. Diversion causes the wave to circumvent the scar and conduct retrogradely through the isthmus between the two scar regions. Under the right circumstances, the wave may propagate out of the isthmus and continue in self-sustaining reentrant circuits around the scars and back through the isthmus.

The extent of myocardial scarring is proportional to the severity and duration of ischemia, resulting in large variations of infarct scar patterns presenting in the clinic. The area of fibrotic tissue varies with time post-infarction. Fibrosis continues to occur as a healing mechanism months after the cessation of ischemia. In addition, there is large variation in the location of infarct scars in the patient population. Scars can be located anywhere around the myocardium and can be predominantly epicardial, predominantly endocardial or span the myocardium transmurally. The extent of variation in the size, shape and location of infarct scars gives rise to endless variations in resulting wave propagation.

2.6.3 Electrophysiological Remodelling in the Infarct BZ

A region of tissue surrounding the fibrotic infarct scar, known as the border-zone (BZ) also displays ischemic damage (Kazbanov et al., 2014). Tissue within the BZ remains excitable, however structural remodelling of the tissue resulting in dispersed fibrosis, the alteration of the location of gap junctions, in addition to the changes in gap junction conductance all play a role in altering CV through the BZ. Ionic remodelling occurring in the BZ alters the AP which in turn, affects the excitability of the tissue and success of propagation through the BZ. Remodelling affecting APD and CV in the BZ also affects the wavelength and therefore, can facilitate reentry, as is discussed below.

Ionic Remodelling

Ionic currents which contribute to the shape of the AP are altered by the electrophysiological remodelling of the BZ. In response to hypoxia, protein subunits of ion channels can become altered, rendering the channel defunct. The conformational change in ion channel proteins causes a decrease in density of functional channels and hence a decrease in ionic current through the channels. BZ displays a decrease in density of I_{Na} which causes a slowing of the upstroke phase of the AP. In turn, the slow upstroke causes a delay in the activation of I_{CaL} which prolongs the plateau phase and prolongs the APD. Also contributing to the prolongation of the AP is the decrease in outward potassium currents which cause the membrane to remain depolarised. Many ion channels are altered in the

BZ and it is the contribution of the remodelling of each channel which acts to produce the altered electrophysiological properties of the BZ. Crucially, remodelled BZ tissue displays lengthened APD, delaying repolarisation and causing increased refractoriness of the tissue. Due to these changes occuring in the BZ, cardiac tissue becomes heterogeneous, displaying different properties in normal and BZ tissue, which is thought to contribute to the initiation of reentrant propagation.

Conduction Velocity in the BZ

Conductivity of the BZ tissue is also altered by a number of mechanisms. One such mechanism is the alteration of the gap junctional current. The Cx43 protein which makes up the subunits of the gap junctions has been shown to be reduced in BZ tissue, which suggests that the number of functional gap junctions may be reduced. The reduction in functional gap junctions results in a decreased density of gap junctional current. In addition, the voltage dependent gating mechanism of the gap junctions is altered, affecting the ionic current through the channels. The remodelling of gap junctions in the BZ results in an overall decrease in CV. Additionally, CV is slowed by the structural presence of fibrotic tissue. Firstly, due to the presence of fibrosis leaving largely longitudinal fibres intact, the activation wave can only propagate in one direction, decreasing the sink and so increasing the source-to-sink ratio and hence increasing CV in the longitudinal direction. However, as activation waves propagate through narrow conduits of surviving myocardium, the path length of the wave increases, resulting in an overall decrease in CV of the activation wave through the scar. As a result of fibrotic tissue bordering surviving myocardium along longitudinal fibres, little to no electrotonic current can flow in the transverse direction, greatly slowing transverse CV and increasing the anisotropy of the tissue. In addition electrotonic effects of propagation through isthmuses can impact CV. On exiting an isthmus and propagating into a larger tissue space, the wavefront is highly curved due to the large sink that the small source current must excite. The curvature of the wavefront serves to decrease the CV and can cause termination of the wave, or wave block (Romero et al., 2013). Finally, the decrease in density of I_{Na} contributes to the slow CV of the wave through the BZ due to the slowed upstroke of APs activating the myocyte. In conclusion, complex mechanisms are involved in the alteration of BZ CV, but combine to produce the characteristic slow CV in the BZ.

2.6.4 Post-MI Arrhythmias

Changes in wave propagation due to the structural and electrophysiological properties of the myocardium as a result of an MI can cause reentrant arrhythmias, such as VT, which can destabilise to VF (Clayton, 2008), potentially resulting in SCD. Propagation of activation waves cannot occur through regions of dense non-conducting fibrotic tissue and so waves are often diverted around the region of structural wave block, initiating a potential reentrant circuit around an infarct scar. Waves may then traverse through tracts of surviving BZ tissue facilitating reentrant propagation due to the altered BZ electrophysiology. Reentry is a term used to describe circuitous propagation which can be self-perpetuating. Reentrant propagation can cause an increase in heart rate, or VT, because the reentrant frequency overrides that of the pacemaker cells in the sinoatrial node. The fast propagation of waves around a reentrant circuit can destabilise and lead to wave-break, causing VF and resulting in unsynchronised contraction of the heart. The implication of desynchronisation of ventricular contractions is that the heart is not able to pump blood efficiently out of the heart around the body to vital organs, which can result in SCD. Ionic, structural and conductivity remodelling in the BZ and scar complex all contribute to the initiation and maintenance of reentrant arrhythmias.

Conduction Wave Block

APD is prolonged in areas of the BZ causing a dispersion of repolarisation throughout the tissue. In addition, restitution effects and the presence of discordant alternans also creates spatial heterogeneity in the refractoriness of the tissue. The isolated regions of lengthened APD are responsible for causing the initial wave block which is a prerequisite for the initiation of reentrant arrhythmias. Depending on the frequency of the stimulation, the propagation of a wave across the tissue will be stopped if the wave approaches a region of refractory tissue which remains depolarised for a lengthened period of time. The wave then diverts around the region of functional block until it can propagate into tissue which is no longer refractory.

Conduction Around a Reentrant Circuit

Non-conducting fibrotic regions of the scar may increase the distance that the propagating wave must travel before propagation into repolarised tissue, increasing the pathlength of

the circuit. Figure 2.7 (*right*) displays a proposed reentrant circuit around fibrotic scar after initial wave block. Here, initial wave block must have occurred at the entrance of the isthmus to initiate diversion of the activation wave around the scar (*black*). The scar regions facilitate the diversion of the wave around the region of block, increasing the path length.

Slowed CV of propagation through BZ tissue allows sufficient time for the BZ region, which caused initial block due to a lengthened APD, to repolarise ready for reactivation. Hence, by the time the slow conducting wave reaches the region of prolonged APD again, the wave can propagate into the region forming a reentrant circuit.

Success of Reentrant Propagation

The critical factor indicating the possibility of success of a reentrant circuit is whether or not an excitable gap occurs. Considering a circular path of propagation, an activation wave propagating in a circle displays a wave head and a wave tail with a gap in between the two, so that the wave can propagate around the circle *ad infinitum*. If the wave is so large that there is no gap between the wave head and the wave tail, the wave will cease to propagate due to the wavefront-waveback collision. Figure 2.8 illustrates how the pathlength affects

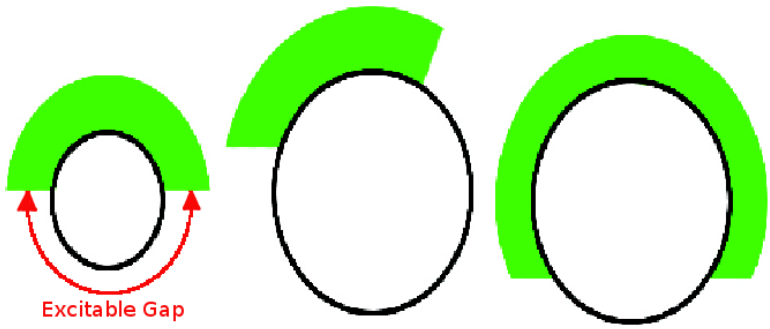

Figure 2.8: An illustration of an excitable gap determining the success of reentrant wave propagation. A wave (*green*) propagates around a circle with an excitable gap between the wavefront and the wave back. An increased pathlength (*middle*) increases the excitable gap, whereas an increased wavelength (*right*) decreases the excitable gap.

the excitable gap. The green area around the circle represents the activation wave which is propagating around the circle. In the $left$ panel, a large excitable gap exists between the wave head and the wave tail. Assuming that the wavelength remains constant, a larger circle, which is analagous to the increased pathlength created by the fibrotic tissue, will give rise to a larger excitable gap and hence facilitate the maintenance of the reentrant circuit (*middle*). A decrease in CV caused by remodelling in the BZ produces a decrease

in wavelength. A smaller wavelength propagating around the circle will also give rise to a large excitable gap facilitating reentry. The image on the *right*, indicates that a larger wavelength, which can be produced by an increase in either APD or CV results in a smaller excitable gap which may result in termination of the propagation wave if the wave head collides with the wave tail.

In summary, the initial wave block and subsequent diversion of a wavefront due to a region of prolonged APD, initiates the abnormal propagation of a wave across the myocardium. The increased path length and a decrease in wavelength contributes to the maintenance of reentry by extending the excitable gap between the wave head and the wave tail.

2.6.5 The Ablation Treatment

VT can be treated with implantable cardioverter defibrillators (ICDs) and antiarrhythmic drugs such as sotalol and amiodarone. However, both treatment strategies can affect quality of life and fail to prevent recurrent episodes. Radiofrequency catheter ablation therapy is a treatment strategy that is often employed to treat recurrences or to initially treat VT which cannot be treated another way.

Radiofrequency catheter ablation aims to terminate reentrant arrhythmias by creating a structural barrier to disrupt propagation of the reentrant electrical wave. The structural barrier is created by burning the tissue with radiofrequency energy resulting in necrosis of the tissue and a non-conducting ablation scar. The lesion is ideally introduced at the exit point of the scar, the point where initial block occurs, and after diversion of the propagation wave, where a reentrant circuit is completed. Figure 2.9 illustrates the ideal scenario in an ablation procedure. The activation wave encounters a region of refractory tissue resulting in wave block and is diverted around the scars. The wave propagates through the isthmus and in a reentrant circuit (*left*), would exit from the isthmus to continue propagation. However, an ablation lesion (*grey*) at the exit point of the scar interrupts the propagation and terminates the reentrant circuit (*right*).

In order to locate the exit point of the scar, the location of the scar must be identified. Recording catheters are inserted into the heart and contact is made between the electrodes and the endocardium. Low voltage electrograms may indicate the presence of the scar during pacing at sinus rhythm. If the VT is haemodynamically stable and can be induced, programmed stimulation is applied to the heart to induce VT in order to better

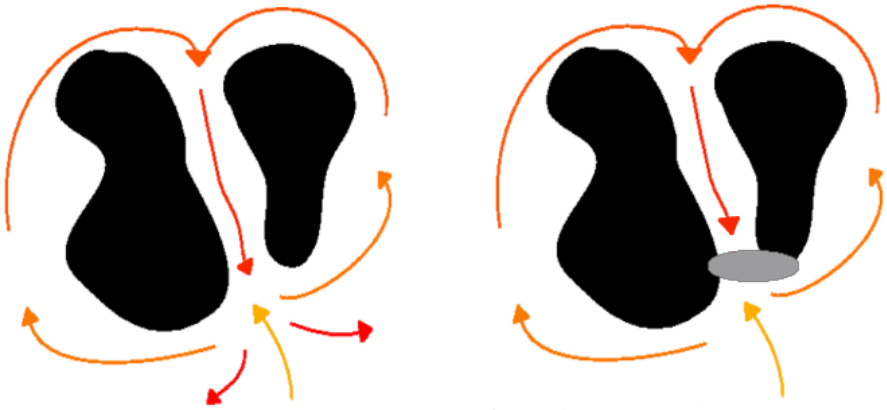

Figure 2.9: The ablation procedure. *Left* - Mechanism of reentry. *Right* - An ablation lesion (*grey*) is introduced at the exit point of the scar, interrupting the circuit and terminating reentry.

map the substrate and locate the exit site. Electrogram traces are again recorded and analysed. Ablation targets may be located by analysing the electrograms using a variety of techniques. By moving the recording catheters around the region indicated as scar, it is possible to trace the low voltage activation through the isthmus which is isolated from the activation of the healthy tissue. Fractionated electrograms which occur due to the slow conduction through the isthmus are also identified by pacing from regions around the scar. The occurrence of fractionated electrograms recorded at the site of the pacing electrode are compared to the time of activation of the healthy myocardium in order to predict the location of the pacing electrode within the reentrant circuit. If the induced VT is haemodynamically unstable, the more accurate mapping techniques can not be performed and the procedure continues without having located precise ablation targets. A more detailed account of the ablation procedure is given in Chapter 3.

Ablation therapy is widely used to terminate reentrant arrhythmias. The fact that more accomplished mapping techniques require VT to be induced increases the danger and decreases the safety of the procedure. Crucially, the mapping procedure is not infallible, sometimes missing the critical exit point of the scar which could result in failure to terminate the VT and ablation must be performed at another site. It is possible that many potential target sites are ablated until one site is ablated which terminates VT. This hit-and-miss approach results in increased areas of ablation lesions which could contribute to mechanical dysfunction of the tissue. Due to these limitations of the technique, the work in Chapters 5 and 6 investigates a method to improve the ablation procedure by more accurate location of the optimal ablation target.

Chapter 3

Literature Review

The previous chapter provided fundamental background information about cardiac electrophysiology, post-MI reentrant arrhythmias and the radiofrequency catheter ablation treatment. This literature review proceeds by discussing the experimental studies which have provided explanations of the physical mechanisms of reentry and the effects of restitution, in terms of electrophysiological remodelling of the BZ. In addition, theories of reentry which have been proposed in the literature are considered in terms of explaining the patterns of post-MI reentrant arrhythmias. An overview is provided of animal and computational models used to investigate post-MI arrhythmias, including a review of the more complex models utilised to represent single cell electrophysiology throughout this Thesis. A review of the landmark studies which have outlined, and facilitated the progression of the ablation treatment strategy is presented along with an indication of how the ablation treatment may be improved. Finally, this chapter is concluded with a discussion of the questions which remain unanswered by the existing body of literature, indicating the motivation for the work presented in Chapters 4, 5 and 6.

3.1 Ischemia Induced Remodelling of Cardiac Tissue

In Chapter 2, we outlined how ischemic damage altered cardiac tissue and facilitated reentry. Here we present the studies which have observed such electrophysiological and structural remodelling. This literature is not only vital for understanding how we model BZ electrophysiology in Chapters 4, 5 and 6, but also provides a deeper understanding of the mechanisms which facilitate reentry, the primary pathology researched in this Thesis.

3.1.1 Alterations Affecting Ionic Currents

Several studies have indicated that conduction block is often caused by the heterogeneity of APD across the tissue (Han and Moe, 1964; Allessie et al., 1976; Kuo et al., 1983; Gough et al., 1985), causing the activation wave to be diverted. The dispersion of repolarisation is exacerbated between healthy and BZ tissue due to ionic remodelling occurring as a result of ischemia (Carmeliet, 1999).

Janse and Wit (1989) proposed that the reduced excitability of the tissue can cause conduction block and lead to reentrant arrhythmias. Such reduced excitability has been reported in BZ tissue where the AP amplitude and upstroke velocity are reduced (Lue and Boyden, 1992). In fact, Spear et al. (1979) documented a reduction in I_{Na} in BZ tissue which could explain the reduced excitability of the tissue leading to CV slowing in the BZ (De Bakker et al., 1988). A reduction in I_{CaL}, also observed in experimental studies (Aggarwal and Boyden, 1995; Dun et al., 2004) could affect the peak amplitude of the AP. In addition to the theory that prolonging APD facilitates conduction block due to refractoriness of the tissue, work by Gough et al. (1988) studying the effect of the drug Clofilium which lengthened APD, showed that the effect of prolonging APD also facilitated arrhythmias by inducing early-afterdepolarisations and triggered activity. The APD has been reported to be prolonged in the BZ due to the reduction in the rectifying potassium currents, I_{K1} (Pinto and Boyden, 1998), I_{to} (Lue and Boyden, 1992), I_{Kr} and I_{Ks} (Jiang et al., 2000). In addition, the slow recovery of calcium transients due to the decreased expression of SR Ca^{2+} ATPase (SERCA), which is a channel protein responsible for the reuptake of cytosolic Ca^{2+} into the SR (Kim et al., 2002), also contributes to the prolongation of the APD.

In light of experimental data documenting ionic remodelling in BZ tissue, a number of studies from the Trayanova group at the Johns Hopkins University have simulated electrophysiological remodelling of BZ tissue in computational models of both rabbit (McDowell et al., 2011; Rantner et al., 2012) and human (Ashikaga et al., 2013) membrane potential, by altering the conductance terms of several ionic currents. Namely, the conductance of I_{CaL} was reduced by 69% based on experimental data from Dun et al. (2004). The conductance term of I_{Na} was reduced by 62% (Pu and Boyden, 1997). Observations by Jiang et al. (2000) from experiments which determined the BZ remodelling of potassium currents motivated the reduction of the conductance terms of I_{Kr} by 70% and I_{Ks} by 80% in the computational modelling studies. These studies provided a basis for the methodology

used in Chapters 4, 5 and 6 to simulate BZ remodelling.

3.1.2 Structural Remodelling

Significant histological studies of the infarcted human heart were conducted by Fenoglio et al. (1983) and De Bakker et al. (1988). On observation of the tissue, they concluded that inexcitable, fibrotic collagen tissue formed as a result of ischemic injury but did not occur homogeneously through the affected tissue. They revealed that fibrosis could be dense, forming large areas of inexcitable tissue, or could be dispersed with tracts of surviving myocardium interspersed with fibrotic tissue. Indeed, Fenoglio et al. (1983) displayed that isthmuses of surviving myocardium may range from one cell thick to a number of cells thick and likewise, either thick or thin fibrotic regions may separate tracts of myocardium. It was observed that the surviving bundles of myocytes thus formed a branching structure with tracts joining and diverging throughout the scar region and ultimately connected one side of the substrate to another. The point at which the activation wave emerged from the myocyte bundles within the scar into the healthy myocardium was termed the exit site or the site of origin. The vastly heterogeneous nature of the substrate has since been well studied and documented and the presence of diffuse fibrosis has been proposed to be the cause of slow conduction through the scar, resulting in reentry (De Bakker et al., 1990, 1993). The slow conduction velocity through isthmuses in the scar tissue is effectively caused by the tortuous route of the activation wave through the substrate, increasing the physical path length (De Bakker et al., 1993; Rutherford et al., 2012).

Electrotonic current flowing through gap junctions in the sarcolemmas underlies the propagation of the activation wave. Fibrotic tissue bordering surviving myocytes decreases the number of cells which are electrically coupled to each other, thus reducing the electrotonic current, leading to a decrease in CV (Luke and Saffitz, 1991). De Bakker et al. (1993) suggested that, due to the arrangement of myocyte bundles, regions of fibrosis border the myocyte fibres primarily along the transverse edge, stemming the transverse propagation of the wave which decreases transverse CV. As a result of ischemia, gap junctions are also altered in a number of ways, affecting the electrotonic current. It has been found that fewer gap junctions are present in intercalated disk structures in BZ myocytes (Luke and Saffitz, 1991). Specifically, it has been shown that Cx43 distribution is altered during ischemia (Peters et al., 1997), which may explain the reduction in gap junctions along the elongated edges of the myocytes (Luke and Saffitz, 1991). Yao et al. (2003)

showed experimentally that cell-cell coupling was reduced in the transverse direction by 90% and that longitudinal cell coupling remained similar. Based on this result, several subsequent computational modelling studies have simulated tissue anisotropy in the BZ by reducing transverse conductivity by 90% (McDowell et al., 2011; Rantner et al., 2012; Ashikaga et al., 2013). This observation motivated the methodology used to simulate BZ electrophysiology in the computational models utilised in Chapters 4, 5 and 6.

3.2 Post-MI Reentrant Arrhythmias

The work presented in Chapters 4, 5 and 6 is based upon quantifying the likelihood of reentry occurring. In order to investigate methodologies to study arrhythmia dynamics, it is essential to understand how reentry occurs and which properties facilitate reentrant circuits. Here, we present the literature which describes the figure-of-eight pattern of reentry which occurs around infarct scars. In addition, we employ the previously proposed leading circle and spiral wave theories of reentry to illustrate how BZ remodelling contributes to the susceptibility of the tissue to reentry. Crucially, this section clarifies the importance of the concept of an excitable gap which was introduced in Section 2.6; a concept which is utilised in Chapter 4 to observe species differences in arrhythmia dynamics and in Chapters 5 and 6 to locate reentrant circuits.

3.2.1 Figure-of-Eight Reentry Around Infarct Scars

Reentry resulting from MI is widely accepted as the cause of post-MI VT (De Bakker et al., 1988). De Bakker et al. (1988) proposed that the highly complex nature of the substrate permits a variety of macro reentrant circuits around the scar and micro reentrant circuits through the BZ. At approximately the same time, the work of Stevenson et al. (1987, 1993) suggested the now widely observed, investigated and well documented figure-of-eight pattern of reentry. When modelling reentry around infarct scars in Chapters 5 and 6, we aimed to simulate this reentrant pattern. Figure-of-eight reentry occurs when a wave encounters conduction block, causing the wave to divert in two arcs around functional and structural barriers and subsequently both waves propagate retrogradely through an area of slow conduction, back towards the site of initial block.

In the case of post-MI reentry, initial activation wave block may occur if the wave travelling from healthy tissue is blocked by refractory BZ tissue as a result of the prolonged

APD in the BZ, causing the wavefronts to divert around the region of functional block into recovered tissue. The presence of fibrotic scar results in the wave circumventing the scar and often, the wave will propagate into an isthmus of surviving tissue, returning towards the site of initial block. When the wavefront reaches the site of initial block, if the tissue there is recovered, it will propagate into that tissue setting up a reentrant circuit. The initial conduction block and subsequent diversion of the wave, in addition to the slow CV in the BZ, allows time for the tissue in that region to recover before the diverted wavefront propagates back to the region of initial block, facilitating reentry (Callans et al., 1996).

Much debate has occurred as to whether initial wave block or slow conduction through BZ tissue is necessary to elicit reentry. Segal et al. (2010) showed that reentry could be initiated by either initial conduction block or slow conduction through the BZ. In addition, they showed that a combination of both wave block and slow conduction can result in reentry. A previous claim reenforces this finding, stating that in many cases both initial activation block and slow conduction through the BZ are required to initiate and maintain reentrant circuits (Stevenson et al., 1987). In the modelling studies in the following chapters of this Thesis, we simulate both initial block and slow BZ CV by modelling prolongation of the APD in the BZ as well as a reduction in BZ CV.

3.2.2 Leading Circle and Spiral Wave Theories of Reentry

Although figure-of-eight reentry describes reentry around a structural substrate such as an MI scar, two other descriptions of reentry can be useful in terms of understanding key concepts of propagation. Comtois et al. (2005) discussed the differences between leading circle and spiral wave reentry, patterns which occur due to functional substrates. The leading circle theory was named by Allessie et al. (1973) and can be depicted by a circular wave propagating around an inexcitable core. It is based on several earlier studies which observed wave propagation around an obstacle (Mayer, 1906; Mines, 1913). Allessie et al. (1973) suggested that the wave can propagate around the circle if the tissue in front of it is recovered. If the tissue in front of the wavefront is occupied by the wave back, conduction block and termination of reentry will occur. Thus, the gap between the wavefront and the wave tail, often termed the excitable gap is a measure of the success of the propagation with a larger excitable gap inferring safe propagation.

A more theoretical view of reentry, spiral wave reentry, was observed by Van Capelle and Durrer (1980) and can be depicted as a wave spiralling outwards in expanding diameter

from a central focal origin. Here, the wave tip is curved and it has been suggested that due to source/sink effects, an increase in curvature in the wave tip decreases the source-to-sink ratio, which could lead to a decrease in CV or wave block (Pertsov et al., 1993). Considering figure-of-eight reentry around an MI scar, the spiral wave concept can describe the safety of conduction of the curved wavefront after it has blocked and is diverting around the scar. In addition, the wavefront curvature concept described in spiral wave theory can predict conduction of the wave out of an isthmus into healthy myocardium and explain how wavebreak due to the mismatched source-to-sink ratio may destabilise the arrhythmia (Qu et al., 2000), leading to induction of VF. Whereas the leading circle theory can predict whether reentry will occur or whether the wavefront will collide with the wave back and terminate reentry. Therefore, post-MI reentry can be thought of as a complex mechanism and propagation around the circuit can be evaluated with concepts from different theories of reentry.

3.2.3 Effects of Remodelling on the Success of Reentrant Propagation

The interaction between the APD and CV and their effect on reentry can be illustrated by the leading circle theory of reentry. It is first necessary to consider the excitable gap which determines if propagation can occur. It is the wavelength which ultimately determines the extent of the excitable gap as in a closed circle of a given path length, the excitable gap is the wavelength subtracted from the pathlength. Thus, if the pathlength is greater than the wavelength, reentry can occur (Mines, 1913; De Bakker et al., 1993). Stevenson, Weiss, Wiener and Nademanee (1989) proposed that it is not only the wavelength which determines the excitable gap but also the size of the inexcitable core, or in the case of post-MI reentry, the size of the structural obstacle. A large wavelength may produce a very small excitable gap, terminating reentry unless the obstacle is very large, in which case the wavelength will be able to propagate around the obstacle because the excitable gap is enlarged but a large wavelength propagating around a small obstacle will reduce the excitable gap leading to conduction block (Xie et al., 1998). In addition, two reseach groups in the nineties observed that if the obstacle is large with respect to the wavelength, the wave anchors to the non excitable core and reentry is stabilised (Pertsov et al., 1993; Xie et al., 1998).

As the wavelength is the product of the refractory period and the CV (De Bakker et al., 1988; Stevenson, Weiss, Wiener and Nademanee, 1989), both APD and CV play

a vital role in determining the success of propagation around a reentrant circuit. The APD governs the wave back and if the APD is prolonged, the wavelength increases. Thus, the wavefront travelling around the circle may collide with the wave back and terminate reentry (Comtois et al., 2005). However, if the APD is decreased, the wavefront will be able to travel into the recovered region and maintain the reentrant circuit.

Importantly, reducing CV in the leading circle analogy decreases the wavelength and facilitates reentry, an effect which was observed by De Bakker et al. (1993). A reduction in CV allows time for the tissue at the wave back to recover before the wavefront arrives. The observed reduction in I_{Na} in BZ tissue is responsible for reducing CV and is thus proarrhythmic. It has also been demonstrated that slow VTs are stable and sustain reentry, whereas fast VTs become unstable and can lead to conduction block and wave break resulting in VF (Stevenson, Weiss, Wiener and Nademanee, 1989; Xie et al., 1998). However, according to the spiral wave theory, a reduction in I_{Na} decreases the source-to-sink ratio and increases the curvature of the wave. The resulting source/sink mismatch can cause conduction block and have an antiarrhythmic effect (Pertsov et al., 1993; Comtois et al., 2005).

3.3 Restitution and its Effect on Arrhythmia Dynamics

It is well known that repolarisation heterogeneity initiates reentry by causing conduction block at a region of depolarised tissue (Janse et al., 1985). Indeed, a larger repolarisation gradient between two areas is arrhythmogenic (Opthof et al., 2007). Moreover, it has been shown by Nash et al. (2006) and Sheridan et al. (2010) that dynamic changes occurring as a result of cardiac restitution can contribute to repolarisation heterogeneity and facilitate reentry.

Pacing according to an S1S2 protocol can illustrate how an increase in pacing frequency facilitates reentry. Considering the scenario on the *right* of Figure 2.7 displaying a reentrant circuit around an infarct scar, a repolarisation gradient would exist between the healthy tissue and the tissue where initial block (also termed the exit site) occurs, as a prolonged APD is likely to occur in BZ tissue. An initial paced beat (S1) will depolarise all of the tissue including the BZ isthmus. However, the prolonged APD at the exit site causes the wavefront of a second paced stimulus (S2) to block as it approaches the BZ region. Importantly, if the APD is shortened in the healthy tissue, as may occur with

an increase in pacing rate due to restitution effects, the S2 wave propagating through the isthmus back to the exit site, is less likely to encounter conduction block on exiting the isthmus, because the healthy tissue will have recovered sooner, and reentry can occur. This experimental evidence clearly illustrates that an increase in pacing frequency alters the wavelength to facilitate reentry and that the prematurity of the stimulus combined with the dispersion of repolarisation is critical in initiating arrhythmias (Boyett and Jewell, 1978; Rosenbaum et al., 1991).

The work of Janse et al. (1985), Garfinkel et al. (2000) and Clayton and Taggart (2005) illustrated that APD alternans occurring as a result of increasing stimulation rate is arrhythmogenic, due to inducing steep repolarisation gradients. As the frequency speeds up, alternans ensue. A beat with an increased APD will be followed by a premature beat with a short APD. As a result, the activation wavefront of the premature beat will be blocked by the lengthened APD of the previous beat. Unstable propagation occurs as a result of APD alternans as waves block and break up, eventually destabilising the reentrant circuit and resulting in the potentially fatal VF arrhythmia, a scenario which has been widely documented in the literature (Koller et al., 1998; Qu et al., 1999). Interestingly, in a paper by Cherry and Fenton (2004), it was explained that decreasing frequency flattens the APD restitution curve, decreasing the risk of alternans and so stabilises propagation. Increased stability of the wave propagation decreases the arrhythmogenic dispersion of repolarisation and in addition, decreases the likelihood of VF occuring.

CV is rate dependent in a similar manner to APD where CV decreases as pacing frequency increases. Qu et al. (1999) investigated the effects of ion channel function on restitution and found that the recovery from inactivation of I_{Na} is a major determinant of steep CV restitution. As the pacing frequency increases and DIs decrease, I_{Na} does not have sufficient time to recover, resulting in a decreased CV. As frequency continues to increase, CV alternans also occur, leading to wave break and possible initiation of VF (Wu et al., 2002). As described in the leading circle theory of reentry, decreasing CV decreases the wavelength and facilitates reentry indicating that increasing pacing frequency is arrhythmogenic in a similar manner to APD. It has also been reported that decreasing CV decreases the rate of the arrhythmia, stabilising reentry (Banville and Gray, 2002). However, Qu et al. (1999) suggested that in fact, increasing CV and flattening the restitution curve promotes wave break, due to the wavefront-wavetail interactions that occur as a result of a smaller excitable gap, suggesting that also increasing the CV could

be arrhythmogenic by a different mechanism.

Having discussed the effects of APD and CV restitution on reentry and considering that the wavelength is the product of APD and CV, it follows that wavelength decreases as pacing frequency increases, facilitating reentry. Indeed, under normal physiological conditions and normal pacing frequencies, the wavelength is long and normally exceeds any substrate induced path length so reentry is unable to occur (Girouard et al., 1996). However, premature beats, or an increase in pacing frequency, increases the susceptibility to initiating and maintaining reentry.

3.4 *In Vivo* Studies of Post-MI Arrhythmias

In Chapter 1 we explained the need to research post-MI reentrant arrhythmias due to the vast health and economic burdens of the disease. We also outlined the importance of *in vivo* research to the field. The following section looks at some of the important studies of post-MI arrhythmias which have been performed *in vivo*, which have contributed to our increased knowledge of the pathology, paving the way for improving therapeutic strategies.

A rigorous ethical review process is required to gain approval for clinical research. As such, *in vivo* research in patients is limited to the least invasive approaches and often is required to be performed during an existing scheduled treatment or investigation of a condition. For example, research into the mechanism of post-MI reentry in humans is often based on non-invasive 12-lead ECGs in combination with midly invasive intracardiac electrophysiological studies measuring extracellular potentials. Many studies have taken this approach, of particular note are the many fundamental studies by Stevenson and his group which have provided insights into the mechanisms of conduction block and slow conduction in figure-of-eight reentry (Stevenson, Weiss, Wiener and Nademanee, 1989; Stevenson et al., 1993) and have enabled the investigation of substrate mapping techniques to guide the ablation procedure (Stevenson et al., 1987; Stevenson, Weiss, Wiener and Nademanee, 1989).

The reentrant circuit can be further investigated by *in vivo* intracellular recordings and histological examination as was performed in a study by De Bakker et al. (1988) in which they excised human hearts and perfused the isolated hearts in a Langendorff preparation. In addition, endocardial resection, a technique which was used prior to radiofrequency ablation to remove the reentrant substrate, provided tissue samples of in-

farcted myocardium. Intracellular membrane potential recordings empirically showed that conduction block occured at regions of functional heterogeneity. Histological examination of the tissue provided crucial evidence about the structure of MI scar tissue and showed that excitable bundles of myocytes were dispersed throughout and separated by fibrotic tissue. Another histological study (Fenoglio et al., 1983) also reported tracts of surviving tissue throughout the fibrotic scar region and in addition, presented evidence that the ultrastructure of myocytes such as the location of gap junctions, differs between states of health and disease. It is clear that such invasive studies can provide essential information about the underlying mechanisms of post-MI reentry. However, such *in vivo* examination is rarely accessible or approved by ethical committees. Hence, invasive and thorough observation of post-MI reentry is usually performed in animal models.

Reentry around an obstacle in cultured rat myocytes has shed light on some fundamental properties of spiral-wave reentry around an infarct scar and has been proposed as a potential model to investigate post-MI reentry and defibrillation. For example, it was found that CV around the obstacle is reduced due to a reduction in membrane excitability because of altered ionic properties (Entcheva et al., 2000). BZ remodelling responsible for alterations in ionic currents has been further studied in rat myocytes in order to validate and propose novel drug therapies which target ionic remodelling (Chang et al., 2009). The study systematically blocked ion channels to simulate remodelling and observed the effect of reentry dynamics. As a result, they concluded that the I_{CaL} channel blocker nitrendipine was antiarrhythmic. Rat myocytes have also been used to examine the source/sink effects at play during reentry. Entcheva et al. (2000) showed that CV is decreased when the wavefront is highly curved due to an increased sink-to-source ratio. It was also shown that source/sink mismatches at the exit point of an isthmus can slow CV, cause conduction block and as a result of AP prolongation at the exit site, reactivation of the isthmus can occur, reversing the direction of the wavefront (Auerbach et al., 2011). MI can be induced in rats by ligation of the LAD and reperfusion of the tissue, which has been shown to faithfully reproduce the progression and characteristics of clinical anterior wall MI, resulting in a non-excitable scar surrounded by BZ tissue (Goldman and Raya, 1995). The model has been used to observe how changing the severity of ischemia results in varying degrees of infarct size and shape, myocardial dysfunction and the effect it has on reentry (Wu et al., 2011). The mechanism and efficacy of angiotensin-II receptor and β-adrenergic receptor blockade has also been studied using this model in order to inform

drug development (Goldman and Raya, 1995).

Guinea pigs have also been used as animal models to study post-MI reentry. Laurita and Rosenbaum (2000) used optical mapping techniques to observe how changes in BCL affect the repolarisation heterogeneity across the myocardium and also observe source/sink effects at the exit site. These properties of the myocardium are both essential to the success of reentry and studies investigating their effects on reentry are crucial to understanding the pathology. A mechanism by which fibrosis causes arrhythmias was also studied in guinea pigs using optical mapping (Pastore and Rosenbaum, 2000). It was found that due to cell uncoupling as a result of fibrosis, APD alternans increased resulting in increased APD heterogeneity and arrhythmia induction. Drug action studies have also been performed in guinea pig models to investigate the I_{Na} channel blockers flecainide and quinidine, which were found to be proarrhythmic due to the action of the drugs decreasing CV by decreasing the rate of recovery from inactivation of the I_{Na} channels (Osadchii, 2014). Sotalol was found to have an antiarrhythmic action only at low frequencies by increasing APD (Girouard and Rosenbaum, 2001) in guinea pig whole-heart models.

Langendorff perfused rabbit hearts have been used in drug studies investigating the APD restitution curve flattening mechanism by which β-blockers stabilise VF to a stable VT rhythm (Pak et al., 2003). It has been shown that increasing gap junctional cell coupling with rotigaptide terminates reentry, whereas decreasing gap junction coupling with carbenoxolene promotes spiral wave reentry and anchoring of the wave to the substrate, by decreasing CV and decreasing wavelength (Takemoto et al., 2012). Dual effect mechanisms of the I_K channel blocker HMR1098 have been shown to increase APD causing the antiarrhythmic effect but increase the slope of APD and CV restitution causing a proarrhythmic effect. Ablation therapy has also been studied in rabbit hearts. Mercader et al. (2012) proposed a methodology to visualise the size of the ablation lesion using fluorescence imaging of the increase in NADH in damaged cells. They claim to be able to visualise lesions with a 0.5mm resolution which could increase the ablation procedure success rates whilst reducing procedure time, although it is questionable whether such a technique could be applied in the clinic due to limited access to the heart.

In summary, studies in animal models can be used to investigate structural substrates and mechanisms of reentry as well as to elucidate drug action and effect. Such *in vivo* studies are limited in humans due to ethical restrictions, sample sizes and applicability of techniques. Animal models are widely used to investigate vital aspects of post-MI reentry

which may otherwise remain elusive.

3.5 Computational Modelling of Post-MI Arrhythmias

Computational models are used as a vital tool to supplement investigation in the clinic and in animal models (Clayton et al., 2011). Whilst animal models overcome many ethical restrictions imposed on clinical research, highly regulated ethical review processes are required for animal studies. Computational models overcome these restrictions as well as providing a low cost alternative to animal models (Goldman and Raya, 1995). Moreover, *in silico* modelling provides a framework to model heart function at multiple levels (Smith et al., 2011), allowing the investigation of arrhythmias from the level of the single cell biophysics to the whole organ level. Crucially, simplified models permit investigators to dissect out the component parts contributing to arrhythmias. Biological systems are inherently exceptionally complex and being able to study one component in a myriad of contributing factors can provide in depth insight into arrhythmia mechanisms (Clayton and Taggart, 2005). We have previously covered the importance of *in silico* models in investigating post-MI arrhythmias (Chapter 1). Here we cite some important studies introducing computational methodologies to model single cell cardiac electrophysiology as well as wave propagation across the heart. In addition, studies which have contributed novel findings to the field of post-MI arrhythmias using a computational modelling approach are reviewed.

3.5.1 Electrophysiological Models of Ventricular Action Potential

The Hodgkin-Huxley Formulation to Determine Ionic Current

In Section 2.5, an outline of the approach to single cell electrophysiology modelling was given. In particular, the mathematical methods of deriving ionic current in order to solve the equation of the membrane potential (Equation 2.5) were discussed. The seminal work by Hodgkin and Huxley (1952) provided the formulation, presented in Section 2.5, to derive the ionic current and hence the membrane potential from a series of ODEs. This formulation provided a methodological foundation for subsequent models of cardiac AP.

Hodgkin and Huxley (1952) formulated a mathematical model to model the propagation of an AP down a squid giant axon. From empirical observation using, at the time, novel techniques such as voltage clamp recordings, they proposed that V_m was largely

determined by three currents; I_{Na}, I_K and I_{leak} and that both I_{Na} and I_K were controlled by voltage-gated ion channels. In the resulting mathematical model, activation variables (m and h for the sodium channels and n for the potassium channels) were associated with the voltage-gating mechanisms, which determined the probability that the channel is open or closed. In turn, for each activation variable, rate constants which were also voltage-dependent, determined how many times an ion channel opened and closed per second. Thus, a series of ODEs incorporating the activation variables and their rate constants, were formulated to solve the ionic current across the membrane which could in turn, be utilised to solve the membrane potential. The fundamental concepts of their mathematical model have been implemented for the purposes of modelling the excitability of cardiac myocytes.

More complex models of cellular AP, examples of which are discussed below, incorporate other ionic currents such as a calcium current and current through active transport pumps. The formulation of I_{ion} may also become more complex, representing the variety and complexity of the gating mechanisms controlling various ionic currents. Invariably models incorporating more ionic currents controlled by more complex gating mechanisms are based upon the Hodgkin-Huxley formulation. Here we describe four mathematical models of ventricular AP for the human, rabbit, guinea pig and rat, which have been presented in the literature and are utilised in Chapters 4, 5 and 6.

Human

The Ten Tusscher model of human ventricular AP (Ten Tusscher et al., 2004) was originally devised to assist in the study of clinical arrhythmias. It was formulated to represent experimentally derived values of AP and its rate-dependence, as well as CV restitution (Morgan et al., 1992; Cao et al., 1999; Nash et al., 2006) in human tissue whilst remaining viable in terms of computational demand. The Ten Tusscher 2 model (TT2) (Ten Tusscher and Panfilov, 2006) used in this study is based on the previous model and incorporates the main ionic currents involved in the AP, such as I_{Na}, I_{CaL}, I_{to}, I_{Kr}, I_{Ks} and I_{K1}, as well as their gating mechanisms regulating conductance and a calcium handling system (Stern et al., 1999; Shannon et al., 2004), resulting in a model with 53 parameters. Experimental data used to create the model were obtained primarily from human (Benitah et al., 1992; Nabauer et al., 1996; Nagatomo et al., 1998) but where human data were unobtainable, some data from animal studies were used (Luo and Rudy, 1994). Characteristics which

render the model useful for studying arrhythmias, are that the model produces spiral waves with an ECG trace similar to that of clinical VT recordings and alternans occur as a result of short DIs at fast pacing frequencies as predicted by the restitution hypothesis.

Alternative human models (Priebe and Beuckelmann, 1998; Bernus et al., 2002) are largely based on the Luo-Rudy (LR) guinea pig model (Luo and Rudy, 1994) and so TT2 was favoured for use here, for the purposes of relating modelling studies to clinical applications. The Grandi model (Grandi et al., 2010) incorporates a calcium handling system from a previously published rabbit model (Shannon et al., 2004) and as such, replicates rabbit APD restitution properties (Holzem et al., 2014). Due to the importance of restitution in this Thesis, we chose to use the TT2 model which best replicates human APD restitution curves. Possibly the most up-to-date model of human ventricular AP is the O'Hara model (O'Hara et al., 2011) which was formulated mainly from human electrophysiological data. However, due to the complications of implementing the cell models at the tissue level, it has been observed that the O'Hara model is unable to replicate the slope of the human APD restitution curve at the tissue level, is unable to produce similar maximum CVs to those observed experimentally, and as a result, VT dynamics produced by the model show discrepancies with clinical VT data with lower frequencies being produced (Elshrif and Cherry, 2014). Due to the fact that the TT2 model is able to replicate clinical VT, a characteristic which is vital to the research presented in this Thesis, we chose to use the TT2 to conduct this research.

Rabbit

We chose to use a model of ventricular AP in the rabbit because it has been suggested that the rabbit displays a similar effective electrical size of the heart to the human (Panfilov, 2006) and we wanted to further investigate that claim at varying pacing frequencies. The model that we used, the Mahajan et al. (2008) model is based on a previous model of rabbit ventricular AP (Shannon et al., 2004) but incorporates an improved calcium handling system. A seven-state Markovian model for the control of I_{CaL} was implemented in order for the model to be able to replicate intracellular calcium cycling (Shiferaw et al., 2003), a feature which causes flux in the intracellular ionic concentration of Ca^{2+}, which in turn affects the dynamics of APD alternans. There are 52 parameters which govern the shape of the AP via the currents I_{Na}, I_{to}, I_{Kr}, I_{Ks}, I_{K1} and I_{NaK} and the more complex calcium handling system. Experimental data used to construct the model are

from a variety of mammalian species due to the Shannon model being based on a previous generalised mammalian model of ventricular AP (Luo and Rudy, 1994). However some currents such as I_{Kr} were reformulated based on rabbit-derived data (Puglisi and Bers, 2001). The model is useful for studying arrhythmias as it was constructed to model the AP at fast heart rates such as might occur during VT. In addition, the incorporated intracellular calcium cycling enables the model to predict the arrhythmogenic wave-break due to APD alternans. In fact, the model was used to elucidate the effect of I_{CaL} and its gating mechanism on the repolarisation of the AP and its effect on APD (Mahajan et al., 2008).

Guinea Pig

The guinea pig model used in this study, the Luo-Rudy phase-2 model (LRdII) (Luo and Rudy, 1994) is an extension of a previous model (LR) from the same group (Luo and Rudy, 1991) and was created to provide a generalised model of mammalian ventricular AP. The original LR model was based on the simple formulations of membrane potential presented by Hodgkin and Huxley (1952) and Beeler and Reuter (1977), incorporating minimal ionic currents and their gating mechanisms. The LRdII model expands on the LR model by adding ionic exchange pump currents and a simple calcium handling system in order to model fluctuations in intracellular ionic concentrations during an AP, a feature which was lacking in previous models. Where available, data from experimental studies on guinea pigs were used to formulate the model (Sakmann and Trube, 1984; Nilius, 1988). However, because the model was created to represent a generalised mammalian cell model, data from other animals, mainly mammals, were also used (Brown et al., 1981; Forbes et al., 1985; Rasmusson et al., 1990).

Rat

The rat is an animal model which is frequently used to study cardiac electrophysiology in healthy hearts (Clark et al., 1993; Shimoni et al., 1995) and hearts post-MI (Qin et al., 1996; Yao et al., 1999) and is also a target for genetic and drug development studies for cardiomyopathies (Cheung et al., 1993; Franz et al., 1997; Lijnen and Petrov, 1999). As such, we chose to study the rat model here, for comparison with other species. The Pandit mathematical model (Pandit) (Pandit et al., 2001) of rat ventricular AP used in this study models the membrane potential as generated by I_{Na}, I_{CaL} I_{to}, various outward

potassium currents, a background leak current, and the ionic exchange currents I_{NaK} and I_{NaCa} in addition to a simple calcium handling system. The majority of data used to create the model were from rat experimental studies (Weis et al., 1993; Stengl et al., 1998; Lee et al., 1999; Volk et al., 2001) but the calcium handling system was adpated from a model of canine electrophysiology (Winslow et al., 1999). The model was created with two variations, an epicardial and an endocardial model. The epicardial model proved a better representation of the AP as observed experimentally (Shimoni et al., 1995) and so was chosen for use in this study.

3.5.2 Anatomical Models

The ability to research transmural activation in real-time in *in vivo* studies remains elusive. A particularly valuable aspect of computational modelling of cardiac function is that three-dimensional, transmural characteristics of activation waves can be studied in real-time (Clayton et al., 2006; Holden et al., 2006). Anatomical models of rabbit ventricles have been reconstructed for the purposes of being able to investigate and observe three-dimensional wave propagation throughout the myocardial wall, a result otherwise difficult to obtain in animal models. Here we describe this anatomical model of rabbit ventricles, which is utilised in Chapter 6 of this Thesis.

Simulations modelling propagation throughout the myocardial wall in Chapter 6, are conducted on an anatomically accurate three-dimensional model of the rabbit ventricles, described previously (Deo et al., 2009) and shown in Figure 3.1 with incorporated fibre

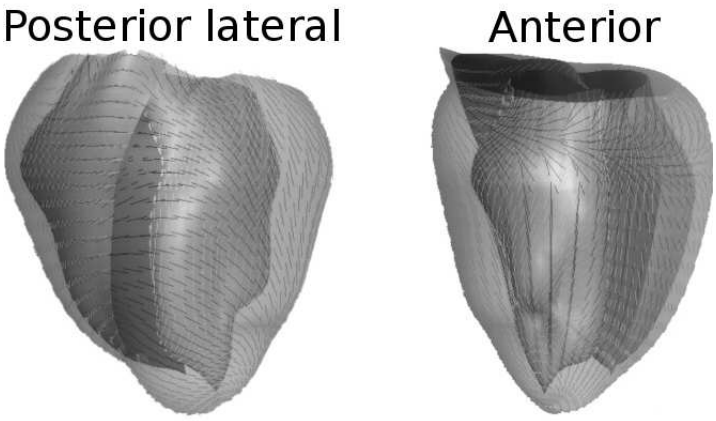

Figure 3.1: 3D model of rabbit ventricles with incorporated fibre orientation information. $Left$ - posterior lateral view and $right$ - anterior view (from Vetter and McCulloch (1998)).

direction information. The model displays an average wall thickness of 4.98mm at the

LV free wall, where reported fibre angles are $-71.0°$ at the epicardium and $59.6°$ at the endocardium with respect to the apex-base axis. The finite element mesh contains 3074982 tetrahedral elements and 547680 node points with, on average, $250\mu m$ between nodes. This model is based upon a preceding model (Vetter and McCulloch, 1998) for which, the geometrical information of the myocardial surfaces, as well as fibre orientations, was acquired manually from histological slices and so whilst being accurate, the model lacks fine-scale structural details such as endocardial trabeculations, papillary muscles and blood vessels. It is essential that the geometrical model used in this study is able to produce arrhythmia dynamics similar to those observed *in vivo*, in order for the results of this research to correlate with those seen in the clinic. The model should be sufficiently accurate to produce these reentry dynamics, but not so detailed that it becomes too computationally demanding to run simulations. Fine-scale anatomical structures, such as those that are absent in the model, have been implicated in playing a role in sustaining arrhythmias in large animal models (Pertsov et al., 1993; Kim et al., 1999; Nielsen et al., 2009), due to structures acting as anchors around which spiral waves rotate. This is contrary to conclusions from rabbit models which do not observe such anchoring effects of micro structures (Chen et al., 2000; Wu et al., 2002). A subsequent study confirmed, with computational modelling, that the gross ventricular geometry, rather than the fine-scale anatomy of the rabbit ventricles largely governs arrhythmia dynamics (Bishop and Plank, 2012). The study also made an important observation that the activation wavelength is relatively short in comparison to heart size in large animal models and wavelength is relatively long in comparison to heart size in humans and rabbits. Therefore, the anchoring effect of small structures observed in large animal models can be attributed to the short activation wavelength, relative to the size of the anatomical structure; the wave is able to sustain propagation around structures without collision and wavefront-wavetail interactions due to the small size of the wavelength. In summary, fine-scale anatomical features may not play a role in governing arrhythmia dynamics in rabbit or human hearts and so the gross anatomical geometrical model used in this study is of sufficient detail to produce propagation as may be seen in the human heart.

3.5.3 Utilisation of *In Silico* Models to Investigate Post-MI Arrhythmias

In the previous paragraphs, we described existing methodologies used to study arrhythmias using computational models. We now consider some of the work which has utilised a computational modelling approach to investigate post-MI arrhythmias.

Computational electrophysiological models of APs permit parameter sensitivity analyses to uncover the effects of solitary parameters or a select combination of parameters on wave propagation and the underlying mechanisms of reentry (Cherry and Fenton, 2004). Isolating such parameters or recording the effects of the investigation is often not possible in animal models. However, a computational model of rabbit AP was utilised to study the effects of reducing I_{Na} on conduction of the wave and results indicated that source/sink mismatches at the wave tip affecting conduction are exacerbated in BZ remodelled tissue (Boyle et al., 2014). Several studies have investigated the effects of pacing and restitution in simplified two-dimensional models on reentry dynamics, verifying that steep resitution slopes result in alternans (Qu et al., 2000) and increase the likelihood of wavebreak (Xie et al., 2002; Groenendaal et al., 2014) and importantly, uncover the mechanisms causing the effect. Of note, several studies have altered ion channel parameters to simulate BZ remodelling based on experimental data and observed the effects on APD and conduction. Decker and Rudy (2010) verified that I_{CaL} and I_{Na} remodelling increased the dispersion of repolarisation causing conduction block. Several studies from the Trayanova group which simulate BZ remodelling (details in Section 3.1) in ventricular models, illustrate that such models can be of tangible use in investigating the effects of BZ tissue anisotropy on arrhythmia dynamics (McDowell et al., 2011), and in investigating and optimising both the defibrillation (Rantner et al., 2012) and ablation (Ashikaga et al., 2013) treatment strategies.

Computational models of post-MI reentry are utilised in order to overcome the limitations of both animal model and clinical research. Importantly, computational models can provide visual, detailed insight into three-dimensional wave propagation dynamics in a way which is unachievable in both animal model and clinical research. A model of infarcted rat ventricles was constructed incorporating the dense fibrotic scar as well as BZ tissue in order to observe three-dimensional propagation post-MI (Rutherford et al., 2012). Electrophysiological membrane potential properties were simulated on the anatomical model and changes in wave propagation due to gap junction remodelling and tissue anisotropy

were observed. The widely used and validated anatomical model of rabbit ventricles which was described above (Deo et al., 2009) has been used to observe the complex propagation in shock-induced reentry. It is important to stress that at present, only computational models could provide such insight into the transmural propagation of a wave based on physiological data.

It has been established that computational models of anatomy and electrophysiology can be of use in simulating both structural MI scar heterogeneity and ionic properties of healthy and BZ tissue in order to thoroughly investigate mechanisms of wave propagation post-MI and potential therapies. Crucially, with the advancements in computational modelling techniques and high-performance computing, *in silico* models are increasingly being studied with the intention of complimenting clinical studies with patient specific computational models. Sermesant et al. (2005) have showed that it is possible to construct models of heart function utilising patient specific data. The resulting models are then used to simulate the patient's pathology and guide the personalised treatment.

3.6 Can Animal Models Replicate Clinical Arrhythmias?

Animal models are used extensively to investigate arrhythmia dynamics which have clinical signficance and potential treatment strategies for clinical use. However, in order to draw conclusions about the relevance of the study to clinical scenarios, it is vital to understand the differences between animals and humans. In particular, when studying arrhythmia dynamics, it is necessary to know how similar wave propagation is around the myocardium of different species.

Panfilov (2006) addressed this question directly. It was originally thought that animals with larger hearts similar to the size of the human heart, such as pigs and sheep were the best animal models for studying reentry, in order to draw conclusions which informed clinical scenarios. However, as previously discussed (Section 2.6), it is not only the size of the heart that is a crucial parameter in determining the success of wave propagation, but also the wavelength plays a vital role in determining the size of the excitable gap. The study compared rabbit, pig and dog hearts to the human heart in order to answer the question about which animal model is most suitable for use in modelling arrhythmias.

Panfilov proposed a metric called the effective electrical size of the heart to determine how similar spatial patterns of VF wave propagation are in different hearts. In order to

calculate the effective size, the size of the tissue was divided by the wavelength. Due to the complex anatomy of the ventricles, the relative size of hearts were used in the calculation. It was assumed that the hearts were of similar shapes and so the cubic root of the mass of the heart ($\sqrt[3]{M}$) was used. The mass of the heart was estimated to be 0.6% of body mass. Wavelengths were estimated using the period of the spiral wave rotation obtained from ECGs to approximate the dominant frequency of the VF.

Species with similar effective sizes displayed similar propagation dynamics, as the calculation determines how propagating waves fit into the physical tissue. Figure 3.2 displays the results of the effective size calculation. Surprisingly, the study concluded that

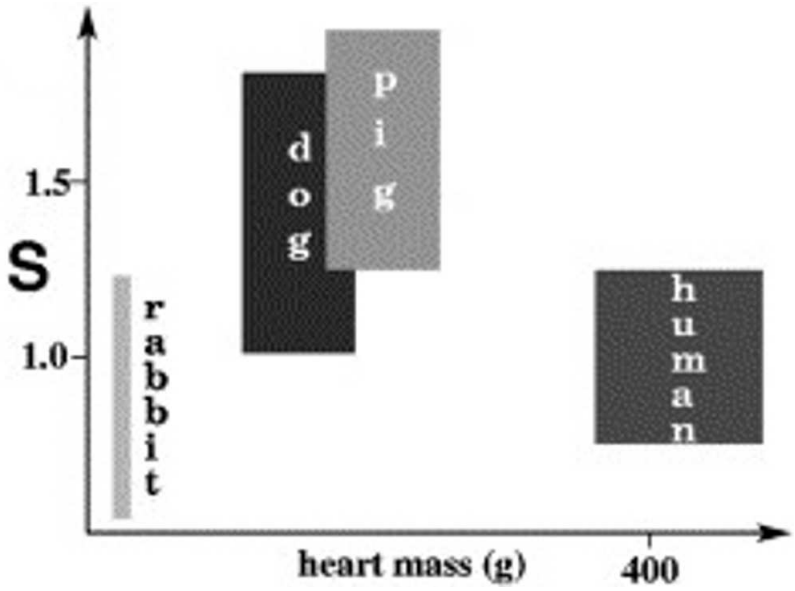

Figure 3.2: Results of the effective size of the heart calculation (from Panfilov (2006)).

the effective size of the rabbit heart was most similar to the human despite having the least similar physical size of the hearts. In fact, both the rabbit and the human displayed small effective sizes suggesting that, in these species, wavelength is relatively large in comparison to the size of the tissue, which may indicate that VT and VF are less likely to occur in these species, than in the pig and the dog.

Importantly, the study suggested that it is the effective size of the heart which can predict how similar the hearts of different species are and provided a method to investigate which species is most likely to replicate arrhythmia dynamics of the human in order to provide clinically useful results. However, considering the importance of rate adaptation of APD and CV resulting in changes in wavelength, and potential species differences in the restitution profiles, it would be expected that restitution dynamics may affect the effective

size and species differences in wave propagation.

3.7 Ablation Treatment

Radiofrequency catheter ablation is a common procedure used to treat post-MI VT. In Section 2.6, we provide an overview of the ablation procedure. Here, we present the studies which have contributed to the development of the ablation procedure methodology. In particular, a critical review of the literature describing techniques to map the infarct scar and determine the ablation lesion location is given.

Since the 1960s intracardiac electrodes have been used to record electrical activity in the heart (Durrer et al., 1967). In the following years, the technique commonly used to terminate VT was endocardial resection, which resulted in significant tissue damage because large amounts of scar and BZ tissue were removed, but success rates of the procedure were high (Stevenson, Weiss, Wiener and Nademanee, 1989; Stevenson et al., 1995). The first closed chest catheter ablation treatment of atrial arrhythmias was performed by Scheinman et al. (1982), which proved a much less invasive procedure. However, lower success rates of ablation therapy suggests that finding the optimal target site for ablation to terminate the VT is inadequate and requires improvement. Since the first ablation treatment in 1981, considerable research has been conducted to improve mapping the scar region in order to determine the optimal location of the ablation lesion.

The endpoint of an ablation procedure is ill defined (Aliot et al., 2009), but can be considered as the termination of a clinical VT. The clinical VT is a spontaneous rhythm that has been recorded by surface ECG. Mapping techniques to identify ablation lesion targets are based on observation of local electrograms and surface ECGs. Scar may be detected by low amplitude voltages on local electrograms and slow conduction indicative of isthmuses through the BZ (Fenoglio et al., 1983; Stevenson et al., 1993) can be detected by fractionated electrograms or isolated diastolic potentials (IDPs) (Stevenson et al., 1995; Lambiase et al., 2004).

3.7.1 Optimal Location of Ablation Lesions

For a sucessful ablation treatment, it is necessary to understand where the theoretical optimal site of the lesion is. The complex nature of the structural substrate results in the possibility of a circuit having multiple exit sites or multiple paths through the scar,

or a variety of completely distinct circuits (Fenoglio et al., 1983; De Bakker et al., 1988; Stevenson et al., 1995). The question then is where should the ablation lesion be located in order to terminate the clinical VT? Fitzgerald et al. (1988) tested possible optimal sites of location lesions by ablating both sites within the slow conducting isthmus and sites located at the exit site of the scar. They found that creating ablation lesions at the exit sites of the scars was only successful 50% of the time and ablating regions within the isthmus itself was more successful. However, later Stevenson et al. (1995) suggested that only the exit point of the circuit needs to be ablated to terminate reentry. Segal et al. (2010) suggested that due to initial block facilitating reentry, the site of initial block should be the target for the ablation lesion. Nonetheless, the removal of one exit site or site of initial block does not ensure termination of other VTs that may occur at a later stage (Fenoglio et al., 1983). Others have suggested that in order to prevent future occurrences of all VTs, all regions of slow conduction should be ablated, although this technique may produce significant damage to the heart and result in later dysfunction (Stevenson, Weiss, Wiener and Nademanee, 1989; Stevenson et al., 1993; Jais et al., 2012).

3.7.2 Mapping the Scar During Ventricular Tachycardia

Activation Mapping

Initially proposed mapping techniques were conducted whilst VT was induced in the patient by programmed stimulation. One such technique is termed activation mapping which compares local electrograms recorded during VT, measured at different locations throughout the scar region to trace the sequence of presystolic IDPs, produced by slow conduction through the isthmus (Stevenson, Weiss, Wiener and Nademanee, 1989; Bogun et al., 1997; Strohmer and Hwang, 2003). De Bakker et al. (1988) showed that from a sequence of electrograms $(a - g)$ activation occurred from $a - c$ where conduction was blocked so the wave travelled around the refractory tissue to g and travelled back to the site of initial activation (a) through a slow conducting isthmus (Figure 3.3). Large deflections occured sequentially in time on the electrograms representing the spread of activation across the myocardium from a. IDPs occurring from $e - a$ depict the propagation through the isthmus back across the initial region of block to synchronise with the second activation of the healthy myocardium at a. They verified this mechanism by recording intracellular membrane potential traces from sites within the isthmus and showed that IDPs on local

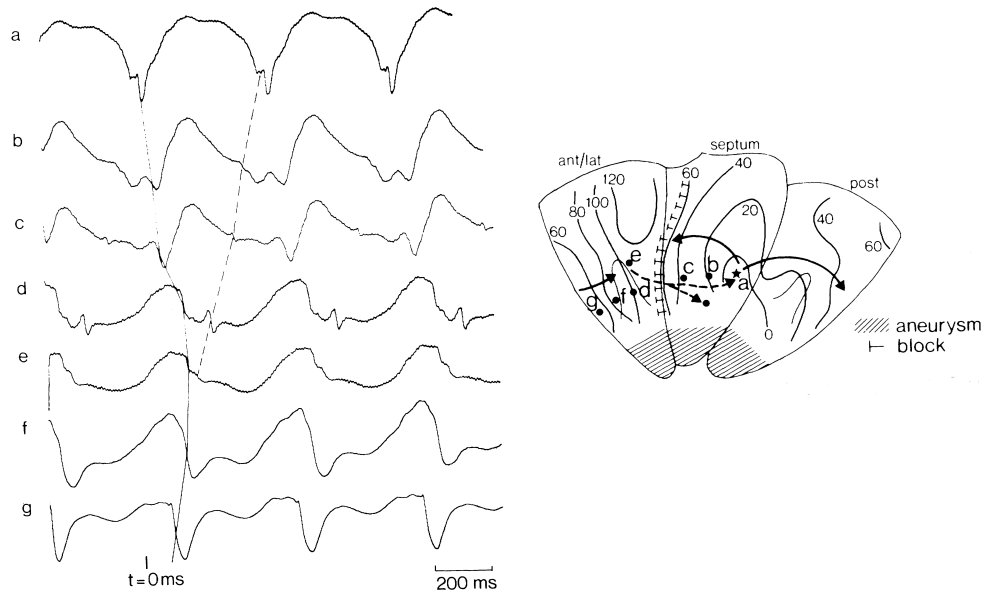

Figure 3.3: Activation mapping reveals propagation of reentrant wave through slow conducting isthmus as IDPs on electrograms (from De Bakker et al. (1988)).

electrograms correspond to depolarisation of the membrane within the isthmus. Stevenson et al. (1993) suggested that the QRS on a surface ECG occurs when the activation wave exits the isthmus and activates the healthy tissue. Therefore, ablation is targeted at sites where electrograms have been recorded which display activation just prior to the QRS, namely the exit point of the scar (Stevenson et al., 1993). However, it is possible that IDPs which may be involved in the circuit are not detected unless the electrode is within $200 - 300\mu$m of the site (Fenoglio et al., 1983).

Entrainment Mapping

Initiation of VT is required in another mapping technique; entrainment mapping. Stevenson et al. (1987) described the method in which pacing is performed from sites of identified IDPs, at rates slightly faster than the VT rate. VT is initiated and fractionated ECGs are sought. If the pacing site is located within a reentrant circuit, the paced VT will display a similar QRS to that of the clinical VT. This is called entrainment with concealed fusion (Stevenson et al., 1993). If during pacing at a certain location entrainment occurs, ablation is carried out at the pacing location. However, it was observed that when the pacing location was changed, the exit point of the scar could also change, invoking possibly a different VT but with identical QRSs, resulting in inaccurate definition of the ablation target. Indeed, half of patients had to undergo the procedure twice because of

its inaccuracy in locating a sufficient ablation lesion target site. Another problem with defining ablation targets based upon ECG and local electrogram QRS patterns is that, during VT, the QRS may become less well defined and is also affected by anti-arrhythmic drugs (Stevenson et al., 1987).

3.7.3 Mapping the Scar During Sinus Rhythm

Crucially, the induction of VT greatly increases the risk of the procedure as the rhythm is able to deteriorate to VF, which needs to be rapidly defibrillated to avoid cardiac arrest. Mapping of the VT therefore requires that the clinical VT be inducible in the clinic at the time of the procedure. Indeed, the clinical VT is often non-inducible during the clinical procedure. Moreover, It is well documented that multiple VTs supported by different reentrant circuits can occur within the same patient (Fenoglio et al., 1983). On average 3-4 different VTs have been reported in any one patient (Stevenson et al., 1995). The induction of the clinical VT is further complicated by the fact that different pacing protocols can induce different VTs (Stevenson, Weiss, Wiener and Nademanee, 1989). In order to ablate the clinical VT, mapping of the scar region needs to be performed when, specifically, the clinical VT is induced which is not always attainable. In addition, VT must be haemodynamically tolerated, that is, not cause haemodynamic compromise to the patient. Whether the VT is haemodynamically stable depends on the severity of the damage caused by the MI and also on the rate of the clinical VT (Stevenson et al., 1995), factors which are highly variable. As a result, it is often not the case that VT is haemodynamically tolerated and so mapping during VT cannot be performed. The VT must also be stable for a period of time in order for electrograms of the paced VT to be recorded, a requirement which is also often not fulfilled. The complications of mapping the substrate during VT have led to the development of techniques to map the substrate during sinus rhythm.

Mapping the VT during sinus rhythm can be performed based on defining areas of slow conduction (Stevenson et al., 1995). Slow conduction occurs through isthmuses in the infarct scar due to the tortuous routes of conduction through surviving myocyte bundles, separated by non-excitable fibrotic tissue. It is supposed that these isthmuses form part of a reentrant circuit, as conduction block and propagation through the substrate are required for figure-of-eight reentry. Stevenson, Weiss, Wiener and Nademanee (1989) suggested that during sinus rhythm, fractionated electrogram signals occur after the QRS complex

is observed on the surface ECG. This is due to the QRS being produced by the activation of the healthy myocardium and slow conduction then occurring through the isthmus, after the activation of the ventricle has finished. However, it has also been noted that these sites may be involved in the reentrant circuit, but may also be bystander sites not involved in the circuit but still displaying the pattern of fractionated electrograms (Stevenson et al., 1987, 1995). As such, fractionated electrograms which may occur throughout the scar and BZ regions are a good indicator of the general region causing the reentry, but not of the specific sites involved in the reentrant circuit.

Pace Mapping

The problem with any technique relying on IDPs or fractionated electrograms such as activation mapping, is that the low amplitude voltages may just be an artefact of the electrogram recording (Stevenson, Weiss, Wiener, Rivitz, Nademanee, Klitzner, Yeatman, Josephson and Wohlgelernter, 1989). A mapping technique which doesn't rely on low-amplitude voltage data is pace mapping, which can be performed in sinus rhythm and is based on determining where the pacing catheter is in relation to the circuit (Stevenson et al., 1993). In the late eighties and early nineties, Stevenson's laboratory described and studied the pace mapping protocol. Pace mapping involves pacing from locations, which have been suggested as being part of a reentrant circuit by the detection of low amplitude electrograms, in the region detected during sinus rhythm (Stevenson, Weiss, Wiener, Rivitz, Nademanee, Klitzner, Yeatman, Josephson and Wohlgelernter, 1989; Bogun et al., 2006). If the QRS resulting from paced rhythm is similar to the clinical VT QRS, it suggests that the pacing location is located near to the exit site of the scar (Stevenson, Weiss, Wiener and Nademanee, 1989). However, the site is not necessarily located within the reentrant circuit (Brunckhorst et al., 2003). More specifically, the time at which the tissue is stimuluted within the reentrant circuit is compared to the surface ECG. This is termed the S-QRS interval. If the S-QRS interval is large, it indicates that pacing was performed within the reentrant circuit and the activation wave propagating through the isthmus conducted slowly towards the exit site of the scar where, on the wavefront spreading from the isthmus to the healthy myocardium, the QRS is initiated. These sites where a large S-QRS is indicated are deemed to be ablation lesion targets (Brunckhorst et al., 2003). If the S-QRS is very small, it indicates that no delay occurred due to slow propagation through the isthmus and the QRS complexes of the paced rhythm and clinical VTs are

very similar (Stevenson, Weiss, Wiener, Rivitz, Nademanee, Klitzner, Yeatman, Josephson and Wohlgelernter, 1989). These sites displaying a small S-QRS would normally not be ablated. However, the exit point of the scar would also display a small S-QRS (Stevenson, 2009) and would not be ablated according to the pace mapping protocol despite being the optimal site of ablation (Stevenson et al., 1992).

Substrate Mapping

Mapping VT in sinus rhythm greatly increases the applicability of the treatment to more patients and a variety of techniques have been proposed (Bogun et al., 2002). Marchlinski et al. (2000) proceeded by performing voltage mapping in sinus rhythm, in order to specify precise voltage limits to distinguish between dense scar, BZ and healthy tissue. They proposed that dense scar could be located by potentials less than 0.5mV and BZ tissue was located at regions displaying voltages of between 0.5 and 1.5mV. Having identified the substrate regions, they performed linear ablation lesions which extended from an estimated exit point of the dense fibrotic scar, all the way to healthy myocardium resulting in potentially very large lesions. Other research groups have also employed the substrate mapping technique in the clinic, ablating sites displaying low voltage ECGs and in addition, search for sites of low excitability which require larger stimulus current to excite the tissue (Stevenson, 2009). Verma et al. (2005) suggested that substrate mapping could fail to identify ablation targets due to diseased myocardium sometimes displaying voltages within the range of healthy myocardium. In addition, many electrogram traces are needed for accurate mapping of the substrate. As such, long procedure times result in the technique being less favourable in the clinic.

3.7.4 Improving the Ablation Treatment

The major problems with current mapping techniques requiring VT induction have already been discussed, but these techniques remain the most accurate with highest success rates. Another problem encountered with current mapping techniques is that they rely on mapping and identifying regions of slow conduction by the presence of IDPs and fractionated electrograms. In fact, due to the resolution of mapping, narrow isthmuses may well not be located (Arenal et al., 2004). It was also found that only 30% of channels identified by IDPs actually formed part of the VT circuit (Mountantonakis et al., 2013) and so multiple ablation lesions were required until one location terminated the reentry. It has also been

found that ablation relying on IDP identification to map the substrate was only 73% effective in terminating the clinical VT and moreover, anti-arrhythmic drugs were still utilised after the procedure to reduce the risk of another VT occurrence (Morady et al., 1993). A study by Verma et al. (2005) suggested that 63% of procedures which ablated within an identified BZ isthmus resulted in termination of the VT. However, their results also indicated that ablation lesions created at sites outside of an identified BZ isthmus were successful in terminating VT. These results suggest that the techniques employed to locate successful ablation lesions are fallible. In addition, reentrant circuits may involve regions of endocardium as well as epicardium and whilst it is routine to map endocardial scar locations, it has been shown that mapping both epicardial and endocardial scar locations may improve ablation success rates (Kaltenbrunner et al., 1991). However, it is possible to ablate transmural circuits from the endocardium if the scar tissue is thin enough or if the lesion is large enough (Stevenson et al., 1995).

Low success rates of the ablation procedure, with some reporting only a 50% success rate in terminating VT (Tung et al., 2010), indicate that susbtantial improvements are required if the treatment is to be a reliable therapy. The major limiting factor in the success of the ablation procedure can be attributed to the mapping technique. Specifically, the lack of accuracy in locating the critical exit point of the scar and the requirement of the VT to be inducible and haemodynamically tolerated, both contribute to the poor procedure success rates. Despite various techniques available to map the substrate during both VT and sinus rhythm, advancement in the accuracy of locating the critical exit point of the infarct scar is required (Stevenson et al., 1987; Stevenson, Weiss, Wiener and Nademanee, 1989; Haqqani et al., 2013) if treatment success rates are to be improved.

A novel application of computational modelling to simulate patient-specific pathologies has been studied by Sermesant et al. (2005). Utilising x-ray and magnetic resonance (XMR) imaging patient data, computational models of anatomy and electrophysiology were created. The study suggested a possible future application of these models which could guide the ablation procedure using the patient-specific computational models. However, as conveyed in the paper, these techniques require long procedure times and expose the patient to large amounts of x-rays. Therefore, despite the potential of this technique, further research needs to be performed in order to more efficiently guide the ablation procedure, so that the methodology may be incorporated into such patient-specific treatments.

3.8 Predicting the Success of Reentrant Propagation

Considering the need for improved scar mapping techniques to increase the success rates of the ablation procedure, we turn our attention to a proposed methodology which can determine whether reentry can occur within a potential circuit. If it is possible to determine whether reentry is able to occur or not, there may be a potential application to guide the ablation procedure by determining ablation lesion targets.

It is evident that many ionic and electrical properties of healthy and diseased myocardium interplay to determine the success of reentry, making it difficult to accurately predict whether a particular circuit could maintain reentry. A pioneering study by Coronel et al. (2009) provided a simple metric based on the leading circle approach and wavelength metrics, to determine the success of propagation.

The group set up a Langendorff-perfused porcine heart and induced repolarisation heterogeneity between two regions of the heart. Namely, the APD was shortened by administration of pinacidil into the left anterior descending (LAD) artery which shortened APD in the anterior LV region which was termed the proximal region. Sotalol was administered into the aortic cannula which increased the APD in an adjoining region of the myocardium, and was termed the distal region. Intracardiac electrodes recorded electrograms from the two regions and ATs and RTs were calculated from the recordings.

An S1S2 pacing protocol was implemented from the proximal region and the premature S2 beat resulted in conduction block as it approached the refractory distal region. Figure 3.4 (*left* hand column) shows that the distal zone repolarises from S1 at 300ms, whereas the S2 beat activates the proximal tissue at 280ms. As such, the wave was diverted around the block until it propagated into the distal region as it recovered, and the wavefront curved in a spiral wave towards the site of intial block. Crucially, they proposed that if the proximal tissue was recovered when the wavefront reached the distal side of the initial block, as seen in the *right* hand column (*top* & *middle*), the wave could propagate into the proximal region forming a reentrant circuit due to uni-directional block (UDB). However, if the proximal tissue remained refractory, the wave would block again causing bi-directional block (BDB) and terminate the wave and reentrant circuit. Considering these conditions, the success of reentry depended on the repolarisation time in the proximal region and the activation time in the distal region.

Coronel et al. (2009) proposed a simple metric, which they termed the fibrillation factor

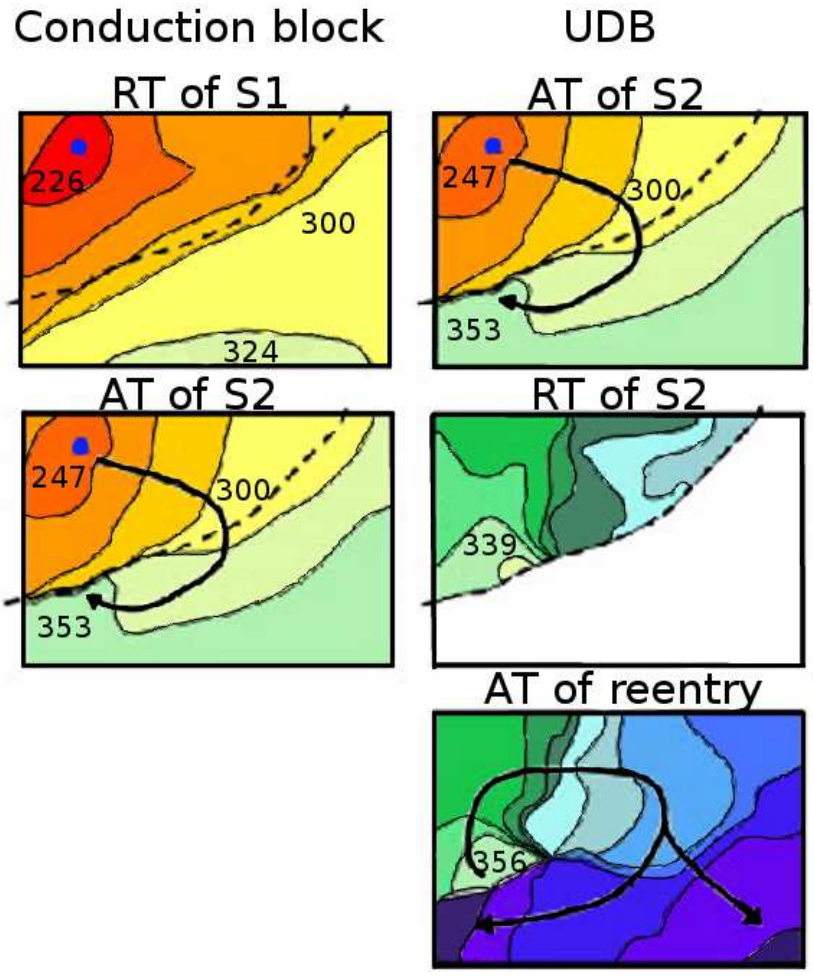

Figure 3.4: AT and RT maps of wave propagation across heterogeneous tissue. The proximal zone is located above the dotted line, the distal zone is located below the dotted line. The *blue* symbol in the proximal region illustrates the stimulus location. Images in the $left$ hand column illustrate initial conduction block of S2 (*bottom*) due to refractory tissue in the distal region resulting from S1 activation (*upper*). The *right* hand column displays the occurrence of reentry. UDB occurs due to the proximal tissue being recovered from S2 activation (*middle*) before S2 activation of the distal zone occurs. A reentrant beat ensues and its activation map is shown *bottom right* (from Coronel et al. (2009)).

(FF), which could be used to predict whether reentry could occur. The FF is the AT at the distal region substracted from the RT at the proximal region. Hereby, it is possible to reveal whether an excitable gap exists and whether reentry can occur. A negative, or low positive FF value suggests that the wave activates the distal region after the proximal region has recovered and the wave can reenter. A higher positive value of FF indicates that no excitable gap is present as the wave activates the distal region before the proximal zone is recovered and reentry cannot occur.

A subsequent paper further investigated the metric by altering the CV to determine the

arrhythmogenic effect (Coronel et al., 2010). It was previously suggested that a reduction in I_{Na} is both pro- and anti- arrhythmogenic and so they set about to investigate the mechanisms involved in reentry resulting from sodium channel blockade.

The same experimental preparation was used and the sodium channel blocker flecainide, was administered into the distal region. Figure 3.5 illustrates the effects of the

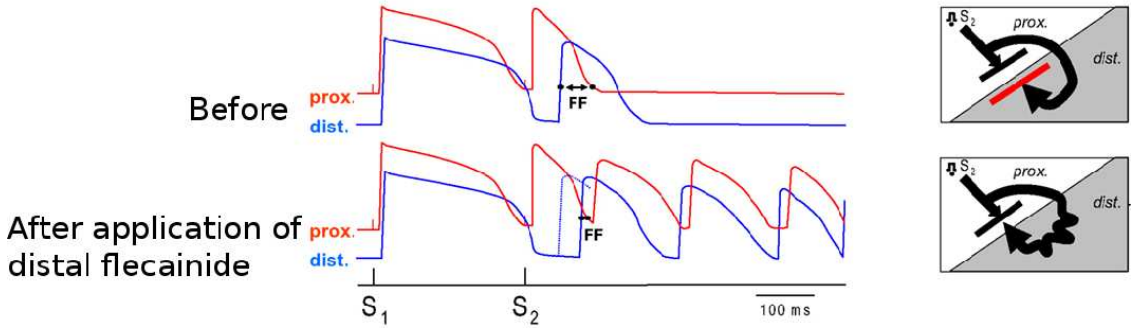

Figure 3.5: Illustrating the FF calculation theory. *Top* row - Membrane potential traces of the proximal and distal zones before flecainide administration results in BDB. *Bottom* row - after flecainide administration in the distal zone, the CV is reduced, delaying the activation of the distal tissue, enabling UDB (from Coronel et al. (2010)).

drug on the FF. The *top* row of images display AP traces in both the proximal (*red*) and distal (*blue*) zones prior to flecainide administration. It is possible to see that the RT of the S2 in the proximal zone occurred after the S2 AT in the distal zone resulting in BDB and a positive FF value. The *bottom* row of images display the effect of flecainide reducing CV in the distal region. The time at which the S2 wavefront arrived at the distal side of the line of block was increased, effectively increasing the AT used in the FF calculation (whilst RT remained the same). As such, the proximal tissue had time to recover before the wave propagated from the distal region and the wave could reenter. The resulting FF values were negative, both substantiating the FF calculation and indicating that a reduction in CV in the distal zone was proarrhythmic. When flecainide was administered to the proximal zone, the CV in the proximal region was decreased which delayed the time in which the activation wavefront reached the line of block. As a result, the repolarisation of the proximal zone was delayed and the effect of reducing CV in the proximal zone was antiarrhythmic. In addition, the delay of the activation wave reaching the distal region from the stimulus site decreased the dispersion of repolarisation resulting in a smaller line of block, which in turn decreased the path length, an effect which was also antiarrhythmic. Despite the complexity of pro- and anti- arrhythmic mechanisms which govern reentrant

circuits, the FF metric appears to be able to predict the success of reentry with minimal calculation and data requirements.

3.9 Summary and Motivation

We have presented a review of the literature in which small animal models are utilised to study post-MI VT. Studies investigating post-MI VT ultimately seek conclusions to inform clinical treatment strategies. As such, animal models used in these investigations should resemble, as closely as possible, clinical VT. We outlined the study by Panfilov (2006) which proposed a method to determine the effective electrical size of the heart. The effective size determines the critical ratio between the heart size and the activation wavelength which in turn indicates the dynamics of wave propagation. Panfilov utilised the methodology to determine the similarities between the human and larger animal model hearts in terms of VF dynamics. Given that small animal models are used widely in research of post-MI VT, as seen in this chapter, it remains to be seen which small animal model most closely replicates the arrhythmia dynamics of the human. In addition, it is necessary to determine which animal model is most suitable to model VT dynamics which occur at slower frequencies than VF. Given the influence of pacing frequency on wavelength via the restitution effect, it could be assumed that restitution may affect the similarities or differences between hearts of different species.

In this chapter we have also demonstrated the importance and benefits of computational modelling and as a result, we utilise the techniques described above to model cardiac function, for the purposes of investigating post-MI VT. In Chapter 4 we employ the effective size calculation to determine which small animal model displays the most similar effective size to the human at pacing frequencies indicative of VT. In addition, we observe the effects that restitution plays on the effective size in each species model. In order to determine which species model is most suitable for investigating scar-related reentry, we simulate BZ remodelling based on protocols described in this chapter and observe how the effective size is affected. We then use the information gained about the most suitable model, to investigate post-MI reentry and utilise those models for further investigation in the following chapters.

In spite of the substantial efforts to improve the accuracy of the mapping techniques utilised in the ablation procedure, there remains to be developed, a technique which can

be performed during sinus rhythm and which does not rely upon location of low voltage or mid-diastolic potentials which require very precise catheter manipulation. The pivotal experimental work by Coronel et al. (2009) describing the FF metric to determine whether reentry could occur based on the temporal excitable gap between the wavefront and the wave back, may lend use to a novel technique to improve mapping of the substrate. If the FF metric can predict reentry based on AT and RT data alone, it suggests that a mapping technique based on the FF metric could improve the accuracy of locating an ablation lesion target. In addition, the fact that the FF can identify BDB indicates that potential reentrant circuits could be identified without the need to induce VT. In Chapter 5 we apply the concepts described by Coronel et al. (2009) to investigate a novel technique which can predict the susceptibility to reentry over a region of tissue rather than between two points. In Chapter 6 we extend the study to investigate the technique in 3D tissue. However, considering the limitations of clinical data as discussed above, we test whether, despite those limitations, the technique remains viable in the clinic and can be used to guide the ablation procedure.

Chapter 4

Assessing the Effects of Species Differences in Activation Wavelength and Heart Size on Reentry Dynamics

Chapter 3 outlined the mechanism of reentry around MI scars and how the relationship between the size of the activation wavelength and the size of the tissue may affect the pattern of propagation around the scar. In addition, it was explained that the cardio-protective property of restitution affects the APD and CV, in turn causing the wavelength to vary depending on pacing frequency. In this chapter, we investigate the relationship between the wavelength and size of the heart by calculating the effective electrical size of the heart. Wavelength restitution and its impact on the effective size is also observed. Also, incorporated in Chapter 3 was a discussion about the importance and the use of animal models in researching post-MI reentrant arrhythmias. Here, we utilise the effective size to infer how reentrant propagation around infarct scars differs between species due to the differences in heart size, activation wavelength and restitution properties, with the aim of concluding which species model most effectively replicates reentry dynamics of the human and hence, provides conclusions which are of value to clinical research.

4.1 Introduction

Arrhythmias caused by reentrant wave propagation around infarct scars can be lethal, necessitating research to understand the mechanisms of induction, propagation and termination, in order to be able to formulate treatment strategies. We saw in Chapter 3 that animal model studies and computational models based on animal data, are an important supplement to clinical studies of arrhythmias, providing the ability to overcome restrictions faced in clinical research such as the inability to conduct the research *in vivo*, insufficient sample sizes, ethical restriction or economic infeasibility. Animal or computational models utilised in such studies are required to faithfully replicate aspects of human *in vivo* cardiac structure or function, which may affect arrhythmia mechanisms. However, inherent species differences in cardiac anatomy and electrophysiology exist (Ten Tusscher et al., 2007, 2009). Indeed, it is plausible to suggest that using clinical data and computational models of human electrophysiology is the best way to investigate clinical pathologies (Kazbanov et al., 2014; Taggart et al., 2014). However, due to the extensive use and important benefits of animal models, it is necessary to determine which species model most closely replicates the essential characteristics influencing the mechanisms of reentry in the human, in order to suggest an optimal animal model for use in studying clinical arrhythmias.

Reentry caused by an MI occurs due to the structural heterogeneity of the tissue formed by the fibrotic scar and the surrounding BZ region displaying altered ionic and conductivity properties (Sections 2.6 and 3.1). As a result, activation waves may propagate around a structural obstacle such as an infarct scar. The ability of a reentrant wave to be sustained around such a circuit, strongly depends upon the relative size of the wavelength to the size of the obstacle, as previously discussed in Sections 2.6 and 3.2. Both of these crucial measures, wavelength and the size of the tissue or heart size, vary between species and may result in species differences in arrhythmia dynamics.

APD, CV and wavelength are dependent on changes in pacing frequency, which in turn can affect wave propagation. The changes in APD and CV as a result of increasing pacing frequency occur, due to the reduced recovery from inactivation of the ionic channels which has been discussed in detail in Sections 2.3 and 3.3. These changes in APD and CV with changing BCL contribute to the phenomenon of wavelength restitution as wavelength can be calculated as the product of APD and CV (See Equation 2.4 in Section 2.3). The

resulting relationship between wavelength and BCL, indicates that wave propagation and arrhythmia dynamics change as pacing frequency varies due to the changing size of the wavelength, relative to the constant size of the tissue.

In order to be able to draw conclusions about arrhythmias from animal experimental models or computational models based on animal data which are relevant to the clinic, species differences in ventricular size and wavelength need to be considered. As explained in Section 3.6, a recent theoretical study sought to determine the similarity of animal models of VF relative to VF in the human (Panfilov, 2006) by calculating the relative effective size of the heart (I), taking into consideration the size of the heart in relation to the wavelength, in order to characterise similarities in wave propagation between species. I is given by the following equation:

$$I = \frac{Heart\ Size}{\lambda} \tag{4.1}$$

By considering the effective size of the hearts of different species such as the dog, pig, rabbit and human, it was suggested that the rabbit provided the closest clinical analogue for studying VF, indicating that wave propagation dynamics in the rabbit are likely to be most similar to that of the human. Hence, important conclusions may be drawn about the use of specific animal models to inform clinical research.

The Panfilov (2006) study compares the effective size between rabbit, dog, pig and human computational models of electrophysiology. However, small animal model studies are increasingly being utilised to study reentrant mechanisms (Section 3.4) with the additional benefits of reduced ethical constraints and economic cost. Inter-species comparisons between small animal models and human models in terms of the similarities in effective size, have not previously been investigated. Here, we perform the analysis, calculating I from *in silico* ventricular AP data, in order to compare wave propagation dynamics between the human and small animal models, for the purpose of drawing conclusions about the most suitable small animal model to use in studies of post-MI VT arrhythmias. Contrary to the Panfilov (2006) study in which I was calculated at fast pacing frequencies, similar to those produced by VF, we compare the effective size between species at slower pacing frequencies, to observe the important inter-species differences that may occur during scar-related reentry, which typically occurs at slower frequencies than VF. In addition, APD, CV and wavelength restitution and the effect of varying pacing frequency on the effective

size is observed. The characteristics of these restitution effects may vary between species and may cause augmented species differences in wave propagation. Observing the effect of restitution on the effective size will determine the suitability of the different small animal models in replicating post-MI VT arryhthmia dynamics of the human. BZ remodelling is known to affect both APD and CV around the perimeter of infarct scars (Sections 2.6 and 3.1). A crucial step in this study is to simulate BZ remodelling and study the effect of remodelling on the effective size. Such information can provide insight into reentrant propagation in the critical BZ region where activation waves propagate around the scar (Lim et al., 2006). This work therefore presents a first step towards suggesting the best species to model post-MI VT.

We study APD restitution in both single cell and tissue models in addition to CV and wavelength restitution at the tissue level, by observing how these metrics change with varying pacing frequency. I was calculated by taking into consideration wavelength and heart size and the effects of restitution on the effective size were investigated. The method was implemented in four different species models to be able to draw conclusions about which species model most closely replicates that of the human model in terms of effective size and hence, wave propagation dynamics. The protocol consisted of replicating electrophysiological BZ remodelling in the models for the purposes of indicating species differences in wave propagation, in relation to the human model, around infarct scar substrates.

4.2 Investigating APD Restitution in Healthy Single Cells

4.2.1 Computational Model Set-Up

Simulations in this chapter and throughout the Thesis were carried out on a Dell Optiplex 990 PC with eight 3.40GHz processing cores and 1TB of disk space, running the Linux Ubuntu 12.04 operating system. All data analysis was performed in the Matlab environment on the same PC.

For the purpose of elucidating species differences, four widely used computational models of ventricular ionic membrane potential were utilised in the following simulations. The models used were the Ten Tusscher and Panfilov (2006) human model, the Mahajan et al. (2008) rabbit model, the Luo and Rudy (1994) guinea pig model and the Pandit et al. (2001) rat model. These electrophysiological models are described in detail in Section 3.5

along with an account of why these models were chosen. The Ten Tusscher and Panfilov (2006) model provides a model of human ventricular AP which has largely been formulated from human data and is an extensively validated model. We utilise the model here to compare the effective size of the human to that of other small animals. The Mahajan et al. (2008) rabbit model, the Luo and Rudy (1994) guinea pig model and the Pandit et al. (2001) rat models are used here to make comparisons between the electrophysiological characteristics of the human model and these small animal models. Each of these models incorporates the main ionic currents and calcium handling system which drive the membrane potential and in addition, are widely used in the literature. The sub-package BENCH, of the CARP software (Section 2.5) was employed to solve the membrane potential in the following single cell simulations. Cell models run in CARP are implemented from the cell model library, LIMPET. Models published in this library are validated against the variable outputs from the source code and other published characteristic traces.

4.2.2 Steady State Pacing Protocols

Electrophysiological models must undergo a prolonged period of pacing at slow pacing frequencies before simulation protocols are performed, in order for the models to reach a steady state. After an initial stimulus current is applied, gating variables of the ionic currents and ionic concentrations are in flux, resulting in a membrane potential with an increased amplitude. The model requires time and steady pacing to recover from the effects of the initial stimulus, in order for the gating variables, ionic concentrations and hence, the membrane potential to reach a steady state and provide accurate membrane potential data for use in subsequent studies.

A parameter sensitivity analysis was conducted using the four electrophysiological models to ascertain the steady state pacing protocols required for each species model. The number of stimulus beats were varied in the analysis. Graphs of intracellular ionic concentrations and APD were outputted to observe how many stimulus beats were required for the model to reach a steady state. The BCLs at which the models were paced to conduct the parameter sensitivity analysis were chosen to be longer than the frequency of sinus rhythm. The BCL of the steady state protocol performed for the human model was 1000ms, for the rabbit model was 400ms, for the guinea pig model was 500ms and for the rat model was 500ms.

Graphs revealing the results of the steady state parameter sensitivity analysis in the

human model are presented in Figure 4.1. The graphs display how intracellular ionic

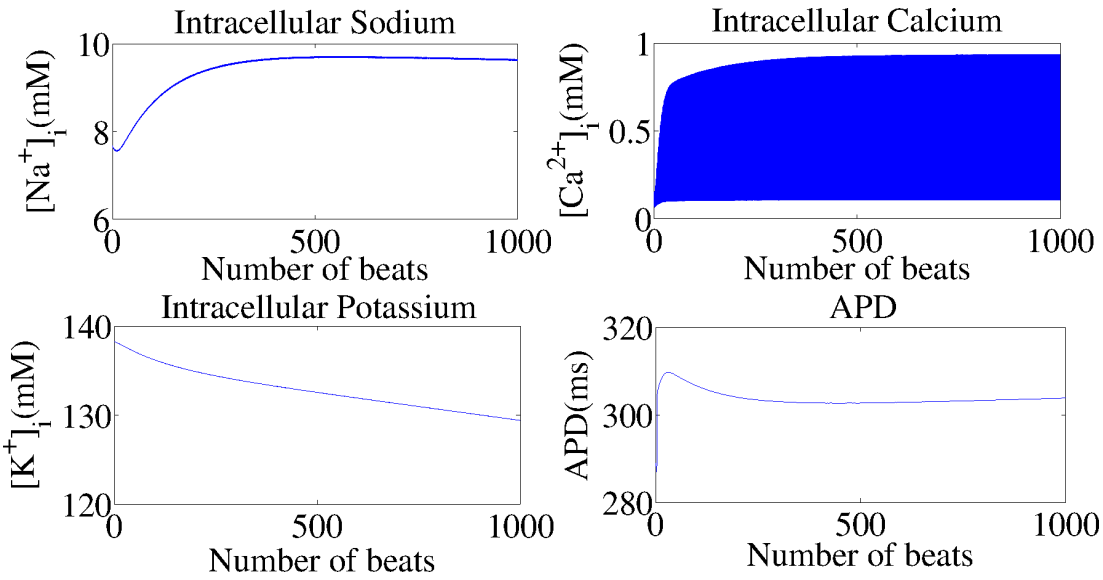

Figure 4.1: Parameter sensitivity analysis determining a steady state pacing protocol in the human model.

concentrations and APD vary as the model is paced for an increasing number of beats, whilst the model was paced at a BCL of 1000ms. On observation of the results of the parameter sensitivity analyses in each cell model, the steady state pacing protocols were formulated using the BCLs given above. The human model was paced for 500 beats, the rabbit model was paced for 1000 beats, the guinea pig model for 100 beats and the Pandit model was paced for 50 beats. These steady state protocols were used prior to all single cell simulations.

4.2.3 Restitution Pacing Protocols

Models were paced to a steady state according to the protocol described above prior to commencing the restitution protocols. Dynamic and S1S2 protocols described in Section 2.3, were implemented in order to replicate both a gradual change in pacing frequency to represent changes in heart rate observed, for example, during exercise (dynamic protocol), and to replicate ectopic beats known to be involved in the initiation of reentry (S1S2).

Implementing the dynamic pacing protocol, we began with pacing the model at the longest BCL stated for each model in Table 4.1. After the completion of 20 beats at that frequency, the BCL was decreased by 20ms without halting the simulation and a further 20 beats were paced at the new frequency. This pattern of stimulating the model for 20 beats at each test frequency and decreasing the BCL by 20ms each time was continued

Table 4.1: BCLs (ms) used in each restitution protocol for each species model.

		Human	*Rabbit*	*Guinea Pig*	*Rat*
Single Cell	*Dynamic*	1000-200	400-160	500-280	500-200
	S1S2	1000-340	400-200	500-260	500-80

until the BCL being utilised resulted in loss of capture. 20 beats were conducted at each pacing frequency in order for the model to stabilise and reach a steady state at each new pacing frequency before data was recorded.

The S1 section of the S1S2 protocol consisted of the model being paced for 20 beats at the longest BCL utilised for each model (Table 4.1) in order to simulate a steady state. On completion of the S1, a single premature stimulus (S2) was initiated at a test frequency. In order to vary the frequency of the S2 beat, the complete S1S2 protocol was repeated but the BCL of each subsequent S2 beat was decreased by 20ms until a BCL was utilised which resulted in the loss of capture. The range of BCLs used for the S2 beat is displayed in Table 4.1.

4.2.4 Restitution Analysis

The restitution analysis of the single cell modelling, utilised APD values calculated by the BENCH software (Section 2.5). APDs produced by the dynamic pacing protocol were determined for both the 18th and 19th beat at each frequency for the purposes of observing the presence of alternans. For analysis of the S1S2 restitution protocol, APDs were calculated for the S2 beat at each frequency. Graphs of APD were plotted against BCL and the maximum gradients of the restitution plots were calculated.

4.2.5 The Restitution Effect of Single Cell Models

Restitution Response to Dynamic Pacing

Figure 4.2 displays APD restitution curves produced by dynamic stimulation of the human, rabbit, guinea pig and rat single cell models for both the 18th (*blue*) and 19th (*red*) beats of the stimulation protocol and the calculated maximum gradients of each line. The human, rabbit and guinea pig graphs all display a positive restitution curve; as BCL increases, APD increases also. This result reflects the physiological occurrence of APDs decreasing as pacing frequency increases, in order to maintain functional contractility of the heart. Whilst the major patterns of the restitution graphs of the rabbit and guinea pig models are

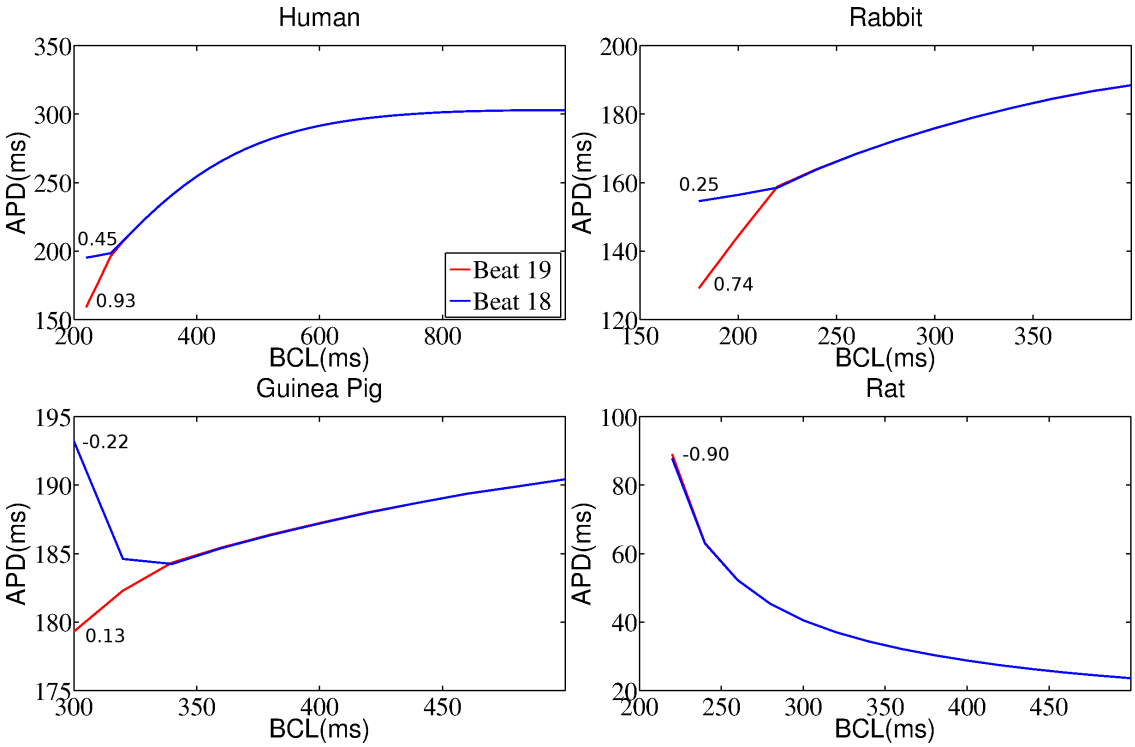

Figure 4.2: APD restitution graphs for human, rabbit, guinea pig and rat single cell models produced by the dynamic pacing protocol. APDs for beats 18 (*blue*) and 19 (*red*) are displayed and maximum gradients of each beat are displayed alongside the graphs.

similar to those of the human model, values of the maximum gradients of the restitution curves show that the human model produces a much steeper restitution curve, which could potentially predict the occurrence of species differences in wave propagation with varying pacing frequencies. Of note, the rabbit displays the most similar maximum gradient (0.74) of the restitution graph to the human (0.93).

A negative restitution curve is produced by the rat model with APD increasing as the BCL decreases. This is confirmed by the negative value of the maximum gradient of the graph. In fact, the negative slope of the graph is very steep with a maximum gradient of -0.90. A negative restitution curve is physiologically unlikely as if APD increased with decreasing BCL, APs would cease to be intiated due to sustained depolarisation of the membrane and the heart would be unable to function. The negative slope of the restitution curve of the rat model therefore indicates that the model does not replicate physiological restitution properties (Kondratyev et al., 2007; Fenton and Cherry, 2008; Sallé et al., 2008) and the results should be interpreted with caution.

The graphs of the human, rabbit and guinea pig models display pronouced bifurcations at faster BCLs indicating the presence of alternans, with the APD of beat 19 decreasing

as the BCL decreases, whilst beat 18 produces a much longer APD. Alternans occur as a protective mechanism to ensure that at faster pacing frequencies, a regular heart rate is maintained. Beat 19 consistently displays the highest maximum gradient compared to beat 18 as the APD of beat 19 gets progressively shorter with an increase in pacing frequency and the opposite occurs at beat 18. The similarity between beats 18 and 19 in the graph of the rat model suggests no alternans occurred at faster BCLs.

Restitution Response to S1S2 pacing

The restitution graphs displayed in Figure 4.3 display similar trends to those produced by

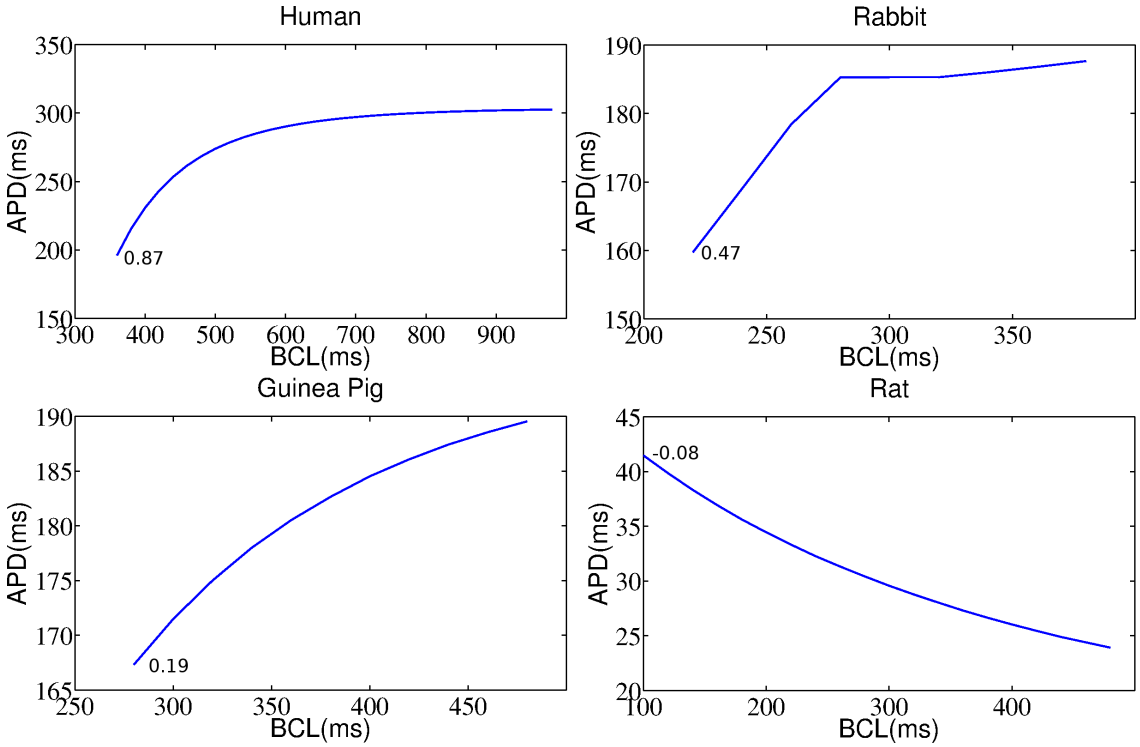

Figure 4.3: APD restitution graphs for the human, rabbit, guinea pig and rat single cell models paced according to the S1S2 protocol with maximum gradient values displayed beside the graphs.

the dynamic pacing protocol with the human, rabbit and guinea pig models all displaying positive restitution curves and the rat model displaying a negative slope. Maximum gradient values displayed beside the graphs suggest that the human and guinea pig models produced a similar restitution curve with a similar maximum gradient during dynamic and S1S2 pacing. Although the shape of the restitution curve of the rabbit displays a decrease in APD as BCL decreases during S1S2 pacing, the maximum gradient value reveals that the slope of the rabbit restitution curve produced by S1S2 stimulation is significantly less

steep than the graph produced by the dynamic pacing protocol, with a decrease in maximum gradient of 0.27. The rat model again produced a negative restitution curve but with a significantly decreased maximum gradient which was reduced by -0.84 during S1S2 pacing compared to the dynamic protocol. These slight variations in restitution curves between pacing protocols suggests that variations in wave propagation due to varying pacing frequency may occur depending on whether the increase is gradual (such as during exercise) or abrupt (such as an ectopic beat).

Interestingly, despite the variation in maximum gradient values produced by the dynamic and S1S2 pacing protocols between the human and rabbit models, the restitution curve of the rabbit model remains most similar to that of the human in terms of the significant decrease in APD as the BCL increases. This result again suggests that whilst species differences occur between the two models, the rabbit model displays a restitution curve most similar to the human and therefore, may better replicate variations in wave propagation due to increasing pacing frequency in the human.

4.3 Observing APD, CV and Wavelength Restitution in Healthy Tissue Models

4.3.1 Geometrical Model

A simplified geometrical model was utilised in the following simulations for the purpose of calculating the CV and wavelength produced by the four species models at varying pacing frequencies. Later in this chapter, the wavelengths measured across this geometrical model are utilised to calculate the effective size of the heart. It could be assumed that if a study aims to investigate wave propagation in the heart, that performing simulations on an anatomically accurate model of the heart may be the optimal approach. Whilst it is important to consider the many aspects of cardiac anatomy and electrophysiology which affect wave propagation, it is also important to be able to study the individual components which affect wave propagation to produce a deeper understanding of a particular mechanism (Clayton and Taggart, 2005). Utilising the simple geometrical model described below, we can observe restitution dynamics of the electrophysiological models without the results being affected by other parameters which may affect wave propagation, such as complex anatomical structures and electrotonic effects. In this simplified model, performing the dynamic restitution protocol, utilising 6 cores of the PC described

in Section 4.2, took approximately 1hr to perform the 20 beats for each pacing frequency (depending on pacing frequency and model used). As such, it was feasible to run large numbers of simulations to perform a comprehensive parameter sensitivity analysis. Performing a sensitivity analysis on a much more complex geometrical model would be very much more computationally demanding. The geometrical model utilised in these tissue level simulations provided sufficient results with an acceptable computational demand, an important consideration in any modelling study (Clayton and Panfilov, 2008).

Electrophysiology at the level of the tissue was modelled on a simple 2D rectangular geometry measuring 5mm-by-1mm-by-0.005mm (Figure 4.4). A rectangular model was

Figure 4.4: Model utilised in tissue level simulations. The stimulus site and the node from which data were sampled are indicated in *red*.

chosen in order to observe the propagation of the wavefront across the tissue and observe CV and wavelength properties. In addition, the shape of the model allowed the node from which data were sampled, to be located away from the stimulus location to ensure that no unusual electrotonic effects associated with the stimulus affect the results.

The mesh generator software, Mesher (carp.meduni-graz.at), was utilised to generate the tetrahedral finite element mesh which had a resolution of 50μm between nodes. The resulting model consisted of 10000 elements and 4242 nodes. The low computational demands required to perform simulations on the simple model allowed the use of a relatively high resolution finite element mesh, providing very accurate wave propagation data.

By default, simulations were conducted with the fibres arranged in the longitudinal direction. For the purposes of comparison, in some simulations, fibre direction was switched to the transverse direction.

4.3.2 Simulation Protocol

The CARP software (Section 2.5) was utilised to solve the monodomain equation to simulate propagation in tissue. A detailed explanation of the mathematical methods required to model wave propagation in tissue and an outline of how CARP solves the membrane potential across a finite element model was given in Section 2.5. As in the previous single cell analysis, electrophysiological models of human (Ten Tusscher and Panfilov, 2006), rabbit (Mahajan et al., 2008), guinea pig (Luo and Rudy, 1994) and rat (Pandit et al., 2001) ventricular AP were utilised. Electrical propagation across the geometrical mesh used throughout this study was visualised in the software Meshalyzer (written by Dr Edward Vigmond).

The model utilised in simulating wave propagation in tissue was stimulated along the shorter side of the model as displayed in Figure 4.4. This resulted in a plane electrical activation wave travelling down the longer dimension of the model.

Conductivity Parameters

Conductivity parameters are a required input of CARP in order to simulate the electrotonic current which conducts the electrical activation signals between cells and across the tissue. Intracellular and extracellular, longitudinal and transverse conductivity are required input parameters for CARP but as the monodomain equation is solved throughout the simulations in this Thesis, the bulk conductivity tensor replaces the bidomain conductivities in the monodomain equation.

Due to the large intraspecies variation in reported CV values, previously reported conductivity values (Clerc, 1976) were utilised for each electrophysiological model as shown in Table 4.2.

Table 4.2: Conductivity values utilised in simulations (Clerc, 1976).

Parameter	*Description*	*Value*
g_i^l	*longitudinal intracellular conductivity*	0.17S/m
g_i^t	*transverse intracellular conductivity*	0.019S/m
g_e^l	*longitudinal extracellular conductivity*	0.62S/m
g_e^t	*transverse extracellular conductivity*	0.24S/m

Steady State Protocol

In order for the tissue models to reach a steady state, first the cell models were paced to a steady state according to the protocols described in Section 4.2. The resulting parameters were saved and used as initial starting parameters in further tissue simulations. A further 10 beats at the pacing frequency used in the cell model steady state protocols, were paced in the tissue simulation to ensure that the parameters in the tissue model reached a steady state. This method describes the steady state pacing protocols required to stabilise the membrane potential after initial stimulation, before any further simulations are performed.

Restitution Protocols

A description of the restitution protocols used in this chapter is given in Section 4.2. The same protocols were utilised in this tissue level study and the range of BCLs utilised are presented in Table 4.3.

Table 4.3: BCLs (ms) used in each restitution protocol for each model.

		Human	*Rabbit*	*GuineaPig*	*Rat*
Tissue	*Dynamic*	1000-280	400-180	500-200	500-220
	$S1S2$	1000-360	400-220	500-200	500-80

4.3.3 Restitution Analysis

Restitution data in the tissue model were analysed using Matlab. Data were analysed from a node located away from the stimulus (Figure 4.4) in order to avoid sampling electrophysiological data where stimulus artifacts may affect the sampled data. In order to observe APD restitution effects, ATs and RTs were calculated for beats 18 and 19 using a linear interpolation algorithm to find the time points at which V_m crossed -40mV on the upstroke and -70mV during the repolarisation phase respectively. APDs were calculated by subtracting the AT from the RT and were plotted against BCL to produce an APD restitution graph. Graphs of CV restitution were created by plotting CV against BCL. CV was calculated by determining the speed that the activation wave took to travel between the stimulus site and the node from which the data were sampled. Equation 2.4 was utilised to calculate wavelength. Wavelength was plotted against BCL in order to create the graph of wavelength restitution.

4.3.4 APD, CV and Wavelength Restitution in Healthy Tissue Models

Restitution Response to Dynamic Pacing

Figure 4.5 displays APD, CV and wavelength restitution curves and their maximum gra-

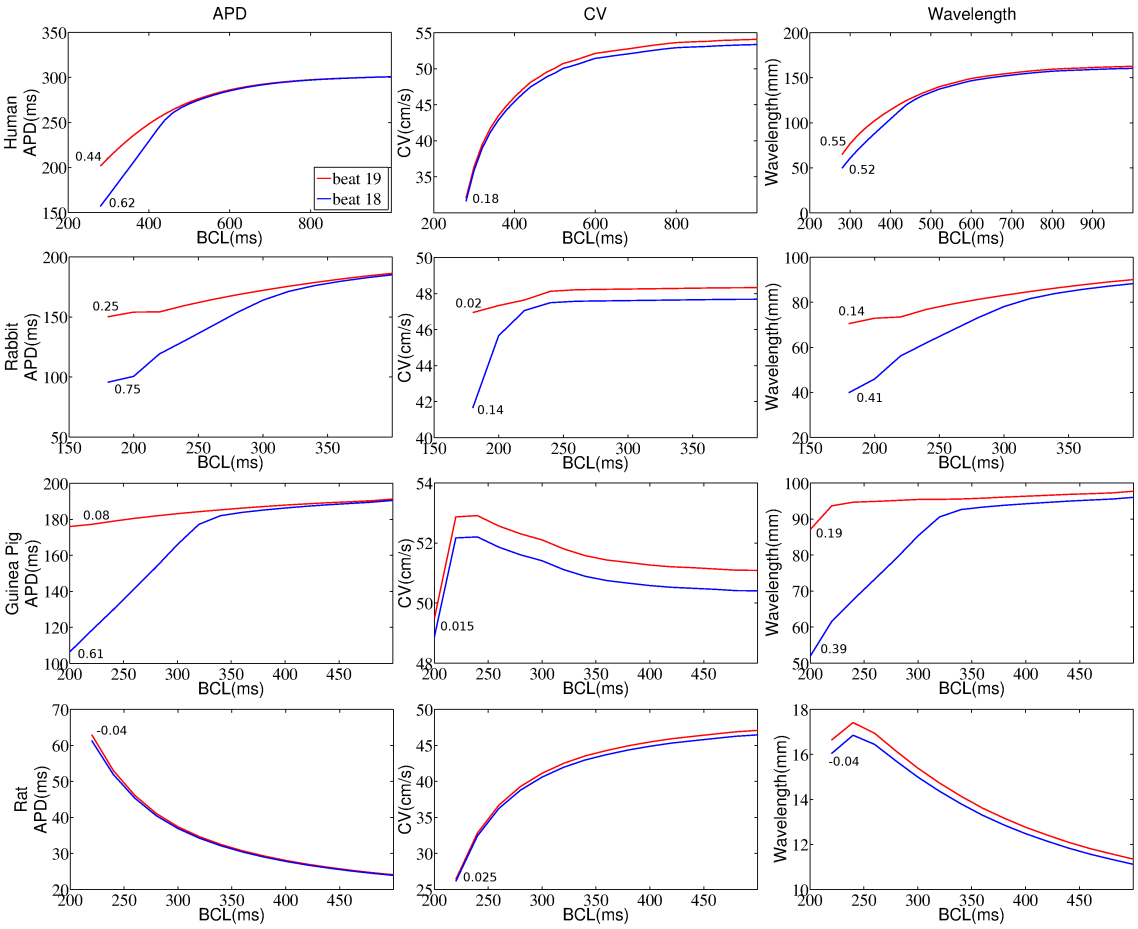

Figure 4.5: APD, CV and wavelength restitution graphs for each species model. Tissue models were paced according to the dynamic protocol. Maximum gradients are displayed alongside each line graph. Units of maximum gradient of the CV restitution curve are cm/s/ms and units of the maximum gradient of the wavelength restitution curve are mm/ms.

dient values for each species tissue model paced according to the dynamic protocol. The APD curves of the human, rabbit and guinea pig are all positive however, the rat model displays a negative restitution curve, as observed in the single cell restitution analysis. Importantly, the maximum gradient of the human APD restitution curve decreased in comparison to the restitution graph in the single cell analysis and the slope of the rabbit APD restitution graph remained similar between single cell and tissue analysis. This results in the maximum slope of the human and rabbit APD restitution curves being more

similar at the tissue level than at the single cell level. Decreased maximum gradients of the APD restitution graphs observed in the tissue analysis compared to the single cell analysis, suggest that the electrotonic effects occurring at the tissue level decrease the occurrance of very short APDs, when the model is paced at short BCLs. Such electrotonic effects occur in tissue due to the positive charge of the depolarised cells surrounding the cell in question, slowing down the repolarisation phase of the cell, causing a prolongation of the APD at the tissue level. Bifurcations of the human, rabbit and guinea pig graphs are also present in the tissue analysis suggesting the occurrence of alternans.

CV restitution graphs displayed in Figure 4.5 show that positive CV restitution curves are produced by human, rabbit and rat models and a biphasic curve is produced by the guinea pig model. In general, as BCL decreases, CV decreases. The shape and maximum gradient of the CV restitution curve of the rabbit model is again most similar to the human (difference of 0.04cm/s/ms) with both the rat and guinea pig models producing a curve with a much more shallow maximum gradient (difference of approximately 0.16cm/s/ms compared to human).

The wavelength restitution curve displayed in Figure 4.5 is the product of the APD and CV restitution curves. As such, the human, rabbit and guinea pig models display a positive wavelength restitution graph and the rat model produces a negative wavelength restitution curve. In the human, rabbit and guinea pig models, wavelength decreases as BCL decreases. The human model restitution curve displays the steepest maximum gradient (approximately 0.5mm/ms) compared to the rabbit and guinea pig models producing a maximum gradient of approximately 0.4mm/ms for beat 18.

Simulations conducted with fibres arranged in the transverse direction produce APD restitution graphs of a similar morphology to those produced by simulations in which fibres are orientated longitudinally. However, changing the fibres to be arranged in the transverse direction reduced CV by approximately half and the range of CV values decreased also, due to the preferential conduction of the activation wave longitudinally. As a result, maximum gradients of wavelength restitution graphs are also reduced.

Restitution Response to S1S2 Pacing

Figure 4.6 displays the results of the APD, CV and wavelength restitution analysis produced by S1S2 pacing in tissue models. The human, rabbit and guinea pig models displayed positive APD, CV and wavelength restitution curves similar to the results produced by

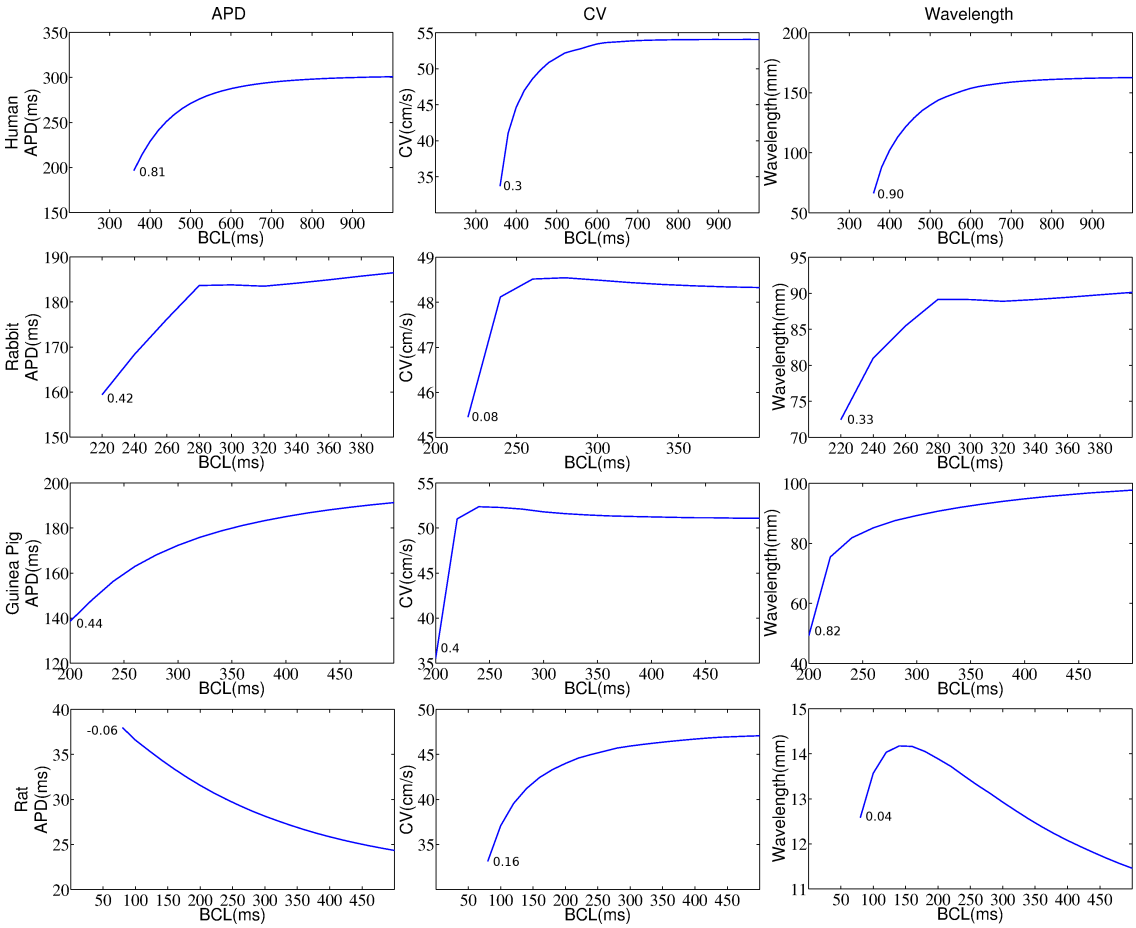

Figure 4.6: APD, CV and wavelength restitution graphs for each species tissue model paced according to the S1S2 protocol. Maximum gradients are displayed alongside each line graph. Units of maximum gradient of the CV restitution curve are cm/s/ms and units of the maximum gradient of the wavelength restitution curve are mm/ms.

models paced according to the dynamic protocol. However, the maximum gradient of the human APD restitution graph increased by approximately 0.2 compared to the result when the model was paced according to the dynamic protocol.

The maximum gradient of the human and guinea pig CV restitution graphs increased very slightly during S1S2 pacing whereas the maximum gradient of the rabbit and rat graphs decreased. The maximum gradient of the wavelength restitution curve increased in the human, rabbit and guinea pig graphs compared to those produced by the dynamic pacing protocol. Importantly, the difference between the maximum gradients of wavelength restitution of the dynamic and S1S2 analysis appear small in the tissue analysis as well as at the single cell level.

Changing fibre direction so that fibres are arranged in the transverse direction results in the loss of capture occurring at longer BCLs. This is due to the slower conduction in the

transverse direction causing an increase in wavelength and therefore subsequent propagation waves paced at very short BCLs will be blocked by the preceding waveback. Hence, slight reductions in the maximum gradient of APD restitution graphs occur, compared to those produced by simulations conducted with longitudinal fibre direction. CV is reduced due to the transverse fibre direction in all species models, contributing to a decrease in wavelength. However, the relative effects of changing fibre direction remain similar in all species models.

4.4 Investigating Species Differences in Effective Size

4.4.1 Calculating the Effective Size

Utilising the results of the tissue simulations, the relationship between the activation wavelength in relation to the size of the heart was calculated. We utilised Equation 4.1 proposed by Panfilov (2006) to determine the effective electrical size of the heart.

The measure of heart size utilised in the study by Panfilov (2006) was the cubic root of the mass ($\sqrt[3]{M}$), estimated as 0.6% of body weight. This metric was used for the purposes of comparing heart sizes between species, despite the highly complex shapes involved. Hence, the cube root of volumes were compared by calculating $\sqrt[3]{M}$, assuming that shapes and densities were consistent.

Primarily, $\sqrt[3]{M}$ was used as the size metric in the effective size calculation. In addition two further size metrics were utilised in the calculation, in order to determine whether the size metric greatly affects the relationships of the effective size restitution curves between different species. Due to the propagation patterns of reentrant waves travelling around the heart and throughout the walls, two metrics were utilised which are tangibly related to the wave propagation dynamics around the myocardium. These two metrics were the diameter of the heart across both ventricles measured in the coronal plane in the centre of the heart (*diameter*) and thickness of the LV wall (*LV wall*). Measures were either obtained from MRI data analysed using Seg3D or from the literature. The value of each metric for each species model is displayed in Table 4.4.

The effective size was calculated using wavelength values from simulations paced according to the dynamic and S1S2 pacing protocols, with fibres arranged in the longitudinal direction. Confidence limits were calculated by scaling each heart size metric by $+/-20\%$ in order to account for error in the heart size measurements and considering the species

Table 4.4: Measurements of heart size used in the effective size calculation.

	Human	*Rabbit*	*GuineaPig*	*Rat*
$\sqrt[3]{M}(g)$	7.1791	2.9240	1.7100	1
$Diameter(mm)$	85	24	19 (Girouard et al., 1996)	12
$LV\ wall(mm)$	9 (Troy et al., 1972)	5	4 (Dhalla and Singal, 1994)	3

variation in conductivity values, which were kept constant in the modelling simulations.

4.4.2 Species Differences in Effective Size

Figure 4.7 displays the results of the effective size calculation, when $\sqrt[3]{M}$ was utilised as the

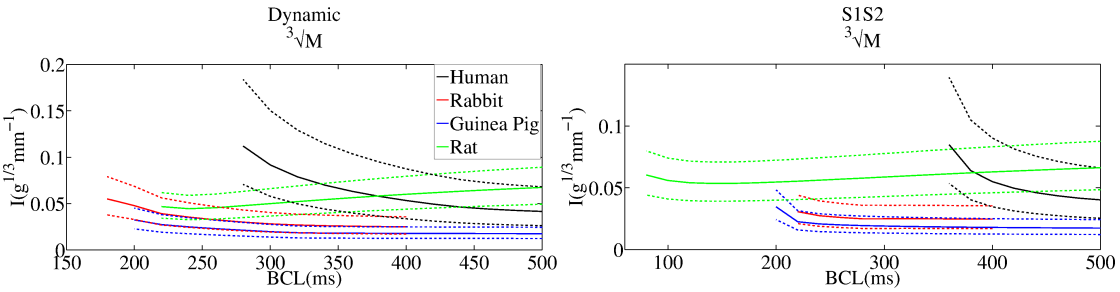

Figure 4.7: Graphs of I calculated using $\sqrt[3]{M}$ as the measure of heart size, for both the dynamic ($left$) and S1S2 ($right$) pacing protocols. Confidence limits are shown by the *dotted lines*.

measure of heart size, produced by both dynamic and S1S2 pacing protocol simulations. Graphs for the human (*black*), rabbit (*red*), guinea pig (*blue*) and rat (*green*) models are displayed, with the confidence limits (*dotted lines*) on each graph for comparison.

Analysis of I calculated, utilising $\sqrt[3]{M}$ as a measure of heart size, shows that the shape of the rabbit and guinea pig graphs are similar to that of the human. That is, as BCL decreases, I increases. This is contrary to the graph produced by the rat model. Importantly, the rat model does not display similar restitution properties of I to the human and therefore, it could be concluded that as pacing frequency varies, wave propagation dynamics in the rat model do not replicate those of the human.

Values of I of the rabbit graph are lower than the human graph and values of the guinea pig graph are still lower than the rabbit, suggesting that the rabbit model may best replicate the restitution effect of wave propagation dynamics in the human. Additionally, as the BCL decreases, I increases rapidly in the human model. This effect is most closely replicated by the rabbit model with the guinea pig model displaying a flatter curve of I with varying pacing frequency.

Graphs of I restitution produced by models paced according to the S1S2 protocol (*right*) differ, compared to those produced by the dynamic protocol (*left*). It is evident that I restitution is affected by pacing protocol, due to the differences in wavelength restitution between the two pacing protocols. What seemed like small differences in maximum gradient of wavelength restitution between the two protocols, are clearly large enough to affect I. The graph of I restitution of the human, maintains its steep negative gradient as BCL decreases. The similar pattern of the rabbit model seen in the dynamic protocol graph is not replicated in the S1S2 graph. In fact the gradient of the rabbit graph becomes less steep with decreasing BCL and the gradient of the guinea pig graph more closely replicates that of the human at fast pacing rates. The differences between the rat and human model observed in results of the dynamic protocol are lessened with the positive slope of the rat graph decreasing in the S1S2 graph.

Figure 4.8 displays the results of I analysis using *diameter* and *LV wall* size metrics

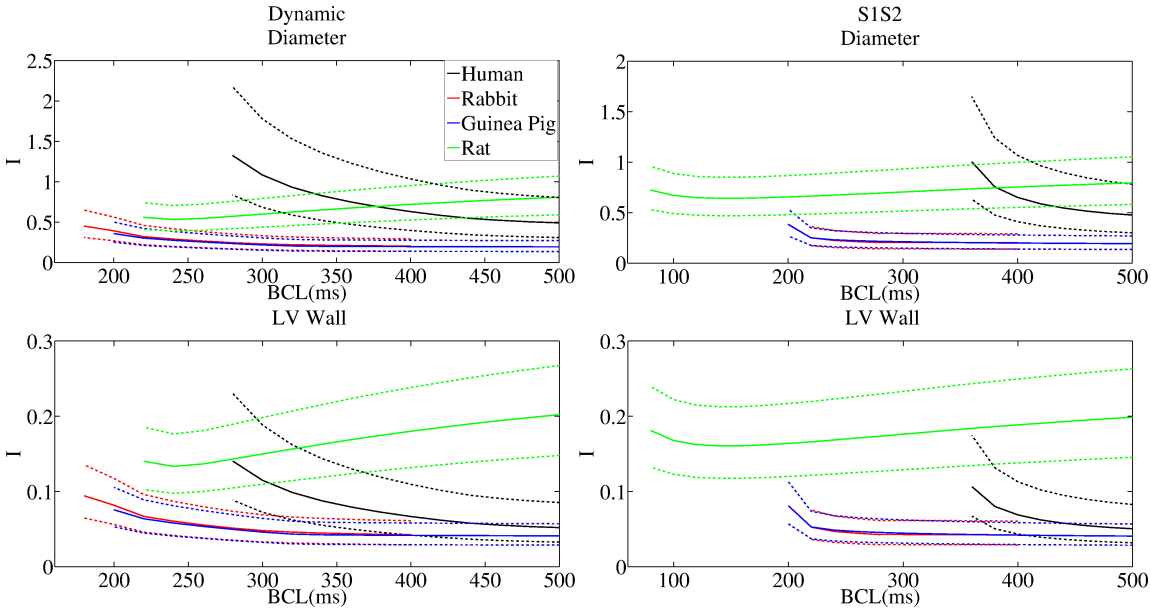

Figure 4.8: Graphs of I calculated using both *diameter* (*top*) and *LV wall* (*bottom*) measures of heart size. Data were obtained from simulations paced according to both the dynamic (*left*) and the S1S2 (*right*) protocols.

in the calculation for both dynamic and S1S2 pacing protocols. Comparing the analysis of I utilising different measures of heart size in the calculation, it is possible to see that the measure of heart size used in the calculation can change the relationship of I between different species. Altering the size metric used in the calculation only changes the numerator of the equation (Equation 4.1) hence, only shifts the graphs up and down with relation to

each other and doesn't alter the shape of the I restitution graphs. Indeed, it is possible to see that although the values of I vary slightly using *diameter* and *LV wall* metrics, the shape of the graphs and relationships of I with varying BCL remain the same.

Utilising the *diameter* measure of heart size produced I relationships very similar to those seen in the graphs of I using $\sqrt[3]{M}$ as the heart metric. Interestingly, utilising *LV wall* as the size parameter, served to decrease the magnitude of I of the human heart, resulting in the human heart displaying an I much more similar to that of the rabbit and guinea pig. This can be seen by the overlapping graphs of the human, rabbit and guinea pig, particularly at slower pacing frequencies.

Considering the restitution of I calculated using wavelength produced by dynamically paced simulations with fibres arranged in the transverse direction, the graphs, and importantly, the relationship between species, remain similar to the results produced by the longitudindal fibre direction simulations. Altering fibre direction alters the magnitude of the wavelength and not the gross morphology of the wavelength restitution graph. Hence, the graphs of I only differ in their magnitude, not in their shape or relation to each other.

4.5 Investigating the Effect of BZ Remodelling on the Effective Size

4.5.1 Simulating BZ Remodelling

This section aims to observe the effects of BZ remodelling on the effective size. Based on the conclusion of the Panfilov (2006) study and the results observed in Section 4.4, suggesting that the rabbit model displays the most similar effective size to the human heart, we performed the following simulations using only the human and rabbit models.

Single Cell Models

Single cell simulations were conducted as described in Section 4.2. Simulations were performed in BENCH and models were paced to a steady state before the dynamic restitution protocol was initiated. APD data were calculated in the BENCH software.

Sections 2.6 and 3.1 describe the alterations to both the ionic currents and conduction velocity which occur in the BZ as a result of ischemic damage. Here we compare the electrophysiological properties of healthy cells to those of BZ remodelled cells. Healthy cellular electrophysiology was simulated by using the human (Ten Tusscher and Panfilov,

2006) and rabbit (Mahajan et al., 2008) models of ventricular AP. BZ alterations to the ionic currents were modelled by varying parameters of the electrophysiological models, based on previous protocols which have been implemented in both human and rabbit models to replicate BZ ionic current remodelling (Ashikaga et al., 2013; McDowell et al., 2011; Rantner et al., 2012). All changes to ion channel conductances were motivated by data produced from patch-clamped BZ cells, which displayed a decrease in the ionic currents (Litwin and Bridge, 1997; Pu and Boyden, 1997; Jiang et al., 2000). The maximal conductance value of I_{Na} was reduced to 38% of normal, the strength of the I_{CaL} flux was decreased to 69% of normal, I_{Kr} was reduced to 30% of normal, I_{Ks} was decreased to 20% of normal and the maximal I_{NaCa} was increased to 132% of normal. This BZ remodelling protocol was implemented in both the human and rabbit models.

Graphs of V_m were plotted to compare APs in healthy cells to APs in BZ remodelled cells. We compare APD restitution between healthy cells and BZ remodelled cells by plotting APD against BCL for both models.

Tissue Level Models

In models of tissue electrophysiology, it is possible to simulate not only BZ remodelling of ionic currents but it is also possible to model alterations to conduction velocity which occur in the BZ. In order to observe the effect of the altered ionic currents and conduction velocity on the effective size, four different models were utilised. A model simulating healthy tissue with no remodelling affecting the ionic currents or conduction velocity ($Ion_{norm}Cond_{norm}$) was used for comparison. The other models incorporated ionic current BZ remodelling and normal conduction velocity ($Ion_{BZ}Cond_{norm}$), normal ionic current parameters and BZ conduction velocity ($Ion_{norm}Cond_{BZ}$) and BZ remodelled ionic currents and conduction velocity ($Ion_{BZ}Cond_{BZ}$). Ionic current remodelling was incorporated into the models according to the protocol described previously in this section. To simulate conduction velocity in healthy tissue, conductivity values were assigned as previously described (Table 4.2). Conductivity remodelling was modelled by decreasing the transverse conductivity values to 10% of normal values as previously described in studies which have replicated BZ remodelling in human and rabbit computational models (Ashikaga et al., 2013; McDowell et al., 2011; Rantner et al., 2012).

Simulations were performed using each model as described in Section 4.3 using both the human and the rabbit cell models. Due to the transverse conductivity remodelling,

simulations were run on the geometrical model (Figure 4.4) with fibres arranged in the transverse direction. The models were paced to a steady state before the tissue level steady state protocol was implemented and the dynamic restitution pacing protocol was performed.

Data obtained from the simulations were analysed as described in Section 4.3. Graphs of APD, CV and wavelength restitution were produced.

The effective size of the heart was calculated according to Equation 4.1, using $\sqrt[3]{M}$ as the measure of heart size and the wavelength produced by the tissue simulations described in this section. The effective size was calculated for each BZ remodelling condition for both the human and rabbit models.

4.5.2 APD Restitution in BZ Single Cell Models

Figure 4.9 displays APs produced by human (*left*) and rabbit (*right*) models. The *blue*

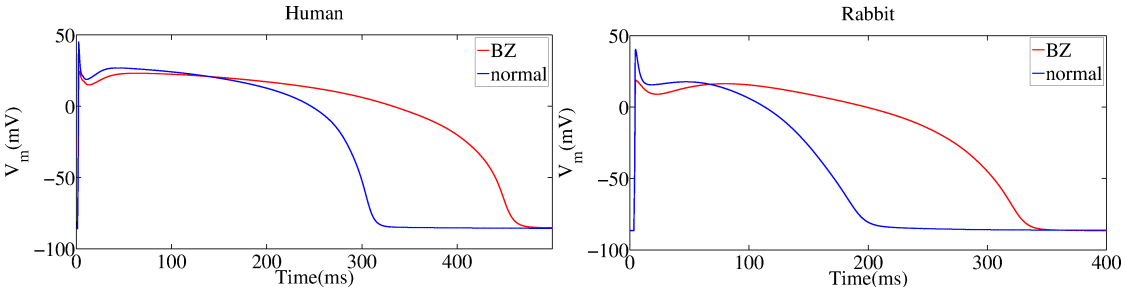

Figure 4.9: Graphs of APs of the human (*left*) and rabbit (*right*) models produced by both a normal model (*blue*) and a model incorporating BZ remodelling (*red*).

lines show normal healthy APs with the *red* lines depicting BZ remodelled APs. BZ remodelling significantly alters the shape of the AP. In both models, BZ remodelling increases the APD by approximately 150ms. In addition, remodelling in both the human and rabbit models causes a decrease in the peak and a prolonged notch phase of the AP. It appears that BZ remodelling has a similar effect on the APD in both the human and the rabbit model.

The results of BZ remodelling on APD restitution is displayed in Figure 4.10. Considering the graph of human (*left*) APD restitution and comparing the graphs of the BZ remodelled simulations (*solid line*) to the normal (*dotted line*) cell simulations, it is evident that BZ remodelling causes a prolongation of APD by approximately 150ms. Graph bifurcations occur in both healthy and BZ remodelled cases at low BCLs, indicating the presence of alternans. Due to the increase in APD, the model with incorporated BZ remodelling

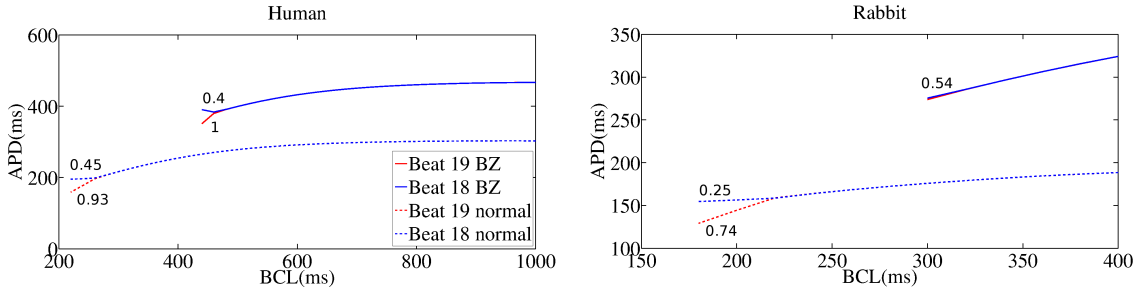

Figure 4.10: Graphs of human (*left*) and rabbit (*right*) APD restitution, comparing differences in BZ (*solid line*) and healthy (*dotted line*) APDs. Maximum gradients are displayed beside each graph.

was unable to be paced at the fastest BCLs. Importantly, although the graphs display disparity in the values of APD between the normal and BZ remodelled models, the shape of the restitution curve remains similar, reflected in the similarity of the maximum gradient values displayed on the graphs. This finding could suggest the restitution effect on wave propagation is similar between healthy and BZ remodelled tissue.

The APD restitution curves of the rabbit model (*right*) also show that BZ remodelling causes an increase in APD of approximately 150ms, which can be seen in Figure 4.9. These results can be expected, considering that the same BZ remodelling protocol was implemented in both the human and rabbit models. The increase in APD caused the loss of capture at lower BCLs in the BZ model which in turn provided a short restitution graph for comparison. The maximum gradients of the restitution graphs of the BZ remodelled case remain in the range of the maximum gradients of the normal tissue graphs. Again, this result could suggest that the effective size restitution of healthy tissue will display similar dynamics to the effective size restitution of the BZ remodelled rabbit model.

4.5.3 APD, CV and Wavelength Restitution in BZ Tissue Models

Figure 4.11 displays graphs of APD (*top*), CV (*middle*) and wavelength (*bottom*) restitution for human (*left*) and rabbit (*right*) models. Graphs of $Ion_{norm}Cond_{norm}$ (*green*), $Ion_{norm}Cond_{BZ}$ (*blue*), $Ion_{BZ}Cond_{norm}$ (*red*) and $Ion_{BZ}Cond_{BZ}$ (*black*) models were plotted on the same graph for comparison. Observing the APD restitution graphs of both the human and rabbit models, it is evident that ionic remodelling in $Ion_{BZ}Cond_{norm}$ (*red*) and $Ion_{BZ}Cond_{BZ}$ (*black*) models increases the APD by approximately 150ms in each model. In general, the human displays steeper APD restitution graphs than the rabbit model indicating that as pacing frequency increases, APDs decrease to a greater extent

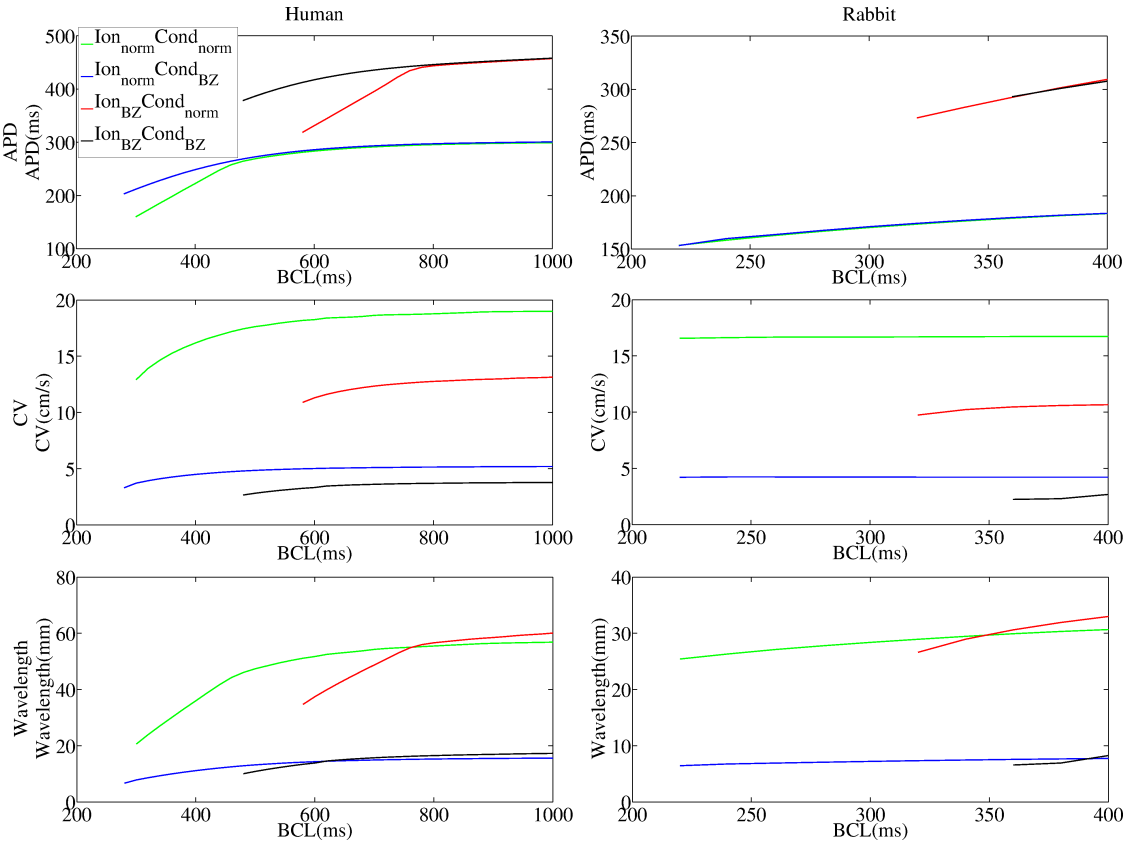

Figure 4.11: Graphs of APD (*top*), CV (*middle*) and wavelength (*bottom*) restitution for human (*left*) and rabbit (*right*) models which either have normal or BZ remodelled ionic current and conduction velocity parameters.

in the human model than in the rabbit model. Interestingly, in only the human model, $Cond_{BZ}$ remodelling (*black* and *blue* curves) causes further prolongation of APDs at lower BCLs resulting in a more shallow APD restitution curve. During a very slow conducting wave, more of the tissue is activated at a particular time and so the electrontonic current from activated tissue contributes to the slower repolarisation of the tissue from which the data are sampled in this case.

The graphs of CV (*middle*) display a general decrease in CV compared to those shown in Figure 4.5, due to the fibres arranged in the transverse direction in the model used to run these simulations. Conductivity remodelling decreases CV as can be seen from the CV restitution graphs produced by both models (*blue* and *black* curves). In addition, Ion_{BZ} remodelling also causes a decrease in CV (compare *red* to *green* graphs) due to the reduction of the maximal conductance of I_{Na}. Whilst the CV restitution curves of the human model display a slight reduction in CV as the BCL decreases, the CV restitution curves produced by the rabbit model are very flat, a trait which can also be seen in Figure

4.5.

Evident from the wavelength restitution curves, $Cond_{BZ}$ remodelling causes a decrease in wavelength in both models (compare *black* and *blue* graphs to *green* and *red* graphs). The graphs produced by $Cond_{BZ}$ remodelled simulations (*black* and *blue*) are more shallow in both models than the $Cond_{norm}$ graphs. This result suggests that when CV is slowed in BZ tissue, a decrease in BCL does not cause an even greater reduction in CV, resulting in flatter wavelength restitution graphs. The magnitude of the wavelengths produced by the rabbit model are approximately half of those produced by the human model and in addition, the gradients of the wavelength restitution graphs of the human model are generally steeper than those produced by the rabbit model, due to the steeper APD and CV restitution curves in the human model.

4.5.4 Species Differences in Effective Size in BZ Models

Figure 4.12 compares the graphs of I of the human (*black*) and rabbit (*red*) models for

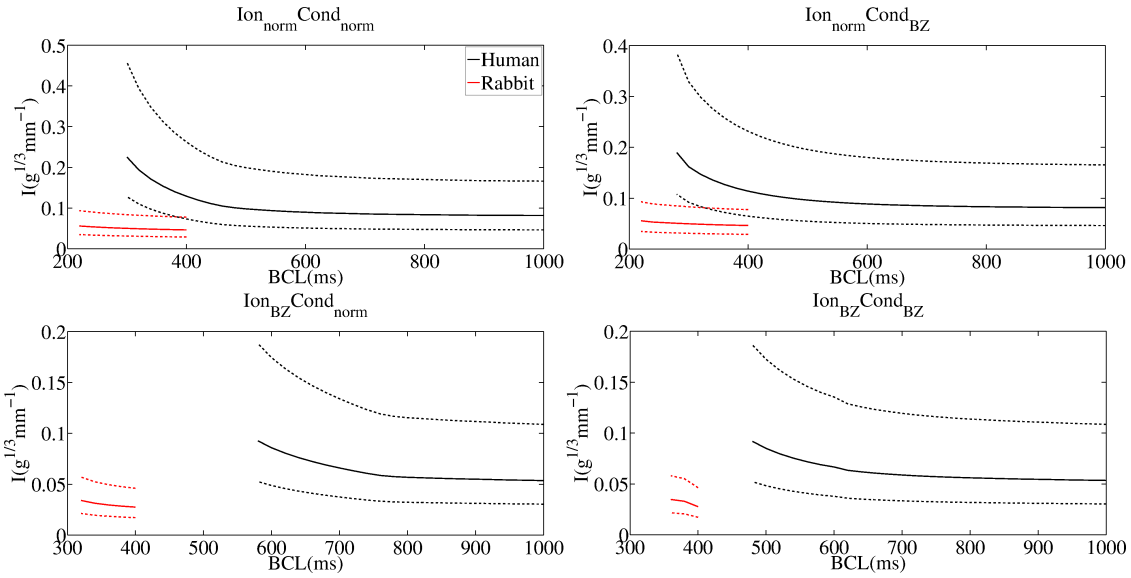

Figure 4.12: Graphs of I produced by models of normal or BZ remodelled ionic current or conduction velocity properties. *Black* - human, *red* - rabbit.

the four cases: $Ion_{norm}Cond_{norm}$, $Ion_{norm}Cond_{BZ}$, $Ion_{BZ}Cond_{norm}$ and $Ion_{BZ}Cond_{BZ}$. There remains disparity between the I of the human and the rabbit models in all four cases as a result of differences in wavelength.

The magnitude of I varies between the human and rabbit model as a result of the difference in the magnitude of the wavelengths between the human and rabbit models.

The human produces a longer wavelength and hence, a larger I, suggesting that the wavelength in the human model is smaller compared to the size of the tissue than the rabbit, and so reentry is more likely to occur in the human than the rabbit model.

In general, the human model displays a steeper gradient of I restitution than the rabbit model. The flatter wavelength restitution graphs of the rabbit models displayed in Figure 4.11 contribute to the shallow gradients of I restitution. Particularly in the human model, the steepness of I restitution occurring at smaller BCLs indicates that reentry is more likely to occur at shorter BCLs, due to the decrease in wavelength increasing the excitable gap.

Comparing the results of I restitution between the models with Ion_{norm} (top) and Ion_{BZ} $(bottom)$, the magnitude of I decreases as a result of Ion_{BZ} remodelling. This result can be explained by the lengthened APD as a result of Ion_{BZ} remodelling contributing to a longer wavelength which in turn, would decrease I and the likelihood of reentry. The gradient of I restitution appears to be reduced by $Cond_{BZ}$ remodelling $(right)$ when compared to graphs of $Cond_{norm}$ $(left)$. This is possibly due to the fact that with reduced CV in the BZ, CV can not decrease further with decreasing BCL. This effect can be seen in the CV restitution curves in Figure 4.11.

From the results presented in this section it is evident that species differences occur, such as the magnitude and restitution of I. The differences in I between species suggest that susceptibilty to reentry is increased in the human model but perhaps most importantly, decreasing the BCL increases the susceptibilty to reentry in the human model more than in the rabbit model. Interestingly however, the effects of BZ remodelling on I restitution appear to have similar effects in both the human and rabbit models which could suggest that alterations in wave propagation around infarct BZs could be similar in both the human and the rabbit.

4.6 Discussion

4.6.1 Limitations

Despite the previous idea that the rabbit model is most similar to the human in terms of effective size compared to the dog and pig at pacing frequencies akin to those during VF (Panfilov, 2006), it would be beneficial to compare the effective size of larger animal models to the human at slower pacing frequencies, similar to those observed during scar-

related VT. The results could validate the claim made here, that in fact the rabbit model does display the most similar effective size to the human over a complete range of species models and pacing frequencies.

Due to limited experimental data available on the remodelling of ionic currents in human BZ, the same remodelling protocol was utilised for both the human and rabbit models. The protocol utilised was formulated based upon data from rabbit and canine animal studies and so there could be discrepancies between the BZ remodelling which occurs in animals and that which occurs in humans, post-MI. Potentially, differences in ionic current remodelling could alter the restitution dynamics of the effective size, altering the relationship of effective size between species.

4.6.2 Summary

Results from the APD restitution analysis of the single cell models and the results of APD, CV and wavelength restitution analysis from tissue models, suggest that APD, CV and wavelength all display positive restitution graphs for the human, rabbit and guinea pig models. Therefore, as BCL decreases, APD, CV and wavelength all decrease in a rate-dependent manner which replicates a well documented restitution effect.

Another important restitution effect which is replicated by the human, rabbit and guinea pig in both single cell and tissue models is observed by the presence of alternans. As the pacing frequency increases, alternans may occur in order to maintain CO. Here we verify that these mathematical models of electrophysiology replicate the important restitution properties observed in animal studies and can therefore be utilised in studying aspects of heart function which are dependent upon restitution, such as wave propagation.

The rat model is the only model which produces a negative restitution graph. That is, as BCL decreases, APD increases. As a result, in the tissue models, wavelength restitution also follows the same rate-dependent trend. This effect is not physiologically possible. As pacing frequency increases, the APD must decrease in order for the heart to maintain CO and sustain life. In addition, the results of the effective size of the rat model reflect the negative wavelength restitution curve, contrary to the restitution curves of the other models. Therefore, the results of the the rat model should be treated with caution and it can be suggested that the Pandit rat model is not a suitable model to replicate restitution dynamics of the human.

A crucial result is that APD, CV and wavelength restitution curves illustrate that the

rabbit model displays restitution effects most similar to the human model. In addition these two models are most similar in terms of the magnitude of the wavelength. Due to these similarities, it was found that the rabbit model produced an effective size most similar to the human model in terms of both magnitude and rate-dependency. This important result supports the conclusion of a previous study (Panfilov, 2006), suggesting that the rabbit displayed the most similar effective size to the human, at pacing rates indicative of VF. We can suggest here, that the rabbit and human models display the most similar effective size at pacing rates indicative of VT. Hence, we can propose that, compared to the other models tested, the rabbit model is the most useful model to replicate wave propagation dynamics of the human and could be of potential use in informing clinical studies.

It should be noted that whilst the effective size of the human and rabbit models are most similar, species differences in the magnitude of the effective size still exist. The human model produces a larger effective size, indicating that the model is more susceptible to reentry than the rabbit model. In addition, the rate-dependency of the effective size of the human model is greater than that of the rabbit model, as can be seen by the steeper gradient of the human graph at faster pacing frequencies. Hence, we conclude that despite similarities, species differences occur between the effective size of the human and rabbit which may suggest the presence of important species differences in wave propagation dynamics between the models. Thus, we can suggest that for the most robust conclusions to be drawn about wave propagation dynamics in humans, the human model of AP should be utilised. However, the rabbit model provides a respectable alternative if necessary which can approximate the wave propagation dynamics of the human and its rate-dependency.

Observing the effect of changing the size parameter in the calculation of the effective size, it is evident that changing the numerator of the calculation only alters the magnitude of the graphs between the species and does not affect the restitution dynamics of the effective size. Indeed, changing the size parameter from $\sqrt[3]{M}$ to *diameter* or *LV wall* increases the similarity between the human, the rabbit and the guinea pig models. However, changing the measure of the heart size in the calculation does not alter the main conclusion discussed above; that the rabbit provides the most similar model to the human in terms of the magnitude and the restitution dynamics of the effective size.

Results of restitution dynamics produced by the two pacing protocols, the S1S2 and dynamic protocols remain similar in both the single cell and tissue level models suggesting

that the rate-dependency of APD, CV and wavelength remain similar, whether a gradual or an abrupt change in pacing frequency occurs. Although slight differences occur in effective size depending on the pacing protocol, namely that the restitution effect of the effective size in the rabbit model was decreased using the S1S2 pacing protocol, the main result remains that the human and rabbit models have the most similar effective size irrespective of pacing protocol.

In light of the similarities in the effective size between the human and rabbit models, only these models were utilised to study the effect of BZ remodelling on the effective size. Although species differences between the human and rabbit occur in terms of the magnitude and the extent of the rate-dependent properties of the effective size, BZ remodelling produces similar effects in both the human and rabbit models. Specifically, ionic current BZ remodelling decreases the magnitude of the effective size and conductivity remodelling decreases the gradient of restitution in both models. Therefore, it could be suggested that the rabbit model produces similar changes in wave propagation dynamics which occur in BZ tissue, to those that occur in the human.

Chapter 5

Investigation of a Method to Determine the Success of Reentrant Propagation

In Chapter 4 we investigated the effective electrical size of the heart in terms of species differences and demonstrated that whilst the rabbit displays the most similar effective size to that of the human, clear species differences remain. We utilise our findings from the previous chapter by progressing our studies using a human electrophysiological model. Additionally, it is essential to consider the work of the previous chapter regarding the effective size of the heart, as the topic of this chapter focuses on quantifying reentry, a mechanism which is governed by wavelength and its relation to the size of the tissue, the definition of effective size. Here we investigate a proposed metric to identify regions of tissue which are susceptible to reentry based on wavefront-waveback interactions.

5.1 Introduction

Reentrant arrhythmias are characterised by activation waves propagating in a circuitous fashion. Often, reentry occurs as a result of UDB caused by APD heterogeneity in the tissue. Propagation of an electrical impulse wave is blocked as it travels from healthy tissue towards tissue which remains refractory due to a lengthened APD, causing diversion of the wave around the region of block. Crucially, once a reentrant circuit has been established, the continuation of reentry depends on the excitable gap, as described in Sections 2.6 and

3.1. If there is an excitable gap, the wave can propagate into repolarised tissue within the circuit, facilitating the maintenance of the reentrant propagation. Reentrant arrhythmias cause a significant number of deaths, hence research into the mechanisms of reentry and possible clinical therapies is of great interest.

A metric was proposed by Coronel et al. (2009) (Section 3.8) to highlight regions of tissue susceptible to reentry by taking into consideration potential interactions between the wavefront and the wave back around a possible reentrant circuit. Experiments were conducted on a Langendorff perfused porcine heart. Dispersion of repolarisation was induced, resulting in half of the tissue (the proximal half) displaying a shorter APD than the other half of the tissue (the distal half). This is represented in Figure 5.1 where AP

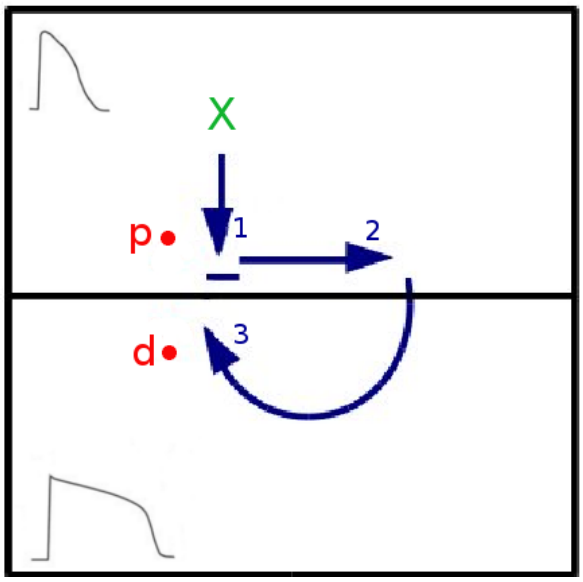

Figure 5.1: Experimental model set-up to investigate the RVI described by Coronel et al. (2009). *Green X* indicates the stimulus site in the proximal region. APs in *left hand* corners show the lengthened APD in the lower region. Labelled arrows depict wave propagation from the stimulus site and subsequent block (1), diverted propagation (2) and propagation back towards the site of initial block (3). Points p and d show sites from which electrophysiological data were sampled.

traces in the left-hand corners of the tissue illustrate that a longer APD was initiated in the distal (d) half of the tissue. The longer APD in the distal region is responsible for causing initial wave block, as depicted by *arrow* 1, because the distal half remains depolarised due to the lengthened APD. The wave is then forced to divert around the region of block, until the distal region has repolarised (*arrow* 2). The wave then propagates through the distal region towards the site of initial wave block (*arrow* 3). Crucially now, whether or not the wave can propagate back into the proximal region forming a reentrant circuit, depends

on the membrane potential in the proximal side of the tissue. If the proximal tissue has repolarised, the wave from the distal region will be able to reenter. If the proximal tissue remains depolarised, the wave from the distal region will block again and not reenter. Hence, a metric was devised to compare the time of repolarisation at p with the time of activation at d. An electrode grid over the tissue recorded electrophysiological data from which AT and RT values were deduced. The metric takes into consideration the RT at point p in the upper region (ie. prior to the activation wave block) and the AT at point d after the diversion of the wave around the region of refractory tissue. The concept of the metric is simply; if d is activated by the time that p is recovered, propagation can occur from d to p resulting in UDB, initiating a reentrant circuit. Conversely, a situation in which BDB occurs, and hence no reentry, would be indicated by the activation at d occurring before p is repolarised, because the wave would not be able to propagate from d into depolarised p. The FF calculation they proposed was

$$FF = RT_p - AT_d \tag{5.1}$$

Implementing the equation, a negative FF result would be produced by a scenario where RT_p is smaller than AT_d indicating reentry. Low, positive values of FF indicate BDB. The results from the study showed that utilising this calculation can determine the susceptibility to reentry between two points, not only when UDB occurs but also when BDB occurs.

A subsequent study (Child et al., 2015) proposed a clinical application of the metric, utilising the same concepts to produce a spatial map of the susceptibility to reentry across the heart. Sections 2.6 and 3.1 describe how MI scars create both structural and functional heterogeneity in the tissue, due to fibrosis and ionic remodelling of the BZ. These substrates provide the prerequisites for reentry: lengthened APD in the BZ regions and structural barriers around which propagation waves are diverted. Figure 5.2 depicts a representation of an infarct scar and the typical pattern of reentry around it. The wave is blocked at the region of lengthened APD which occurs in the BZ (*blue*) and is diverted around dense non-conducting fibrotic tissue (*black*), entering the BZ isthmus distally and propagating back towards the site of initial block. It is this figure-of-eight reentry around infarct scars which causes life threatening arrhythmias and so methodologies to terminate episodes of reentry are vitally important. In Chapter 3, the limitations of the current ablation

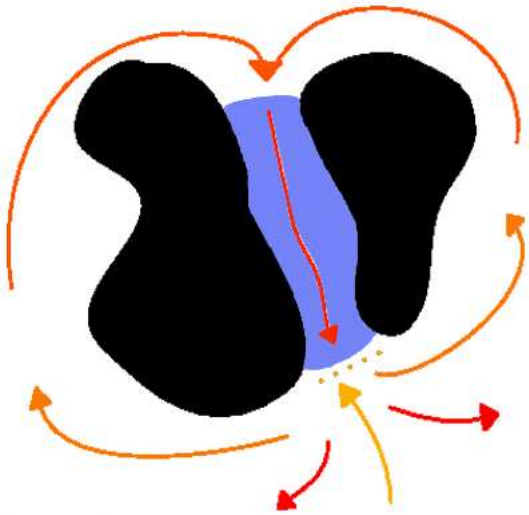

Figure 5.2: The typical pattern of figure-of-eight reentry around an infarct scar. The wave is blocked (*dotted yellow line*) by the refractory tissue in the BZ (*blue*) facilitating reentrant propagation around the infarct scar (*black*).

procedure technique were discussed in detail. Specifically, it was shown that the method of mapping the scar to locate the optimal site for the ablation lesion is inaccurate and requires improvement. Therefore, a method to highlight regions susceptible to reentry, such as the method proposed by Child et al. (2015), could prove an important tool to improve the clinical ablation procedure by providing a technique to locate the optimal ablation lesion site. The clinical study utilises the concept described previously (Coronel et al., 2009) to locate regions of tissue susceptible to reentry. However, instead of producing a result between only two points, the metric is calculated between points over the entire surface of the endocardium, to produce a spatial map of regions susceptible to reentry, in order for clinicians to use the map to guide where an ablation lesion is to be created.

Rigorous analysis of the methodology proposed by Child et al. (2015) is needed in order to draw firm conclusions. The calculation has been tested using experimental porcine data and has been implemented in the clinic on an individual patient. Therefore, the utility of the method needs to be further investigated. Moreover, the preclinical study utilising the calculation only implemented the analysis in situations of functional reentry. Considering the clinical application of the algorithm in guiding the ablation procedure, the methodology requires investigation in models of post-MI reentry. In addition, further analysis is needed for optimisation of the methodology and to ensure that the technique is robust under varying physiological conditions.

From the results presented in Chapter 4, we observed that species differences in the ef-

fective size and hence, wave propagation dynamics, do occur and that if possible, utilising a human model of electrophysiology would be the optimal approach in order to simulate human wave propagation dynamics. Therefore, in this chapter, we investigate the proposed calculation (Child et al., 2015) using human *in silico* data. The benefits of utilising computational models to study post-MI arrhythmias have been discussed in Section 3.5. Considering investigating a proposed calculation for use in the clinic, computational modelling allows the thorough study of the methodolgy using human electropyhsiological data whilst not being restricted by sample sizes, ethics or clinical practice. Hence, we simulate propagation using a model of human ventricular AP (Ten Tusscher and Panfilov, 2006) on a simple 2D geometrical model, emulating the experimental set-up described by Coronel et al. (2009), and implement the proposed RVI algorithm (Child et al., 2015). Computational modelling also allows us to investigate variations of the methodology to ensure that the method proposed for clinical use is optimal. Therefore, we investigate other possible calculation methods based on the algorithm described previously (Coronel et al., 2009) which may predict susceptibility to reentry over a 2D surface and hence, we may be able to suggest the most effective calculation for this purpose. In addition, we can examine thoroughly, the effect of varying calculation parameters on the result, to draw conclusions about the optimisation of the calculation proposed by Child et al. (2015). Due to not being restricted by the small quantity of patient data available, we are able to verify that the calculation maintains its ability to detect a vulnerability to reentry in varying physiological conditions, such as increasing arrhythmogenicity. The arrhythmogenicity is the ability of the substrate and its properties to facilitate reentrant wave propagation, with increasing arrhythmogenicity describing a substrate which is more likely to facilitate reentry. Here, we alter simulation parameters to increase the arrhythmogenicity of the simulation and observe whether the calculation maintains its ability to locate regions susceptible to reentry. It is possible, utilising computational models, to alter such parameters one at a time, for the purpose of observing the effect of individual parameters. Importantly, we can utilise computational models to incorporate 2D idealised scar regions into the geometrical model in order to investigate the utility of the methodology in post-MI, figure-of-eight reentry, which has not previously been investigated.

5.2 Investigating the Method in a 2D Experimental Model

5.2.1 Computational Model Set-Up

Computational Model Geometry

The geometrical model utilised in simulations throughout this chapter was created in order to replicate the experimental set-up described by Coronel et al. (2009). Therefore, A 2D, 5cm-by-5cm finite element mesh with a resolution of 200μm between nodes was created using the Mesher software (carp.meduni-graz.at). This resulted in a model consisting of 62500 quadrahedral elements and 63000 nodes. The shape of the geometry was chosen to replicate the previous experimental geometry and the square shape permitted the model to be divided into two halves in order to incorporate APD heterogeneity. Moreover, the square shape and the size of the geometry was chosen to permit the propagation of waves around a line of block to form and sustain a reentrant circuit. The resolution of the model was decreased compared to the model utilised in Chapter 4 in order to be able to conduct parameter sensitivity analysis with acceptable simulation run-times and data storage requirements. Importantly, decreasing the resolution of the finite element mesh did not impair the simulation of wave propagation in the model.

Essentially, the experimental model (Coronel et al., 2009) consists of a region of healthy myocardium and a separate region displaying prolonged APD, representing the APD heterogeneity required for the initiation of reentry. We replicated this experimental model by dividing the geometrical model in half parallel to the x-axis, as displayed in Figure 5.3 by assigning separate tags to the elements within each region. Those defining tags enabled each spearate region to be assigned different parameters, forming two regions with distinct properties. Reference to proximal and distal regions of the model refer to the healthy tissue (*white*) and tissue with lengthened APD (*red*) respectively.

Model Parameterisation

Simulations were run utilising the TT2 model of human ventricular AP (Ten Tusscher and Panfilov, 2006), described in Section 3.5. This model was chosen due to the results of Chapter 4 suggesting that due to species differences in the effective size between human and small animal models, the optimum method for studying VT arrhythmias is to utilise human *in silico* data where possible. All of the elements in the mesh were assigned isotropic fibre directions with conductivity values of 0.1S/m in both longitudinal and transverse

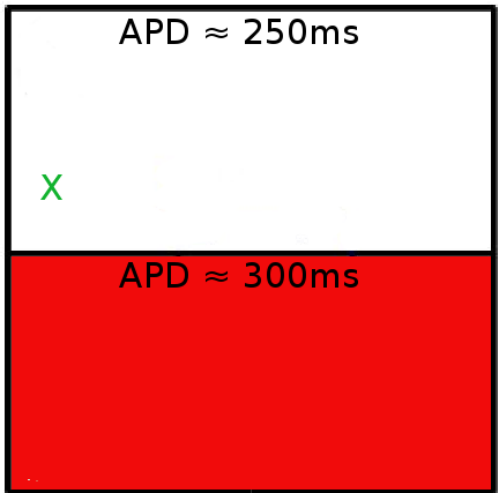

Figure 5.3: Geometrical model utilised to investigate an algorithm to predict the occurrence of reentry. The *white* region depicts healthy tissue and the *red* region depicts tissue displaying a longer APD. The *green X* indicates the site of stimulation.

directions, in order to retain simplicity of the model for the purposes of understanding the fundamental mechanisms affecting the results of the calculation.

In order to introduce a sufficient gradient of repolarisation to cause conduction block, the conductance term (G_{Ks}) of I_{Ks} was varied from the value stated in the TT2 model; 0.4nS/pF (Ten Tusscher and Panfilov, 2006). An APD of approximately 250ms was produced in the *white* region of the model (Figure 5.3) by increasing G_{Ks} to 0.75nS/pF. APD was lengthened in the *red* region to approximately 300ms by decreasing G_{Ks} to 0.2nS/pF.

Stimulation Protocol

Steady state pacing protocols were implemented as described in Section 4.3. The model was stimulated at the location of the *Green X* in Figure 5.3, in the region of shorter APD and located off-centre in order to be able to view the sideways propagation of the wave due to conduction block. In order for the heterogeneous repolarisation of the tissue to initiate conduction block, a premature stimulus is required so that the wavefront reaches the border between the two regions prior to the *red* region being repolarised. Therefore, after obtaining a steady state, an S1S2 protocol was initiated, by stimulating the model prematurely (S2), 300ms after the previous stimulation (S1). The model was stimulated for 3ms with a current of 300μA. To run an S1S2 simulation, it took approximately one hour and the resulting data files were approximately 300MB. Resulting simulations were visualised using the software Meshalyzer.

5.2.2 Producing a Spatial Map of Susceptibility to Reentry

Child et al. (2015) proposed a calculation termed the reentry vulnerability index (RVI), which produces a spatial map of the susceptibility to reentry over a surface. The RVI calculation was implemented to produce the results of this study. The RVI is based on the concept described by Coronel et al. (2009) however, the calculation is conducted over all nodes in the model rather than between only two points and an averaged spatial map of the results is produced. Described here is the protocol used to produce a map of the RVI.

Experimental Data

The *in silico* data used in the calculation are the AT and RT data obtained from the simulations described in this section. The output of the simulations are membrane potential traces and so AT and RT data must be calculated from the simulation output. ATs and RTs were calculated for both the S1 and the S2 beats at each node in the geometrical model using a linear interpolation algorithm to find the time points at which V_m crosses -40mV on the upstroke and -70mV during the repolarisation phase respectively. APDs were calculated by subtracting the AT from the RT at each node.

The RVI Calculation

Figure 5.4 illustrates the method utilised in calculating the RVI. The following calculation protocol was performed on every successive node in the model ($node_i$) (*red*). A spatial radius (r_s) (*black circle*) was created around $node_i$ for the purposes of determining potential pairs of calculation nodes. r_s was formulated utilising the equation

$$(X - X_i)^2 + (Y - Y_i)^2 <= r \tag{5.2}$$

where X and Y are x and y coordinates of all nodes within the model, X_i is the X coordinate of $node_i$, Y_i is the Y coordinate of $node_i$ and the radius of the r_s circle is r . Any nodes which satisfied Equation 5.2 and hence their coordinates fell within r_s were of potential use in the RVI algorithm. Nodes within r_s were further screened and only those nodes activated after $node_i$ on the S2 beat (downstream nodes) were utilised in the RVI calculation. Downstream nodes were determined by comparing the ATs of the S2 beat between $node_i$ and all other nodes within r_s. The image at the *top* of the figure depicts the identification of downstream nodes (*orange*) with the superimposed AT map.

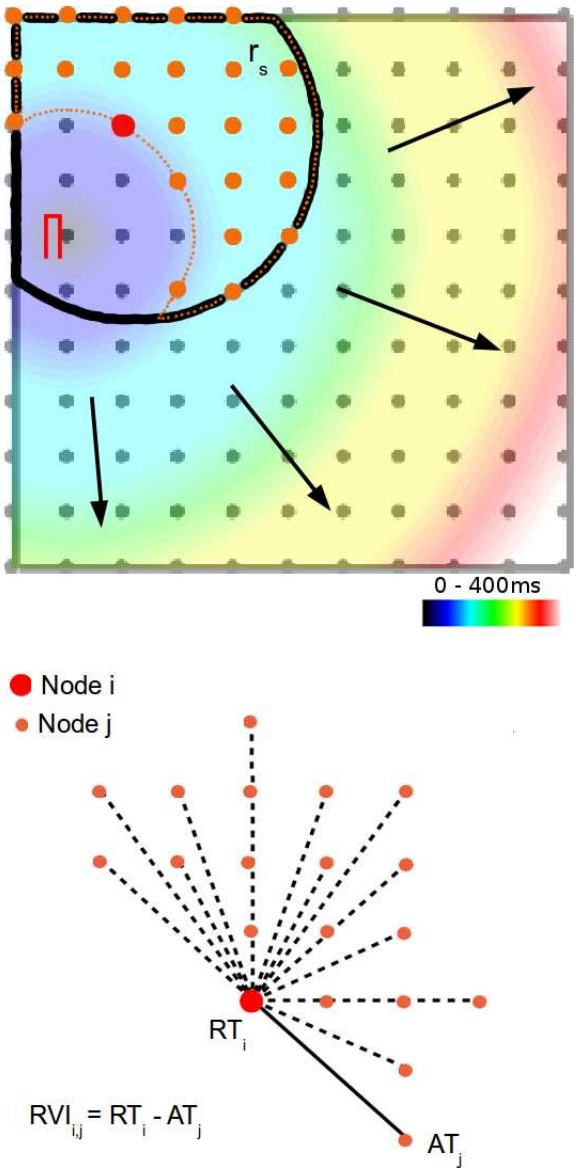

Figure 5.4: RVI calculation methodology. *Top* - Search radius (r_s, *black circle*) around *red* node ($node_i$) is used to determine calculation node pairs. Nodes within r_s and activated after $node_i$ (see underlying AT map) are denoted $node_j$ (*orange*) and used in the RVI calculation. *Bottom* - Summarises method of RVI calculation between each node pair ($node_i$ and each $node_j$).

Downstream nodes were denoted $node_j$ (*orange*) and the RVI algorithm was calculated between $node_i$ and each $node_j$ as depicted by the image at the *bottom* of the figure, to produce a number of RVI values. Equation 5.3 was used to calculate the RVI between each node pair:

$$RVI_{i,j} = RT_i - AT_j \tag{5.3}$$

The RVI essentially calculates a time between the wave back and the wavefront between a

pair of nodes to determine whether reentry is able to occur. If the pair of calculation nodes are a great distance apart from each other, the calculated time gap between the nodes becomes meaningless due to the distance the wave would have to travel to complete the hypothetical circuit, hence a spatial radius is required to determine potential calculation nodes. Only downstream nodes were utilised in the calculation to ensure that $node_j$ was distal in time, to the stimulus site, compared to $node_i$. In this case, if wave block occurred between the two nodes, $node_i$ was always located prior to the block and $node_j$ was always located after block occurs. This method ensures that the calculation subtracts a value nearer to the wavefront, from a value which is sampled nearer to the wave tail. This situation is identical to the experimental set up used to propose the fundamental concept of the calculation (Coronel et al., 2009).

Plotting a Spatial Map of the RVI

For each calculation node pair, a spatial midpoint was calculated between the two nodes and the nearest node to the midpoint was identified. The RVI calculated between each pair was associated with their respective midpoint node. For visualisation, an average of the RVIs was taken and plotted at each node point. The resulting RVI map was visualised using the software Meshalyzer.

5.2.3 Examining the Optimum Protocol to Identify Susceptibility to Reentry

The methodology described in the previous paragraphs is the method which is employed to produce the results which are presented in this chapter. However, in order to ensure that the methodology described above is the optimum method to produce a spatial map which displays the susceptibility to reentry, other methods were tested. In doing so, some important findings shed light on the mechanism of the RVI calculation and the important findings are described below.

Identifying Calculation Node Pairs

In order to be of clinical use, it is necessary that a method is devised which can predict susceptibility to reentry over a relatively large surface, such as that of the heart. The original FF algorithm was based upon calculating the FF between two nearby points and so the proximity of the proximal and distal nodes used in the calculation must be taken

into consideration. Considering that the experimental model used in this study measured 5cm-by-5cm, the algorithm calculating a possible excitable gap between nodes that could potentially be 5cm apart becomes obsolete, as the wave would have 5cm to complete the hypothetical circuit, making times calculated between RT_i and AT_j meaningless. Consider a scenario in which $node_i$ was 5cm apart from $node_j$. The RT of $node_i$ may have occurred after the AT of $node_j$, indicating that the tissue at $node_i$ would not be repolarised, and unable to conduct an activation wave returning from $node_j$. However, by the time the activation wave returned to $node_i$ after travelling 5cm from $node_j$, the tissue may have repolarised and so be able to sustain a reentrant circuit. As such, it was thought perhaps, to be necessary to account for the distance between calculation node pairs. Several different techniques were tested to account for the distance between $node_i$ and $node_j$. Firstly, the result of the algorithm was normalised for distance using the equation

$$\frac{RT_i - AT_j}{distance_{i,j}} \tag{5.4}$$

Secondly, a term was added to the algorithm (Δt) which accounted for the time it would take for the wave travel from $node_i$ to $node_j$, to complete the hypothetical circuit between the calculation node pair. Δt was calculated by finding the difference between the AT of S1 at $node_i$ and $node_j$. This technique was implemented utilising the equation

$$RT_i - (AT_j + \Delta t) \tag{5.5}$$

Both equations produced maps displaying critical low values clustering more strongly around the site of initial wave block than maps produced by a calculation which didn't account for distance between the calculation node pair. Yet a more accurate way of considering this crucial distance is to only calculate the algorithm between node pairs within a certain distance of each other, dispelling the need to account for the distance within the algorithm. This technique was implemented in the RVI calculation used in this chapter by creating a spatial radius, r_s around nodes to determine calculation node pairs.

The algorithm described by (Coronel et al., 2009) sampled the RT from a node proximal to the stimulus site ($node_p$) and the AT at a node distal to the stimulus site ($node_d$) to determine the excitable gap between the two points. This method however fails to take into account the direction of wave propagation. In our more complex model, with electrophysiological data being sampled from many different nodes, it was observed that

a scenario could occur (see Figure 5.5) in which a node could be defined as $node_p$ (as it

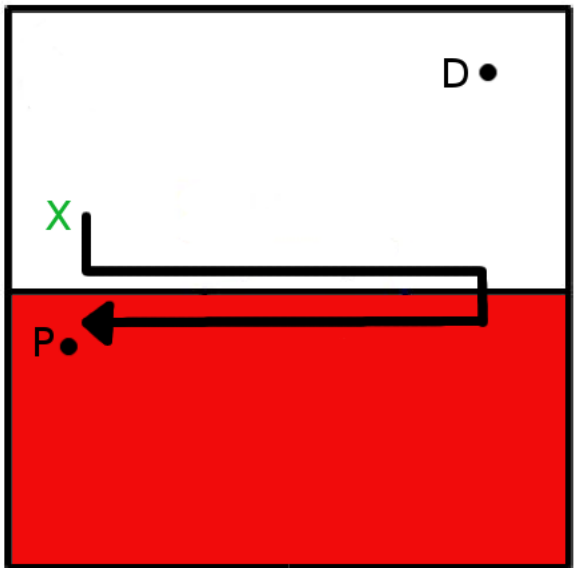

Figure 5.5: Illustration of the problem with defining $node_p$ and $node_d$ from proximity to the stimulus site (*green X*). $Node_p$ is proximal to the stimulus site compared to $node_d$ but is activated after $node_d$.

is in closest proximity to the stimulus site) which is activated after $node_d$, due to the line of block and subsequent conduction delay of the wavefront reaching $node_p$. In this case, the fundamental concept of the algorithm, subtracting an AT at a later point in a circuit from an RT at a point earlier in a circuit to calculate the time of an excitable gap (or lack of), is lost.

Several different techniques of determining $node_p$ and $node_d$ to ensure that $node_p$ was activated before $node_d$ were tested. However, the only technique robust enough to ensure that $node_p$ was indeed activated before $node_d$ was the technique utilised in the RVI calculation described above, in which the ATs of each possible node pair were compared.

Plotting the Results on a 2D Surface

It was also necessary to consider how the results of the calculation were to be plotted, in order to identify regions which are susceptible to reentry. Considering the large number of calculations between node pairs which are performed over the model, not all of the calculated values could be displayed on the model concurrently. Considering that low values of RVI indicate a susceptibility to reentry, the minimum result calculated within each radius was found and plotted on the model. Interestingly, the results from this method indicated that the minimum value calculated within a radius was always calculated

between $node_i$ and a $node_j$ which was activated last. In addition, across the map, the minimum values were clustered around the stimulus site due to the fact that repolarisation occurs first at that location. The method produced a large area of low values and the lowest values were very negative (approximately -200ms), much more negative than values previously reported (Coronel et al., 2010; Child et al., 2015). In order to overcome the issue of very negative values clustering around the stimulus site, all values calculated within the radius were considered in the final protocol utilised in this study by taking an average, rather than only the minimum value.

In the previously described experimental protocol (Coronel et al., 2009), the value of the result was associated with the two calculation nodes. After performing the calculation in the computational model, result values were plotted as lines between the calculation node pair (node_p and node_d) and colour coded according to the value of the result. This methodology of plotting the result provided a map with very poor clarity due to the amount of lines produced, with some lines displaying different values superimposed, possibly masking critical values. The method also produces a very diffuse region exhibiting the critical low result values, as they are plotted between potentially two distant points.

For improved visualisation and ability to locate a specific region of low values, results were plotted on individual nodes rather than as lines between a calculation node pair. The results of the calculation were plotted only on proximal nodes. This method provided a clear map of results for visualisation and a specific region displaying critically low RVI values. However, plotting results only on the proximal nodes may skew results and displace values indicating a susceptibility to reentry in another area.

Plotting values of the RVI either as lines between the node pairs or on one node of the node pair did not produce clear, reliable results. Hence, a method of plotting the result on the spatial midpoint between the calculation node pair was utilised in the RVI methodology in the following study, in order to provide a full and accurate spatial map of the RVI results.

5.2.4 Can the RVI Predict Susceptibility to Reentry?

Figure 5.6 displays the AT (*top*), RT (*middle*) and RVI (*bottom*) maps for UDB ($left$) and BDB ($right$) simulations. The site of initial wave block is evident ($left\ hand\ side$) in the AT maps of both UDB and BDB simulations. Notably, the activation wave travelled further in the UDB simulation before entering the lower half of the model than the acti-

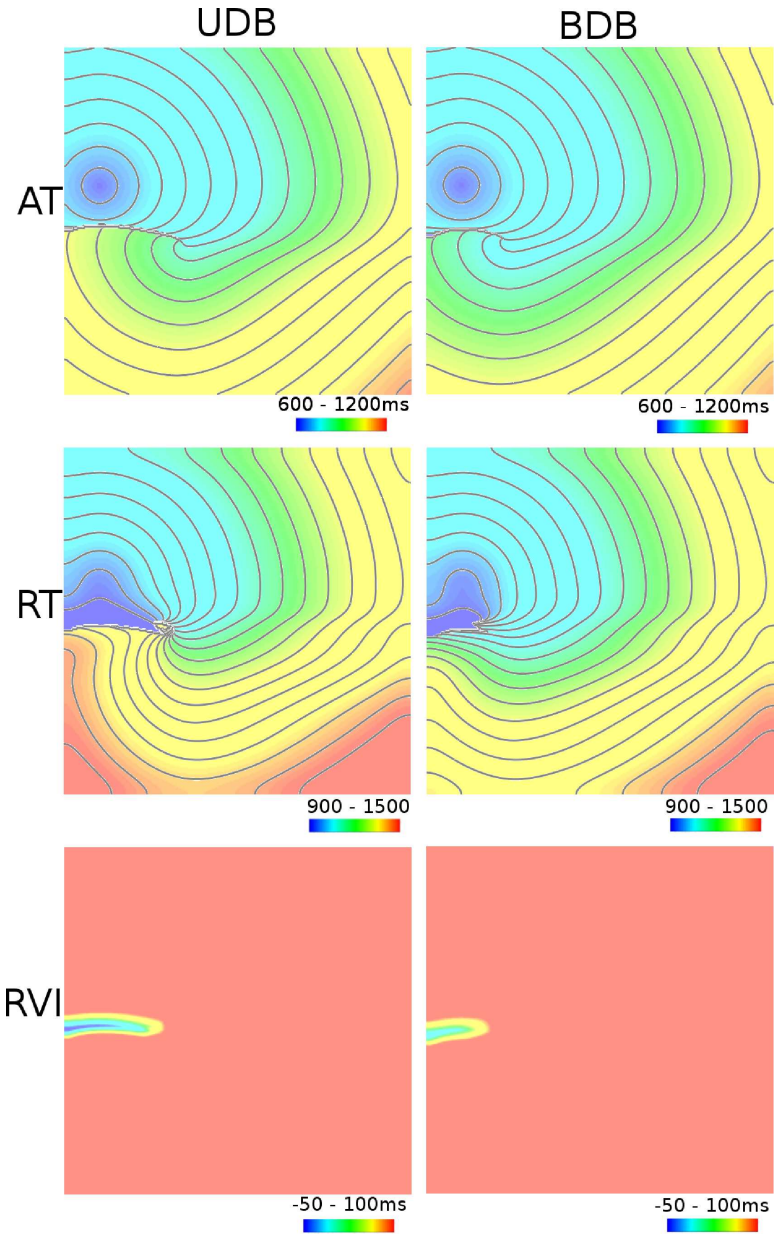

Figure 5.6: Results of the RVI algorithm in the 2D experimental model. *Top* - AT maps, *middle* - RT maps, *bottom* - RVI maps for UDB (*left*) and BDB (*right*) simulations.

vation wave in the BDB simulation. This resulted in an increased delay of the wavefront reaching the lower half, producing slightly larger ATs in this region (approximately 900ms) compared to the same region in the BDB map (approximately 750ms). In turn, the larger ATs in the lower half of the UDB map produce a more negative RVI at the region of block (approximately -50ms) than that in the BDB map (approximately -15ms). In addition, there is a smaller area of the lowest RTs in the BDB RT map than the UDB RT map due to the electronic effects at the smaller line of wave block. This smaller area of low

RTs in turn produces a smaller area of low RVI in the BDB map. Crucially, a specific region of low RVI values is located at the site of initial wave block in both UDB and BDB simulations with more negative values being produced by the UDB simulation. In simulations where no wave block occurs (not shown), the wave propagates normally over the tissue with a plane wavefront and the corresponding RVI values are homogeneously high ($> +100$ms). The result substantiates the results of previous experiments utilising porcine data and validates the method using a human model of ventricular AP. The lack of species specificity of the methodology is expected due to the method assessing the likelihood of reentry occurring based on the fundamental AT and RT parameters.

5.2.5 Optimisation of the RVI Calculation: Data Resolution Parameter Sensitivity Analysis

The computational model provided *in silico* data from 63000 nodes. In the clinic, data are obtained from recording catheters at much lower resolutions, as described in Section 2.4. Typically, a decapolar catheter is repositioned around the endocardium 20 times to provide approximately 200 recording locations (Child et al., 2015). In order to determine the effect of decreased sampling resolution on the result of the RVI, the resolution of the nodes utilised in the calculation was decreased.

Simulations continued to be conducted on the full resolution model. Analysis was conducted using data from a UDB simulation. The radius of r_s utilised in the analysis was 25mm in order to be able to calculate RVI values between node pairs on a model with a resolution of 10mm between nodes. Instead of sampling AT and RT data from every node in the model (which lay 0.2mm apart), the resolution between nodes from which data was sampled was decreased in a parameter sensitivity analysis, with distances between nodes ranging from 0.4mm to 10mm. The calculation proceeded as described above, utilising data only from the nodes in the low resolution model and results were only plotted on the nodes of the low resolution model. New meshes of the low resolution models were created for the purposes of plotting the RVI results on a surface rather than vertices, producing a smooth result for improved visualisation.

Metrics to describe the results across the entire model were calculated for the purposes of analysing parameter sensitivity analyses. The metrics used were the minimum RVI in the model (RVI_{min}) and the percentage of the model which displayed an RVI less than 50ms ($RVI_{area<50}$).

5.2.6 The Effect of Altering Data Resolution on RVI

The images at the top of Figure 5.7 display RVI maps produced by the calculation con-

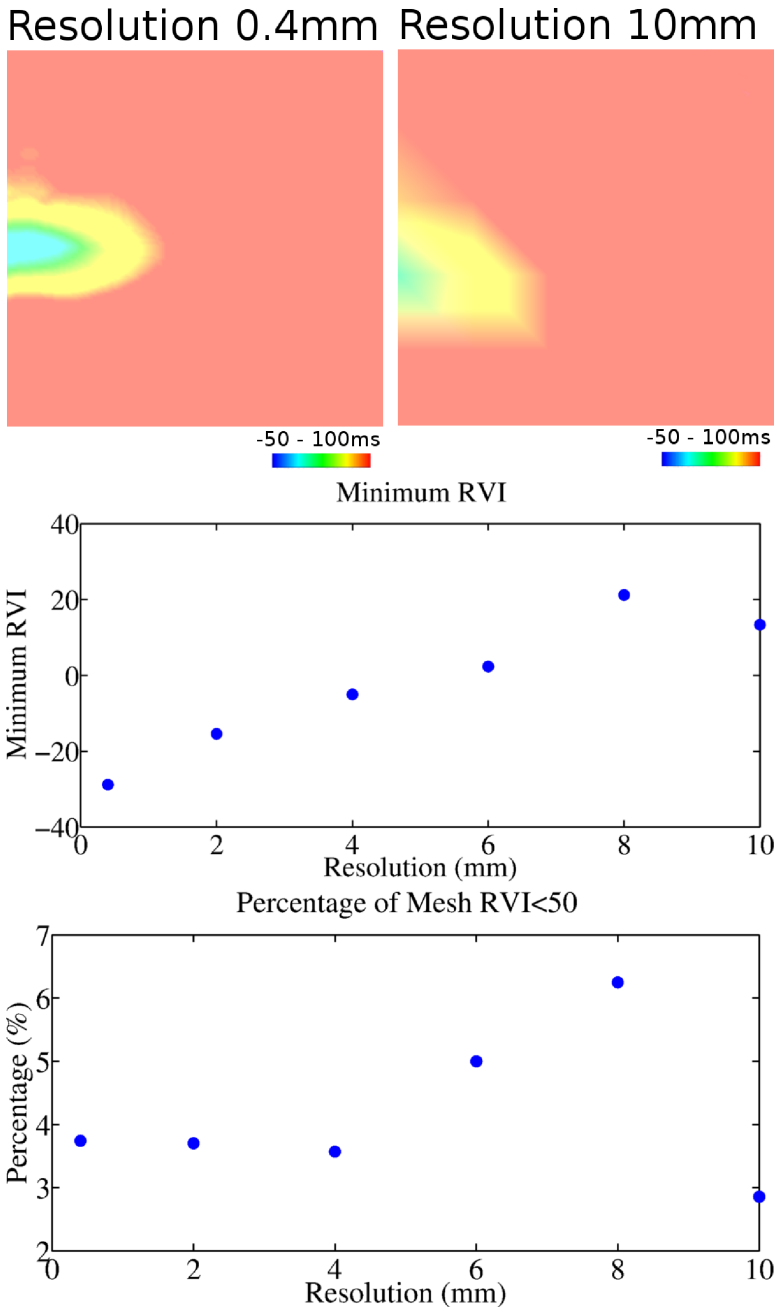

Figure 5.7: Result of varying data resolution. *Top* - RVI maps calculated from data with resolutions of 0.4mm (*left*) and 10mm (*right*). *Middle* - effect of varying resolution on RVI_{min}. *Bottom* - effect of varying resolution on $RVI_{area<50}$.

ducted on models with resolutions of 0.4mm (*left*) and 10mm (*right*). A region of low RVI values (approximately 0ms) is located around the site of initial wave block irrespective of the resolution of the model. Results were less well defined in the 10mm resolution model,

because plotting the results on the surface of a mesh with 10mm between nodes rather than on vertices spaced 10mm apart, inherently involved some blurring of the results. As displayed in the *middle* panel showing the effect of varying the resolution on the RVI_{min}, results of the RVI calculated on smaller resolution models produced more negative values of RVI. The RVI_{min} found in the 0.4mm resolution model was approximately -30ms compared to approximately 15ms in the 10mm resolution model. The $RVI_{area<50}$ generally increased as distance between nodes increased from approximately 4% in the 0.4mm resolution model to approximately 6% in the 8mm resolution model. The results produced in this parameter sensitivity analysis verify that sampling data at smaller intervals is more likely to capture the data at immediately either side of the line of block which produces the most negative values of RVI, most accurately indicating the region susceptible to reentry. In addition, using an increased number of nodes in the plotting method, produces a spatial map which more accurately indicates the critical region, as results can be plotted close to the actual midpoint, rather than being plotted on a node which may be some distance away from the calculated midpoint.

As can be seen from Figure 5.7, there is very little difference in RVI_{min} and $RVI_{area<50}$ between 0.4mm and 1mm resolution models. Therefore, further analysis throughout the study was conducted on a model with a resolution of 1mm between nodes.

5.2.7 Optimisation of the RVI Calculation: Search Radius Parameter Sensitivity Analysis

Due to the low resolution of data recorded in the clinic, the radius of r_s was large (25mm) (Child et al., 2015) in order to determine an acceptable number of downstream nodes, hence an acceptable number of RVI values are averaged and plotted to produce an accurate representation of RVI across a tissue. Here, we investigate the effect that the size of r_s has on the result of the RVI by varying the radius of r_s. The effect of varying the size of r_s on the result of the RVI was studied utilising data from a UDB simulation and the radius was varied between 1mm and 25mm.

5.2.8 The Effect of Altering the Size of the Search Radius on the RVI

The results of varying the size of r_s on the RVI are displayed in Figure 5.8. The images at the *top* of the figure display RVI maps for calculations using a radius of 5mm ($left$) and 25mm ($right$). Irrespective of r_s size, the calculation can locate the area susceptible

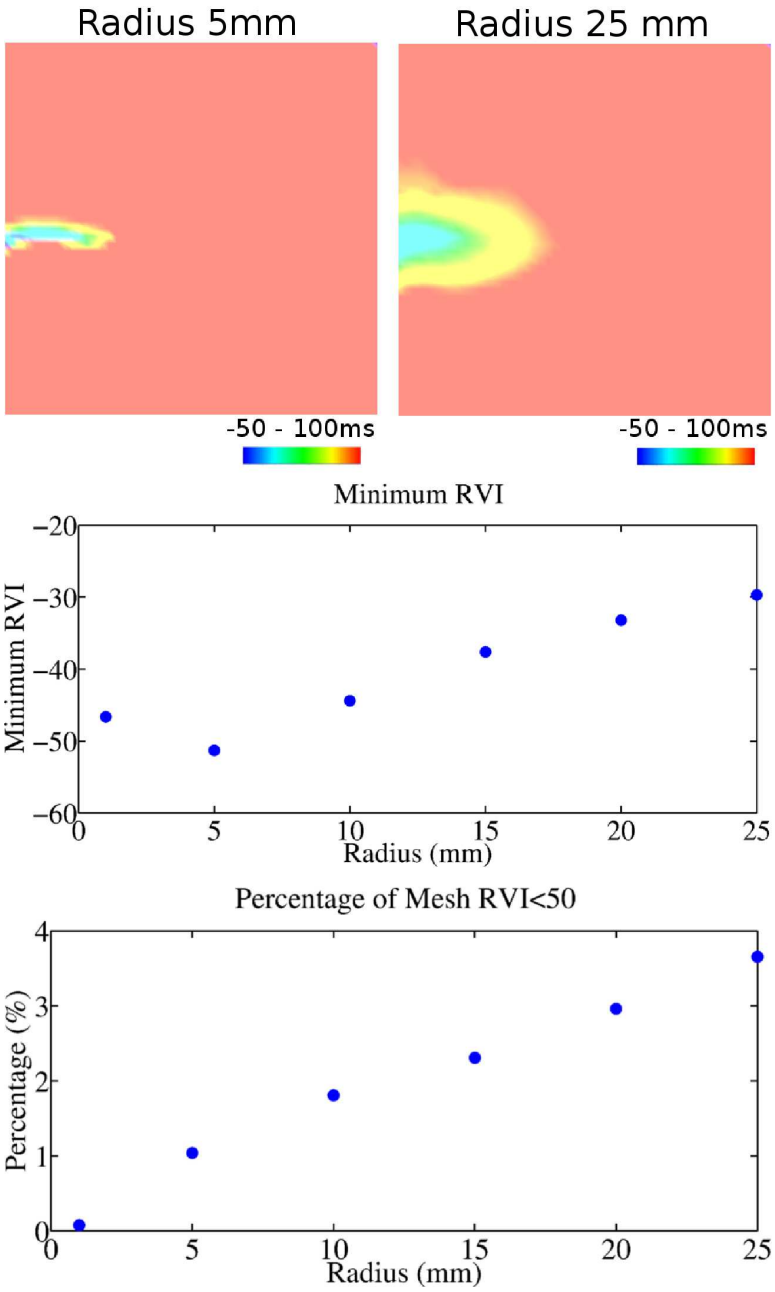

Figure 5.8: Result of varying the size of r_s on the RVI. *Top* - RVI maps calculated utilising a radius of 5mm (*left*) and 25mm (*right*). *Middle* - effect of varying the size of r_s on RVI_{min}. *Bottom* - effect of varying the size of r_s on $RVI_{area<50}$.

to reentry with low values of RVI at the site of initial block. It is evident that varying the size of r_s has a significant effect on the RVI_{min} (*middle*) with a smaller r_s producing more negative values of RVI. The difference between RVI_{min} calculated with an r_s with a radius of 5mm and the RVI_{min} calculated with an r_s with a radius of 25mm is approximately 20ms, indicating that using a smaller r_s in the RVI algorithm may be more effective

than using a larger r_s. This effect is due to the method of plotting an average RVI on the midpoint between the calculation node pair. If a smaller r_s is utilised to determine calculation node pairs, a smaller number of values of RVI will be produced and so fewer values will be averaged on each node, resulting in a more diverse range of values being plotted on the model. A smaller r_s results in a smaller $RVI_{area<50}$ (*bottom*). Values of RT and AT which produce the most negative RVI values are sampled at nodes immediately either side of the line of block. Using both a small and a large r_s results in data being sampled from nodes either side of the line of block. However, using a small r_s results in only a small number of calcuation node pairs which incorporate these data and so a small number of negative RVIs are produced and are localised within the region of initial block.

These effects indicate that whilst a smaller r_s may more accurately locate the region susceptible to reentry, using a larger r_s may produce more reliable results. Hence, an r_s with a radius of 25mm was utilised in subsequent analysis.

5.2.9 Investigating the Effect of Varying Arrhythmogenicity on the RVI

Utilising computational models permits parameters to be changed which cannot be done in *in vivo* studies. Varying parameters such as APD and CV alters the arrhythmogenicity of the model. The arrhythmogenicity of the model was varied in order to determine whether the algorithm was robust in varying physiological scenarios and if the RVI result could indicate the severity of the arrhythmogenicity of the model. Qualitative results of the simulations were observed in Meshalyzer to study whether UDB, BDB or no block occurred, prior to RVI analysis. In order to illustrate the qualitative results of the simulations, bar charts were produced to indicate whether UDB (*red*), BDB (*blue*) or no block (*green*) occurred. Line graphs were produced in the analysis in the calculation optimisation sections, because only data from one simulation was analysed. In contrast, here different simulations were run producing different wave propagation patterns, so bar charts were produced to represent the different wave propagation patterns. The arrhythmogenicity of the simulations was altered by changing BCL, APD in the lower half of the model and CV in the lower half of the model.

Increasing stimulation frequency is well known to increase arrhythmogenicity and hence, the prematurity of the S2 beat was varied between 300ms and 360ms. Pacing at a faster frequency results in the S2 beat reaching the depolarised lower half of the model prematurely, causing the wavefront to be diverted further around the site of initial

block, in order for the lower half of the model to repolarise before conduction of the S2 wave into the region. This allows time for the upper half of the model to repolarise before the wavefront (propagating from the lower half) reaches the upper region and a reentrant circuit can be initiated.

APD was only increased in the lower half of the model in order to increase the gradient of repolarisation between the two halves, an effect which is well documented to increase arrhythmogenicity. Similar to increasing BCL, increasing the dispersion of repolarisation between the two halves increases arrhythmogenicity by extending the pathlength of the wave which has to travel further around the site of initial wave block, delaying conduction into the lower half of the model, allowing the upper half to repolarise ready for reactivation by the reentrant wave. G_{ks} was decreased in the lower half of the model to produce an increase in APD. G_{ks} was altered from 0.8nS/pF to 0.4nS/pF producing APDs of approximately 294ms and 328ms respectively.

Altering CV was implemented by changing the conductivity values in the lower half of the model from 0.05S/m to 0.4S/m to produce CVs of 22cm/s and 63cm/s respectively. Increasing CV in the lower half of the model was predicted to decrease the arrhythmogenicity of the simulation as it enables the wavefront entering the lower half of the model after initial block to travel faster towards the point of reentry, reducing the time that the upper half of the model has to repolarise.

Effect of Varying Arrhythmogenicity on RVI

Figure 5.9 displays the results of varying BCL and its effect on the RVI. The *top* two images show RVI maps of simulations where UDB occurred when the models were paced at a BCL of 300ms or 320ms. Pacing the simulation at slower BCLs resulted in no wave block occurring. The RVI maps illustrate the ability of the algorithm to locate regions susceptible to reentry in both scenarios indicating that the algorithm is robust in varying physiological situations. The graph displaying the effect of varying BCL on the RVI_{min} (*middle*) shows an important trend: as the arrhythmogenicity of the simulation increases, the RVI_{min} decreases, with negative values being produced in UDB simulations (*red*) and positive values being produced by simulations in which no block occurred (*green*). This important finding indicates that the results of the RVI algorithm can predict not only whether reentry occurs but also, if reentry does occur, the algorithm can indicate the severity of the arrhythmia from the values of the RVI. The $RVI_{area<50}$ increases

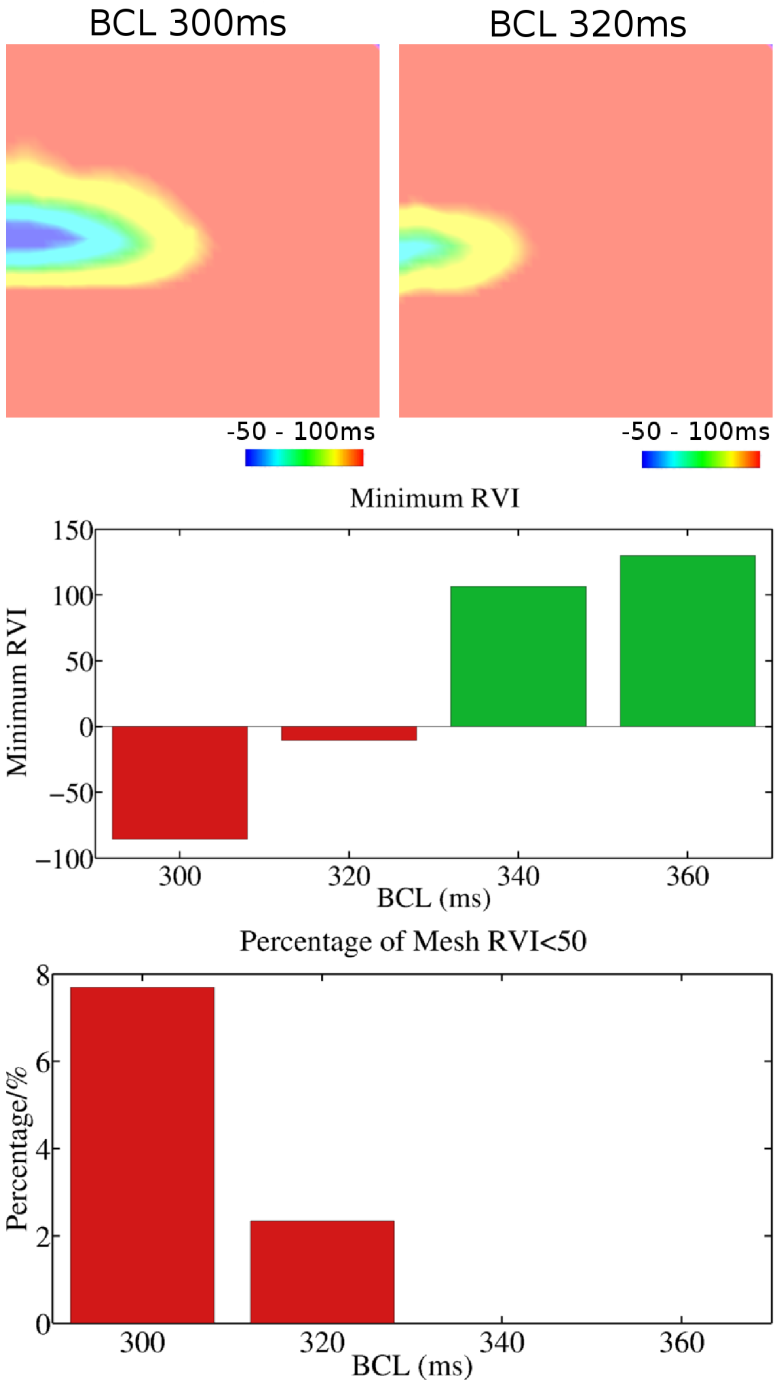

Figure 5.9: Effect of varying BCL on RVI. *Top* - RVI maps calculated with data from simulations paced at 300ms (*left*) and 320ms (*right*). *Middle* - effect of varying BCL on RVI_{min}. *Bottom* - effect of varying BCL on $RVI_{area<50}$. *Red* - UDB simulations, *green* - no block simulations.

with increasing arrhythmogenicity confirming the use of the algorithm in predicting the likelihood of reentry occurring.

It is evident in the *top* two images of Figure 5.10, showing the RVI maps calculated

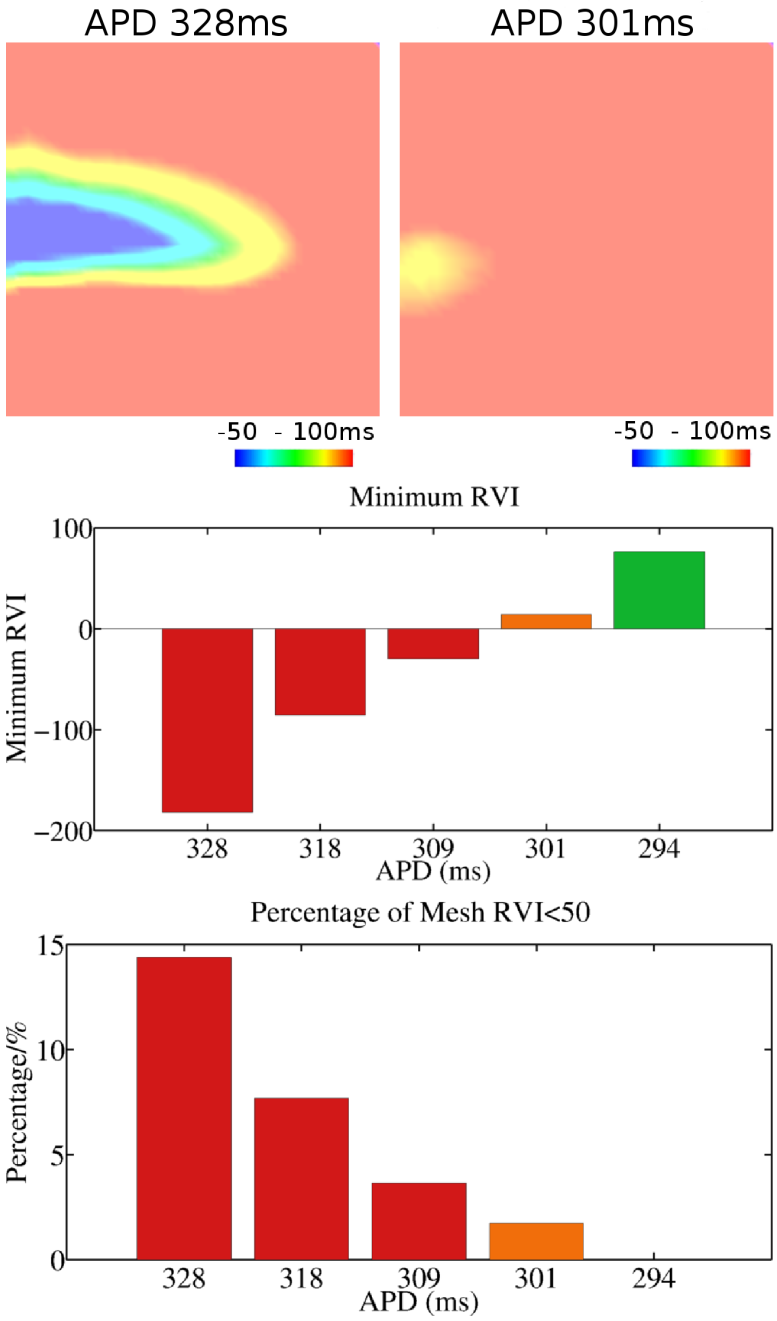

Figure 5.10: Effect of varying APD in the lower half of the model on the RVI. *Top* - RVI maps calculated with data from simulations exhibiting an APD of 328ms (*left*) and 301ms (*right*) in the lower half of the model. *Middle* - effect of varying APD in the lower half of the model on RVI_{min}. *Bottom* - effect of varying APD in the lower half of the model on $RVI_{area<50}$. *Red* - UDB simulations, *orange* - BDB simulations *green* - no block simulations.

using data from simulations with an APD of 328ms (*left*) and 301ms (*right*) in the lower half of the model respectively, that the algorithm locates regions susceptible to reentry in both cases. Interestingly, UDB occurred in the simulation used to produce the RVI map

on the $left$, whereas only BDB occurred in the simulation used to produce the RVI map on the $right$. It can be concluded that the RVI algorithm can predict susceptibility to reentry from data which doesn't produce reentry. The *middle* graph shows the relationship between RVI_{min} and varying APD. The most arrhythmogenic UDB (red) simulation with an APD of 328ms in the lower half of the model produced an RVI_{min} of approximately -180ms, whereas a BDB ($orange$) simulation with an APD of 301ms produced an RVI_{min} of approximately 15ms and a simulation where no block ($green$) occurred with an APD of 294ms produced an RVI_{min} of approximately 75ms. It is evident from these results that the RVI algorithm is robust in situations of varying physiology and can even imply the likelihood of reentry occurring. The result is also substantiated in the *bottom* graph of $RVI_{area<50}$ with an increasingly large percentage of $RVI_{area<50}$ being produced by more arrhythmogenic simulations, a small $RVI_{area<50}$ (approximately 2%) being produced by BDB simulations and no $RVI_{area<50}$ being produced by simulations where no block occurred.

The effects of increasing the CV in the distal half of the model produces a biphasic result shown in Figure 5.11. Between conductivities of 0.05S/m and 0.2S/m (producing CVs of 22cm/s and 45cm/s respectively), arrhythmogenicity of the simulation decreases, producing less negative RVI results. UDB simulations produce negative RVI_{min} results from -170ms to -30ms for conductivities of 0.05S/m to 0.15S/m and a BDB simulation with a conductivity of 0.2S/m produces low positive values of RVI_{min}, approximately 30ms. However, simulations run with conductivities greater than 0.3S/m (producing CVs greater than 55cm/s) in the lower half of the model result in UDB and RVI_{min} becomes more negative. A potential explanation of this biphasic pattern is that when CV is slow, it increases the time that the upper half of the model has to repolarise in order to allow conduction of a reentrant wave. When CV is fast, the wavelength in the lower half of the model will increase, increasing the dispersion of repolarisation, causing the wavefront to be diverted further around the site of initial block, effectively increasing the pathlength which the wave must traverse in order to propagate into the lower half and back towards the site of initial block. This effect facilitates reentry due to the increased time that the wave takes to travel around the larger area of refractory tissue before reaching the site of initial block. During this lengthened period of time, the tissue in the upper half may have recovered from inactivation and be able to conduct the reentrant wavefront. This finding validates the previous results and conclusions drawn from the results of varying arrhythmogenicity

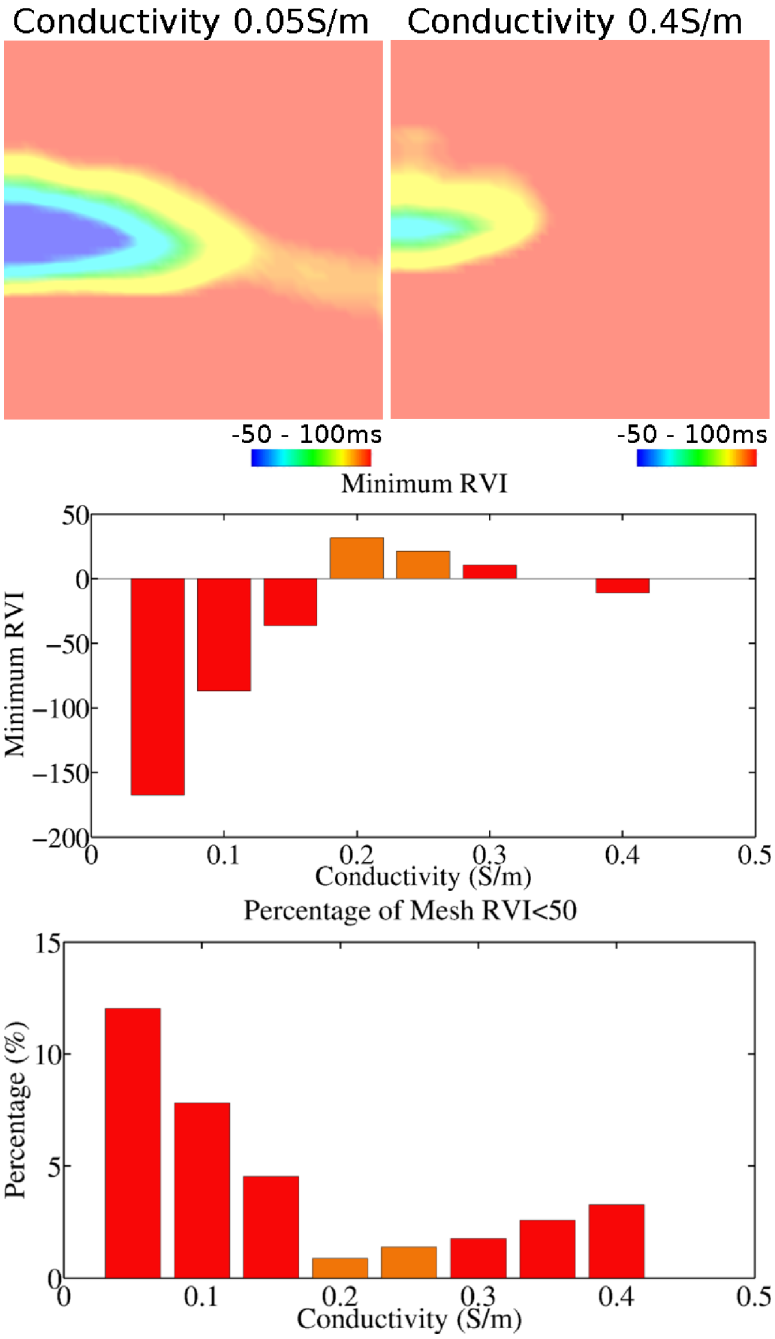

Figure 5.11: Effect of varying conductivity in the lower half of the model on the RVI. *Top* - RVI maps calculated with data from simulations run with conductivity of 0.05S/m (*left*) and 0.4S/m (*right*) in the lower half of the model. *Middle* - effect of varying conductivity in the lower half of the model on RVI_{min}. *Bottom* - effect of varying conductivity in the lower half of the model on $RVI_{area<50}$. *Red* - UDB simulations, *orange* - BDB simulations.

and its effect on the RVI, and highlights the importance of the algorithm being able to elucidate the arrhythmogenicity of the simulation from which the data are sampled.

5.3 Analysis of the RVI in a Model Incorporating Infarct Scars

The clinical application of the RVI algorithm currently being investigated is to predict the susceptibililty of tissue to reentry around infarct scars in order to guide the ablation procedure. Mechanisms of reentry around infarct scars have been discussed in Sections 2.6 and 3.1 but crucially, the non-conducting fibrotic tissue of the scar and the remodelling of the ionic currents in the BZ cause the conduction block and wave diversion required to elicit reentry. In order to study the RVI algorithm in a more clinically realistic model, an idealised scar and BZ region was introduced into the 2D computational model.

5.3.1 Computational Model Set-Up

Computational Model Geometry

The scar and BZ geometry utilised here was motivated by the concept that waves propagate via conducting isthmuses dispersed throughout fibrotic scar tissue as displayed in Figure 5.2. Crucially, tissue within the isthmus displays slowed CV and a region of lengthened APD at the exit site-end of the isthmus, as it has been observed that functional block occurs at only a specific site and not throughout the BZ region (Segal et al., 2010).

Figure 5.12 depicts the 2D geometrical model utilised in this study which is based on the concept illustrated in Figure 5.2. The same 5cm-by-5cm finite element mesh with a resolution of 200μm between nodes was created as described in Section 5.2, resulting in a model consisting of 62500 quadrahedral elements and 63000 nodes.

In order to introduce a scar region in to the tissue, two back-to-back semicircular fibrotic scar regions (*black*) were created in Matlab by finding coordinates of nodes within regions which satisfied equations for right and left semicircles. The two semicircles, spaced approximately 5mm apart, each measured approximately 1cm wide by 2cm tall and the scar complex was positioned in the centre of the model. Nodes whose centroids fell within these regions were tagged with an identifier so that they could be modelled as non-conducting tissue.

A BZ region displaying slow CV (BZ_{cond}) was introduced into the model. The BZ_{cond} (*blue*) was created in Matlab by finding nodes which fall within an ellipse, located in the same region and the same size as the scar complex (approximately 2.5cm-by-2cm). Nodes whose centroids fell within this region and not within the scar regions were tagged with

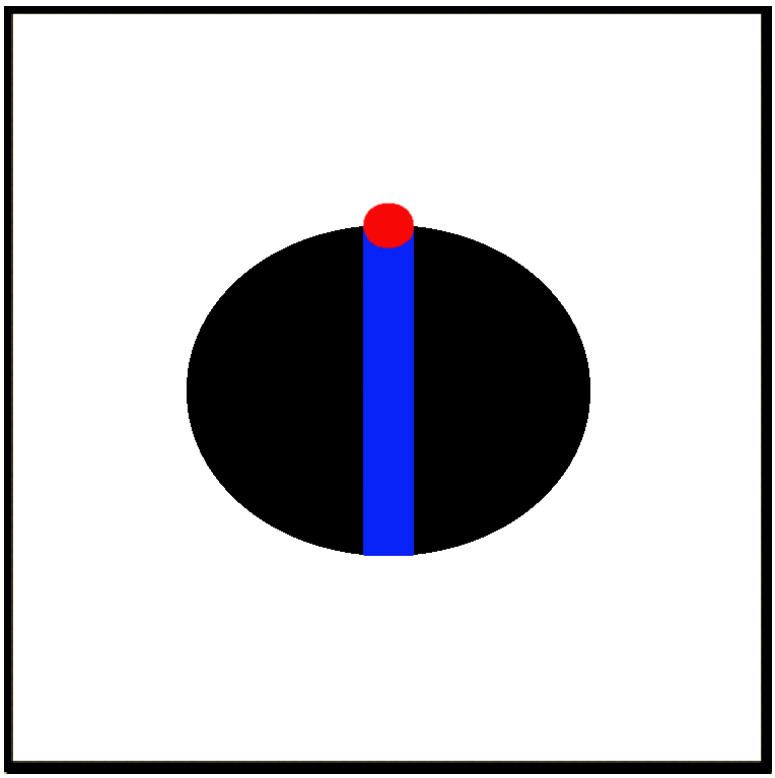

Figure 5.12: 2D model geometry with incorporated scar and BZ regions. *White* - healthy tissue, *black* - scar, *red* - BZ_{APD}, *blue* - BZ_{cond}.

an identifier which enabled assignment of BZ_{cond} parameters to the region.

A circle with a diameter of approximately 5mm was created at one end of the BZ_{cond}, between the two scar regions, to represent BZ with a lengthened APD (BZ_{APD}) at the exit point of the scar. The circle was again created in Matlab to determine the centroids of elements which fell within the bounds of the circle in order to tag the elements as BZ_{APD} for parameter assignment.

Model Parameterisation

All elements in the model were assigned isotropic fibre directions with conductivity values in the BZ_{cond} being $0.05S/m$ in both longitudinal and transverse directions, compared to $0.1S/m$ in healthy tissue.

The electrophysiology of healthy tissue was modelled utilising the human model of ventricular AP (Ten Tusscher and Panfilov, 2006). In the BZ_{APD} region, the APD was lengthened by altering the parameters of the human model based on previously described protocols (Rantner et al., 2012; Ashikaga et al., 2013). The maximal conductance value of I_{Na} was reduced to 38% of normal, I_{CaL} to 69%, I_{Kr} to 30% and I_{Ks} to 20% and the

maximal value of I_{NaCa} was increased to 132% of normal. These changes produced an increase in APD of approximately 150ms in the BZ_{APD}.

5.3.2 Stimulation Protocol

Simulations were run according to the protocol described in Section 5.2, with the model being paced to a steady state and the S1S2 pacing protocol initiated. The model was stimulated in the centre of the model in the x-direction, approximately 5mm above the BZ_{APD}, with a stimulus current of 300μA applied for 3ms.

5.3.3 RVI maps in a 2D Model with Incorporated Infarct Scar

The algorithm described in Section 5.2 was conducted utilising data from simulations run on the 2D scar model. Nodes within the scar region were not utilised as $node_i$ or $node_j$ in the RVI calculation due to the lack of data at the non-conducting nodes of the model. However, the result of the RVI could be plotted on scar nodes to produce a spatial map of RVI over the entire surface of the model.

Figure 5.13 displays the AT (*top*), RT (*middle*) and RVI (*bottom*) maps for both UDB ($left$) and BDB ($right$) simulations. It is evident from the AT maps that the propagation wave is blocked at the BZ_{APD} and circumvents the scar regions before entering the isthmus from below. RTs prior to the line of block are approximately 1100ms in both simulations. The ATs within the isthmus below the line of block differ between UDB and BDB simulations with the AT occurring later in the UDB simulation than the BDB simulation due to the wave taking longer to propagate around the scar region and back up through the isthmus. This results in the tissue above the isthmus, at the exit point of the scar, having sufficient time to repolarise and so is able to conduct the wave propagating from the isthmus to form a reentrant circuit. The AT in the BDB simulation at the same region occurs before the tissue above the isthmus is repolarised and so the wavefront collides with the wave back and terminates propagation. In both the UDB and BDB simulations, low values of RVI are situated around the point of initial wave block and at regions of non-conducting, scar-like tissue, with lower RVI values being produced by the UDB simulation. However, unlike the results produced by the experimental model in Section 5.2, the lowest values of RVI in the UDB RVI map are positive at approximately 50ms. An explanation for the less negative result observed is that the region of initial block and therefore, the regions displaying the most extreme values of AT and RT which will give the most negative

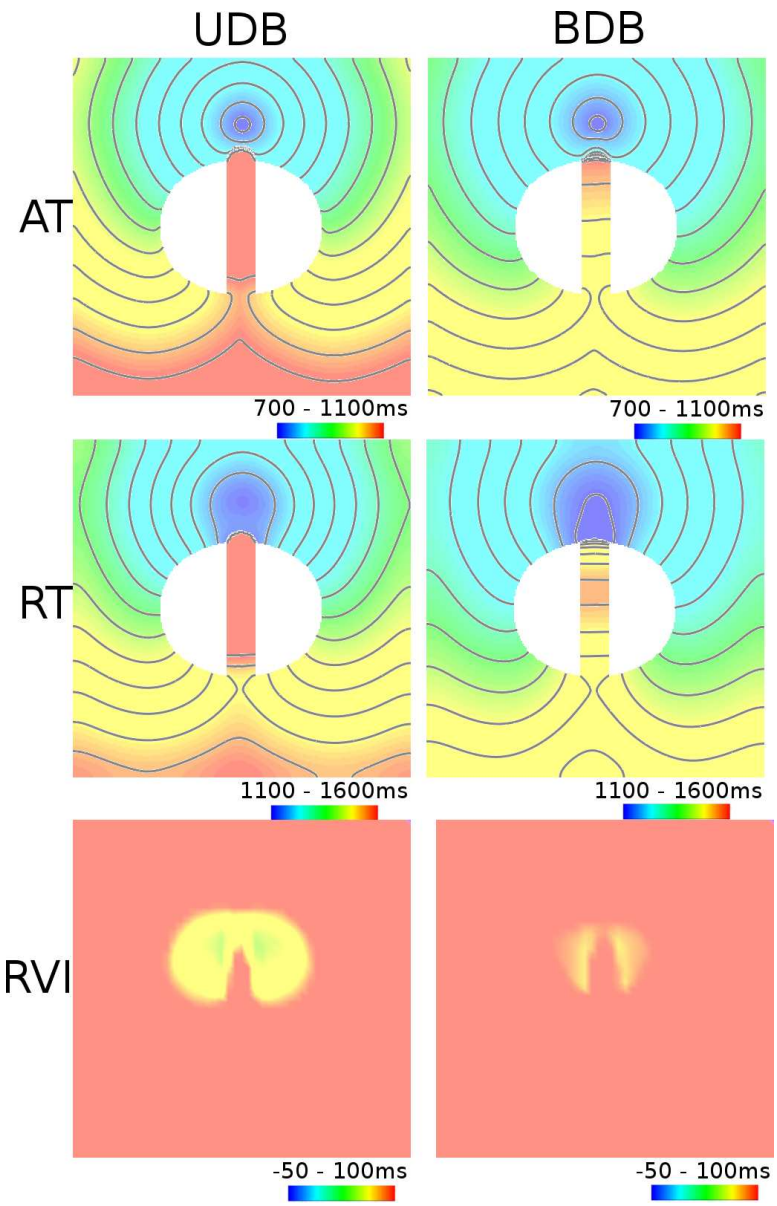

Figure 5.13: Results of the RVI algorithm in the 2D model with incorporated scar and BZ. *Top* - AT maps, *middle* - RT maps, *bottom* - RVI maps for UDB (*left*) and BDB (*right*) simulations.

RVI result, is very small in comparison to the area in the experimental model. Although negative values of RVI are produced by the UDB simulation, only a small number are produced which get averaged in the plotting method, contributing to the positive values of RVI displayed here. This result verifies that the RVI algorithm maintains its ability to identify a susceptibility to reentry in a more physiologically realistic scar geometry.

5.3.4 Optimisation of the RVI: Resolution and Radius Parameter Sensitivity Analyses

The resolution of the calculation model and the size of r_s utilised in the RVI calculation were varied as previously discussed in Section 5.2. The analysis was repeated here to ensure that the effects of varying these parameters remained consistent, despite vast changes in the geometry of the model. Analysis was conducted utilising data from a UDB simulation.

The graphs in Figure 5.14 show RVI maps calculated on 0.4mm ($left$) and 8mm ($right$) resolution meshes and how varying the resolution affects RVI_{min} ($middle$) and $RVI_{area<50}$ ($bottom$). The RVI maps indicate that both the value of RVI and the area of low RVI are similar between both resolution parameters. The $middle$ panel depicts how RVI_{min} varies with varying resolution between nodes in the model. Interestingly, varying resolution between 0.4mm and 8mm does not have a significant effect on RVI_{min} which remains relatively constant at approximately 30ms. This result does not replicate the positive correlational trend observed in the simple experimental model, possibly due to the significant averaging effect of the plotting technique which produces a more positive RVI_{min} due to the smaller area of conduction block. The RVI_{min} significantly increases to approximately 115ms in a model with a resolution of 10mm between nodes. It is possible that data from either side of the line of block producing the most negative RVI values are not sampled in the 10mm resolution model so no negative values of RVI contribute to the averaged RVI map. In addition, the $RVI_{area<50}$ graph shows a general decrease in $RVI_{area<50}$ as the resolution decreases suggesting that sampling data at finer resolutions will more accurately locate regions susceptible to reentry. Further analysis was conducted on a model with a resolution of 1mm between nodes.

Varying the size of r_s in the scar geometry replicated the results observed in the experimental model. Figure 5.15 displays the results of varying the size of r_s in the model with incorporated scar region. The *black* regions in the RVI map on the $left$ have no RVI values associated with them due to the smaller r_s not spanning the scar regions (which have no data associated with them). An RVI value calculated between a node pair is plotted on a spatial midpoint between the pair, which does not lie in the scar regions if r_s does not span the scar. This artefact does not alter the efficacy of the RVI algorithm. It can be seen from the RVI map using a radius of r_s of 10mm, that the exit site of the scar is highlighted by low values of RVI. Decreasing r_s produced a more negative RVI_{min} with an RVI_{min} of approximately -120ms being produced using the smallest radius of r_s (1mm) and an

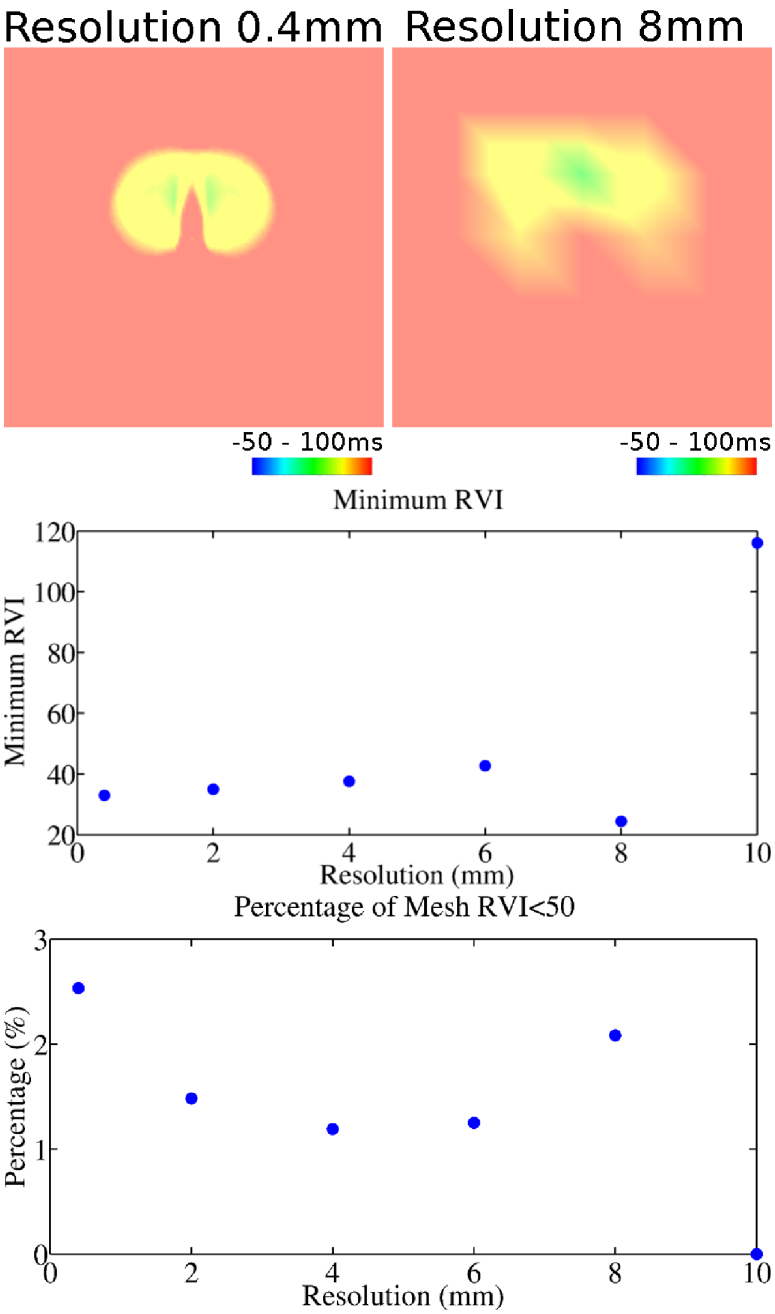

Figure 5.14: Effect of varying calculation mesh resolution on the RVI in the scar model. *Top* - RVI maps calculated from models with resolutions of 0.4mm (*left*) and 8mm (*right*) between nodes. *Middle* - effect of varying resolution on RVI_{min}. *Bottom* - effect of varying resolution on $RVI_{area<50}$.

RVI_{min} of approximately 40ms being produced using the largest radius of r_s (25mm). This effect is also seen in the experimental model. However, in the experimental model, a radius of r_s of 25mm was able to produce negative values of RVI in simulations of UDB. In this model, a radius of r_s of 25mm is not able to locate the exit site of a reentrant circuit with negative values of RVI. As such, a radius of r_s of 10mm was chosen to conduct subsequent

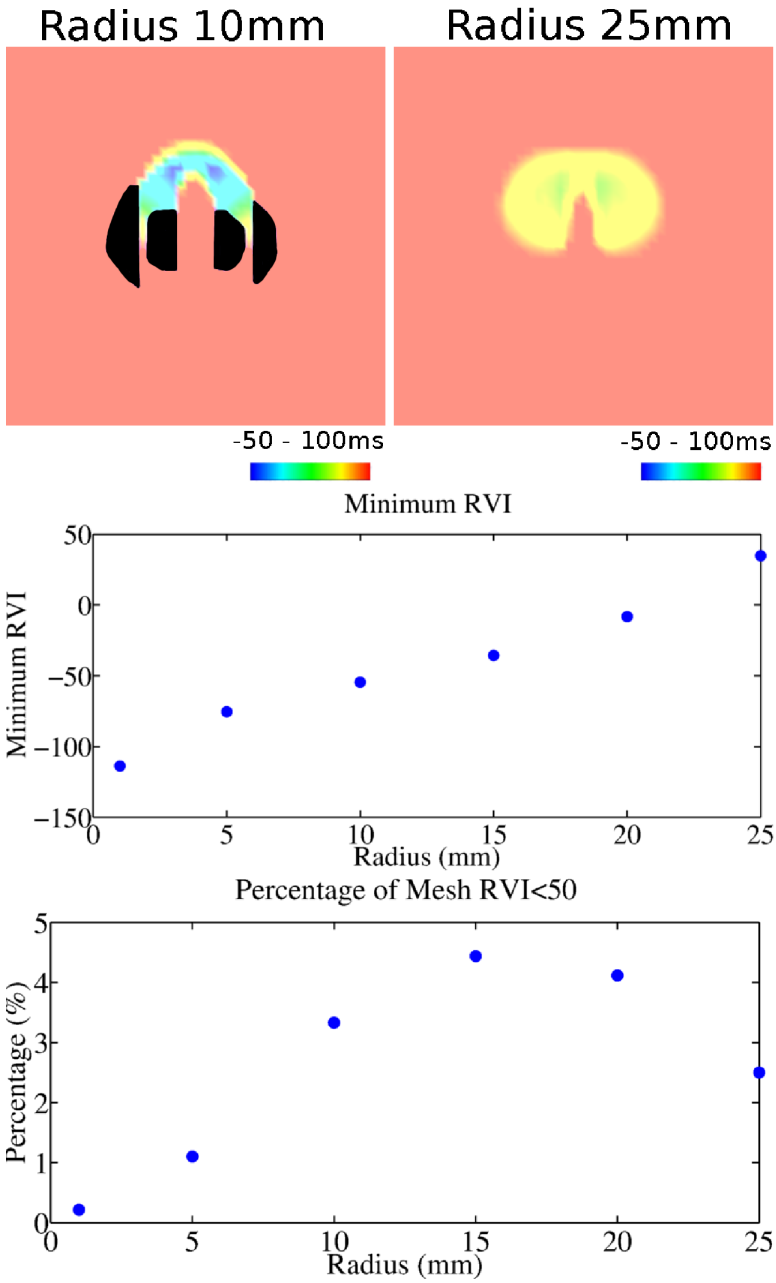

Figure 5.15: Effect of varying the size of r_s used in the RVI calculation. *Top* - RVI maps calculated using a radius of r_s of 10mm (*left*) and 25mm (*right*). *Middle* - effect of varying the size of r_s on RVI_{min}. *Bottom* - effect of varying the size of r_s on $RVI_{area<50}$.

analysis in this section in order to be able to produce results displaying negative values of RVI in simulations of UDB. Similarly to the results produced by the experimental model, there is a general trend showing that the $RVI_{area<50}$ increases as the radius increases due to the effect of averaging larger amounts of data produced by utilising a larger r_s. However, the $RVI_{area<50}$ decreases at the largest r_s due to higher values of RVI being produced.

5.3.5 Investigating the Effect of Varying Arrhythmogenicity on the RVI in the Scar Model

Figure 5.16 displays the effects of increasing the arrhythmogenicity of the simulation on

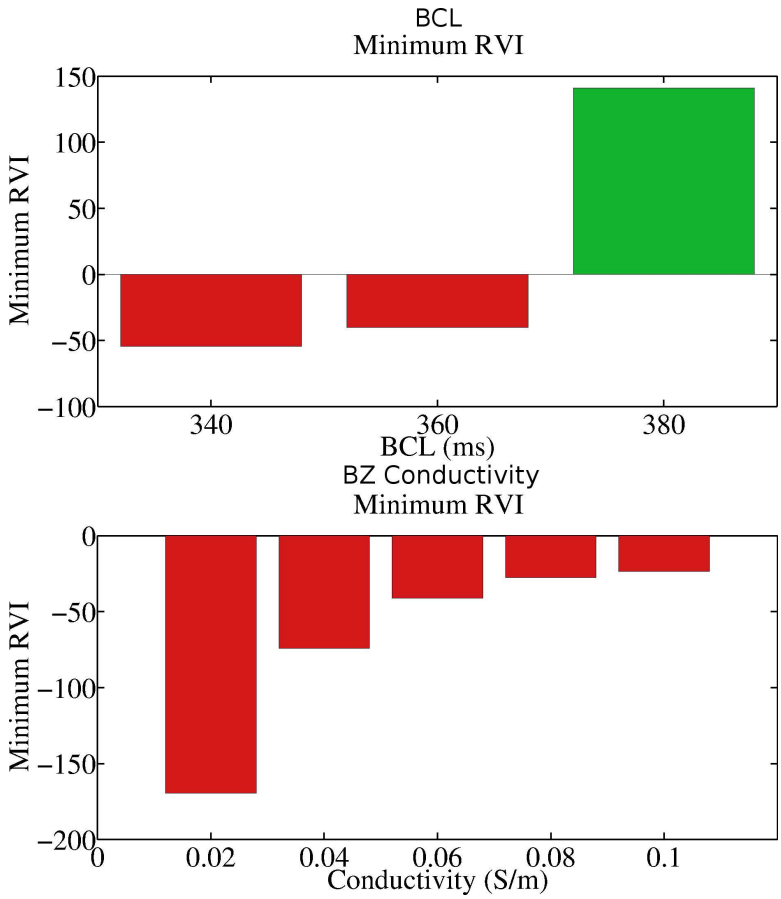

Figure 5.16: The effect of increasing arrhythmogenicity on the RVI. Graphs of RVI_{min} with varying BCL (*top*) and BZ conductivity (*bottom*). *Red* bars indicate UDB and *Green* bars show no block.

the RVI. The graph at the *top* of the figure displays the effect of varying BCL on RVI_{min}. Decreasing the BCL increases the arrhymogenicity of the simulation due to the earlier repolarisation of the tissue prior to the line of block. Unlike, the scenario in the experimental model, the pathlength of the propagation wave around the scar region remains the same in all simulations and so does not contribute to increasing arrhythmogenicity. A negative RVI_{min} value of approximately -50ms was produced by the most arrhythmogenic UDB (*red*) simulation (BCL = 340ms), with the less arrhythmogenic UDB simulation (BCL = 360ms) producing a less negative RVI_{min}; a trend that was also seen in the results of the 2D experimental model. The simulation in which no block occurred (*green*) produced high positive values of RVI_{min} of approximately 140ms.

A similar trend was observed in simulations with varying BZ conductivity in BZ_{cond}. Decreasing the CV in BZ_{cond} provided the tissue prior to the line of block the time to recover from activation, before the reentrant wave propagating from the isthmus arrived at the region. As a result of the wavefront propagating at a slow speed, increased ATs are sampled from downstream activated nodes within the BZ, contributing to the more negative RVI values. Decreasing CV produced more negative values of RVI_{min} with the most arrhythmogenic simulation displaying an RVI_{min} of approximately -170ms and the least arrhythmogenic simulation displaying an RVI_{min} of approximately -30ms.

The results observed in the parameter sensitivity analysis in which arrhythmogenicity of the simulations was increased, suggests that the RVI algorithm can be performed successfully in an idealised scar model geometry in a variety of different physiological conditions. Moreover, results of the RVI algorithm produced in the experimental model are substantiated in the scar model, suggesting that more arrhythmogenic simulations produce more negative RVI values.

5.4 Discussion

5.4.1 Limitations

The 2D models utilised in this study represent highly simplified geometries. It is possible that more realistic scar geometries may produce very different RVI results and it is unknown whether the algorithm would maintain its ability to predict susceptibility to reentry in such models.

In addition the 2D models do not take into consideration the complex 3D wave propagation that occurs *in vivo*. It remains to be seen how the RVI calculation performs in 3D tissue and whether the method can identify sites vulnerable to reentry throughout the heart. The 2D models utilised in this study do not allow for such investigation which could be vital to comment on the clinical application of this work.

In light of these limitations, the work presented in Chapter 6 aims to investigate some of the uncertainties described above. In particular, we will simulate wave propagation around infarct scars in a 3D ventricular model in order to test whether the RVI methodology retains its ability to identify sites vulnerable to reentry throughout the ventricle wall, based on 3D *in silico* data. The more realistic geometry will allow for the investigation of how the RVI calculation performs in a more clinical setting. In order to study whether

the RVI maintains its accuracy and applicability in a clinical setting, we will observe the effect of low resolution, endocardial data sampling in the 3D ventricular model.

5.4.2 Summary

Implementing the RVI method in a 2D simple experimental model incorporating dispersion of repolarisation showed that the method can predict regions susceptible to reentry and display the results on a spatial map. This result suggests that the RVI methodology can be successfully implemented and produces RVI maps which can accurately identify the exit point of the scar, whilst utilising human electrophysiological data. Previously the technique has only been demonstrated using porcine data (Child et al., 2015). Here we demonstrate the method's use on human data.

Importantly the RVI is able to locate regions susceptible to reentry in cases where both UDB and BDB occur. Negative values of RVI are produced by UDB and BDB simulations produce low positive values of RVI. However, in comparison to the rest of the tissue, these values are still low and can identify the region which may be susceptible to reentry. The low values of RVI are located at the point where initial block occurs, which also coincides with the point at which the wave completes a reentrant circuit; the exit point of the scar.

Due to the limitations of the sampling techniques used in the clinic, both resolution and r_s parameters were varied in order to provide information about the optimal data recording and analysis techniques which could be of use in the clinic. It was found that increasing the resolution of the sampled data used in the algorithm produced more negative values of RVI and in addition, produced a smaller area of lower RVI values. These results indicate that using a higher resolution will provide a more robust and accurate indication of the susceptibility to reentry. Decreasing r_s produces more negative RVI values and a smaller region of low values which indicates that a small r_s could be more effective in locating regions susceptible to reentry.

Increasing the arrhythmogenicity of the simulations by decreasing BCL and increasing the heterogeneity of repolarisation across the tissue is more likely to produce UDB. Likewise, decreasing the CV in the lower half of the tissue increases the arrhythmogenicity due to the increase in excitable gap. However, results showed that increasing the CV could also facilitate reentry as the increase in CV lengthens the wavelength in the lower half of the model during the S1 beat. As a result, the S2 beat propagating from the upper half of the model encounters a more significant area of block which in turn increases the

path length as the wave must travel further around the region of block, increasing the excitable gap. These complex interactions between varying CV and reentry success have been discussed elsewhere in the literature (Coronel et al., 2010). Importantly more arrhythmogenic simulations produced more negative RVI values. This is a crucial finding as we can deduce that the RVI algorithm can indicate the severity of the arrhythmia based on the values of the RVI. In addition, it can be concluded that the RVI is able to locate regions susceptible to reentry across varying physiological scenarios, an important trait if the algorithm is to be of use in the clinic where biological variation is inherent.

The present study also validates the use of the RVI algorithm in a simplified model of post-MI reentry. Low RVI values are produced in both UDB and BDB simulations at the exit point of the scar. This region has previously been suggested to be the optimal location to introduce an ablation lesion in order to terminate post-MI VT (Segal et al., 2010). Hence, the RVI method may prove to be very useful in guiding the ablation procedure. Due to the small region of wave block involved in the scar geometry model, less negative values of RVI are produced by the algorithm using data from a UDB simulation. However, in comparison to the RVI values in the rest of the tissue, the RVI is still able to locate regions susceptible to reentry.

Testing the optimisation of the clinical recording and analysis techniques by altering the resolution of sampled data and the r_s shows that in the model with incorporated scar region, varying the resolution of the data does not affect the result of the RVI. Similarly to the experimental model, decreasing the r_s produces more negative RVI values suggesting again, that a smaller r_s may improve the ability of the RVI to locate regions susceptible to reentry in the clinic.

Additionally, increasing the arrhythmogenicity of the simulations by decreasing the BCL and altering the CV in the BZ increases the likelihood of initiating reentry. Moreover, simulations of increased arrhymthogenicity produce more negative RVI values indicating the severity of the simulation in the scar geometry model.

Computational modelling techniques utilised in this study have provided us with the opportunity to alter parameters which affect the arrhythmogenicity of the simulations. These parameters are not so easily changed over a wide parameter space in animal models and have provided important insights into the scope of the RVI method. In addition, changing the arrhythmogenicity of the simulation has enabled the validation of the algorithm under varying physiological conditions, and we can conclude that the RVI algorithm

is robust when utilised in different physiological conditions.

It has been shown here that the RVI can predict susceptibility to reentry in cases where both UDB and BDB occur. This finding could have great impact on the use of the algorithm in the clinic and suggests that VT needn't be induced in order to map the VT substrate. Inducing VT during the ablation procedure increases the risk of the treatment and decreases the applicability to many patients due to the difficulties in initiating the clinical arrhythmia. Hence, a technique which could identify the exit point of the scar without having to induce VT could be of great importance.

Chapter 6

Modelling Clinical Data Recording and RVI-Guided Ablation in a Ventricular Model

In Chapter 5 we validated the RVI calculation using human in silico data, showing that the RVI locates regions susceptible to reentry in a simplified 2D geometrical model with incorporated idealised scar and BZ regions. Here, we wish to extend the study to investigate the RVI in a 3D ventricular model in order to be able to draw conclusions which will facilitate the implementation of the methodology in the clinic. In Chapter 4 we investigated species differences in the effective electrical size of the heart and showed that, due to species differences in effective size, the optimal approach to study post-MI VT was to utilise human data where possible. Given that an anatomically accurate ventricular model of the human heart is very computationally demanding, in this chapter, we required a less computationally demanding approach. In Chapter 4 we demonstrated that the rabbit displayed an effective size most similar to the human, therefore in this chapter, a 3D model of rabbit ventricles is used. We investigate how low data resolution in the clinic affects the results of the RVI, in particular, whether regions of low RVI values indicating a susceptibility to reentry are still identifiable at low data resolutions. In addition, the RVI map is used as a guide, as we model the ablation procedure, where regions of low RVI are targeted for ablation and subsequent stimulation of the model reveals the outcome of the procedure.

6.1 Introduction

VT remains a significant, life-threatening condition due to its possible progression to VF and SCD (Koplan and Stevenson, 2009). Treatment of VT therefore constitutes a vitally important area of research in terms of improving life expectancy and quality of life and reducing the economic burden of the disease.

Infarct scars occurring as a result of an MI can be a cause of VT if the scar region alters conduction of the excitation wave in such a way that it disrupts normal propagation. In Sections 2.6, 3.1 and 5.1 we described a classic scenario of initiation of reentry around infarct scars. To recapitulate; non-conducting scar regions are separated by tracts of BZ tissue which display altered ionic current and conductivity properties. Figure 5.2 shows that on approach of a premature excitation wave, the lengthened APD in the BZ region causes the wavefront to be blocked as the tissue remains depolarised. The wavefront diverts around the scar regions, increasing the activation pathlength of the circuit. In addition to the decrease in CV in the BZ, the increased pathlength results in the tissue at the site of initial wave block having sufficient time to repolarise by the time the diverted wave returns to the site and so the tissue is reactivated, completing the reentrant circuit. Thus, VT as a result of ischemic heart disease is caused by this sustained reentrant wave propagation around the MI scar region.

Current treatment strategies for MI induced VT include radiofrequency catheter ablation, drug therapy and ICDs. The problems associated with drug therapy and ICD treatment, such as having a negative impact on the quality of life, medical contraindications and application of painful shocks, contribute to catheter ablation being a common choice of treatment for MI scar-related VT. In Sections 2.6 and 3.7, we described in detail different approaches to the ablation procedure, as well as the limitations of current techniques. We described how, during catheter ablation, mapping of the tissue is conducted in order to locate regions within the scar and target them for ablation. Ideally, tissue within a critical isthmus of the scar should be ablated to terminate reentry. However, current mapping techniques identifying ablation targets are not always applicable to all patients and are not always sufficiently accurate. As such, in some cases, the optimal site for ablation is not identified and areas other than those within the critical isthmus are often ablated as shown in Figure 6.1. The *red*, *green* and *light blue* areas on the CT scan image show a scar region as indicated by low voltages during contact mapping. *White*

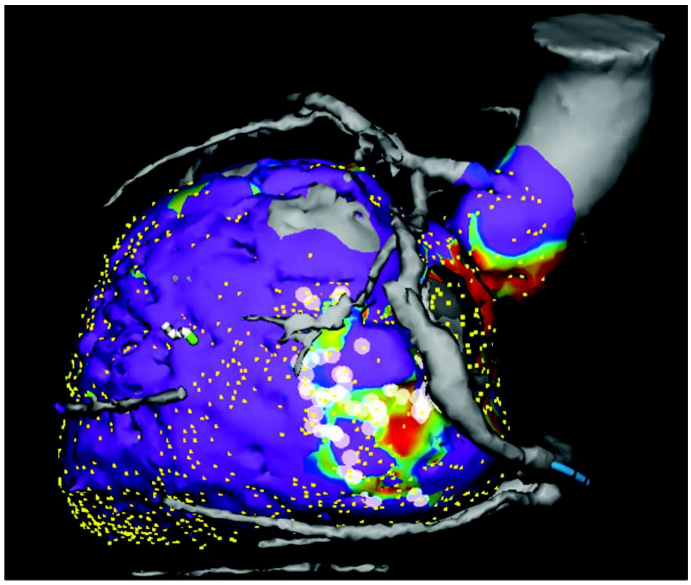

Figure 6.1: Map highlighting the inaccuracy of identifying the target for ablation. *White* - ablation lesions. *Dark blue* - healthy tissue as indicated by normal voltages during contact mapping. *Red*, *green* and *light blue* - scar tissue as indicated by low voltages during contact mapping (Tung et al., 2010).

areas show the extent and number of dispersed ablation lesions (Tung et al., 2010), indicating the inaccuracy of locating ablation targets. This results in the possibility that the procedure may not be successful in terminating reentry due to the ablation target being incorrect. In addition, in order to ablate the correct region of tissue, more tissue than necessary may be ablated, possibly leading to later mechanical dysfunction.

In Chapter 5 we showed that the RVI method locates regions susceptible to reentry in a simple geometrical model utilising a model of human electrophysiology. Crucially, the RVI calculation has a potential clinical application in guiding the ablation procedure, by more accurately locating the exit site of the scar as the ablation target, increasing the applicability, accuracy and success rates of the treatment. A previous study implemented RVI-guided catheter ablation in a patient displaying ischemic heart disease and VT (Child et al., 2015). Electrograms were recorded during S1S2 pacing and ATs and RTs were derived from the data. The RVI calculation was performed on the data and the region of low RVI indicating a susceptibility to reentry was ablated, terminating the VT. Hence, the method has been validated in the clinic but only in one patient. Therefore, the method requires further validation in hearts of varying geometries and with varying electrophysiological properties. In order to calculate a map of RVI across the myocardium, electrophysiological data need to be sampled at a number of points around the ventricular

wall. However, in the clinic the number of recording locations is limited by the catheter used, its manual manipulation around the ventricles and the allocated procedure time. In addition, due to the available access via the femoral artery, data are only recorded from the endocardial surface of the ventricles. It remains to be seen how both the low resolution, and endocardial recording of data in the clinic affects the result of the RVI, particularly in hearts with varying scar locations and geometries. Also difficult to quantify in the clinical study is the accuracy and specificity of the RVI with respect to locating the critical region of the scar. Although the clinical study provided initial validation of the RVI-guided ablation procedure, further validation and investigation into the methodology is required.

The following study implements the RVI method in 3D ventricular models with varying MI scar geometries to provide further validation of the technique. Utilising a FE geometrical model provides the opportunity to investigate the effects of varying data resolution on the result of the RVI by comparing RVI maps generated using data sampled at varying resolutions. Moreover, in the computational models, data are generated across the entire ventricular myocardium including throughout the 3D ventricular wall and on the epicardial surface. As such, it is possible to calculate the RVI throughout the 3D model and observe how 3D RVI maps differ from endocardial RVI maps produced according to the clinical protocol. We investigate the application of the RVI method to guide the ablation procedure in varying geometries and observe the accuracy of the RVI map and the resulting wave propagation post-modelling of the ablation procedure. This investigation is vital in order to further validate the clinical method, thoroughly investigate its application to guide the ablation procedure and to suggest potential limitations of the clinical protocol.

In this chapter, we incorporate idealised scars into a 3D rabbit ventricular geometry and simulate wave propagation across the model. The resulting *in silico* data are utilised in the RVI calculation to produce 3D RVI maps. The ablation procedure is modelled by creating non-conducting ablation lesions in the model in regions where RVI is less than a threshold value. Clinical data sampling methods are replicated, sampling data from only the endocardial surface and decreasing the resolution of the data utilised in the calculation. The ablation procedure is also modelled utilising the RVI maps produced from endocardial, low resolution data to replicate clinical procedure. For the purposes of investigating how the location of the scar within the myocardial wall affects the result of the RVI, we create a series of simple 3D models with idealised scars located at increasing

depths beneath the surface and calculate RVI maps on the surface of the model.

6.2 Validation of the RVI Methodology in Ventricular Models

6.2.1 Ventricular Rabbit Model

Simulations in this chapter were conducted on an anatomically accurate 3D model of the rabbit ventricles (Deo et al., 2009) described previously (Section 3.5), in order to reduce the computational demand compared to that required by an equivalent human model. The similarities in the effective size of the heart between the human and rabbit as previously shown by Panfilov (2006) and in Chapter 4 suggests that wave propagation and reentry dynamics are similar in both species due to the size of the activation wavelength in comparison to the size of the tissue. Hence, due to these similarities and considering the computational demands of the two models, we chose to study the RVI using a 3D model of rabbit ventricles, scaling experimentally derived conductivity values (Clerc, 1976) in order to produce a wavelength which would produce a similar effective size to that of the human. We were confident that the model used in this study, with the scaled conductivity values, would produce similar RVI results as would be expected in the human, that it would replicate the arrhythmia dynamics in the human and that it provided sufficient complexitity to answer the questions posed whilst being computationally efficient. Simulations run on the model could be performed on a PC in an acceptable time frame (approximately three hours) and without large data storage requirements (data files were approximately 2GB).

It is also important to consider that the RVI algorithm is not species specific. It is a metric based on ATs and RTs around a region of MI scar tissue. In fact, it has rececntly been shown that the RVI algorithm performed in the human, pig and sheep maintains the ability to locate regions of tissue susceptible to reentry irrespective of species differences in wave propagation that may occur (Child et al., 2015). Whilst it is necessary to replicate propagation dynamics in the human in order to investigate how clinical methodologies affect the RVI, the calculation maintains its ability to identify regions susceptible to reentry in different species.

6.2.2 Incorportaing Infarct Scars into the 3D Model

Idealised representations of scar and surrounding BZ were incorporated into the 3D model of rabbit ventricles in three different orientations. The conformation of the 3D scar region used throughout this chapter is based on the scar geometry that was utilised in the 2D study in Chapter 5. The scar geometries are based on a previously proposed reentrant circuit mechanism (Stevenson, 2009) and incorporate regions of non-conducting fibrotic tissue interspersed with a conducting BZ isthmus. This highly simplified geometry is used for the purposes of thoroughly investigating the RVI result in a 3D model, in the absence of additional complexity as would occur *in vivo*. The scar regions introduced into the 3D model incorporate two ellipsoid scar-like objects separated by a cuboid slow conducting isthmus (BZ_{cond}) and a cuboid region of slow conduction and lengthened APD (BZ_{APD}). The lengthened APD was located towards the exit site end of the isthmus as it has been observed that functional block occurs at only a specific site and not throughout the BZ region (Segal et al., 2010). The resulting anatomical models were utilised throughout this study in order to simulate ischemic heart disease and produce reentry in the model. Varying the location of the scar region establishes whether the RVI method was able to identify the critical isthmus, irrespective of the location of the scar around the myocardial wall and the depth of the scar region below the endocardial surface.

Regions of scar were modelled as non-conducting tissue and were incorporated into the model by defining the 3D coordinates of the centres of each ellipsoid scar ($centre_x$, $centre_y$, $centre_z$). Radii ($r_x,\ r_y,\ r_z$) were specified and each ellipsoid was calculated using the Equation 6.1

$$\frac{(X - centre_x)^2}{{r_x}^2} + \frac{(Y - centre_y)^2}{{r_y}^2} + \frac{(Z - centre_z)^2}{{r_z}^2} = 1 \tag{6.1}$$

where $X,\ Y,\ Z$ are x,y,z coordinates of all nodes within the model. Coordinates of the centroids of elements in the model were calculated and if any centroid in the model laid within the bounds of either ellipsoid (ie. Equation 6.1 $<= 1$), the corresponding element was tagged with a number which would define scar in the simulation.

In a similar manner, BZ was created by defining central coordinates of each BZ region and forming a cuboid around them by extending x, y and z mm in x, y and z directions. Elements whose corresponding centroids fell within the cuboid region were tagged with different numbers depending on whether they were included in the BZ_{APD} or BZ_{cond}

regions. The tags allowed for the subsequent assignment of unique parameters to each BZ region.

In each geometrical model the diameters of the ellipsoid scar regions were 6mm x 4mm x 3mm, the BZ_{cond} was 3mm x 3mm x 2mm and the BZ_{APD} was 4.5mm x 3.5mm x 2mm. The apical-basal length of the scar complex covered slightly less than a third of the length of the ventricles and the lateral width of the complex also spanned approximately a third of the width of the heart at the base. The depth of the scar measures 4mm which approximates to the depth of the interventricular septum measured at the base, although the amount of penetration of the scar complex within the myocardial wall depends on its location. In patients displaying VT, the size of the scar is documented to cover approximately $12 \pm 7\%$ of the ventricles (Alexandre et al., 2014), however the size of MI scars is highly variable due to the severity and duration of the ischemia, and the time elapsed and degree of healing of fibrosis since the MI. Based on approximate volumetric comparisons, the size of the scar incorporated into the rabbit model is approximately 10% of the ventricular model which is comparable to the reported size of MI scars in patients displaying VT.

Figure 6.2 displays 3 different models, the anterior LV transmural scar (AntLV_{trans}), the interventricular septum transmural scar (IV_{trans}) and the posterior LV endocardial scar (PostLV_{endo}), with the scar region located at varying sites across the ventricles, from an epicardial (*left*), a transmural (*middle*) and an endocardial (*right*) view. The scar is displayed in *black*, the BZ_{APD} in *red* and the BZ_{cond} in *blue*.

LV Transmural Scar

The scar and BZ protrude slightly from the epicardium in the AntLV_{trans} model (Figure 6.2 (*top*)) and span most of the LV wall with only the BZ extending to the endocardial surface. The scar is located on the anterior LV wall, roughly midway between the apex and base. Closest to the apex of the heart is the BZ_{APD} (red).

Interventricular Septum Transmural Scar

Panels in the *middle* row of Figure 6.2 show the IV_{trans} model with the scar region located on the interventricular septum, in the middle of the heart in the apex-base direction. The scar protrudes slightly at both surfaces of the myocardium, again with the BZ_{APD} located closest to the apex.

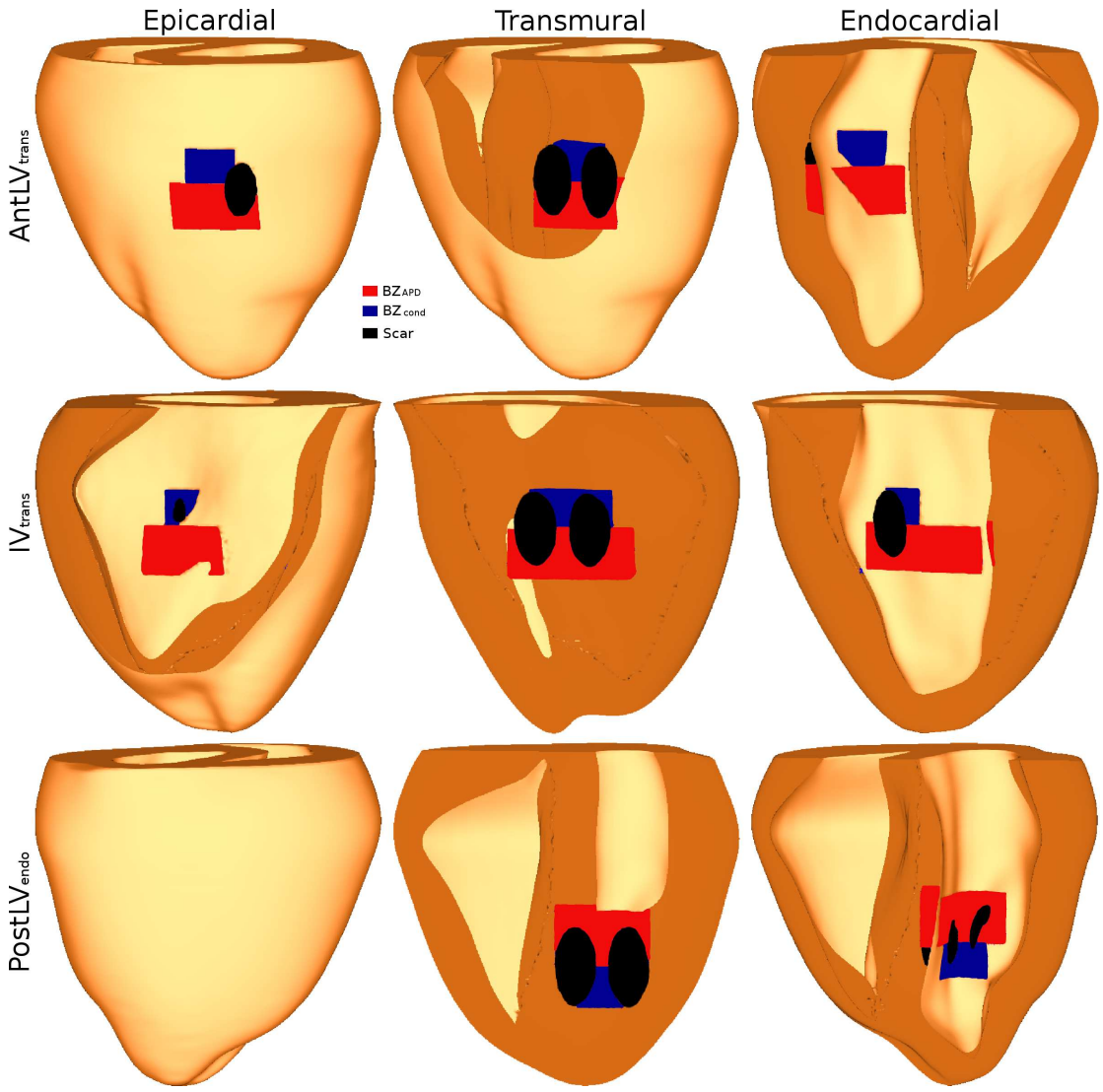

Figure 6.2: 3D models with incorporated scar and BZ regions. Scars are displayed from different angles; *left* - epicardial, *middle* - transmural and *right* - endocardial.

LV Endocardial Scar

The scar region in the final model, the posterior LV endocardial model (PostLV_{endo}) (Figure 6.2 (*bottom*)) is located towards the apex at the junction between the LV posterior wall and the interventricular septum. As can be seen in the figure, the BZ_{APD} (*red*) is located nearer the base of the heart, contrary to the location of the BZ_{APD} in the other two models. This geometry is also unique as the scar region is incorporated on the endocardial surface and extends transmurally to roughly half the depth of the wall so there is no protrusion of the scar region at the epicardium.

6.2.3 Simulation of Electrical Activation

Simulations were run in CARP (Section 2.5) using the previously described computational set-up (Section 4.2). The Mahajan et al. (2008) rabbit model of ventricular AP was used to model the electrophysiology in the healthy tissue. Anisotropic conductivity values were assigned to the model's existing fibre architecture. In order to be able to sustain reentry, and in accordance with previous studies (Li et al., 2009; Ripplinger et al., 2009; Rantner et al., 2012), conductivity was reduced in the healthy tissue, replicating a 25% slowing of conduction velocity to reduce the activation wavelength of the rabbit model, mimicking the effective size of the human heart.

Modelling BZ Tissue

Ionic changes in the BZ_{APD} were based on previously described methods of modelling BZ changes in rabbit, human and canine models (Decker and Rudy, 2010; McDowell et al., 2011; Rantner et al., 2012; Ashikaga et al., 2013) where the maximal conductance value of I_{Na} was reduced to 70% of normal, I_{Kr} to 30% and I_{Ks} to 5% and the strength of I_{CaL} flux was increased to 150% of normal. Figure 6.3 displays APs for both healthy ($left$)

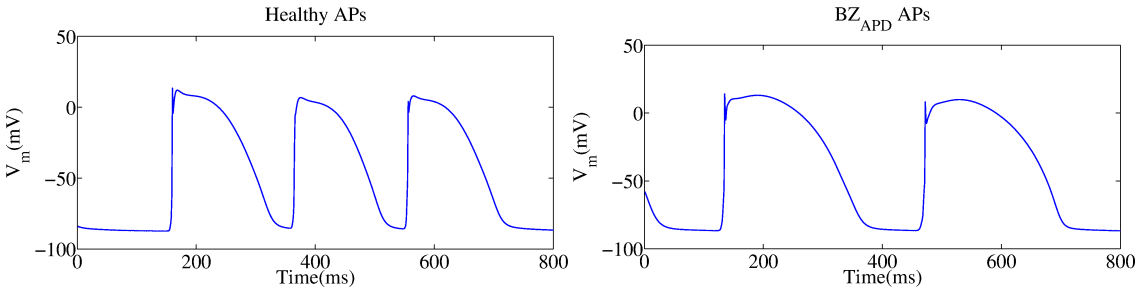

Figure 6.3: APs produced from simulations in the 3D geometry using a model of rabbit electrophysiology. $Left$ - AP from healthy tissue. *Right* - AP from BZ_{APD}.

and BZ_{APD} tissue (*right*). The APD in the healthy tissue measures approximately 170ms compared to the APD in the BZ_{APD} measuring approximately 230ms.

Conductivities in both the BZ_{cond} and BZ_{APD} regions were decreased to model the CV slowing observed in BZ tissue (Luke and Saffitz, 1991). Conductivities were reduced by 30% compared to healthy tissue, a protocol which has previously been utilised to model BZ conductivity remodelling in rabbit, human and canine studies (Decker and Rudy, 2010; McDowell et al., 2011; Rantner et al., 2012; Ashikaga et al., 2013).

Although the geometry and size of the scar regions incorporated in to the rabbit model

and the ionic and conductivity parameters used in this study were motivated in part by previous studies and clinical observations, the choices were also made to ensure that the model produced reentry. The present study of quantifying the likelihood of reentry in structural heart disease requires that the models used here are able to sustain a figure-of-eight reentrant circuit around the scar region as occurs in patients with a history of MI. The two non-conducting fibrotic scars separated by a conducting isthmus and the altered BZ_{APD} and BZ_{cond} parameters ensured that the model displayed the required figure-of-eight reentry with propagation through the BZ isthmus.

Implementing the S1S2 Pacing Protocol

The heart was paced at the apex, with a strength of 400μA for a duration of 3ms in all simulations. Cell models were pre-conditioned to reach a steady state by pacing the models at 340ms, a frequency slighty faster than sinus rhythm (400ms), for 10 beats. The S1S2 protocol was then implemented with the S2 beat being initiated 200ms after S1 for both AntLV$_{trans}$ and IV$_{trans}$ models and 190ms for the PostLV$_{endo}$ model in order to produce reentry. Reentry was defined as an episode in which the wavefront blocked at the BZ_{APD}, circumvented the scar region, returned to the region of initial block and continued propagation (as shown in Figure 6.4).

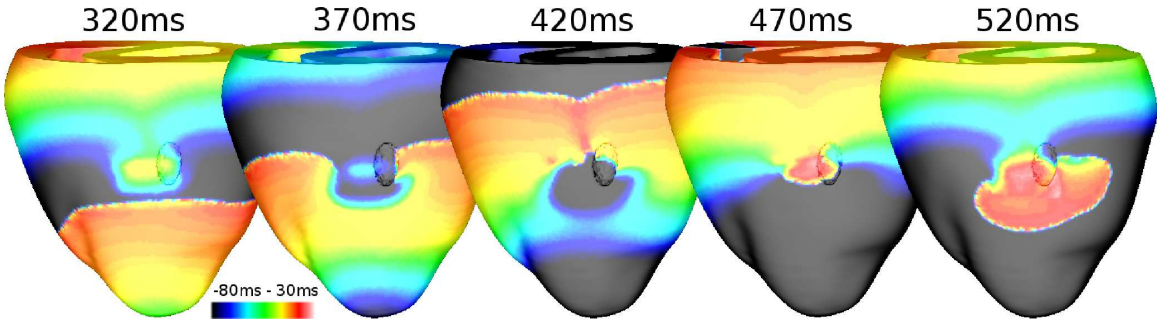

Figure 6.4: Time series of electrical activation illustrating reentry. Times are stated above. Wavefront of S2 is blocked by delayed S1 repolarisation in the BZ (T = 320ms). The wavefront of S2 travels around the region of block and scar tissue (T = 370ms) and propagates back through the isthmus (T = 470ms). Reentry is defined as occuring when the activation wave propagates out of the exit site of the scar, past the point of initial wave block (T = 520ms).

6.2.4 Calculating the RVI in 3D Models

The principles of calculating the RVI are similar to that described in the 2D model in the previous chapter. Initially, ATs and RTs are calculated at each node in the model to provide the data used in the RVI calculation. The calculation is performed using AT and RT data from two nodes in the model to determine the extent of the excitable gap between the nodes. The RVI values calculated between node pairs are then plotted at a midpoint between the node pair to create a spatial map of RVIs across the tissue.

Data Acquisition

ATs and RTs were calculated at each node for only the S2 beat using a linear interpolation algorithm to find the time points at which V_m crosses -40mV on the upstroke and -70mV during the repolarisation phase respectively, and the APDs were calculated by subtracting the AT from the RT at each node. The data from a particular node were only utilised in the RVI calculation if the APD was shorter than 250ms, a plausible APD length. Very long APDs can occur at the border of the fibrotic scar region, due to the wavefront anchoring around the scar. As the wave propagates around the non-conducting scar, the lack of an electrical sink causes the prolongation of the APD. In fact, in the clinic, low amplitude electrograms sometimes displaying long APDs may be recorded from dense fibrotic regions within the scar. If this occurs, data displaying long APDs or low amplitude electrograms are not used in the calculation of the RVI (Child et al., 2015) in order for the RVI result not to be affected by such data. Hence, data with long APDs in the vicinity of the scar are discounted here.

Determining Node Pairs

The RVI is calculated between pairs of nodes throughout the model in order to calculate the excitable gap, the RVI, between each node pair. The following section describes the method of determining the calculation node pairs.

As described in Section 5.2, it is essential that the calculation node pair lie within close proximitiy of each other. The RVI algorithm calculates a time difference between the wave tail (RT) and the wave head (AT) in a reentrant circuit. If the RT and AT are sampled within close proximity of each other, it is accepted that the time difference between the wave head and tail, calculated by the RVI, can infer whether or not reentry can occur.

However, if the RT and AT are sampled from two points which are far apart, the calculated time difference between the wave head and tail becomes meaningless. Consider that the RT and AT of an excitation wave are sampled from two points which are located some distance away from each other. The AT sampled at $node_i$ occurs before the RT sampled at $node_j$ suggesting that the wavefront would be blocked by the wave tail. However, the wave continues to propagate towards $node_j$ from which the RT is sampled and by the time the wavefront reaches $node_j$, the tissue here has in fact had sufficient time to repolarise and so the wavefront can propagate and reenter. Hence, it is necessary to sample points which lie within close proximity to each other.

Node pairs are defined from within a spatial radius, r_s in order to ensure that the AT and RT data are within a short distance of each other, as in the protocol described in Section 5.2. Due to the large number of nodes in the 3D model, previous methods of creating r_s based on distances between Cartesian coordinates proved too computationally demanding and so an alternative method was used. A 3D grid of 0.1mm resolution was imposed over the nodes of the 3D ventricular model. For each subsequent node in the model ($node_i$), nodes within a certain distance are found by extending 1000 voxels in each dimension from $node_i$. It is determined whether the nodes within this boundary are downstream nodes (activated after $node_i$) and if they are, they are deemed $node_j$.

The RVI Equation

The RVI calculation is performed as described in Section 5.2. In short, each $node_i$ forms a calculation node pair with multiple $node_j$, as $node_j$ is defined as any downstream node which falls within r_s of $node_i$. The RVI calculation is performed between $node_i$ and each $node_j$ and in turn, the calculation is repeated for each $node_i$ in the model, according to Equation 5.3. The RVI calculation subtracts the AT from $node_j$ from the RT of $node_i$ in order to calculate the excitable gap.

Plotting the RVI Results on the 3D Model

The 3D grid is also utilised in determing a spatial midpoint between node pairs for the purposes of plotting the RVI. A grid voxel at the midpoint between nodes i and j is determined. If the voxel contains a node, the RVI is stored on that node. If the voxel contains no node point, the RVI is stored on a node within the next nearest voxel which contains a node. An average of RVI values stored on each node is taken to produce the

RVI map.

6.2.5 Results of the RVI in 3D Models

Simulations using each 3D model produced reentry as can be seen from the time series images in Figure 6.5. The series diplays the wavefront of the S2 beat being blocked by the BZ_{APD} which has not had time to repolarise because of its altered ionic current properties ($T1$). Due to this region of block, the wavefront is diverted around the scar ($T2$ and $T3$) and propagates through the isthmus, contrary to the direction of the wavefront which had emanated from the pacing location (apex) ($T4$). Slow conductivity in the BZ_{cond} causes the wavefront to propagate slowly through the isthmus and so as the wavefront reaches the exit point of the scar, the tissue at the exit site has had time to repolarise and is ready for reactivation. This phenomenon allows the wave to propagate out of the scar region and form a reentrant wave ($T5$).

The AT and RT maps reiterate that the propagation wave is able to form a reentrant circuit. The region prior to the initial block displays a low RT (*dark blue*) of around 400ms and the region which caused the initial wave block displays a high AT (*red*) of around 500ms, due to the circumnavigation of the wave around the scar before activation. Implementing the RVI calculation (RVI = RT - AT) at this region gives 400ms - 500ms = -100ms. This suggests that there is an excitable gap of 100ms, easily facilitating reentrant wave propagation. The RVI map indicates that this is the case as low RVI values (*dark blue*) occur in the same region, the region of initial block.

The magnitude of the RVI, although low, does not directly correspond to the speculative calculation described giving an RVI of -100ms, instead the map shows an RVI of around 0ms in the same region. This result is a consequence of the methodology of plotting the RVI. An average of the RVI values that had been associated with their corresponding midpoints was taken, resulting in an average RVI being displayed which incorporates AT and RT data from the immediate area either side of the line of block, in addition to AT and RT data from elsewhere in the model with a midpoint in the region of interest. Averaging the RVI in this manner produces the effect of lessening the magnitude of the low RVI in the critical region. However, the region at the exit point of the scar, the region of initial block is still accurately identified by a specific area displaying RVI values considerably lower than the remainder of the model. Moreover, this ability of the RVI to locate a region of interest occurs in each of the 3D geometries suggesting that the algorithm works

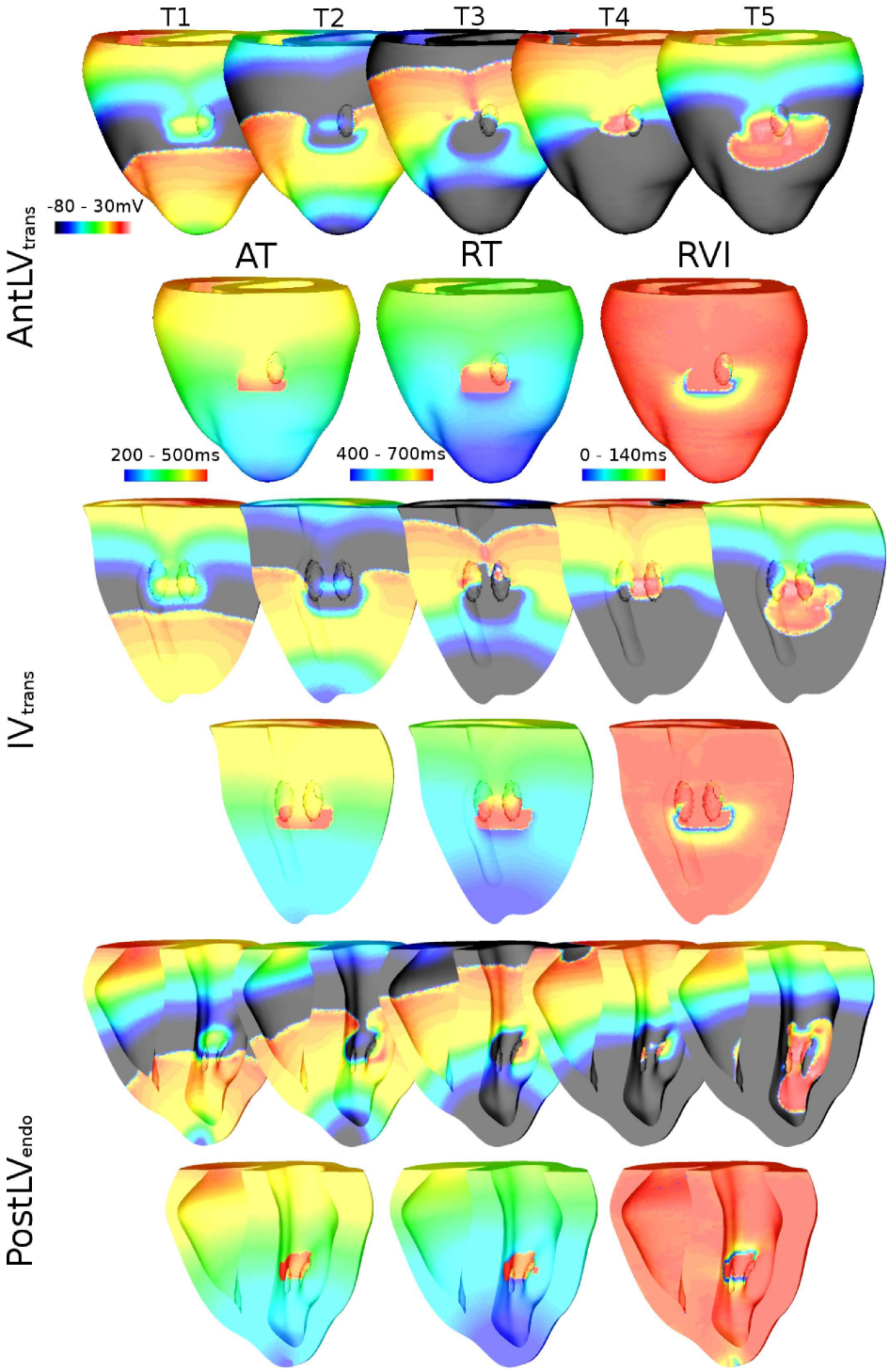

Figure 6.5: Results of the RVI protocol producing UDB in three, 3D geometries. For each geometry; five top-most images - Time sequence displaying S2 propagation wave approaching ($T1$) and blocking ($T2$) at the line of heterogeneity, circumventing the scar regions ($T3$), entering the isthmus ($T4$) and reentering ($T5$). Three bottom-most images - Corresponding AT, RT and RVI maps.

independent of scar location in the heart and depth within the myocardial wall.

The RVI calculation, implemented in a 3D model, displays a very similar result to that which occurs in 2D simulations and analysis, confirming the validity of the fundamental concepts of the RVI due to the result remaining consistent in varying 2D and 3D models. In addition, the result of the RVI calculated in 3D suggests that the method is able to accurately locate regions susceptible to reentry which could prove important for future clinical applications.

An interesting finding appears when the scale of the RVI maps are optimised to show the whole range of data within the map as shown in Figure 6.6. In addition to the region

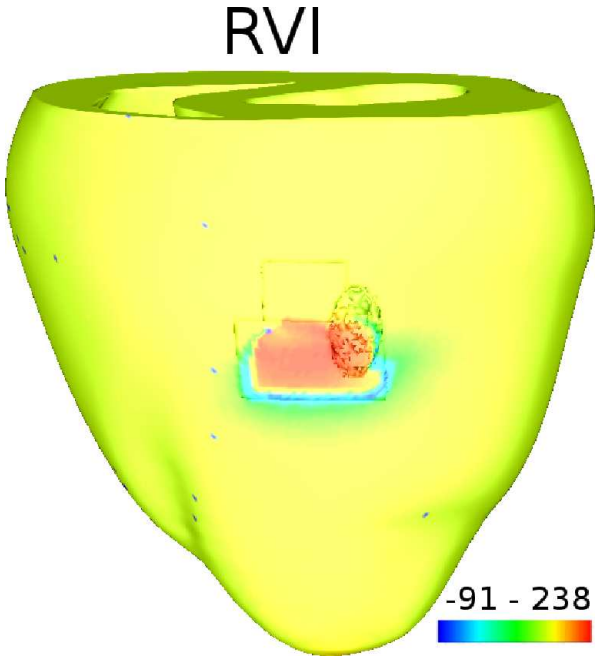

Figure 6.6: RVI map displayed with optimised scale.

of low RVI, apparent in the image as a region of *light blue* beneath the scar, is a relatively large region of high RVI (∼200ms). A high RVI value is produced by subtracting a small AT from a large RT. Referring to Figure 6.5 ($AntLV_{trans}$ (AT and RT maps)), it might be considered that a high RVI value could be produced by subtracting an AT from the *light blue* region just below the line of block (300ms) from an RT from the *red* region just above the line of block (700ms). Indeed, $700 - 300$ produces $RVI = 400$ms. This value of RVI is in excess of the highest value seen in the RVI map in Figure 6.6, but additionally this described scenario could not contribute to the high RVI value because $node_i$ (RT data node) must be activated before $node_j$ (AT data node); not the case in this scenario. Considering the *red* regions in the AT and RT maps in Figure 6.5, they

correspond to the location of the BZ_{APD}, a region of lengthened APD. It is in fact an RVI produced by subtracting an AT from the bottom of the *red* region (500ms) from an RT at the top of the *red* region (700ms), which constitutes the region of high RVI in Figure 6.6 (200ms). Notably, the value of high RVI in the region (∼230ms) is comparable to the APD in the region due to the fact that the RVI is calculated over a small distance where normal wave propagation occurs. This results in the ATs and RTs of the region remaining relatively consistent and therefore RVI ≈ APD ($RT - AT$). In fact, where normal wave propagation occurs over a small distance regardless of the location within the tissue, RVI ≈ APD. Due to the lengthened APD in BZ_{APD}, the RVI produced in this region is larger than in the rest of the tissue which displays a shorter APD. Whilst it is understood that these regions of high RVI which border the region of low RVI are produced as an approximation of the APD, it is possible that the high RVI values may interfere with clinical analysis, particularly in cases where data resolution is decreased.

6.3 Utilisation of the RVI Map to Guide the Ablation Procedure

6.3.1 Creating an Ablation Model

Modelling the ablation procedure in 3D was conducted on the AntLV$_{trans}$ model. Using the previously produced RVI map, all values of RVI below a threshold value were considered ablation targets. In practice, the elements of the model whose connected nodes all displayed an RVI of less than the threshold value were designated as ablation scars. Figure 6.7 shows on the $left$, an element whose nodes all display an RVI less than the threshold (*blue*) and so the properties of that element would be altered to create a non-conducting ablation scar by assigning no fibre direction to the element. On the *right* hand side of the figure, 3 out of the 4 nodes display an RVI less than the threshold (*blue*), but one has an RVI which is greater than the threshold (*red*) and so this element is not 'ablated'; its ionic and conductivity properties remain the same.

A parameter sensitivity analysis of threshold values was conducted for the purposes of determining a threshold limit that would terminate a reentrant circuit. The area of the resulting ablation lesion was calculated for each model.

Figure 6.8 displays RVI maps (*top*), at cross sections throughout the myocardium, highlighting RVI below a threshold (30ms on the $left$, 40ms on the *right*) apparent as a

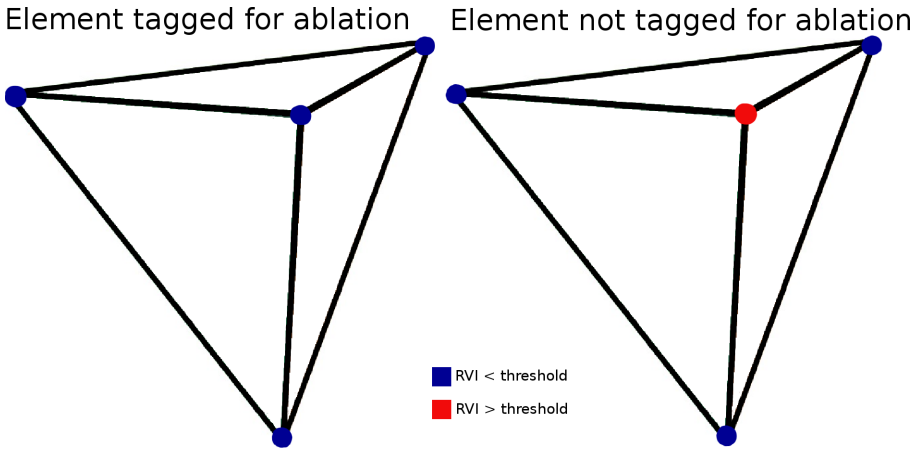

Figure 6.7: Methodology for creating an ablation model. Element on $left$ is a target for ablation (all nodes have RVI < threshold (*blue*)). Element on *right* is not a target for ablation as one node has RVI > threshold (*red*).

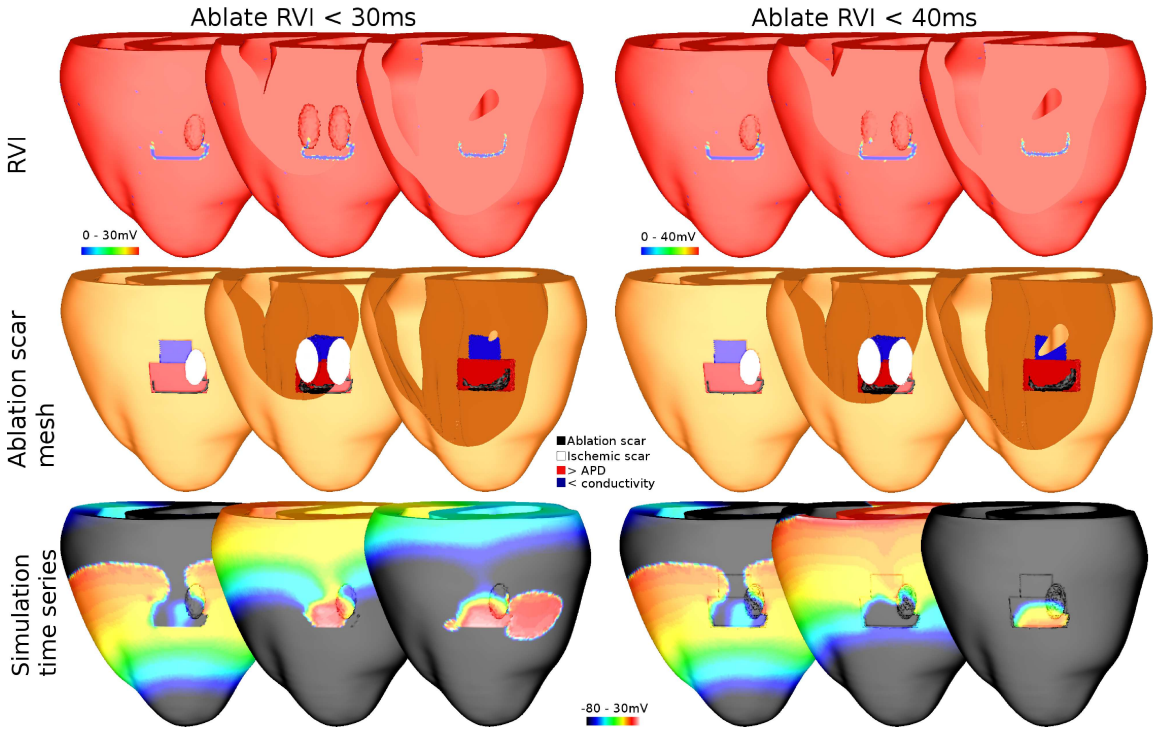

Figure 6.8: Modelling the ablation procedure, guided by the RVI. $Left$ - ablation of the myocardium where RVI < 30ms. *Right* - ablation of the myocardium where RVI < 40ms. *Top* - RVI maps at sections through the myocardium, displaying regions below threshold. *Middle* - sections through the model resulting from ablation of regions below threshold. *Bottom* - time series displaying wave propagation in a simulation using the ablation model.

blue region just below the scar. It is evident that the maps resulting from the detection of the 2 different threshold values are very similar; the area of RVI less than each threshold value is virtually the same. In fact, the percentage of the mesh with an RVI less than 30ms

is 0.12% and the percentage of the mesh with an RVI less than 40ms is 0.15%. The areas less than the respective threshold values (*blue* on the RVI map) were then established as non-conducting regions to model an ablation lesion. These geometrical ablation models can be seen in the second row of Figure 6.8 in which cross sections across the myocardium are displayed. Again, the resulting geometrical models appear very similar.

Simulations modelling the ablation procedure were conducted on the geometrical models including the ablation scars using the protocol previously described (Section 6.2) because of its known ability to elicit reentry. The model was paced from the apex to a steady state at a BCL of 340ms for 10 beats, before proceeding with the S1S2 protocol paced at 200ms.

6.3.2 Wave Propagation Post-Ablation

The RVI algorithm specifically highlights the critical region with low values of RVI and the validity of the algorithm to detect these regions is emphasised by the success of modelling ablation guided by the RVI map. Despite the ablation models appearing very similar in terms of lesion size and location, the result of the simulation run on the respective models is very different. Ablating the region of RVI below 30ms still elicits a reentrant wave due to the wavefront propagating out of a gap between the scar and ablation lesion (Figure 6.8, *bottom*, $left$). This gap is not present when all regions of the model with an RVI below 40ms is ablated and so the wave terminates at the lesion and halts the reentrant wave pattern (*bottom*, $right$).

This study substantiates the result observed in the clinic, that the ablation procedure can be informed by the result of the RVI algorithm. The RVI locates, accurately enough, a region susceptible to reentry so that an ablation lesion created at that area is able to terminate post-MI reentry. In the clinic, the ablation lesions created by radiofrequency catheter ablation are much larger and all tissue within a certain radius of the ablation catheter is ablated. However here, we aim to determine the accuracy of the RVI algorithm in ablating the VT circuit. Therefore we investigate the minimum size of the ablation lesion necessary to terminate the arrhythmia by only ablating a very specific region of tissue which displays an RVI less than a threshold value. Such small ablation lesions are unable to be produced in the clinic due to the nature of the ablation catheters but the technique applied in these models can illustrate the accuracy of the RVI algorithm in guiding the ablation procedure.

6.4 Modelling the Clinical Application of the RVI Methodology

The clinical method differs from the method of calculating RVI in the 3D model in this study in two major ways. Firstly, clinical AT and RT data are only obtained at the endocardial surface. In addition, ablation catheters which administer the radiofrequency to produce an ablation lesion, ablate the tissue from only the endocardium. Secondly, the quantity of AT and RT data is greatly reduced (Child et al., 2015). In order to validate the use of the methodology in the clinic and to understand its potential drawbacks, the clinical method is replicated in the model here.

6.4.1 Creating an Endocardial RVI map

Clinical RVI analysis only takes into account data from endocardial nodes because electrophysiological data from catheter recordings are only acquired there and hence, the RVI is only calculated and plotted on the endocardium. In order to obtain data only from the endocardial surface, a list of all LV endocardial nodes is obtained, discounting those which pertain to endocardial scar. Only AT and RT data from the LV endocardial nodes and their coordinates are used in further analysis.

In this analysis the AntLV_{trans} and the PostLV_{endo} models were used. Simulations run previously for 3D analysis (Section 6.2) provided AT and RT data, and RVI analysis proceeded as described in the 2D RVI analysis (Section 5.2) due to the vastly reduced number of calculation nodes.

At each $node_i$ on the endocardium, endocardial nodes within a 5mm radius (in 3D space) of $node_i$ were identified to match the clinical approach (Child et al., 2015). Of those nodes within the sphere, downstream endocardial nodes (those activated after $node_i$ on the S2 beat) were found and denoted $node_j$. The RVI was calculated between the RT at $node_i$ and the AT of each $node_j$ individually. In order to plot the RVI on the endocardial surface, a midpoint between the two calculation nodes was determined and the RVI plotted on the nearest node to the midpoint. An average of RVI on each node was then taken and these data were used to produce the RVI map.

6.4.2 Endocardial RVI Maps

Due to the relatively small amount of data on the endocardial surface being analysed in this study, the resulting RVI map displayed nodes which had no RVI result associated with them because the node was never indicated as a midpoint between calculation nodes. This can be seen in Figure 6.9 where, on the *left* hand side, small specks of *dark blue*

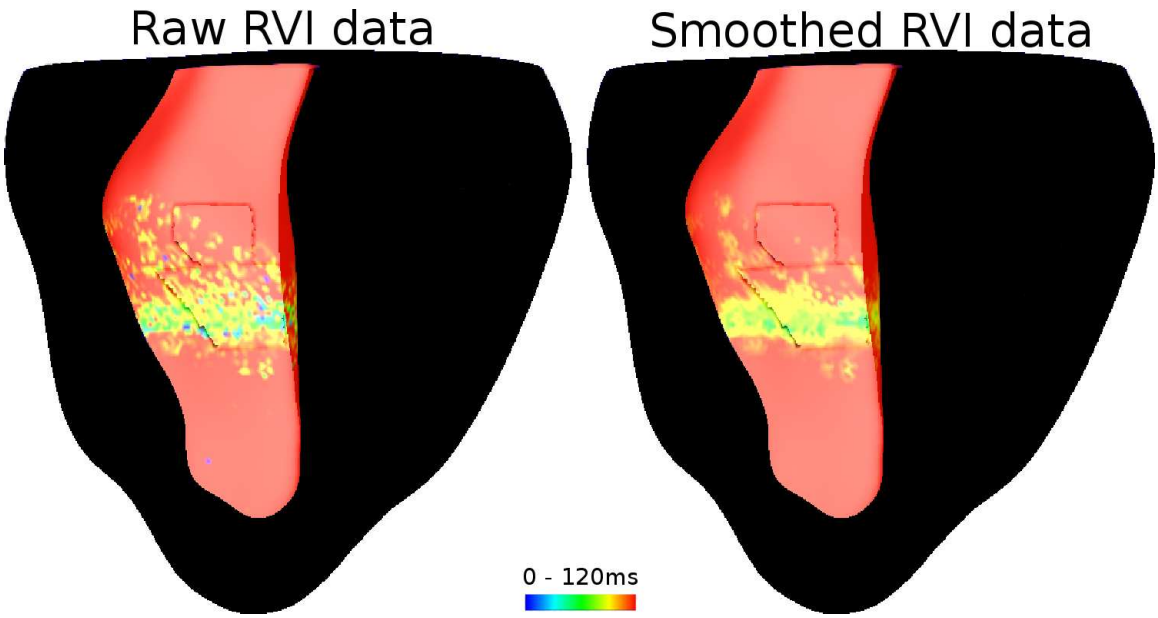

Figure 6.9: Smoothing the RVI result. *Left* - non smoothed RVI map. *Right* - smoothed RVI map.

appear throughout the model. Approximately 10 nodes out of 13000 non-scar endocardial nodes in the model displayed no RVI result. In addition, the RVI did not appear to be smooth as seen in the full 3D analysis but rather that low RVI, although clustered around the exit point of the scar, appeared sporadically in the model (*left*) because less data were averaged to produce a smooth RVI map. For the purposes of presenting a more coherent result, an additional analysis step was required to smooth the data, the result of which is presented on the *right* hand side of the figure. To ensure all endocardial nodes display RVI data, nodes with no associated RVI value were found and for each of these nodes, an average of the RVI data from their element-connected nodes was taken and the average, plotted on the node in question. In order to smooth all RVI data across the endocardial surface, a similar technique was utilised. For each node on the endocardium, an average of its element-connected nodes was taken and the average stored on that node. This step was included in all further endocardial RVI analysis.

Figure 6.10 displays the AT and RT maps (*first* and *second* images) of the data on

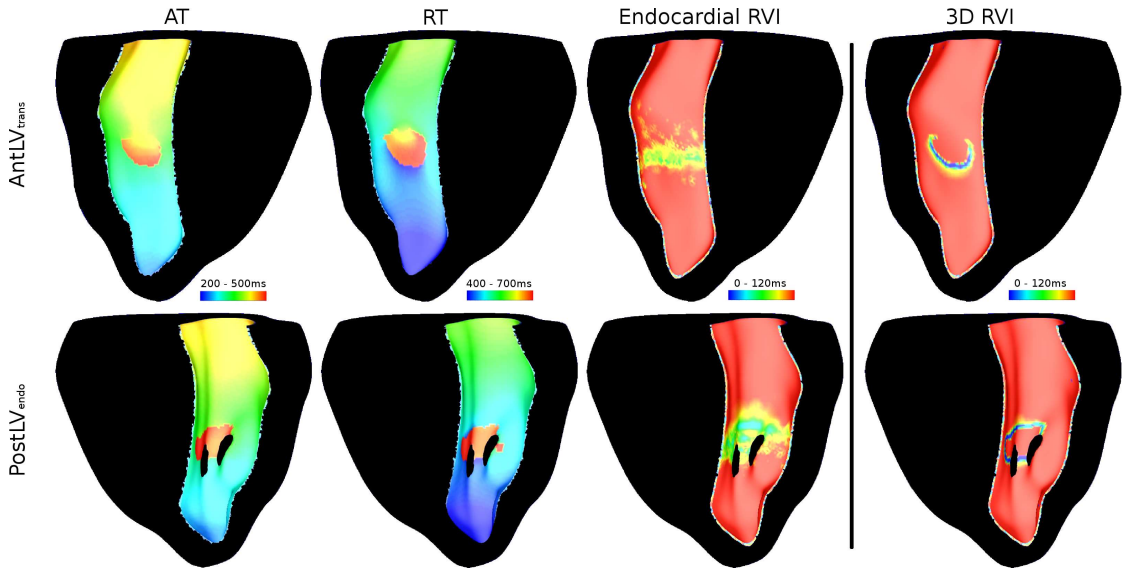

Figure 6.10: Endocardial RVI produced from endocardial data for the 3D models: *top* - AntLV$_{trans}$, *bottom* - PostLV$_{endo}$. *Left* and *Middle* - endocardial AT and RT maps respectively. Two right-most images compare the endocardial RVI map produced by endocardial data and the RVI map produced by complete 3D data with only the endocardial surface displayed.

only the endocardial surface of the AntLV$_{trans}$ (*top*) and the PostLV$_{endo}$ (*bottom*) models. Again, it is possible to see from the AT maps illustrating the wave block and subsequent circumnavigation of the scar, that wave block occurs shown by the sharp delineation between a relatively short AT and a long AT. The RT maps show the BZ_{APD} with colours in the *red* spectrum denoting a long APD which causes the initial wave block and contributes to the low values of RVI around the region of block which can be seen in the RVI maps (*third* image).

For comparison, the endocardial RVI map (*third* image) and the 3D RVI map (*fourth* image) are shown side-by-side. It is evident that the region of low RVI in the endocardial RVI map is considerably more dispersed and less negative than can be seen in the 3D RVI map. There are considerably less data used in the calculation of the endocardial RVI map which produces a less accurate result. However, it is still possible to identify a region of RVI that is lower than that of the rest of the model and identify this as a critical region.

Interestingly, the region of interest in the endocardial RVI map of the PostLV$_{endo}$ model, whilst still being diffuse, seems to be more accurate and displays lower RVI values than the RVI map of the AntLV$_{trans}$ model. Of note in this case, is the fact that the scar region protrudes from the endocardial surface of the PostLV$_{endo}$ model whereas the

scar region of the AntLV$_{trans}$ model is transmural. This disparity between the results of the two models leads to an important conclusion; that the depth of the scar within the myocardium, and more specifically, the depth at which the critical site of initial block occurs, may well affect the accuracy of the RVI algorithm.

6.4.3 Guiding Ablation Utilising an Endocardial Map of the RVI

Creating Ablation Lesions

Nodes on the endocardial surface which display an RVI less than a threshold value are targets for ablation. However, the ablation lesion must penetrate into the 3D model in order to replicate the clinical procedure and for successful termination of a reentrant circuit. Here, contrary to the protocol described in the previous section, we model the clinical ablation protocol in which tissue within a radius of a region of low RVI on the endocardium is ablated.

After determining an area of RVI below a threshold value on an endocardial RVI map, a centre point of the region was determined by estimating its location and the coordinates obtained. Nodes on the endocardium, within a radius of 2.25mm of the centre point which display an RVI less than the threshold value were determined. A lesion with a radius of 2.25mm was chosen by scaling the size of ablation lesions created in a human heart, to the size of the rabbit heart. The myocardial wall in the human, measures approximately 14mm from the endocardium to the epicardium (Ho, 2009) and ablation lesions created in patients measure approximately 7mm, half the depth of the myocardium (Lai et al., 2004). The rabbit myocardial wall is approximately 4.45mm thick (Mahaffey et al., 1995) and so we assumed the lesion size in the rabbit to measure half of the depth of the rabbit myocardial wall. For each of these specified nodes, the surrounding nodes in a 3D radius of either 2.25mm or 5mm were found and each element containing that node was tagged to identify it in order to be able to assign non-conducting tissue properties to the element for the purposes of modelling an ablation lesion. Parameter sensitivity analyses were conducted to determine the threshold values.

The Success of the Ablation Procedure

It was predicted that using the endocardial RVI to guide the modelled ablation procedure may be less successful than using the whole 3D RVI map due to the lack of accuracy of the

endocardial analysis. It can be seen from the endocardial RVI maps (*left*) in Figure 6.11 that setting a threshold value of RVI less than 60ms defines a very small portion of the

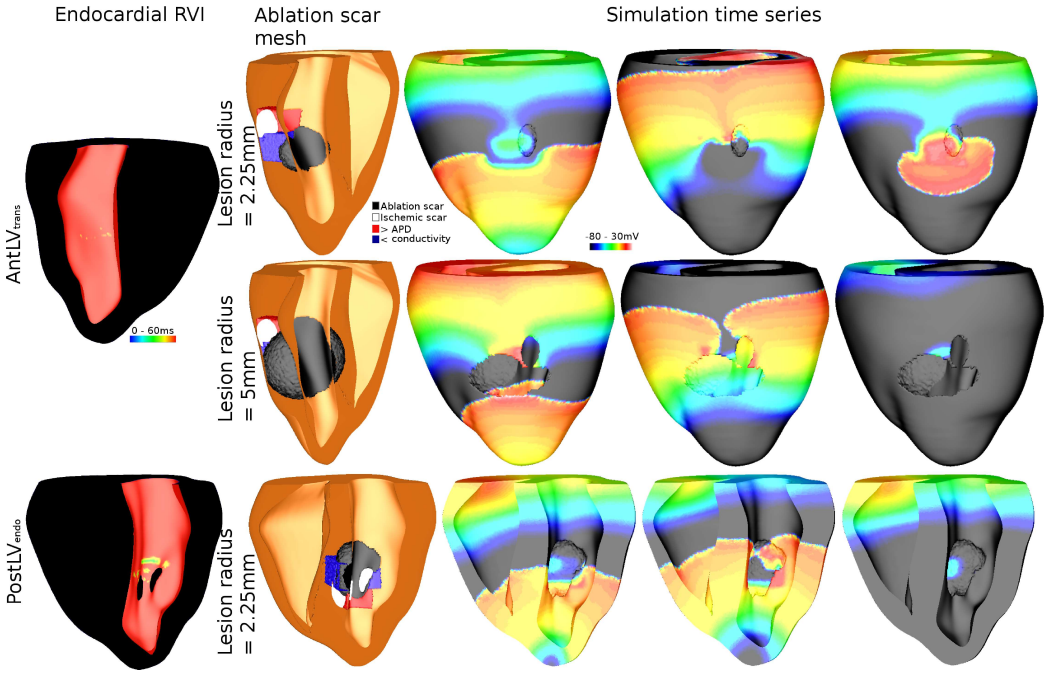

Figure 6.11: Modelling ablation utilising the endocardial RVI map. Endocardial RVI maps showing regions of the model with an RVI less than 60ms (*left*) for both the AntLV$_{trans}$ and PostLV$_{endo}$, were used to produce the ablation models (*second* image from left) with either 2.25mm or 5mm lesion radii. Ablation lesion is shown in *black*, the ischemic scar in *white*, the BZ_{APD} in *red* and the BZ_{cond} in *blue*. A series of images in time for each ablation model shows the outcomes of simulations conducted using the models.

model, particularly in the transmural AntLV$_{trans}$ model. However, a distinct region of the model can be determined when setting this threshold; the values of RVI less than 60ms are gathered in a specific area. An ablation model was produced by modelling the regions with an RVI less than 60ms as non-conducting tissue. The ablation lesion of this radius produced in the AntLV$_{trans}$ model did not extend far enough into the myocardial wall to stem the propagation wave from reentering around the ischemic scar (*second* image from left) and this is evident in respective time series images (*top*) where the wave propagates out of the isthmus after initial block. It could be thought that increasing the threshold value could result in the termination of reentry. However, increasing the threshold value, and ablating nodes which displayed values less than 100ms, whilst increasing the size of the ablation lesion on the endocardial surface, still did not terminate reentry due to the lesion not penetrating deep enough into the myocardium to stem the wave propagating around the scar transmurally. If the radius of the ablation lesion is increased to 5mm in

the AntLV$_{trans}$ model, the lesion extends far enough into the LV wall (*middle*) to halt the propagation wave around the ischemic scar and stop reentry occurring (*middle*, time series images). In comparison, a lesion produced using the smaller 2.25mm radius, in the endocardial PostLV$_{endo}$ model, was able to halt a reentrant circuit due to the depth of the scar within the LV wall. The extent of the ablation lesion (*black*) can be seen in conjuction with the depth of the ischemic scar (*white*) in the *second* image from the left (*bottom*). The time series images of the simulation (*bottom*) show that the propagation wave was halted at the ablation lesion. Regardless of the depth of the ablation lesion, it is evident that the endocardial RVI may be used to guide the ablation procedure and successfully terminate reentrant circuits. It is important to note that whilst an appropriate guide to the diameter of the ablation lesion was determined, in the clinic, the lesion radius varies and if the scar is particularly transmural, radiofrequency is applied through the ablation catheter for a longer period of time, forming a larger lesion to halt the arrhythmia. This is similar to what has been modelled here by extending the diameter of the ablation lesion.

6.4.4 Guiding the Ablation Procedure with Low Resolution RVI Maps

Varying the Data Resolution and Search Radius Size

The clinical recording catheter has 10 electrodes spaced evenly along its length and is relocated around the endocardium approximately 20 times (Child et al., 2015) resulting in 200 recording sites. In contrast, the endocardial surface of the 3D model has approximately 13000 node points, all of which can provide data to be used in the RVI calculation. In order to more closely replicate the clinical method, the sampling points used in the model are reduced by taking a subset of endocardial nodes to use in analysis.

To reduce the number of data points in the model, AT and RT data were calculated as normal but only a subset of the data was used by utilising every nth data point. The endocardial RVI algorithm was then performed as described in Section 6.4, calculating the RVI using only the low resolution subset of AT and RT data to produce a low resolution endocardial RVI map. A parameter sensitivity analysis was conducted, reducing the data points to every 5th, 10th and 20th node, to divulge the effect of reducing the number of data points on the RVI.

The size of r_s used to search for downstream nodes was also altered in a parameter sensitivity analysis. We varied r_s between 1mm and 5mm for the purpose of observing the

effect that both r_s in conjunction with the resolution of the sampling points has on the RVI.

A parameter sensitivity analysis altering the size of r_s used in the RVI algorithm was performed on a model with a resolution of every 20th node. Figure 6.12 displays the results

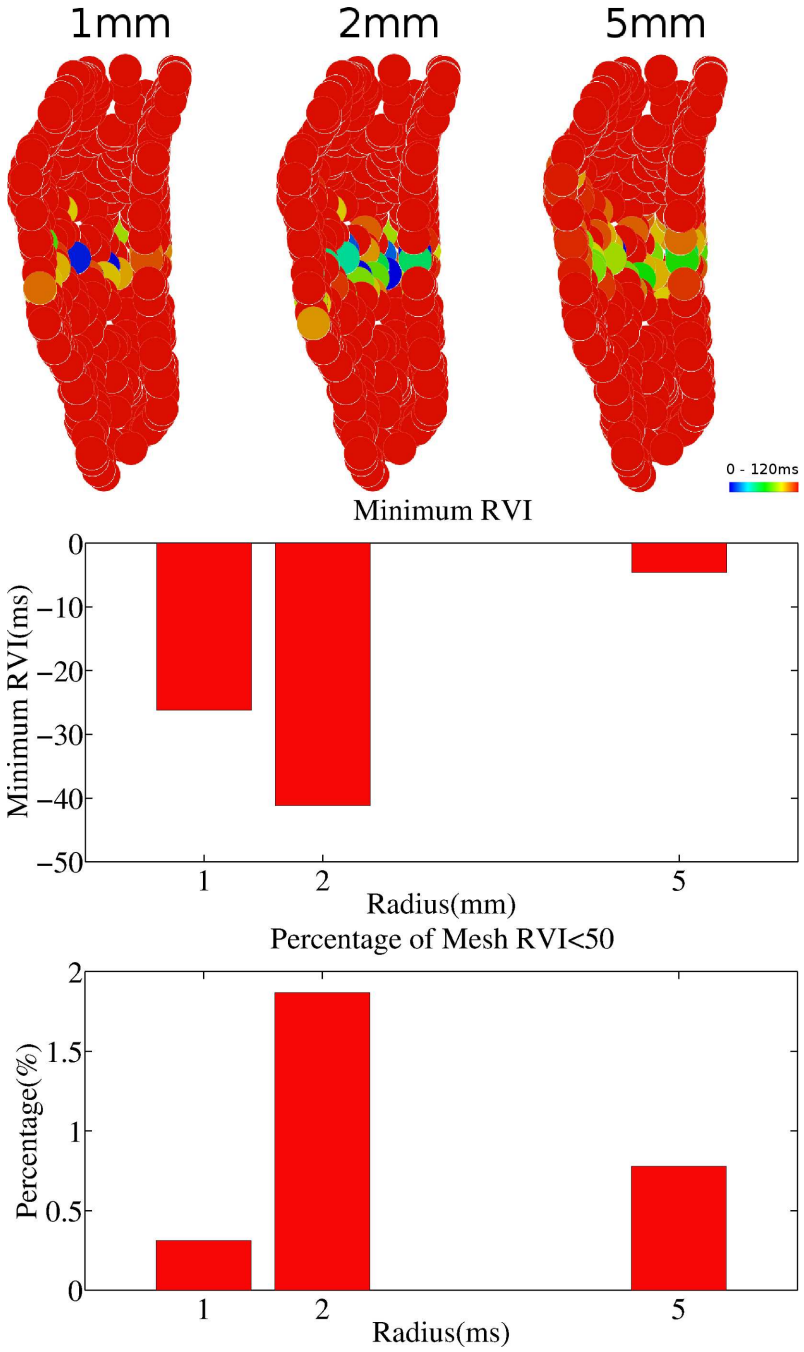

Figure 6.12: Effect of varying r_s on 3D RVI when using data only from every 20th node on the endocardium of the AntLV$_{trans}$ model. *Top* - RVI maps calculated using a radius of r_s of 1mm (*left*), 2mm (*middle*) and 5mm (right). *Middle* - effect of varying size of r_s on RVI_{min}. *Bottom* - effect of varying the size of r_s on the $RVI_{area<50}$.

of varying the size of r_s. The RVI maps at the top of the figure show that a critical region of low RVI values is located by the RVI algorithm, indicating a susceptibility to reentry. It appears that lower values of RVI are produced by the calculation using a smaller r_s and that a larger area of lower RVI values is produced in calculations using a larger r_s.

The graph of RVI_{min} $(middle)$ illustrates that using a 2mm radius of r_s produces the most negative RVI_{min} of approximately -40ms, as can be observed by the *dark blue* regions of the RVI map (top). Using a larger r_s of 5mm in the RVI calculation produces a less negative RVI_{min} of approximately -5ms and the regions of $green$ in the RVI map $(top, right)$ also illustrate this result. This is due to the fact that, with a smaller r_s, fewer values of RVI are produced and therefore, fewer values are averaged in order to plot the RVI map resulting in greater variation in the data being displayed.

As the RVI map produced using a radius of r_s of 2mm shows $(top, middle)$, utilising r_s with a radius of 2mm produces the largest region of $RVI_{area<50}$. The smallest r_s produces a smaller $RVI_{area<50}$ due to fewer very low RVI values being produced and averaged to create the RVI map. The RVI map on the $left$ illustrates that only a very few values of low RVI and hence, a low $RVI_{area<50}$ are produced. Whilst the RVI map on the $right$, displaying the results produced by using an r_s with a radius of 5mm in the RVI calculation, indicates that the low RVI values are more diffuse, the graph of $RVI_{area<50}$ $(bottom)$ shows that only a small $RVI_{area<50}$ is actually produced. This is due to the fact that the less negative values of RVI are produced when an r_s with a radius of 5mm is used, as can be seen in the graph of RVI_{min} $(middle)$. As a result of these combined findings, an intermediary r_s was chosen in order to proceed with the resolution parameter sensitivity analysis.

Figure 6.13 displays the results of varying the resolution of the model on the RVI. Observing the RVI maps; compared to the RVI map of the full resolution model $(left)$, the lower resolution models determine approximately the same region of interest as flagged by the lower RVI values in both AntLV_{trans} and PostLV_{endo} models.

The graph of the RVI_{min} produced by the AntLV_{trans} model $(middle)$ shows that the RVI_{min} remains relatively constant at approximately -35ms irrespective of whether the RVI is calculated utilising a lower or higher resolution model. This is relatively surprising as it would be expected that sampling the AT and RT data immediately from either side of the line of block, potentially more likely to occur in higher resolution models, would give the lowest value of RVI and that this may be missed as the resolution decreases. However,

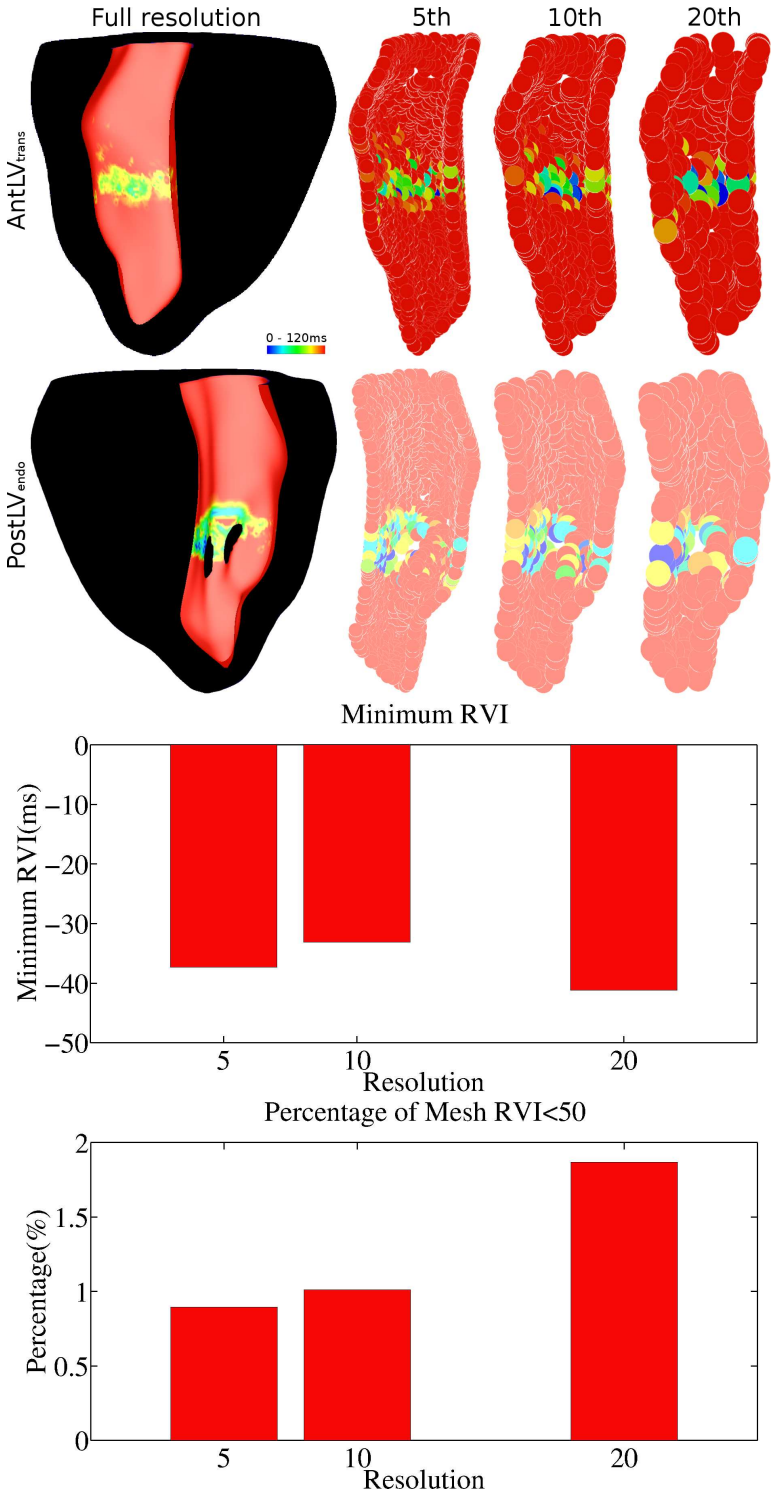

Figure 6.13: Effect of varying data resolution on 3D RVI, analysed with a search radius size of 2mm. *Top* - The AntLV$_{trans}$ model and PostLV$_{endo}$ results are shown. Full resolution RVI maps are shown on the *left* for comparison between RVI maps which display data analysed from every 5th, 10th and 20th node. *Middle* - effect of varying resolution on RVI_{min} in the AntLV$_{trans}$ model. *Bottom* - effect of varying resolution on the $RVI_{area<50}$ in the AntLV$_{trans}$ model.

the results do not reflect this.

The $RVI_{area<50}$ increases from approximately 1% to 2% as the resolution is decreased from using every fifth node in the model in the RVI calculation to using every 20th node as shown by the graph of $RVI_{area<50}$ (*bottom*) produced by the AntLV$_{trans}$ model. Again, a more diffuse region of low RVI values is expected when using a lower resolution model due to the method of taking an average of the RVI values to create the RVI map. In the clinical setting, a decapole catheter acquires the data and is moved around the myocardium 20 times, this gives 200 sites which data can be recorded from. Using every 20th node in the model also gives approximately 600 data points. This similarity, in conjuction with the fact that using a model with a resolution of every 20th node indicates a larger critical region, was motivation for using the resolution model of every 20th node in order to model the ablation procedure using this RVI map in the following study.

6.4.5 Guiding Ablation with Low Resolution Endocardial RVI Maps

The low resolution endocardial RVI map was used to guide the ablation procedure according to the method described in detail in Section 6.4 in the AntLV$_{trans}$ model, by identifying nodes on the low resolution endocardial RVI map with an RVI less than the threshold value. A parameter sensitivity analysis was conducted in order to derive threshold values which would either produce reentry or no reentry following ablation. Ablation lesions penetrated 5mm into the full resolution model myocardium and was modelled as non-conducting tissue. A smaller ablation lesion was not able to terminate reentry in this model due to the location of the scar complex within the myocardial wall, as seen in previous results in this section.

Surprisingly, very low threshold values of RVI could terminate reentry as shown in Figure 6.14. Ablation of nodes displaying an RVI less than -20ms resulted in termination of the reentrant circuit (*top*, *right*) whereas ablation of nodes displaying an RVI less than -30ms could not terminate reentry (*bottom*, *right*) depicted by the continued propagation of the activation wave past the site of initial block after circumventing the scar region. Again, there is very little difference in the area that is ablated between the models of different threshold values but the outcomes of the simulations are vastly different. The magnitude of the threshold value which can terminate reentry suggests that only a small portion of the very low RVI values is required for use in the ablation procedure. Importantly, this substantiates the accuracy of the RVI algorithm and proves that it accurately

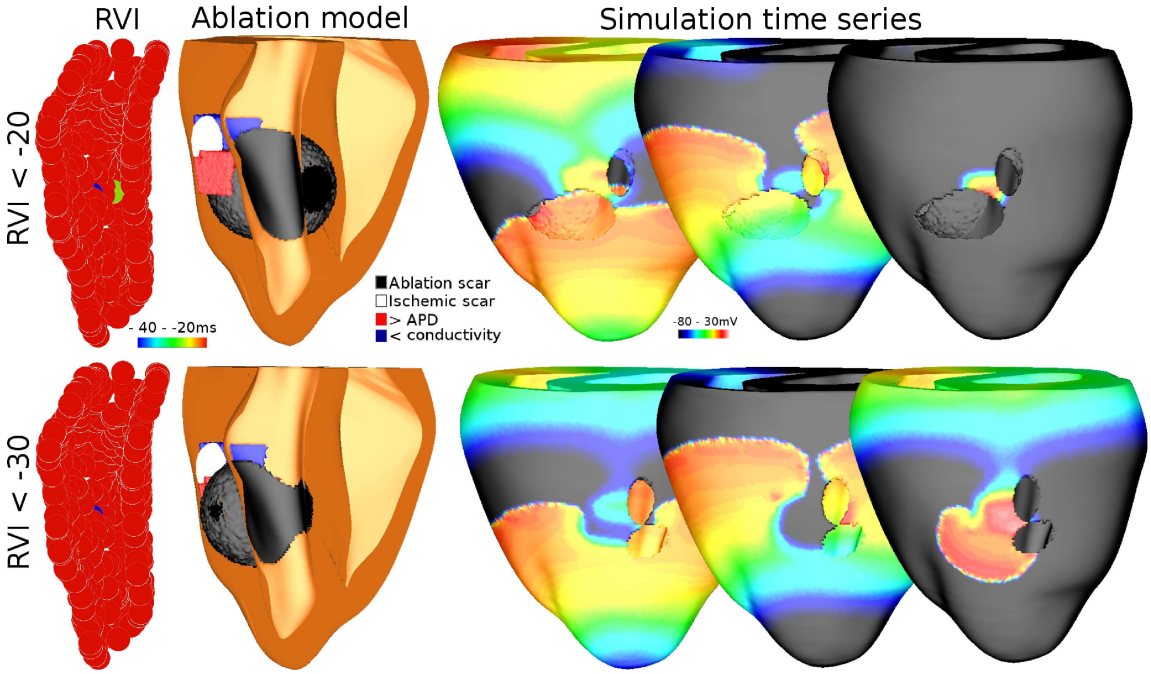

Figure 6.14: Utilising the reduced resolution endocardial RVI map to guide ablation. *Top* - RVI threshold -20ms, *bottom* - RVI threshold -30ms. *Left* - RVI maps displaying nodes below threshold. *Middle* - Resulting ablation models. *Right* - Time series of simulation displaying wave propagation outcome of ablation modelling.

locates regions susceptible to reentry. Moreover, the algorithm is validated even when limitations are imposed such as reduced resolution. Although reducing the resolution of the endocardial RVI seemed to produce a less accurate RVI map, utilising it in ablation modelling still provided the desired result; termination of reentry.

6.5 Investigating the Effect of the Depth of the Scar on the RVI

A study was performed in order to determine the effect of the depth of the scar within the myocardial wall on the result of the RVI algorithm. Clinical data are only obtained from the endocardial surface as described in Section 2.4 but scars may occur anywhere in the myocardium from endocardial, transmural or epicardial locations although endocardial scars are more commonly seen. Here, we investigate whether the endocardial RVI, as performed in the clinic, can accurately determine a location susceptible to reentry irrespective of depth within the myocardial wall.

6.5.1 Incorporating Scar at Varying Depths Below the Surface

In this section, we return to utilising a simplified model in order to investigate the effect that scar location within the myocardial wall has on the RVI. Section 1.3 describes the importance of computational models in the study of post-MI arrhythmias. Here we wish to investigate a particular parameter; depth of the scar underneath the surface of the endocardium, and its effect on the RVI. Therefore, we utilise a simplified model in order to reduce the complex dynamics which may obscure the result. A 2cm x 2cm x 1cm model was created with a resolution of 200μm between nodes, resulting in a model containing 520250 node points and 2500000 tetrahedral elements. The depth of the model (1cm) was chosen as it lay within the bounds of the average thickness of a healthy myocardial wall. The uppermost 2cm x 2cm surface was denoted the endocardium as depicted in *red* in the *top* image of Figure 6.15. 3D scar regions were incorporated into the models using the

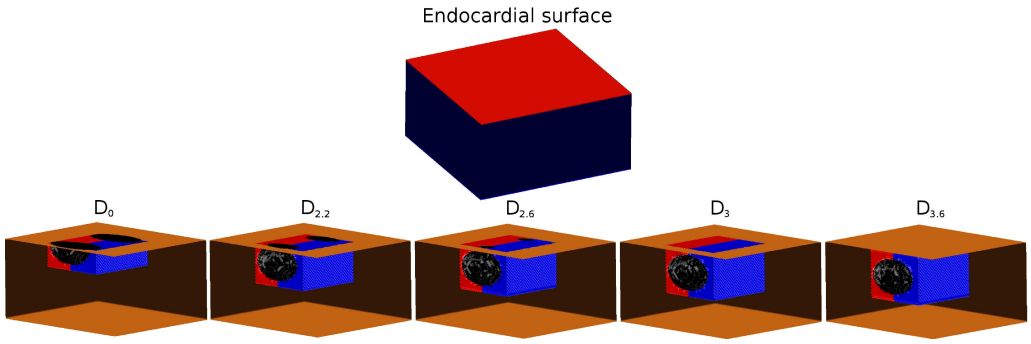

Figure 6.15: Models used in investigating the effect of scar depth on the RVI. *Top* - endocardial surface for which RVI is calculated. *Bottom* - Geometrical models with increasing scar depth (*left* to *right*).

same method as previously described in Section 6.2. Again, the scar regions contained 2 ellipsoid non-conducting scars (*black*) separated by an isthmus of BZ_{cond} (*blue*) and BZ_{APD} (*red*). Scars were placed in the middle of the plane parallel to the endocardium in each model, but models differed in the depth of the scar from the endocardial surface. Figure 6.15 also displays the geometrical models used in this study, showing the depth of the scar regions from the endocardial surface. Model D_0 possessed the scar region lying on the endocardial surface, so that exactly half of the scar region lay within the model whilst the other half protruded from the endocardial surface. The centre of model $D_{2.2}$ lies 2.2mm from the endocardial surface with some scar protruding from the endocardium, $D_{2.6}$ contains the scar region 2.6mm away from the endocardial surface with the scar just touching the surface, the scar in D_3 lies just below the surface with the centre of the scar

lying 3mm away from the endocardium and in model $D_{3.6}$, the scar lies 3.6mm away from the endocardial surface.

Model Parameterisation

The human model of ventricular AP (Ten Tusscher and Panfilov, 2006) was used to simulate electrophysiological membrane dynamics in healthy tissue. In the BZ_{APD}, the APD was lengthened by altering the model parameters based on previously described protocols (Rantner et al., 2012; Ashikaga et al., 2013). The maximal conductance value of I_{Na} was reduced to 38% of normal, I_{CaL} to 69%, I_{Kr} to 30% and I_{Ks} to 60% and the maximal value of I_{NaCa} was increased to 132% of normal.

Isotropic fibre orientations were assigned to the healthy tissue as described in the 2D experimental model (Chapter 5) in order to observe the effect of the depth of the scar within the myocardial wall on the RVI algorithm without introducing further complexity to the model. Conductivities were reduced by 50% in the BZ_{cond} to represent slow conduction.

Whilst the parameterisation of the model is based upon previously described protocols, it was essential that the reentry could be initiated in the models in order to study the RVI. The protocol described here produced reentry in all of the models.

Implementation of the S1S2 Pacing Protocol

Plane activation waves were produced by stimulating the entire 2cm x 1cm side of the cuboid in order to simulate the shape of an activation wave after having possibly travelled a distance from the clinical pacing location (most often the apex) to the site of infarction. The models were paced to a steady state at 480ms for 10 beats with a stimulus duration of 3ms. Subsequently, the S1S2 protocol was performed with a BCL of 300ms and a stimulus duration of 3ms, producing reentry in each model.

6.5.2 The Effect of the Depth of the Scar Within the Myocardium on the RVI

ATs and RTs were calculated as described previously (Section 6.2) and the RVI map was created using only data on the endocardial surface (Section 6.4), to produce an endocardial RVI map.

Important conclusions can be drawn from the results, displaying the effect that the depth of the scar region within the myocardial wall has upon the RVI. Figure 6.16 displays

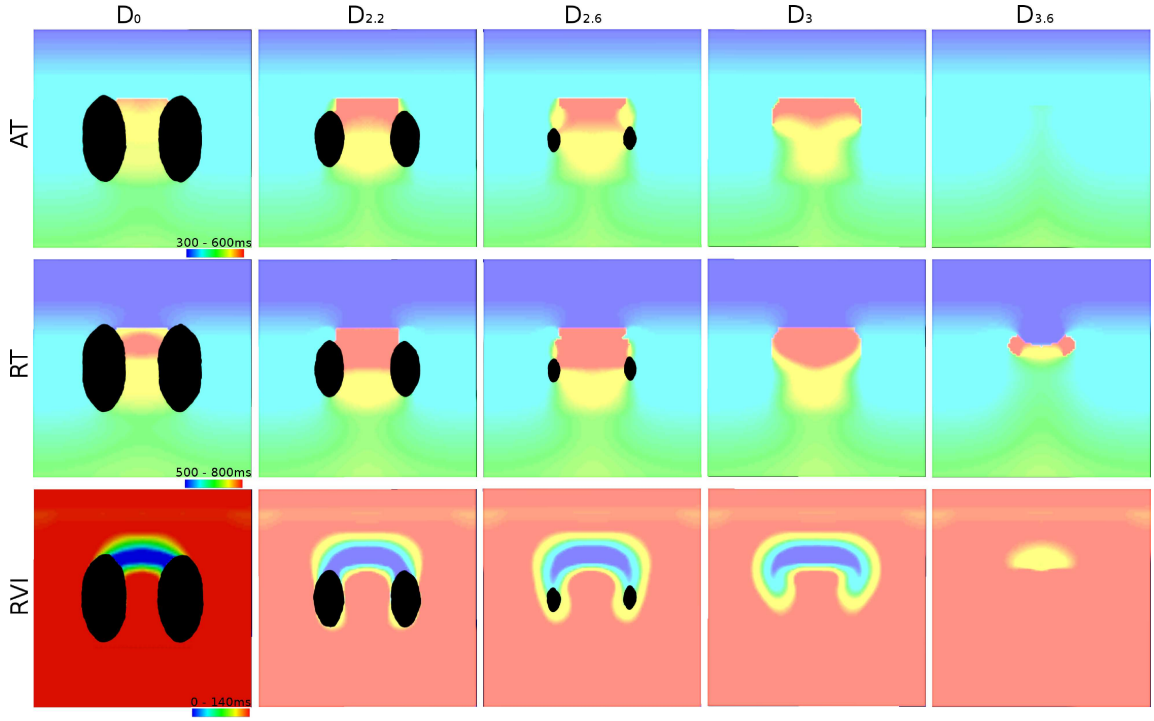

Figure 6.16: The effect of depth of scar region on the RVI. AT (*top*), RT (*middle*) and RVI (*bottom*) maps are displayed for models with the scar region lying 0mm (D_0), 2.2mm ($D_{2.2}$), 2.6mm ($D_{2.6}$), 3mm (D_3) and 3.6mm ($D_{3.6}$) underneath from the endocardial surface (*left* to *right*).

AT (*top*), RT (*middle*) and RVI maps (*bottom*) for models with the scar region incorporated at increasing depths beneath the endocardial surface (*left* to *right*). The black regions in the first 3 models are the area of the scars protruding at the endocardial surface. The nature of the wave propagation around the scar complex can be seen in the AT and RT maps. It is evident from the RT map of $D_{3.6}$ (*middle*, *right*) that although the scar and BZ complex lie underneath the endocardial surface, regions of late RTs compared to the rest of the tissue can be seen around the scar complex. This is possibly due to electrotonic effects of the scar and BZ which lie just underneath the endocardial surface, causing the prolongation of the APD in nearby tissue.

In each model, a region of low RVI can be defined, compared to the RVI in the rest of the model, which corresponds to the regions susceptible to reenty. It appears that the closer the scar region to the endocardial surface, the more precise the RVI algorithm is at locating regions susceptible to reentry. This could be due to the AT and RT information

at the surface of the model representing the exact line of block and reentry. When the scar regions lie beneath the surface of the model, the AT and RT maps are less accurate at portraying that critical event because the abrupt block occurs at the exit point of the scar, which no longer lies on the surface of the model. The effect on the RVI is that as the scar becomes more intramural and less evident on the endocardium, the RVI becomes less precise but importantly, critical regions are still able to be resolved.

These findings are quantified in Figure 6.17 which displays the RVI_{min} (*top*) and

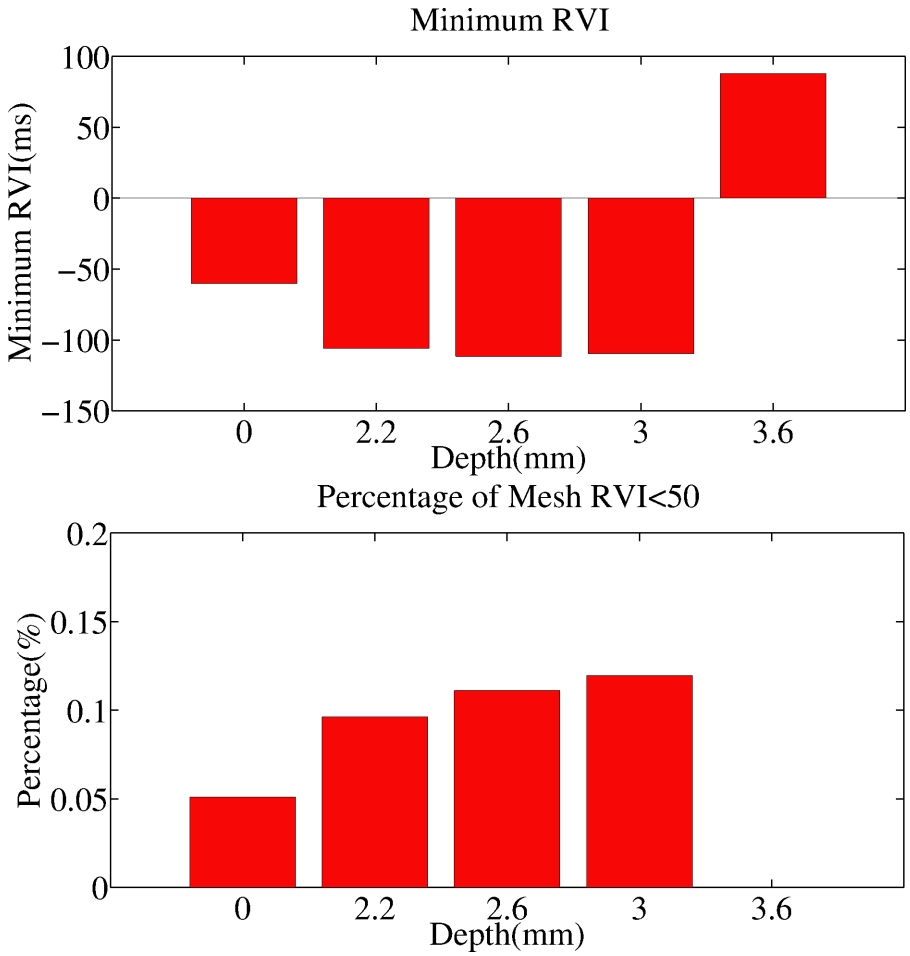

Figure 6.17: Graphs showing how the depth of the scar under the endocardial surface affects the RVI. *Top* - effect of varying scar depth on RVI_{min}. *Bottom* - effect of varying scar depth on the $RVI_{area<50}$.

$RVI_{area<50}$ (*bottom*) for each model. Interestingly, as the scar is located further away from the endocardium, the RVI_{min} becomes more negative, increasing from approximately -50ms to -100ms. A possible explanation for this trend is that as the fibrotic scars disappear below the endocardium, more BZ regions are displayed on the endocardium. It is the heterogeneity between the healthy and BZ tissue which causes the initial wave block and

determines subsequent reentrant success and so it is plausible to think that an increased region of BZ tissue could contribute to more negative RVI values. As both the scar and BZ regions disappear from the endocardial surface in $D_{3.6}$, the RVI algorithm is no longer able to predict a region susceptible to reentry with very low RVI values despite UDB occurring.

The graph of $RVI_{area<50}$ shows that as the depth of the scar beneath the surface of the endocardium increases, the $RVI_{area<50}$ increases also. Again, this is possibly due to the increasing region of BZ tissue contributing to producing lower RVI values as the scar region disappears below the surface of the endocardium. However, when the scar is located 3.6mm below the endocardial surface in this model, although a region of low RVI can be located in comparison with the remainder of the RVI values, the values are very high and the RVI calculation loses the ability to locate the exit point of the scar with low values of RVI.

6.6 Discussion

6.6.1 Limitations

Idealised scar geometries were used in this study to investigate the potential use of the RVI in the clinic to guide the ablation procedure. Although unlikely, it is possible that utilising such simplistic scar models could alter the efficacy of the RVI algorithm due to much more complex wave propagation patterns, which would occur around more realistic complex scar geometries. The models that we used ultimately were capable of producing reentry which was required for the investigation. However, a large BZ_{APD} region was required in order to initiate reentry which may not be physiologically accurate. In addition, the previously reported methodologies for modelling BZ tissue (McDowell et al., 2011; Rantner et al., 2012; Ashikaga et al., 2013) were altered in order for the models to produce reentry. The alterations of the BZ remodelling protocol could potentially affect the magnitude of the RVI but shouldn't affect its ability to locate regions susceptible to reentry, as simulated by the models.

Realistic scar geometries may incorporate multiple exit sites whereas the models used here only displayed one exit site. It is unknown whether the RVI could indicate multiple exit sites which would be of benefit in the clinic, ensuring that no further VTs produced by different physiological circuits could ensue after the ablation of the clinical VT.

In order to test the results of the ablation modelling and observe whether the protocol was able to terminate reentry, the same S1S2 protocol was conducted which was initially conducted to produce reentry in the model. A more robust protocol to test the success of the ablation procedure may be to implement multiple stimulation protocols, for example; pacing from different locations or with different pacing frequencies. A different stimulation protocol may be able to elicit reentry in the ablation model which was not possible with the S1S2 protocol performed in this study.

6.7 Summary

This study verifies that the RVI can locate regions suscpetible to reentry throughout the myocardial wall in a 3D model of rabbit ventricles. The region of low RVI which indicates the susceptibility to reentry is again located around the region of the exit site of the scar which has been noted to be an optimal ablation target. This conclusion is vital in order to display that the RVI algorithm may be of use in a clinical scenario. In addition, it is shown here that the RVI maintains its ability to identify a location which is susceptible to reentry in varying geometrical models, suggesting that the RVI algorithm may be robust in different patients who will certainly have varying heart shapes and sizes as well as varying scar locations and geometries.

Crucially, it has been shown in this study that it is possible to utilise the RVI map to guide ablation. Based on RVI maps, identified regions of low RVI values were targeted for ablation which effectively removed the conductive tissue from the target region. On induction of a S1S2 pacing protocol after ablation, depending on the threshold of RVI set as the target for ablation, the reentrant circuit was terminated. This, in the clinic would be a positive outcome of the ablation procedure. Indicating that the RVI algorithm could be of use in the clinic is of great interest as it could potentially provide a novel methodology which could accurately map the exit point of the scar without inducing VT, something which current ablation treatments fail to do very effectively.

In the clinic, data are only sampled from the endocardium which could have rendered the RVI algorithm, which depends on AT and RT data sampled near to the exit site, useless. However, after performing the RVI algorithm on only endocardial data and producing endocardial RVI maps, it is evident that, although slightly less accurate, the RVI is still able to predict regions susceptible to reentry with low RVI values. Moreover, the

algorithm performed on endocardial data is effective whether the scar is located endocardially or transmurally. On utilising the endocardial RVI maps to guide the ablation simulation, it was found that it was possible to terminate reentry by ablating regions of low RVI. However, the success was dependent on the depth of the exit site within the myocardial wall and the size of the ablation lesion that was created. A more transmural scar required a larger ablation lesion performed from the endocardium to be created, a scenario that also presents in the clinic.

The vast reduction in data sampling resolution which is inherent in clinical data recording could result in the algorithm being less able to locate the regions susceptible to reentry, a result which was indicated in the previous chapter. The decrease in endocardial sampling resolution was modelled here and it was found that despite loss of accuracy of the RVI result, the calculation was still able to locate regions susceptible to reentry. This is a major finding which validates the use of the RVI algorithm in the clinic. The result is further supported by the ability to terminate reentry by modelling ablation of the regions indicated by low RVI values on the low resolution endocardial RVI map.

Lastly, the study investigated the effect of the depth of the substrate within the myocardial wall on the RVI map. It was assumed that the RVI map would become less able to identify susceptibility to reentry when the substrate is deep within the myocardial wall. However, results indicate that the RVI algorithm can identify regions susceptible to reentry even when the substrate is located underneath the surface of the tissue, suggesting that RVI guided ablation could be of use in ablating transmural MI-scars involved in VT circuits. Moreover, we have shown here that the RVI technique is successful when performed on the endocardium but the technique could also be applied to the epicardium, acquiring and utilising epicardial data in the calculation of the RVI. Hence, the RVI algorithm could provide a technique with which to treat both endocardial and epicardial infarct scars.

Computational modelling has enabled the study of many factors such as endocardial data sampling and low resolution data sampling which could impact the results of the RVI. The techniques used here have enabled questions to be answered that can not currently be answered by *in vivo* techniques.

Chapter 7

Discussion

7.1 Summary

Reentrant arrhythmias are a cause of hundreds of thousands of deaths each year due to the loss of cardiac function and blood supply to vital tissues, the treatment of which is exceptionally costly to the Health Services. As such, much research has been performed to study the causes, initiation, maintenance and treatment of arrhythmias but despite this, death rates remain high. As the incidence of risk factors such as obesity, diabetes and high cholesterol increase, it is likely that arrhythmias will continue to be a significant cause of death. Ischemic damage to the tissue as a result of an MI can cause reentrant arrhythmias to occur around infarct scars, which if untreated, can lead to VF and SCD. Research is targeted at understanding the mechanisms of reentrant propagation to enhance treatment strategies, halting the arrhythmia and returning the heart to normal rhythm.

Throughout the thesis we adopt a computational modelling approach to simulate wave propagation across the heart and use simple measures of wavelength to determine the dynamics of reentrant propagation. Computational models are used here to provide novel insight into real-time intramural wave propagation which is currently unattainable in the clinic due to ethical restrictions and the limitations of clinical data recording. At present, clinical recording techniques are unable to provide the high-resolution, 3D data that can be produced by models. The low financial burden of computational models and the lack of ethical restrictions permits us to study wave propagation over large sets of physiological parameters quickly and with relative ease. Potentially one of the most important benefits of using *in silico* models is that it is possible to study wave propagation with varying degrees of complexity, by altering single electrophysiological parameters or increasing the

complexity of geometrical models, in order to provide detailed insight into the mechanisms of reentry.

The investigations conducted in this Thesis were fundamentally rooted in a concept highlighted in the leading circle theory of reentry. This theory states that if wavefront-wave back interactions occur as a wave propagates around a circuit, reentry will be terminated. However, if an excitable gap is present between the wavefront and the wave back, the wavefront will be able to continue to propagate into the gap, facilitating reentry.

The first research chapter in this Thesis, Chapter 4, begins by determining the similarity of reentry dynamics between species. Many small animal models are used to investigate arrhythmias in order to draw conclusions which may be of clinical use. However, in order to provide clincally relevant conclusions, small animal models should replicate the wave propagation dynamics of the human, particularly in terms of the disrupted wave propagation and arrhythmia dynamics which occur around infarct scars. Importantly, species differences such as the size of the heart and the electrophysiological properties of the myocardium can affect wave propagation. Here we investigated which species model most closely replicates the wave propagation dynamics observed in the human, in order to be able to suggest the optimal model to use in further research pertaining to reentrant arrhythmias. To do this we compared the effective electrical size of the heart, which compared the wavelength to the size of the heart, to determine the likelihood of reentry occurring. Importantly, we studied the restitution profiles of the effective size of the hearts of each species to observe whether the models became equally more susceptible to reentry at faster cycle lengths, indicative of those which occur during VT arrhythmias. Alterations to ionic currents and conductivity properties occur in the BZ tissue surrounding the scar. As such, we investigated the effect of BZ remodelling on the effective size, in addition to observing whether BZ remodelling would serve to increase the species differences in wave propagation dynamics. The results of Chapter 4 motivated the use of the models utilised in Chapters 5 and 6.

In Chapters 5 and 6, we studied reentrant wave propagation by quantifying whether or not reentry could occur based on AT and RT data using the RVI calculation. In other words, we observed whether or not the wavefront may collide with the wave back. Crucially this work has significant clinical impact in treating post-MI arrhythmias. Currrent ablation treatment has relatively low success rates due to the difficulties in accurately locating the scar region and in particular, locating the exit point of the scar which has

been suggested as the optimal ablation target. In some cases the treatment is potentially dangerous due to the need to induce VT in order to locate the scar. Therefore, we investigated the RVI methodology and in particular, its application for use in the clinic. Firstly, we validated the method in simple 2D models, producing a spatial map of RVI values to locate regions susceptible to reentry and observed how increasing arrhythmogenicity affected the results. We progressed the study by using 3D models to research how accurate the RVI is at locating the exit point, utilising 3D data to produce 3D RVI maps. In addition, we modelled the clinical method used to produce RVI maps, taking into consideration the low resolution, endocardial data that are recorded in the clinic for the purposes of observing how the clinical method may affect the RVI results. Finally we modelled the ablation procedure using the RVI maps to demonstrate the efficacy of the RVI method in guiding the ablation procedure.

7.2 Important Findings and Key Contributions

The species differences in effective size between small animal models were tested at frequencies indicative of VT for the first time in Chapter 4 due to the large amounts of literature studying reentrant arrhythmias, utilising small animal models. Restitution curves of APD and CV in both the single cell and tissue models illustrated that the parameters decreased with increasing frequency. This finding supports the evidence that as pacing frequency increases, slow recovery from inactivation of the ionic channel gating mechanism causes the decrease in APD and CV. Interestingly, as a result of the wavelength being calculated as the product of APD and CV, wavelength also decreases with increasing cycle length. Moreover, we show that although the wavelength restitution graphs of different species share the same trend, differences occur in the magnitude of the change in wavelength as pacing frequency increases. Specifically, we have shown that the human model displays the steepest wavelength restitution curve, with wavelength decreasing considerably as the pacing frequency decreases. By the leading-circle theory of reentry, decreasing the APD, CV and wavelength, all increase the excitable gap, suggesting that reentry is more likely to occur at faster pacing frequencies. Due to the species differences in the magnitude of the restitution curve, we can suggest that as pacing frequency increases, reentry is more likely to occur in the models as a result of the increase in excitable gap. But crucially, due to the largest change in wavelength with pacing frequency, we can speculate that

the human model is more susceptible to reentry at fast pacing rates than the other small animal models tested here.

The one exception displaying negative restitution graphs of APD, CV and wavelength was the rat model (Pandit et al., 2001). Negative restitution of the rat model has been reported in the literature at the both the single cell and tissue levels (Kondratyev et al., 2007; Fenton and Cherry, 2008; Sallé et al., 2008). This phenomenon is not physiologically possible, for if the APD continued to increase whilst the heart rate increased, there would become a point when the myocardium would no longer be able to contract fast enough to maintain the required CO. It is possible that such restitution reported in the literature, is due to the nature of data acquisition and the use of EGTA in patch clamp recordings and optical mapping dyes and mechanical uncoupling agents at the tissue level. Therefore, we can suggest that the rat model requires reformulation with newly acquired data which do not display the negative restitution artefact, if the model is to be useful in studying arrhythmia mechanisms.

Observing the effective electrical size of the hearts of the human, rabbit, guinea pig and rat models, it is possible to suggest that the rabbit model displays the most similar effective size to the human model. In fact the human model displays a greater effective size than the rabbit and yet a greater effective size still, than the guinea pig model. These results suggest that the human is more likely to be susceptible to reentry than the other models. Although there is a difference in magnitude of effective size between the human and rabbit models, the restitution properties of the effective size are most similar. This is due to the similarity in wavelength restitution between the models which showed that the steepness of the wavelength restitution graphs of the human was most similar to the rabbit model in both the single cell and tissue models. Therefore, the increase in effective size as pacing frequency increases in the human model is also seen in the rabbit model, illustrating the fact that the tissue becomes more susceptible to reentry as the pacing frequency increases. This similarity in effective size between the human and rabbit models suggests that, although species differences occur, the rabbit model may be the most useful model to study clinical arrhythmia dynamics.

Incorporating ionic current and conductivity BZ remodelling into both the human and rabbit models resulted in an increase in APD and a decrease in CV respectively. The effects of BZ remodelling on the effective size of both species, illustrates that despite the rabbit model displaying an effective size most similar to the human model, important

species differences in both the magnitude and restitution remain and could be enhanced in BZ regions, through which reentry may occur. Thus we propose that in order to model reentrant arrhythmias to draw conclusions which may be applicable to the clinic, a human *in silico* model should be used. However if, due to the computational demands of human model simulation, this is impractical, or indeed if the most suitable animal model is being sought for *in vivo* research, the rabbit model proves to be the most suitable animal model to study reentrant arrhythmias. The rabbit model does display a similar effective size and response to BZ remodelling to the human, which is crucial to the study of post-MI reentry.

Results from Chapters 5 and 6 suggest that studying the wavelength to determine whether reentry can occur or not, may prove useful in guiding the clinical ablation procedure. The RVI algorthim was proposed to create a spatial map which can predict a susceptibility to reentry (Child et al., 2015). The method works by comparing the times at which the wavefront and wave back reach nearby points in a circuit to determine whether an excitable gap exists and whether reentry is likely to occur there. The results of these chapters indicate that regions highlighting a susceptibility to reentry may provide accurate targets for ablation which could improve the success rates of the ablation procedure.

When implemented in simple 2D models, the results of the RVI calculation showed that regions susceptible to reentry could be located across a 2D surface by the presence of negative values of RVI in cases where UDB occurs and low positive values where BDB occurs. We further tested the methodology by producing data from many simulations ranging in arrhythmogenicity. For example, increasing the prematurity of the S2 beat increased the arrhythmogenicity of the simulation as expected, resulting in reentry and interestingly, produced a greater area of more negative RVI values. Not only do these results suggest that the RVI can indicate the severity of the arrhythmia but they also support the idea that the RVI algorithm can predict regions susceptible to reentry over a wide variety of physiological conditions. This validation was necessary due to the methodology previously only being tested on one patient. In addition, we were able to use computational models to observe how varying parameters such as the resolution of the data being used and the r_s implemented to determine calculation node pairs, affects the RVI results. In the clinic, sampling of data is limited due to the number of recording electrodes on the catheter, the manual manipulation of the catheter and the time constraints of the procedure. As such, low resolution data sets, compared to data produced by computational models, are collected and used for analysis in the clinic. The r_s is a parameter utilised in the calcu-

lation of the RVI to determine calculation node pairs in order to ensure that the RVI is calculated between two nearby points. We found that the RVI highlights regions of low RVI even when low resolution AT and RT data are used in the calculation. However, RVI calculated from low resolution data has a tendency to be less accurate due to plotting the result on a low resolution model. The RVI calculated from low resolution data also indicates critical regions with less negative RVI values. This methodology replicates the clinical scenario and results suggest that the limitations of clinical data recording affect the results of the RVI only minimally and that the RVI calculation is still of significant use in the clinic. Likewise, increasing r_s to a size which is comparable to that used in the clinic, also results in a less accurate RVI map of the critical region, due to large numbers of RVI values being calculated and averaged in order to produce the RVI map. Despite these parameters resulting in less accurate RVI maps being produced, the calculation is still able to locate critical regions of the tissue.

Integrating a simplified scar geometry into the model allowed us to visually verify whether or not the RVI was able to locate the exit point of the scar and determine the accuracy of the RVI. Incorporating the scar and simulating wave propagation in the model produced figure-of-eight reentry patterns comparable to those which may cause clinical VT. Indeed, results showed that the RVI calculation located the exit point with low values when either UDB or BDB occurred. Similar results to those of the experimental model were reported suggesting that more negative values of RVI were produced in more arrhythmogenic simulations. In addition, higher resolution data which are possible to obtain from computational models increase the accuracy of the RVI results. In addition, using a smaller r_s in the RVI calculation to determine calculation node pairs also increased the accuracy of the RVI results. Importantly, even using low resolution data and large r_s sizes in the calculation of the RVI, areas susceptible to reentry, namely the exit point, are still able to be distinguished from the rest of the tissue, in a similar manner to the results produced by the simple experimental model.

The aim of Chapter 6 was to thoroughly investigate how the clinical recording procedure may affect the results of the RVI algorithm and demonstrate that RVI maps can improve the ablation procedure. Current problems with ablation treatment include the inaccuracy of locating the ablation target, resulting either in multiple sites being ablated which may have a negative impact on cardiac function, or VT recurring at a later date. In addition, in some cases VT is induced to map the scar region which increases the danger

of the procedure. We suggest that the RVI algorithm can improve the ablation treatment by addressing both of these issues by accurately locating the exit point of the scar without having to induce VT. Moreover, the RVI technique only requires AT and RT data from sites across the endocardial surface, data which are acquired with relative ease. Currently, techniques to map the substrate involve skillful catheter manipulation to record data from sites within the scar and expert opinion to analyse the electrograms. In addition, recording voltages from the scar and BZ region can result in either false positive or false negative indication of the correct target location. In order to investigate the clinical application of the technique, we employed a detailed model of 3D rabbit ventricles to be able to investigate transmural propagation and reentry. A rabbit model was used here based on the results of Chapter 4 in which we showed that the rabbit model displayed the most similar effective size, in terms of magnitude and restitution effects, to the human in both health and BZ remodelled tissue. Here we utilised the rabbit model in order to reduce the computational demand that a 3D human model would require. Important to note is that the RVI technique is not species specific and that the quantification of wavefront-back interactions using AT and RT data is the same across species.

We began the Chapter by implementing the RVI algorithm in three 3D models each incorporating scar at different locations around the ventricular wall and at different depths within the myocardium. Performing the RVI calculation on the 3D data showed that low values of RVI highlight the exit point of the scar irrespective of the scar's location. Again, the use of different models here provided extra validation of the technique and showed that it is robust enough to be used in the clinic where biological variation is inherent.

The effects of clinical data recording were investigated by calculating the RVI using only endocardial data to produce an endocardial RVI map. Recording data in this manner replicated the collection of data in the clinic. Our simulations predicted that exit points would be less accurately located by the RVI if they were located more transmurally and we found this to be the case, although the RVI could still indicate the critical region but less accurately and with less negative RVI values. We modelled the ablation procedure by simulating ablation of the regions of low RVI values and found that ablation of even very small regions highlighted by the RVI map could terminate reentry. To further investigate the potential to guide the ablation procedure using RVI maps, areas of the model displaying RVI values below varying threshold values were ablated in order to investigate the accuracy of the RVI map. Previously, we showed that endocardial RVI maps are less accurate at

locating regions suscpetible to reentry with low values of RVI and so it was predicted that guiding the ablation procedure with endocardial maps would be less successful. However, using these maps to suggest ablation targets still resulted in termination of the arrhythmia. We further investigated clinical procedure by reducing the resolution of the endocardial data which resulted in yet less accurate and precise location of regions susceptible to reentry by the RVI map, however identification of the critical exit point was still possible. Therefore, we can suggest that the low resolution endocardial RVI maps produced in the clinic remain effective at locating the optimal ablation lesion targets. What remains a problem, is that if the scar is transmural and catheter ablation is performed from the endocardium, the ablation lesion has to penetrate transmurally to reach the exit point to be successful in terminating VT. It should be considered that the RVI technique could be implemented on the epicardium and so transmural and epicardial scars may still be able to be treated with success rates similar to those achieved for endocardial scars.

Simplified models of scar regions embedded at different depths in the myocardium were used to observe how the transmural depth of the scar affected the RVI result. RVI maps created on the endocardial surface showed that the RVI was less accurate at locating critical regions as the depth of the scar below the endocardium increased. However, it was also shown that as the depth of the scar beneath the surface increased, the values of RVI became more negative and the area of the lowest RVI values increased. These results suggest that it is still possible to detect regions of low RVI values even when the scar was located transmurally.

7.3 Future work

The research in this Thesis has suggested the optimal animal model to study reentrant arrhythmias and therefore can inform methodological practise. In addition, the research has provided important validation for the use of the RVI in the clinic. However, if the RVI is to be implemented routinely in clinical procedures, further investigation could be performed to validate and optimise its use. Suggestions of potential future research avenues are presented here.

In the clinic, opinions on the desired end point of the ablation procedure are divided (Aliot et al., 2009). In Chapter 6, we assumed that the ablation procedure which we modelled had been successful if, on performing the same stimulation protocol which was

used to initiate reentry in the model before ablation, the activation wave was blocked by the ablation lesion, terminating the reentrant circuit. In a patient, scar geometries are both complex and varied. In fact, it has been reported that multiple potential reentrant circuits exist within a patient, which can act as a substrate for VT. Indeed, the cause of many recurring arrhythmias post-ablation treatment occur as a result of reentrant waves propagating around other VT circuits. Current ablation techniques aim to terminate the clinical VT without taking into account that multiple potential VT circuits can occur in a patient, therefore, another VT may occur at a later date. In Chapter 6 we investigate the RVI method in a simplified model with one possible reentrant circuit. However, the RVI method should be able to detect multiple circuits based on the wave propagation dynamics around the scar. In order to do this, either UDB or BDB around the other VT circuits needs to be induced in order for the RVI to be able to indicate each exit point of the scar. Therefore, rigorous pacing protocols which can elicit UDB or BDB in each possible reentrant circuit around the scar need to be performed. At present, such a protocol does not exist. We propose that computational models displaying more anatomically realistic scar geometries with multiple potential circuits, can be utilised to perform parameter sensitivity analyses, varying both the pacing rate and the pacing location in order to determine a protocol which enables detection of all VT circuit exit points in the scar region. If all exit sites of the scar which are involved in potential reentrant circuits can be detected by the RVI method and ablated, the long-term success rates of the ablation treatment should increase.

Regarding the well-documented complexity and vast variation in infarct scars observed in patients, it would be of signifcant use to observe the effect of such complexity on the results of the RVI. In Chapters 5 and 6, very simplified scar geometries were incorporated into the models. A vital next step to this research in order to further validate the RVI would be to integrate multiple different realistic scar geometries into the computational models at multiple locations replicating the biological variation observed in patients. Initially, anatomically realistic scars could be incorporated into the model of rabbit ventricles used in Chapter 6 in order to reduce computational demand as a large number of scar geometries are tested. Again, the results of Chapter 4 indicate that the rabbit model is the most suitable small animal model to use in investigating VT arrhythmias and is the model which is most able to replicate wave propagation dynamics of the human in healthy and BZ tissue. The next stage would be to integrate realistic scar geometries into patient

models in order to test whether the RVI maintains its ability to locate the exit points in the scar in anatomically realistic models of the human infarcted heart. We would however, expect the RVI results produced in humans to be similar to those produced by a rabbit model.

In addition to the simplified geometries used in Chapters 4, 5 and 6, BZ remodelling was implemented in these models based on previous protocols which were in turn based upon canine and rabbit data due to the lack of data regarding ionic current and conductivity remodelling in the human. As BZ remodelling data of the human becomes available, utilising the data to investigate wave propagation around infarct scars such as in the research presented in this Thesis, could improve the accuracy of modelling BZ wave propagation. However, the RVI algorithm is validated based upon AT and RT data irrespective of the nature of wave propagation.

7.4 Concluding Remarks

In this Thesis, we showed that species differences occur, between human and small animal models, in the effective size of the heart. We suggested that due to these species differences in magnitude of the effective size and the restitution properties of the effective size, that the optimal approach to modelling VT arrhythmias would be to study wave propagation in the clinic or in a computational model of human data. However, if the required investigation is not possible in the clinic or if computational demand of a human model is too high, the results in Chapter 4 show that the rabbit most closely replicates the effective size and its restitution properties of the human and hence, is the best model for investigating VT arrhythmia wave propagation dynamics. In Chapters 5 and 6 we utilised the methodological conclusions drawn from Chapter 4 to validate the proposed RVI algorithm, which aims to identify regions of tissue susceptible to reentry, utilising AT and RT data, for the purposes of guiding the ablation procedure. We showed that the exit point of the scar could be located by low values of RVI during both UDB and BDB and that the highlighted regions of low RVI values could be used as ablation lesion targets. In doing so, the accurate location of the exit point by the RVI required only small areas of tissue to be ablated to result in successful termination of the VT. We tested the method over a variety of varying physiological parameters and geometries to conclude that the RVI would be of use in a clinical setting for many patients even considering the limitations

imposed by clinical data recording. From the results of this Thesis we can conclude that the RVI calculation can improve the safety of the treatment, as well as the accuracy and hence success rates of the ablation procedure.

Bibliography

Aggarwal, R. and Boyden, P. A. (1995). Diminished Ca2+ and Ba2+ currents in myocytes surviving in the epicardial border zone of the 5-day infarcted canine heart. *Circulation Research.* **77**(6), p.1180–1191.

Alexandre, J., Saloux, E., Lebon, A., Dugué, A. E., Lemaitre, A., Roule, V., Labombarda, F., Champ-Rigot, L., Gomes, S., Pellissier, A., Scanu, P. and Milliez, P. (2014). Scar extent as a predictive factor of ventricular tachycardia cycle length after myocardial infarction: implications for implantable cardioverter-defibrillator programming optimization. *Europace.* **16**(2), p.220–226.

Aliot, E. M., Stevenson, W. G., Almendral-Garrote, J. M., Bogun, F., Calkins, H., Delacretaz, E., Della Bella, P., Hindricks, G., Jaïs, P., Josephson, M. E., Kautzner, J., Kay, G. N., Kuck, K., Lerman, B. B., Marchlinski, F., Reddy, V., Schalij, M., Schilling, R., Soejima, K. and Wilber, D. (2009). EHRA/HRS expert consensus on catheter ablation of ventricular arrhythmias. *Heart Rhythm.* **6**(6), p.886–933.

Allessie, M. A., Bonke, F. I. M. and Schopman, F. J. G. (1973). Circus movement in rabbit atrial muscle as a mechanism of tachycardia. *Circulation Research.* **33**(1), p.54–63.

Allessie, M. A., Bonke, F. I. and Schopman, F. J. G. (1976). Circus movement in rabbit atrial muscle as a mechanism of tachycardia. *Circulation Research.* **39**(2), p.186–177.

Arenal, A., Del Castillo, S., Gonzalez-Torrecilla, E., Atienza, F., Ortiz, M., Jimenez, J., Puchol, A., García, J. and Almendral, J. (2004). Tachycardia-related channel in the scar tissue in patients with sustained monomorphic ventricular tachycardias. *Circulation.* **110**(17), p.2568–2574.

Ashikaga, H., Arevalo, H., Vadakkumpadan, F., Blake, R. C., Bayer, J. D., Nazarian, S., Muz Zviman, M., Tandri, H., Berger, R. D., Calkins, H., Herzka, D. A., Trayanova,

N. A. and Halperin, H. R. (2013). Feasibility of image-based simulation to estimate ablation target in human ventricular arrhythmia. *Heart Rhythm.* **10**(8), p.1109–1116.

Auerbach, D. S., Grzda, K. R., Furspan, P. B., Sato, P. Y., Mironov, S. and Jalife, J. (2011). Structural heterogeneity promotes triggered activity, reflection and arrhythmogenesis in cardiomyocyte monolayers. *The Journal of Physiology.* **589**(9), p.2363–2381.

Azene, E. M., Trayanova, N. A. and Warman, E. (2001). Wave front–obstacle interactions in cardiac tissue: a computational study. *Annals of Biomedical Engineering.* **29**(1), p.35–46.

Baker, L. C., Wolk, R., Choi, B.-R., Watkins, S., Plan, P., Shah, A. and Salama, G. (2004). Effects of mechanical uncouplers, diacetyl monoxime, and cytochalasin-D on the electrophysiology of perfused mouse hearts. *American Journal of Physiology. Heart and Circulatory Physiology.* **287**(4), p.H1771–H1179.

Banville, I. and Gray, R. A. (2002). Effect of action potential duration and conduction velocity restitution and their spatial dispersion on alternans and the stability of arrhythmias. *Journal of Cardiovascular Electrophysiology.* **13**(11), p.1141–1149.

Beeler, G. W. and Reuter, H. (1977). Reconstruction of the action potential of ventricular myocardial fibres. *Journal of Physiology.* **268**(1), p.177–210.

Benitah, J., Bailly, P., D'Agrosa, M., Da Ponte, J., Delgado, C. and Lorente, P. (1992). Slow inward current in single cells isolated from adult human ventricles. *Pflugers Archiv.* **421**(2-3), p.176–187.

Bernus, O., Wilder, R., Zemlin, C. W., Verschelde, H. and Panfilov, A. V. (2002). A computationally efficient electrophysiological model of human ventricular cells. *American Journal of Physiology. Heart and Circulatory Physiology.* **282**(6), p.H2296–H2308.

Bishop, M. J. and Plank, G. (2012). The role of fine-scale anatomical structure in the dynamics of reentry in computational models of the rabbit ventricles. *Journal of Physiology.* **590**(18), p.4515–4535.

Bogun, F., Bahu, M., Knight, B. P., Weiss, R., Goyal, R., Daoud, E., Man, C., Strickberger, S. A. and Morady, F. (1997). Response to pacing at sites of isolated diastolic potentials during ventricular tachycardia in patients with previous myocardial infarction. *Journal of the American College of Cardiology.* **30**(2), p.505–513.

Bogun, F., Bender, B., Li, Y., Groenefeld, G., Hohnloser, S. H., Pelosi, F., Knight, B., Strickberger, A. S. and Morady, F. (2002). Analysis during sinus rhythm of critical sites in reentry circuits of postinfarction ventricular tachycardia. *Journal of Interventional Cardiac Electrophysiology.* **7**(1), p.95–103.

Bogun, F., Good, E., Reich, S., Elmouchi, D., Igic, P., Lemola, K., Tschopp, D., Jongnarangsin, K., Oral, H., Chugh, A., Pelosi, F. and Morady, F. (2006). Isolated potentials during sinus rhythm and pace-mapping within scars as guides for ablation of post-infarction ventricular tachycardia. *Journal of the American College of Cardiology.* **47**(10), p.2013–2019.

Boyett, M. R. and Jewell, B. R. (1978). A study of the factors responsible for rate-dependent shortening of the action potential in mammalian ventricular muscle. *Journal of Physiology.* **285**(1), p.359–380.

Boyle, P. M., Park, C. J., Arevalo, H. J., Vigmond, E. J. and Trayanova, N. A. (2014). Sodium current reduction unmasks a structure-dependent substrate for arrhythmogenesis in the normal ventricles. *PLOS One.* **9**(1), p.1–9.

Brown, A. M., Lee, K. S. and Powell, T. (1981). Sodium current in single rat heart muscle cells. *Journal of Physiology.* **318**(1), p.479–500.

Brunckhorst, C. B., Stevenson, W. G., Soejima, K., Maisel, W. H., Delacretaz, E., Friedman, P. L. and Ben-haim, S. A. (2003). Relationship of slow conduction detected by pace-mapping to ventricular tachycardia re-entry circuit sites after infarction. *Journal of the American College of Cardiology.* **41**(5), p.802–809.

Callans, D. J., Zardini, M., Gottlieb, C. D. and Josephson, M. E. (1996). The variable contribution of functional and anatomic barriers in human ventricular tachycardia: an analysis with resetting from two sites. *Journal of the American College of Cardiology.* **27**(5), p.1106–1111.

Cao, J., Qu, Z., Kim, Y., Wu, T., Garfinkel, A., Weiss, J. N., Karagueuzian, H. S. and Chen, P. (1999). Spatiotemporal heterogeneity in the induction of ventricular fibrillation by rapid pacing. *Circulation Research.* **84**(11), p.1318–1331.

Carmeliet, E. (1999). Cardiac ionic currents and acute ischemia: from channels to arrhythmias. *Physiological Reviews.* **79**(3), p.917–1017.

Chang, M. G., Zhang, Y., Chang, C. Y., Xu, L., Emokpae, R., Tung, L., Marbán, E. and Abraham, M. R. (2009). Spiral waves and reentry dynamics in an in vitro model of the healed infarct border zone. *Circulation Research*. **105**(11), p.1062–1071.

Chen, J., Mandapati, R., Berenfeld, O., Skanes, A. C. and Jalife, J. (2000). High-frequency periodic sources underlie ventricular fibrillation in the isolated rabbit heart. *Circulation Research*. **86**(1), p.86–93.

Cherry, E. M. and Fenton, F. H. (2004). Suppression of alternans and conduction blocks despite steep APD restitution: electrotonic, memory, and conduction velocity restitution effects. *American Journal of Physiology. Heart and Circulatory Physiology*. **286**(6), p.H2332–H2341.

Cheung, P. H., Pugsley, M. K. and Walker, M. J. A. (1993). Arrhythmia models in the rat. *Journal of Pharmacological and Toxicological Methods*. **29**(4), p.179–184.

Child, N., Bishop, M. J., Hanson, B., Coronel, R., Opthof, T., Boukens, B. J., Walton, R. D., Efimov, I. R., Bostock, J., Hill, Y., Rinaldi, C. A., Razavi, R., Gill, J. and Taggart, P. (2015). An activation-repolarization time metric to predict localized regions of high susceptibility to reentry. *Heart Rhythm*. **12**(7), p.1644–1653.

Clark, R. B., Bouchard, R. A., Salinas-Stefanon, E., Sanchez-Chapula, J. and Giles, W. R. (1993). Heterogeneity of action potential waveforms and potassium currents in rat ventricle. *Cardiovascular Research*. **27**(10), p.1795–1799.

Clayton, R. H. (2008). Vortex filament dynamics in computational models of ventricular fibrillation in the heart. *Chaos*. **18**(4), p.1–11.

Clayton, R. H., Bernus, O., Cherry, E. M., Dierckx, H., Fenton, F. H., Mirabella, L., Panfilov, A. V., Sachse, F. B., Seemann, G. and Zhang, H. (2011). Models of cardiac tissue electrophysiology: progress, challenges and open questions. *Progress in Biophysics and Molecular Biology*. **104**(1), p.22–48.

Clayton, R. H. and Panfilov, A. V. (2008). A guide to modelling cardiac electrical activity in anatomically detailed ventricles. *Progress in Biophysics and Molecular Biology*. **96**(1), p.19–43.

Clayton, R. H. and Taggart, P. (2005). Regional differences in APD restitution can initiate wavebreak and re-entry in cardiac tissue: A computational study. *Biomedical Engineering Online*. **4**(54), p.1–14.

Clayton, R. H., Zhuchkova, E. A. and Panfilov, A. V. (2006). Phase singularities and filaments: simplifying complexity in computational models of ventricular fibrillation. *Progress in Biophysics and Molecular Biology*. **90**(1), p.378–398.

Clerc, L. (1976). Directional differences of impulse spread in trabecular muscle from mammalian heart. *Journal of Physiology*. **255**(2), p.335–346.

Collins, F. S., Green, E. D., Guttmacher, A. E. and Guyer, M. S. (2003). A vision for the future of genomics research. *Nature*. **422**(6934), p.835–847.

Comtois, P., Kneller, J. and Nattel, S. (2005). Of circles and spirals: bridging the gap between the leading circle and spiral wave concepts of cardiac reentry. *Europace*. **7**(2), p.10–20.

Coronel, R., DeBakker, J. M., Wilms-Schopman, F. J., Opthof, T., Linnenbank, A. C., Belterman, C. N. and Janse, M. J. (2006). Monophasic action potentials and activation recovery intervals as measures of ventricular action potential duration: experimental evidence to resolve some controversies. *Heart Rhythm*. **3**(9), p.1043–1050.

Coronel, R., Opthof, T., Taggart, P., Tytgat, J. and Veldkamp, M. (1997). Differential electrophysiology of repolarisation from clone to clinic. *Cardiovascular Research*. **33**(3), p.503–517.

Coronel, R., Wilms-Schopman, F. J. G. and Janse, M. J. (2010). Anti- or profibrillatory effects of Na+ channel blockade depend on the site of application relative to gradients in repolarization. *Frontiers in Physiology*. **1**(10), p.1–9.

Coronel, R., Wilms-Schopman, F. J. G., Opthof, T. and Janse, M. J. (2009). Dispersion of repolarization and arrhythmogenesis. *Heart Rhythm*. **6**(4), p.537–543.

De Bakker, J. M. T., Coronel, R., Tasseron, S., Wilde, A. A. M., Opthof, T., Janse, M. J., Van Capelle, F. J. L., Becker, A. E. and Jambroes, G. (1990). Ventricular tachycardia in the infarcted, Langendorff-perfused human heart: role of the arrangement of surviving cardiac fibres. *Journal of the American College of Cardiology*. **15**(7), p.1594–1607.

De Bakker, J. M. T., Van Capelle, F. J. L., Janse, M. J., Wilde, A. A. M., Coronel, R., Becker, A. E., Dingemans, K. P., Van Hemel, N. M. and Hauer, R. N. W. (1988). Reentry as a cause of ventricular tachycardia in patients with chronic ischemic heart disease: electrophysiologic and anatomic correlation. *Circulation.* **77**(3), p.589–606.

De Bakker, J. M., Van Capelle, F. J., Janse, M. J., Tasseron, S., Vermeulen, J. T., De Jonge, N. and Lahpor, J. R. (1993). Slow conduction in the infarcted human heart. 'Zigzag' course of activation. *Circulation.* **88**(3), p.915–926.

Decker, K. F. and Rudy, Y. (2010). Ionic mechanisms of electrophysiological heterogeneity and conduction block in the infarct border zone. *American Journal of Physiology. Heart and Circulatory Physiology.* **299**(5), p.H1588–H1597.

Deisboeck, T. S., Zhang, L., Yoon, J. and Costa, J. (2009). In silico cancer modelling: is it ready for prime time. *Nature Clinical Practice Oncology.* **6**(1), p.34–42.

Deo, M., Boyle, P., Plank, G. and Vigmond, E. (2009). Arrhythmogenic mechanisms of the Purkinje system during electric shocks: a modeling study. *Heart Rhythm.* **6**(12), p.1782–1789.

Dhalla, A. K. and Singal, P. K. (1994). Antioxidant changes in hypertrophied and failing guinea pig hearts. *American Journal of Physiology.* **266**(4), p.H1280–H1285.

Dun, W., Baba, S., Yagi, T. and Boyden, P. A. (2004). Dynamic remodeling of K+ and Ca+2 currents in cells that survived in the epicardial border zone of canine healed infarcted heart. *American Journal of Physiology. Heart and Circulatory Physiology.* **287**(3), p.H046–H1054.

Durrer, D., Schoo, L., Schuilenburg, R. M. and Wellens, J. J. (1967). Role of premature beats in the initiation and the termination of supraventricular tachycardia in the Wolff-Parkinson-White syndrome. *Circulation.* **36**(5), p.644–663.

Elshrif, M. M. and Cherry, E. M. (2014). A quantitative comparison of the behavior of human ventricular cardiac electrophysiology models in tissue. *PLOS One.* **9**(1), p.1–13.

Entcheva, E., Lu, S. N., Troppman, R. H., Sharma, V. and Tung, L. (2000). Contact fluorescence imaging of reentry in monolayers of cultured neonatal rat ventricular myocytes. *Journal of Cardiovascular Electrophysiology.* **11**(6), p.665–676.

Evans, G. A. (2000). Designer science and the "omic" revolution. *Nature Biotechnology*. **18**(2), p.127.

Fedorov, V. V., Lozinsky, I. T., Sosunov, E. A., Anyukhovsky, E. P., Rosen, M. R., Balke, C. W. and Efimov, I. R. (2007). Application of blebbistatin as an excitation-contraction uncoupler for electrophysiologic study of rat and rabbit hearts. *Heart Rhythm*. **4**(5), p.619–626.

Fenoglio, J. J., Pham, T., Harken, A. H., Horowitz, L. N., Josephson, M. E. and Wit, A. L. (1983). Recurrent sustained ventricular tachycardia: structure and ultrastructure of subendocardial regions in which tachycardia originates. *Circulation*. **68**(3), p.518–533.

Fenton, F. H. and Cherry, E. M.. (2008). *Models of cardiac cell*. [Online] Available from: http://www.scholarpedia.org/article/Models_of_cardiac_cell. [Accessed: July 2015].

Fink, M., Niederer, S. A., Cherry, E. M., Fenton, F. H., Koivumäki, J. T., Seemann, G., Thul, R., Zhang, H., Sachse, F. B., Beard, D., Crampin, E. J. and Smith, N. P. (2011). Cardiac cell modelling: observations from the heart of the cardiac physiome project. *Progress in Biophysics and Molecular Biology*. **104**(1-3), p.2–21.

Fitzgerald, D. M., Friday, K. J., Yeung Lai Wah, J. A., Lazzara, R. and Jackman, W. M. (1988). Electrogram patterns predicting successful catheter ablation of ventricular tachycardia. *Circulation*. **77**(4), p.806–814.

Forbes, M. S., Hawkey, L. A., Jirge, S. K. and Sperelakis, N. (1985). The sarcoplasmic reticulum of mouse heart: its divisions, configurations, and distribution. *Journal of Ultrastructure Research*. **93**(1-2), p.1–16.

Franz, W., Rothmann, T., Frey, N. and Katus, H. A. (1997). Analysis of tissue-specific gene delivery by recombinant adenoviruses containing cardiac-specific promoters. *Cardiovascular Research*. **35**(3), p.560–566.

Garfinkel, A., Kim, Y., Voroshilovsky, O., Qu, Z., Kil, J. R., Lee, M., Karagueuzian, H. S., Weiss, J. N. and Chen, P. (2000). Preventing ventricular fibrillation by flattening cardiac restitution. *Proceedings of the National Academy of Sciences*. **97**(11), p.6061–6066.

Girouard, S. D., Pastore, J. M., Laurita, K. R., Gregory, K. W. and Rosenbaum, D. S. (1996). Optical mapping in a new guinea pig model of ventricular tachycardia re-

veals mechanisms for multiple wavelengths in a single reentrant circuit. *Circulation*. **93**(3), p.603–613.

Girouard, S. D. and Rosenbaum, D. S. (2001). Role of wavelength adaptation in the initiation, maintenance, and pharmacologic suppression of reentry. *Journal of Cardiovascular Electrophysiology*. **12**(6), p.697–707.

Goldman, S. and Raya, T. E. (1995). Rat infarct model of myocardial infarction and heart failure. *Journal of Cardiac Failure*. **1**(2), p.169–177.

Gough, W. B., Hu, D. and El-Sherif, N. (1988). Effects of clofilium on ischemic subendocardial Purkinje fibers 1 day postinfarction. *Journal of the American College of Cardiology*. **11**(2), p.431–437.

Gough, W. B., Mehra, R., Restivo, M., Zeiler, R. H. and El-Sherif, N. (1985). Reentrant ventricular arrhythmias in the late myocardial infarction period in the dog. *Circulation Research*. **57**(3), p.432–442.

Grandi, E., Pasqualini, F. S. and Bers, D. M. (2010). A novel computational model of the human ventricular action potential and Ca transient. *Journal of Molecular and Cellular Cardiology*. **48**(1), p.112–121.

Gray, R. A., Pertsov, A. M. and Jalife, J. (1998). Spatial and temporal organization during cardiac fibrillation. *Nature*. **392**(6671), p.75–78.

Groenendaal, W., Ortega, F. A., Krogh-Madsen, T. and Christini, D. J. (2014). Voltage and calcium dynamics both underlie cellular alternans in cardiac myocytes. *Biophysical Journal*. **106**(10), p.2222–2232.

Han, J. and Moe, G. K. (1964). Nonuniform recovery of excitability in ventricular muscle. *Circulation Research*. **14**(1), p.44–60.

Haqqani, H. M., Morton, J. B. and Kalman, J. M. (2013). Channeling post-infarction ventricular tachycardia ablation. *Journal of the American College of Cardiology*. **61**(20), p.2096–2097.

Hayden, W. G., Hurley, E. J. and Rytand, D. A. (1967). The mechanism of canine atrial flutter. *Circulation Research*. **20**(5), p.496–505.

Ho, S. Y. (2009). Anatomy and myoarchitecture of the left ventricular wall in normal and in disease. *European Journal of Echocardiography.* **10**(8), p.iii3–iii7.

Hodgkin and Huxley (1952). A quantitative description of membrane current and its application to conduction and excitation in nerve. *Journal of Physiology.* **117**(4), p.500–544.

Holden, A. V., Aslanidi, O. V., Benson, A. P., Clayton, R. H., Halley, G., Li, P. and Tong, G. (2006). The virtual ventricular wall: a tool for exploring cardiac propagation and arrhythmogenesis. *Journal of Biological Physics.* **32**(3), p.355–368.

Holzem, K. M., Madden, E. J. and Efimov, I. R. (2014). Human cardiac systems electrophysiology and arrhythmogenesis: iteration of experiment and computation. *Europace.* **16**(4), p.77–85.

Jais, P., Maury, P., Khairy, P., Sacher, F., Nault, I., Komatsu, Y., Hocini, M., Forclaz, A., Jadidi, A. S., Weerasooryia, R., Shah, A., Derval, N., Cochet, H., Knecht, S., Miyazaki, S., Linton, N., Rivard, L., Wright, M., Wilton, S. B., Scherr, D., Pascale, P., Roten, L., Pederson, M., Bordachar, P., Laurent, F., Kim, S. J., Ritter, P., Clementy, J. and Haïssaguerre, M. (2012). Elimination of local abnormal ventricular activities. *Circulation.* **125**(18), p.2184–2196.

Janse, M. J., Capucci, A., Coronel, R. and Fabius, M. A. W. (1985). Variability of recovery of excitability in the normal canine and the ischaemic porcine heart. *European Heart Journal.* **6**(D), p.41–52.

Janse, M. J. and Wit, A. L. (1989). Electrophysiological mechanisms of ventricular arrhythmias resulting from myocardial ischemia and infarction. *Physiological Reviews.* **69**(4), p.1049–1169.

Jiang, M., Cabo, C., Yao, J., Boyden, P. A. and Tseng, G. (2000). Delayed rectifier K currents have reduced amplitudes and altered kinetics in myocytes from infarcted canine ventricle. *Cardiovascular Research.* **48**(1), p.34–43.

Kaltenbrunner, W., Cardinal, R., Dubuc, M., Shenasa, M., Nadeau, R., Tremblay, G., Vermeulen, M., Savard, P. and Page, P. L. (1991). Epicardial and endocardial mapping of ventricular tachycardia in patients with myocardial infarction. *Circulation.* **84**(3), p.1058–1071.

Kazbanov, I. V., Clayton, R. H., Nash, M. P., Bradley, C. P., Paterson, D. J., Hayward, M. P., Taggart, P. and Panfilov, A. V. (2014). Effect of global cardiac ischemia on human ventricular fibrillation: insights from a multi-scale mechanistic model of the human heart. *PLOS Computational Biology*. **10**(11), p.1–15.

Kim, Y., Kim, S., Kramer, C. M., Yatani, A., Takagi, G., Mankad, S., Szigeti, G. P., Singh, D., Bishop, S. P., Shannon, R. P., Vatner, D. E. and Vatner, S. F. (2002). Altered excitation-contraction coupling in myocytes from remodeled myocardium after chronic myocardial infarction. *Journal of Molecular and Cellular Cardiology*. **34**(1), p.63–73.

Kim, Y., Xie, F., Yashima, M., Wu, T., Valderrabano, M., Lee, M., Ohara, T., Voroshilovsky, O., Doshi, R. N., Fishbein, M. C., Qu, Z., Garfinkel, A., Weiss, J. N., Karagueuzian, H. S. and Chen, P. (1999). Role of papillary muscle in the generation and maintenance of reentry during ventricular tachycardia and fibrillation in isolated swine right ventricle. *Circulation*. **100**(13), p.1450–1459.

Koller, M. L., Riccio, M. L. and Gilmour, R. F. (1998). Dynamic restitution of action potential duration during electrical alternans and ventricular fibrillation. *American Journal of Physiology*. **275**(5), p.H1635–H1642.

Kondratyev, A. A., Ponard, J. G. C., Munteanu, A., Rohr, S. and Kucera, J. P. (2007). Dynamic changes of cardiac conduction during rapid pacing. *American Journal of Physiology. Heart and Circulatory Physiology*. **292**(4), p.H1796–H1811.

Koplan, B. A. and Stevenson, W. G. (2009). Ventricular tachycardia and sudden cardiac death. *Mayo Clinic Proceedings*. **84**(3), p.289–297.

Kuo, C., Munakata, K., Reddy, C. P. and Surawicz, B. (1983). Characteristics and possible mechanism of ventricular arrhythmia dependent on the dispersion of action potential durations. *Circulation*. **67**(6), p.1356–1367.

Lai, Y., Choy, Y. B., Haemmerich, D., Vorperian, V. R. and Webster, J. G. (2004). Lesion size estimator of cardiac radiofrequency ablation at different common locations with different tip temperatures. *IEEE Transactions on Biomedical Engineering*. **51**(10), p.1859–1864.

Lambiase, P. D., Rinaldi, A., Hauck, J., Mobb, M., Elliott, D., Mohammad, S., Gill, J. S.

and Bucknall, C. A. (2004). Non-contact left ventricular endocardial mapping in cardiac resynchronisation therapy. *Heart*. **90**(1), p.44–51.

Laurita, K. R. and Rosenbaum, D. S. (2000). Interdependence of modulated dispersion and tissue structure in the mechanism of unidirectional block. *Circulation Research*. **87**(10), p.922–929.

Lee, H., Lu, T., Weintraub, N. L., VanRollins, M., Spector, A. A. and Shibata, E. F. (1999). Effects of epoxyeicosatrienoic acids on the cardiac sodium channels in isolated rat ventricular myocytes. *Journal of Physiology*. **519**(1), p.153–168.

Lee, J., Niederer, S., Nordsletten, D., Le Grice, I., Smail, B., Kay, D. and Smith, N. (2009). Coupling contraction, excitation, ventricular and coronary blood flow across scale and physics in the heart. *Philosophical Transactions, Series A, Mathematical, Physical and Engineering Sciences*. **367**(1896), p.2311–2331.

Li, W., Ripplinger, C. M., Lou, Q. and Efimov, I. R. (2009). Multiple monophasic shocks improve electrotherapy of ventricular tachycardia in a rabbit model of chronic infarction. *Heart Rhythm*. **6**(7), p.1–17.

Lijnen, P. and Petrov, V. (1999). Renin-angiotensin system, hypertrophy and gene expression in cardiac myocytes. *Journal of Molecular and Cellular Cardiology*. **31**(5), p.949–970.

Lim, Z. Y., Maskara, B., Aguel, F., Emokpae, R. and Tung, L. (2006). Spiral wave attachment to millimeter-sized obstacles. *Circulation*. **114**(20), p.2113–2121.

Litwin, S. E. and Bridge, J. H. (1997). Enhanced Na(+)-Ca2+ exchange in the infarcted heart. Implications for excitation-contraction coupling. *Circulation Research*. **81**(6), p.1083–1093.

Liu, Y., Cabo, C., Salomonsz, R., Delmar, M., Davidenko, J. and Jalife, J. (1993). Effects of diacetyl monoxime on the electrical properties of sheep and guinea pig ventricular muscle. *Cardiovascular Research*. **27**(11), p.1991–1997.

Lou, Q., Li, W. and Efimov, I. R. (2012). The role of dynamic instability and wavelength in arrhythmia maintenance as revealed by panoramic imaging with blebbistatin vs. 2,3-butanedione monoxime. *American Journal of Physiology. Heart and Circulatory Physiology*. **302**(1), p.H262–269.

Lue, W. and Boyden, P. A. (1992). Abnormal electrical properties of myocytes from chronically infarcted canine heart. *Circulation*. **85**(3), p.1175–1188.

Luke, R. A. and Saffitz, J. E. (1991). Remodeling of ventricular conduction pathways in healed canine infarct border zones. *Journal of Clinical Investigation*. **87**(5), p.1594–1602.

Luo, C. H. and Rudy, Y. (1991). A model of the ventricular cardiac action potential. Depolarization, repolarization, and their interaction. *Circulation Research*. **68**(6), p.1501–1526.

Luo, C. H. and Rudy, Y. (1994). A dynamic model of the cardiac ventricular action potential. I. Simulations of ionic currents and concentration changes. *Circulation Research*. **74**(6), p.1071–1096.

Mahaffey, K. W., Raya, T. E., Pennock, G. D., Morkin, E. and Goldman, S. (1995). Left ventricular performance and remodeling in rabbits after myocardial infarction. *Circulation*. **91**(3), p.794–801.

Mahajan, A., Shiferaw, Y., Sato, D., Baher, A., Olcese, R., Xie, L., Yang, M., Chen, P., Restrepo, J. G., Karma, A., Garfinkel, A., Qu, Z. and Weiss, J. N. (2008). A rabbit ventricular action potential model replicating cardiac dynamics at rapid heart rates. *Biophysical Journal*. **94**(2), p.392–410.

Marchlinski, F. E., Callans, D. J., Gottlieb, C. D. and Zado, E. (2000). Linear ablation lesions for control of unmappable ventricular tachycardia in patients with ischemic and nonischemic cardiomyopathy. *Circulation*. **101**(11), p.1288–1297.

Matthews, G. D. K., Guzadhur, L., Sabir, I. N., Grace, A. A. and Huang, C. L. H. (2013). Action potential wavelength restitution predicts alternans and arrhythmia in murine Scn5a+/- hearts. *Journal of Physiology*. **591**(17), p.4167–4188.

Mayer, A. G. (1906). *Rhythmical pulsation in Scyphomedusae*. Washington DC: Carnegie Institute of Washington.

McDowell, K. S., Arevalo, H. J., Maleckar, M. M. and Trayanova, N. A. (2011). Susceptibility to arrhythmia in the infarcted heart depends on myofibroblast density. *Biophysical Journal*. **101**(6), p.1307–1315.

Mercader, M., Swift, L., Sood, S., Asfour, H., Kay, M. and Sarvazyan, N. (2012). Use of endogenous NADH fluorescence for real-time in situ visualization of epicardial radiofrequency ablation lesions and gaps. *American Journal of Physiology. Heart and Circulatory Physiology.* **302**(10), p.H2131–H2138.

Mines, G. R. (1913). On dynamic equilibrium in the heart. *Journal of Physiology.* **46**(4-5), p.349–383.

Mines, G. R. (1914). On circulating excitations in heart muscles and their possible relation to tachycardia and fibrillation. *Transactions of the Royal Society of Canada.* **IV**, p.43–52.

Mirams, G. R., Davies, M. R., Cui, Y., Kohl, P. and Noble, D. (2012). Application of cardiac electrophysiology simulations to pro-arrhythmic safety testing. *British Journal of Pharmacology.* **167**(5), p.932–945.

Morady, F., Harvey, M., Kalbfleisch, S. J., El-atassi, R., Calkins, H. and Langberg, J. J. (1993). Radiofrequency catheter ablation of ventricular tachycardia in patients with coronary artery disease. *Circulation.* **87**(2), p.363–373.

Morgan, J. M., Cunningham, D. and Rowland, E. (1992). Dispersion of monophasic action potential duration: demonstrable in humans after premature ventricular extrastimulation but not in steady state. *Journal of the American College of Cardiology.* **19**(6), p.1244–1253.

Mountantonakis, S. E., Park, R. E., Frankel, D. S., Hutchinson, M. D., Dixit, S., Cooper, J., Callans, D., Marchlinski, F. E. and Gerstenfeld, E. P. (2013). Relationship between voltage map "channels" and the location of critical isthmus sites in patients with post-infarction cardiomyopathy and ventricular tachycardia. *Journal of the American College of Cardiology.* **61**(20), p.2088–2095.

Nabauer, M., Beuckelmann, D. J., Uberfuhr, P. and Steinbeck, G. (1996). Regional differences in current density and rate-dependent properties of the transient outward current in subepicardial and subendocardial myocytes of human left ventricle. *Circulation.* **93**(1), p.168–177.

Nagatomo, T., Fan, Z., Ye, B., Tonkovich, G. S., January, C. T., Kyle, J. W. and Makielski, J. C. (1998). Temperature dependence of early and late currents in human cardiac wild-

type and long Q-T delta-KPQ Na+ channels. *American Journal of Physiology. Heart and Circulatory Physiology.* **275**(6), p.H2016–H2024.

Nanthakumar, K., Walcott, G. P., Melnick, S., Rogers, J. M., Kay, M. W., Smith, W. M., Ideker, R. E. and Holman, W. (2004). Epicardial organization of human ventricular fibrillation. *Heart Rhythm.* **1**(1), p.14–23.

Nash, M. P., Bradley, C. P., Sutton, P. M., Clayton, R. H., Kallis, P., Hayward, M. P., Paterson, D. J. and Taggart, P. (2006). Whole heart action potential duration restitution properties in cardiac patients: a combined clinical and modelling study. *Experimental Physiology.* **91**(2), p.339–54.

Niederer, S. A., Fink, M., Noble, D. and Smith, N. P. (2009). A meta-analysis of cardiac electrophysiology computational models. *Experimental Physiology.* **94**(5), p.486–495.

Niederer, S. A. and Smith, N. P. (2012). At the heart of computational modelling. *Journal of Physiology.* **590**(6), p.1331–1338.

Nielsen, T. D., Huang, J., Rogers, J. M., Killingsworth, C. R. and Ideker, R. E. (2009). Epicardial mapping of ventricular fibrillation over the posterior descending artery and left posterior papillary muscle of the swine heart. *Journal of Interventional Cardiac Electrophysiology.* **24**(1), p.11–7.

Nilius, B. (1988). Calcium block of guinea-pig heart sodium channels with and without modification by the piperazinylindole DPI 201-106. *Journal of Physiology.* **399**(1), p.537–558.

Nolasco, J. B. and Dahlen, R. W. (1968). A graphic method for the study of alternation in cardiac action potentials. *Journal of Applied Physiology.* **25**(2), p.191–196.

O'Hara, T. and Rudy, Y. (2012). Quantitative comparison of cardiac ventricular myocyte electrophysiology and response to drugs in human and nonhuman species. *American Journal of Physiology. Heart and Circulatory Physiology.* **302**(5), p.H1023–1030.

O'Hara, T., Virag, L., Varro, A. and Rudy, Y. (2011). Simulation of the undiseased human cardiac ventricular action potential: model formulation and experimental validation. *PLoS Computational Biology.* **7**(5), p.1–29.

Opthof, T., Coronel, R., Wilms-Schopman, F. J. G., Plotnikov, A. N., Shlapakova, I. N., Danilo, P., Rosen, M. R. and Janse, M. J. (2007). Dispersion of repolarization in canine ventricle and the electrocardiographic T wave: Tp-e interval does not reflect transmural dispersion. *Heart Rhythm.* **4**(3), p.341–348.

Osadchii, O. E. (2014). Effects of Na+ channel blockers on extrasystolic stimulation-evoked changes in ventricular conduction and repolarization. *Journal of Cardiovascular Pharmacology.* **63**(3), p.240–251.

Pak, H., Oh, Y., Liu, Y., Wu, T., Karagueuzian, H. S., Lin, S. and Chen, P. (2003). Catheter ablation of ventricular fibrillation in rabbit ventricles treated with beta-blockers. *Circulation.* **108**(25), p.3149–3156.

Pandit, S. V., Clark, R. B., Giles, W. R. and Demir, S. S. (2001). A mathematical model of action potential heterogeneity in adult rat left ventricular myocytes. *Biophysical Journal.* **81**(6), p.3029–3051.

Panfilov, A. and Keener, J. P. (1995). Re-entry in an anatomical model of the heart. *Chaos, Solitons and Fractals.* **5**(3), p.681–689.

Panfilov, A. V. (2006). Is heart size a factor in ventricular fibrillation? Or how close are rabbit and human hearts. *Heart Rhythm.* **3**(7), p.862–864.

Pastore, J. M. and Rosenbaum, D. S. (2000). Role of structural barriers in the mechanism of alternans-induced reentry. *Circulation Research.* **87**(12), p.1157–1163.

Pertsov, A. M., Davidenko, J. M., Salomonsz, R., Baxter, W. T. and Jalife, J. (1993). Spiral waves of excitation underlie reentrant activity in isolated cardiac muscle. *Circulation Research.* **72**(3), p.631–650.

Peters, N. S., Coromilas, J., Severs, N. J. and Wit, A. L. (1997). Disturbed connexin43 gap junction distribution correlates with the location of reentrant circuits in the epicardial border zone of healing canine infarcts that cause ventricular tachycardia. *Circulation.* **95**(4), p.988–996.

Pinto, J. M. B. and Boyden, P. A. (1998). Reduced inward rectifying and increased E-4031-sensitive K+ current density in arrhythmogenic subendocardial Purkinje myocytes from the infarcted heart. *Journal of Cardiovascular Electrophysiology.* **9**(3), p.299–311.

Plank, G., Zhou, L., Greenstein, J. L., Cortassa, S., Winslow, R. L., O'Rourke, B. and Trayanova, N. A. (2008). From mitochondrial ion channels to arrhythmias in the heart: computational techniques to bridge the spatio-temporal scales. *Philosophical Transactions, Series A, Mathematical, Physical and Engineering Sciences*. **366**(1879), p.3381–3409.

Priebe, L. and Beuckelmann, D. J. (1998). Simulation study of cellular electric properties in heart failure. *Circulation Research*. **82**(11), p.1206–1223.

Pu, J. and Boyden, P. A. (1997). Alterations of Na+ currents in myocytes from epicardial border zone of the infarcted heart. A possible ionic mechanism for reduced excitability and postrepolarization refractoriness. *Circulation Research*. **81**(1), p.110–119.

Puglisi, J. L. and Bers, D. M. (2001). LabHEART: an interactive computer model of rabbit ventricular myocyte ion channels and Ca transport. *American Journal of Physiology. Heart and Circulatory Physiology*. **281**(6), p.C2049–C2060.

Qin, D., Zhang, Z. H., Caref, E. B., Boutjdir, M., Jain, P. and El-Sherif, N. (1996). Cellular and ionic basis of arrhythmias in postinfarction remodeled ventricular myocardium. *Circulation Research*. **79**(3), p.461–473.

Qu, Z., Garfinkel, A., Chen, P. and Weiss, J. N. (2000). Mechanisms of discordant alternans and induction of reentry in simulated cardiac tissue. *Circulation*. **102**(14), p.1664–1671.

Qu, Z., Weiss, J. N. and Garfinkel, A. (1999). Cardiac electrical restitution properties and stability of reentrant spiral waves: a simulation study. *American Journal of Physiology*. **276**(1), p.H269–H283.

Rantner, L. J., Arevalo, H. J., Constantino, J. L., Efimov, I. R., Plank, G. and Trayanova, N. A. (2012). Three-dimensional mechanisms of increased vulnerability to electric shocks in myocardial infarction: altered virtual electrode polarizations and conduction delay in the peri-infarct zone. *Journal of Physiology*. **590**(18), p.4537–4551.

Rasmusson, R. L., Clark, J. W., Giles, W. R., Robinson, K., Clark, R. B., Shibata, E. F. and Campbell, D. L. (1990). A mathematical model of electrophysiological activity in a bullfrog atrial cell. *American Journal of Physiology. Heart and Circulatory Physiology*. **259**(2), p.H370–H389.

Ripplinger, C. M., Lou, Q., Li, W., Hadley, J. and Efimov, I. R. (2009). Panoramic imaging reveals basic mechanisms of induction and termination of ventricular tachycardia in rabbit heart with chronic infarction: implications for low-voltage cardioversion. *Heart Rhythm.* **6**(1), p.1–19.

Romero, L., Trenor, B., Ferrero, J. M. and Starmer, C. F. (2013). Non-uniform dispersion of the source-sink relationship alters wavefront curvature. *PLOS One.* **8**(11), p.1–12.

Rosenbaum, D. S., Kaplan, D. T., Kanai, A., Jackson, L., Garan, H., Cohen, R. J. and Salama, G. (1991). Repolarization inhomogeneities in ventricular myocardium change dynamically with abrupt cycle length shortening. *Circulation.* **84**(3), p.1333–1346.

Rudy, Y. and Silva, J. R. (2006). Computational biology in the study of cardiac ion channels and cell electrophysiology. *Quarterly Reviews of Biophysics.* **39**(1), p.57–116.

Rutherford, S. L., Trew, M. L., Sands, G. B., LeGrice, I. J. and Smaill, B. H. (2012). High-resolution 3-dimensional reconstruction of the infarct border zone: impact. *Circulation Research.* **111**(3), p.301–311.

Saffitz, J. E. (1994). Myocyte interconnections at gap junctions and the development of anatomic substrates of ventricular arrhythmias. *Cardiovascular Pathology.* **3**(2), p.87–91.

Sakmann, B. and Trube, G. (1984). Voltage-dependent inactivation of inward-rectifying single-channel currents in the guinea-pig heart cell membrane. *Journal of Physiology.* **347**(1), p.659–683.

Sallé, L., Kharche, S., Zhang, H. and Brette, F. (2008). Mechanisms underlying adaptation of action potential duration by pacing rate in rat myocytes. *Progress in Biophysics and Molecular Biology.* **96**(1), p.305–320.

Scheinman, M. M., Morady, F., Hess, D. S. and Gonzalez, R. (1982). Catheter-induced ablation of the atrioventricular junction to control refractory supraventricular arrhythmias. *The Journal of the American Medical Association.* **248**(7), p.851–855.

Segal, O. R., Chow, A. W. C., Peters, N. S. and Wyn Davies, D. (2010). Mechanisms that initiate ventricular tachycardia in the infarcted human heart. *Heart Rhythm.* **7**(1), p.57–64.

Sermesant, M., Rhode, K., Sanchez-Ortiz, G. I., Camara, O., Andriantsimiavona, R., Hegde, S., Rueckert, D., Lambiase, P., Bucknall, C., Rosenthal, E., Delingette, H., Hill, D. L. G., Ayache, N. and Razavi, R. (2005). Simulation of cardiac pathologies using an electromechanical biventricular model and XMR interventional imaging. *Medical Image Analysis*. **9**(5), p.467–480.

Shannon, T. R., Wang, F., Puglisi, J., Weber, C. and Bers, D. M. (2004). A mathematical treatment of integrated Ca dynamics within the ventricular myocyte. *Biophysical Journal*. **87**(5), p.3351–3371.

Sheridan, P. J., Marques, J. L., Newman, C. M., Heller, S. R. and Clayton, R. H. (2010). Rate-dependent measures of repolarization predict inducibility of ventricular arrhythmias. *Europace*. **12**(4), p.553–560.

Shiferaw, Y., Watanabe, M. A., Garfinkel, A., Weiss, J. N. and Karma, A. (2003). Model of intracellular calcium cycling in ventricular myocytes. *Biophysical Journal*. **85**(6), p.3666–3686.

Shimoni, Y., Severson, D. and Giles, W. (1995). Thyroid status and diabetes modulate regional differences in potassium currents in rat ventricle. *Journal of Physiology*. **488**(3), p.673–688.

Smeets, J. L., Allessie, M. A., Lammers, W. J., Bonke, F. I. and Hollen, J. (1986). The wavelength of the cardiac impulse and reentrant arrhythmias in isolated rabbit atrium. The role of heart rate, autonomic transmitters, temperature, and potassium. *Circulation Research*. **58**(1), p.96–108.

Smith, N., Waters, S., Hunter, P. and Clayton, R. (2011). The cardiac physiome: foundations and future prospects for mathematical modelling of the heart. *Progress in Biophysics and Molecular Biology*. **104**(1), p.1.

Spear, J. F., Horowitz, L. N., Hodess, A. B., MacVaugh, H. and Moore, N. (1979). Cellular electrophysiology of human myocardial infarction. *Circulation*. **59**(2), p.247–256.

Stengl, M., Carmeliet, E., Mubagwa, K. and Flameng, W. (1998). Modulation of transient outward current by extracellular protons and Cd2+ in rat and human ventricular myocytes. *Journal of Physiology*. **511**(3), p.827–836.

Stern, M. D., Song, L., Cheng, H., Sham, J. S. K., Tian Yang, H., Boheler, K. R. and Ríos, E. (1999). Local control models of cardiac excitation – contraction coupling. *Journal of General Physiology*. **113**(3), p.469–489.

Stevenson, W. G. (2009). Ventricular scars and ventricular tachycardia. *Transactions of the American Clinical and Climatological Association*. **120**(1), p.403–412.

Stevenson, W. G., Khan, H., Sager, P., Saxon, L. A., Middlekauff, H. R., Natterson, P. D. and Wiener, I. (1993). Identification of reentry circuit sites during catheter mapping and radiofrequency ablation of ventricular tachycardia late after myocardial infarction. *Circulation*. **88**(4), p.1647–1670.

Stevenson, W. G., Sager, P., Nademanee, K., Hassan, H., Middlekauff, H. R., Saxon, L. A. and Wiener, I. (1992). Identifying sites for catheter ablation of ventricular tachycardia. *Herz*. **17**(3), p.158–170.

Stevenson, W. G., Sager, P. T. and Friedman, P. L. (1995). Entrainment techniques for mapping atrial and ventricular tachycardias. *Journal of Cardiovascular Electrophysiology*. **6**(3), p.201–216.

Stevenson, W. G., Weiss, J. N., Wiener, I. and Nademanee, K. (1989). Slow conduction in the infarct scar: relevance to the occurrence, detection, and ablation of ventricular reentry circuits resulting from myocardial infarction. *American Heart Journal*. **117**(2), p.452–467.

Stevenson, W. G., Weiss, J. N., Wiener, I., Rivitz, M., Nademanee, K., Klitzner, T., Yeatman, L., Josephson, M. and Wohlgelernter, D. (1989). Fractionated endocardial electrograms are associated with slow conduction in humans: evidence from pace-mapping. *Journal of the American College of Cardiology*. **13**(2), p.369–376.

Stevenson, W. G., Weiss, J., Wiener, I., Wohlgelernter, D. and Yeatman, L. (1987). Localization of slow conduction in a ventricular tachycardia circuit: Implications for catheter ablation. *American Heart Journal*. **114**(5), p.1253–1258.

Strohmer, B. and Hwang, C. (2003). Ablation of postinfarction ventricular tachycardia guided by isolated diastolic potentials. *Europace*. **5**(4), p.375–380.

Taggart, P., Orini, M., Hanson, B., Hayward, M., Clayton, R., Dobrzynski, H., Yanni, J., Boyett, M. and Lambiase, P. D. (2014). Developing a novel comprehensive framework for

the investigation of cellular and whole heart electrophysiology in the in situ human heart: historical perspectives, current progress and future prospects. *Progress in Biophysics and Molecular Biology*. **115**(2-3), p.252–260.

Taggart, P., Sutton, P. M., Opthof, T., Coronel, R., Trimlett, R., Pugsley, W. and Kallis, P. (2001). Transmural repolarisation in the left ventricle in humans during normoxia and ischaemia. *Cardiovascular Research*. **50**(3), p.454–462.

Takemoto, Y., Takanari, H., Honjo, H., Ueda, N., Harada, M., Kato, S., Yamazaki, M., Sakuma, I., Opthof, T., Kodama, I. and Kamiya, K. (2012). Inhibition of intercellular coupling stabilizes spiral-wave reentry, whereas enhancement of the coupling destabilizes the reentry in favor of early termination. *American Journal of Physiology. Heart and Circulatory Physiology*. **303**(5), p.H578–H586.

Ten Tusscher, K. H. W. J., Hren, R. and Panfilov, A. V. (2007). Organization of ventricular fibrillation in the human heart. *Circulation Research*. **100**(12), p.e87–e101.

Ten Tusscher, K. H. W. J., Mourad, A., Nash, M. P., Clayton, R. H., Bradley, C. P., Paterson, D. J., Hren, R., Hayward, M., Panfilov, A. V. and Taggart, P. (2009). Organization of ventricular fibrillation in the human heart: experiments and models. *Experimental Physiology*. **94**(5), p.553–562.

Ten Tusscher, K. H. W. J., Noble, D., Noble, P. J. and Panfilov, A. V. (2004). A model for human ventricular tissue. *American Journal of Physiology. Heart and Circulatory Physiology*. **286**(4), p.H1573–H1589.

Ten Tusscher, K. H. W. J. and Panfilov, A. V. (2006). Alternans and spiral breakup in a human ventricular tissue model. *American Journal of Physiology. Heart and Circulatory Physiology*. **291**(3), p.H1088–H1100.

Trayanova, N. A. (2011). Whole-heart modeling: applications to cardiac electrophysiology and electromechanics. *Circulation Research*. **108**(1), p.113–128.

Trayanova, N. A. and Rantner, L. J. (2014). New insights into defibrillation of the heart from realistic simulation studies. *Europace*. **16**(5), p.705–713.

Trayanova, N. A. and Rice, J. J. (2011). Cardiac electromechanical models: from cell to organ. *Frontiers in Physiology*. **2**(43), p.1–19.

Troy, B. L., Pombo, J. and Racakley, C. E. (1972). Measurement of left ventricular wall thickness and mass by echocardiography. *Circulation*. **45**(3), p.602–611.

Tung, R., Boyle, N. G. and Shivkumar, K. (2010). Catheter ablation of ventricular tachycardia. *Circulation*. **122**(3), p.e389–e391.

Van Capelle, F. J. L. and Durrer, D. (1980). Computer simulation of arrhythmias in a network of coupled excitable elements. *Circulation Research*. **47**(3), p.454–467.

Verma, A., Marrouche, N. F., Schweikert, R. A., Saliba, W., Wazni, O., Cummings, J., Abdul-karim, A., Bhargava, M., Burkhardt, D., Kilicaslan, F., Martin, D. O. and Natale, A. (2005). Relationship between successful ablation sites and the scar border zone defined by substrate mapping for ventricular tachycardia post-myocardial infarction. *Journal of Cardiovascular Electrophysiology*. **16**(5), p.465–471.

Vetter, F. J. and McCulloch, A. D. (1998). Three-dimensional analysis of regional cardiac function: a model of rabbit ventricular anatomy. *Progress in Biophysics and Molecular Biology*. **69**(2-3), p.157–183.

Volk, T., Nguyen, T. H., Schultz, J., Faulhaber, J. and Ehmke, H. (2001). Regional alterations of repolarizing K+ currents among the left ventricular free wall of rats with ascending aortic stenosis. *Journal of Physiology*. **530**(3), p.433–455.

Weis, T., Berger, F. and Borchard, U. (1993). A slowly inactivating transient outward current in rat ventricular myocytes. *Pflugers Archiv*. **425**(1-2), p.184–186.

Weiss, J. N., Chen, P., Qu, Z., Karagueuzian, H. S. and Garfinkel, A. (2000). Ventricular fibrillation: how do we stop the waves from breaking. *Circulation Research*. **87**(12), p.1103–1107.

Winslow, R. L., Rice, J., Jafri, S., Marban, E. and O'Rourke, B. (1999). Mechanisms of altered excitation-contraction coupling in canine tachycardia-induced heart failure, II: Model Studies. *Circulation Research*. **84**(5), p.571–586.

Wu, T., Lin, S., Baher, A., Qu, Z., Garfinkel, A., Weiss, J. N., Ting, C. and Chen, P. (2004). Mother rotors and the mechanisms of D600-induced type 2 ventricular fibrillation. *Circulation*. **110**(15), p.2110–2118.

Wu, T., Lin, S., Weiss, J. N., Ting, C. and Chen, P. (2002). Two types of ventricular fibrillation in isolated rabbit hearts. *Circulation*. **106**(14), p.1859–1866.

Wu, Y., Yin, X., Wijaya, C., Huang, M. and McConnell, B. K. (2011). Acute myocardial infarction in rats. *Journal of Visualized Experiments*. **48**(2646), p.1–5.

Xie, F., Qu, Z. and Garfinkel, A. (1998). Dynamics of reentry around a circular obstacle in cardiac tissue. *Physical Review E*. **58**(5), p.6355–6358.

Xie, F., Qu, Z., Garfinkel, A. and Weiss, J. N. (2002). Electrical refractory period restitution and spiral wave reentry in simulated cardiac tissue. *American Journal of Physiology. Heart and Circulatory Physiology*. **283**(1), p.H448–H460.

Yang, J. H. and Saucerman, J. J. (2011). Computational models reduce complexity and accelerate insight into cardiac signaling networks. *Circulation Research*. **108**(1), p.85–97.

Yao, J., Hussain, W., Patel, P., Peters, N. S., Boyden, P. A. and Wit, A. L. (2003). Remodeling of gap junctional channel function in epicardial border zone of healing canine infarcts. *Circulation Research*. **92**(4), p.437–443.

Yao, J., Jiang, M., Fan, J., Zhou, Y. and Tseng, G. (1999). Heterogeneous changes in K currents in rat ventricles three days after myocardial infarction. *Cardiovascular Research*. **44**(1), p.132–145.